Note: PDF may contain graphics errors, for example, the delta symbol sometimes changes to '?'

SURFACE WATER VAPOR EXCHANGES ON THE GREENLAND ICE SHEET DERIVED FROM AUTOMATED WEATHER STATION DATA

by

JASON ERIC BOX

B.A., University of Colorado, 1994

M.A., University of Colorado, 1997

A thesis submitted to the

Faculty of the Graduate School of the

University of Colorado in partial fulfillment

of the requirements for the degree of

Doctor of Philosophy

Department of Geography

2001

Box, Jason Eric (Ph.D. Geography)

Surface Water Vapor Exchanges on the Greenland Ice Sheet Derived From Automated Weather Station Data

Thesis directed by Professor Konrad Steffen

Greenland Climate Network (GC-Net) meteorological observations are used to estimate surface water vapor exchanges at Greenland ice sheet sites and for the ice sheet as a whole for the period of mid 1995 to mid 2000. Water vapor fluxes were derived using aerodynamic profile methods and validated with eddy correlation and evaporation pan measurements. A net water vapor flux to the atmosphere predominates in summer below 2000 m elevation sites. The net water vapor flux is -87 ±30 mm y^{-1} water equivalence in the Jakobshavn ablation region at 962 m elevation and -74 ±26 mm y^{-1} at equilibrium line altitude (1150 m) 17 km up-glacier. Net deposition is observed at an undulation trough site, whereas at the adjacent crest site, 6 km away, net water vapor loss is observed. At high elevation sites, the annual water vapor flux is towards the surface, approximately +15 mm y^{-1}. Comparison of monthly values with output from the NCAR Mesoscale Model (MM5) indicate that the month to month variability is well reproduced; yet the magnitude is underestimated by as much as 150%.

Based on a trend surface regression of the temperature lapse rate along the slope, elevation, and latitude, a Greenland ice sheet annual net total water vapor flux of $-7.34 \pm 4.4 \times 10^{13}$ kg y^{-1} is derived. This estimates is similar to the result of -6.18×10^{13} kg y^{-1} [*Ohmura et al.,* 1999] based on atmospheric modeling. The precipitation loss is estimated to be 14%, given an ice sheet accumulation estimate of 5.90×10^{14} kg y^{-1} by *Ohmura et al.* [1999].

Annual blowing snow sublimation is estimated using a bulk snow transport formulation and a conceptual model of maximum blowing snow transport distance. The actual blowing snow transport is estimated using potential transport calculations derived from wind speed records and a snow availability factor derived from air temperature and surface height measurements. Blowing snow sublimation rates are estimated to be as great as 500 mm y^{-1} at sites with strongest winds.

This thesis is dedicated to the taxpayers

Acknowledgements

I would like to acknowledge a number of people and organizations without the support of whom, this thesis would not have been possible. Firstly, the advice and experience of my primary advisor, Dr. Konrad Steffen, from which many valuable lessons were learned, is greatly valued. The NASA Polar Oceans Division is thanked for funding the Greenland Climate Network effort for the past 6 years. Those who willingly pay taxes are also thanked. NSF OPP has sponsored two Greenland Climate Network sites in the north of Greenland. The Summit, NGRIP, and DYE2, GITS, and NASA-U sites were accessible with NSF supported flights from the 109th ANG LC-130H, Scotia, NY, USA. Thanks to PICO and VECO staff and NGRIP personnel for logistics support. N. Cullen maintained eddy correlation measurements in 1999 and 2000. Personal communication with P. Calanca, and critical insight from JGR reviewers is greatly appreciated. Thanks to E. Eisen for technical support. Field work was aided in chronological order by Bob Thomas, Bill Sterling, Gordon Hamilton, W. J. Weber, C. Schneeberger, W. Abdalati, Earl Ramsey, Jay Kyne, P J O'Neil, F. Larsen, N. Cullen, Kate Daniels, and Sandy Starkweather. The understanding of family and friends K. Mezgolits is also invaluable. Thanks to Dr. M. C. Serreze for initial opportunity in climatological research. Classes taught by Dr. R. G. Barry were most valuable. The large amount of experience of Dr. R. D. Tabler in the blowing snow subject was most enlightening. Thanks also to my other advisors Dr. T. Pfeffer and Dr. M. Williams. Thanks to those who shared data based on their individual efforts: Dr. D. Bromwich and Dr. J. Cassano; Dr. Ellen Moseley-Thompson; N. Cullen; and of course Koni Steffen. Thanks to Ted DeMaria, CIRES computing facility people, especially John Kauzlaric, and many others at CIRES who have maintained the infrastructure to carry out scientific research at a high level of quality.

Table of Contents

1 Introduction

1.1 The Greenland Ice Sheet

The island of Greenland is 82% covered by a single ice sheet, 1.736 x 10^6 km^2 in area, 2.6 x 10^6 km^3 in volume, containing 8% of global ice volume [*Thomas,* 1993]. The ice sheet assumes the form of a dome rising to an elevation of 3250 m [*Ekholm,* 1996; *Bamber et al.,* submitted] (Figure 1.1). Isolated glaciers and small ice caps that occur around the periphery total 4.9 x 10^4 km^2 [*Ohmura et al.,* 1999]. The ice sheet is almost 2,400 kilometers long in latitude extent, and its greatest width is 1,100 kilometers at a latitude of 77º N. At present, Greenland's contribution to sea level if completely melted would be 7.4 m [*Warrick et al.,* 1996]. The current contribution of the ice sheet mass balance is unknown but is expected to be on the order of the current observed sea level change [*Reeh,* 1999]. Recent results indicate that Greenland's contribution to sea level was substantially greater than Antarctica during the Eemian [*Cuffey and Marshall,* 2000]. The Greenland ice sheet is huge compared with other glaciers in the world except that of Antarctica, which is roughly 10 times the area and 8 times the volume. Unlike Antarctica, centered near the south pole, the Greenland ice sheet extends 600 km equatorward of the polar circle. The ice sheet is situated in the path of atmospheric planetary wave circulation and imposes a significant orographic barrier [*Barry and Kiladis,* 1982].

Zones of varying snow properties are found on the Greenland ice sheet [*Benson,* 1962]. A zone of net snow accumulation comprising 90% of the ice sheet surface area is found above an average altitude of 1200 m [*Ohmura et al.,* 1999]. Net mass loss by melting and evaporation, known as *ablation*, predominates at the lowest elevations, i.e. below 1000 m in central western Greenland. In between these accumulation and ablation zones is an equilibrium line where in a normal year, annual accumulation and ablation are equivalent.

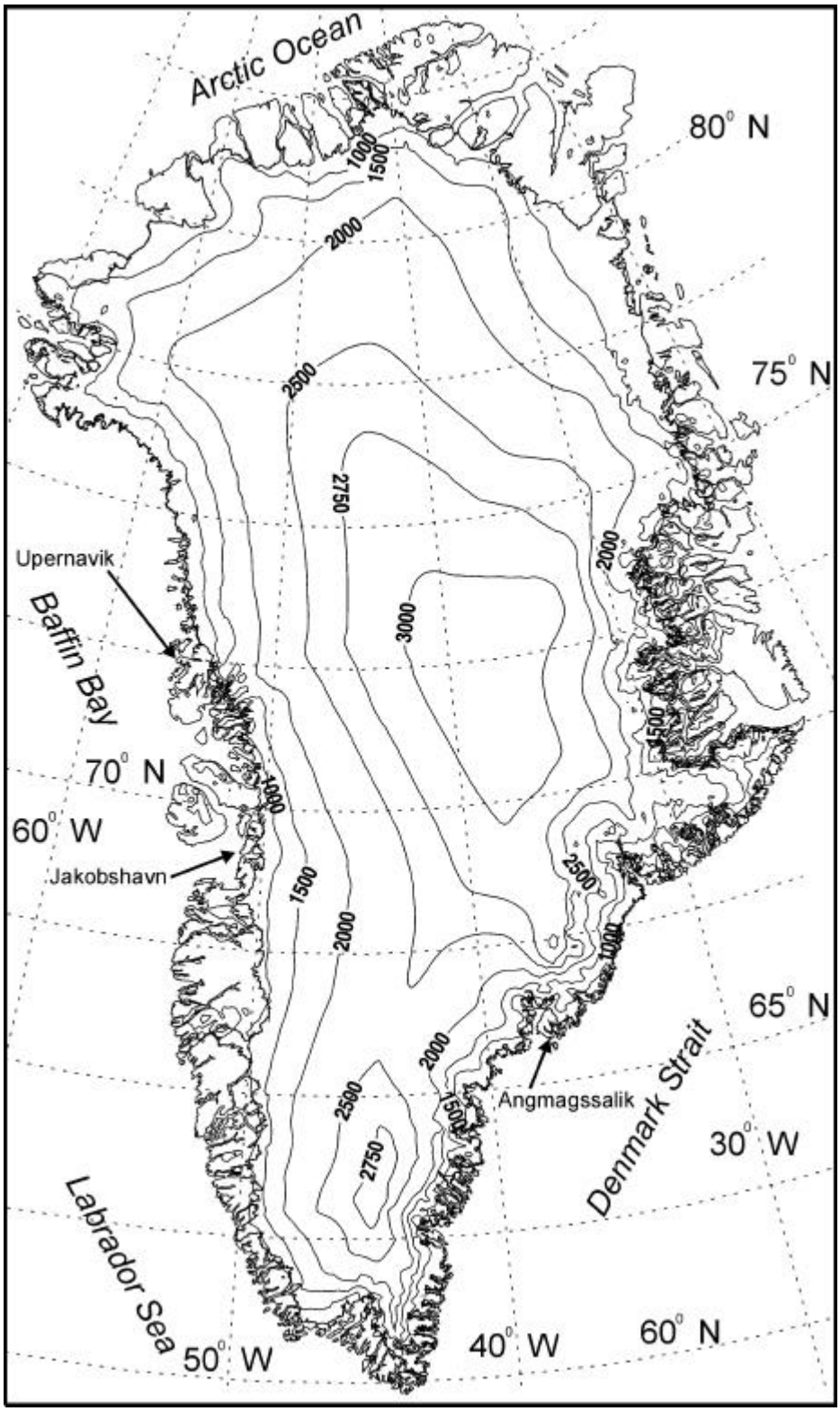

Figure 1.1, Topographic map of Greenland including place names referred to in the text.

This equilibrium line fluctuates vertically about 80 m for a 1° C rise in annual average temperature [*Ambach*, 1985], roughly corresponding to a 10 km inland migration of equilibrium line for each degree C temperature increase. On the gradual slope of Greenland, changes in annual average temperature are characterized by significantly large areal changes in melt extent. Forty to 45% of the ice sheet exhibits some seasonal melt [*Abdalati and Steffen*, 1995]. A permanently dry snow zone presently exists above an altitude of 3100 m in the

south and above 1600 m in the north [*Abdalati and Steffen*, 1997]. Changes in the extent of the dry snow zone associated with climate variability have been measured by satellite scatterometer [*Long, in press*]. An intermediate zone of limited melt is found in the lower accumulation zone is termed the percolation zone.

1.1.1 Ice Sheet Formation

Formation of the Greenland ice sheet is dated as far back as 2.4 million years by ocean sediment layers of ice rafted debris [*Souchez*, 1997]. Ice at its base has been dated to older than 130,000 years [*Dahl-Jensen et al.*, 1997]. Layers are countable down to 90% of the depth or 110 thousand years before present (kybp). Below this horizon, ice exists from the last climatic optimum, the Eemian, dating to 125 kybp. Evident in the ice strata is a climate signal from the most recent large-scale climate cooling. The regional onset of this so called Younger Dryas event occurred within 5 years [*Hammer*, 1997] and lasted roughly 700 years (from 10.8-10.1 kybp). The evolution of the Greenland ice sheet estimated by Huybrechts [1994] shows a decline in ice volume from the mid-Holocene 7.5 kybp to a minimum of about 3.1 x 10^6 km^3 at 4 kybp, and then a gradual increase in ice volume to the present value of 3.15 x 10^6 km^3. The volume of the Greenland ice sheet is thought to have maximized at 5.6 x 10^6 km^3 with values as low as 2.3 x 10^6 km^3 [*Dawson*, 1992], though the timing is not clear because as many as 23 glacier advances are implied by the GRIP and GISP 2 ice core records [*Hammer*, 1997]. Volume decreased from last glacial maximum 11 kybp to 20 kybp until about 4.5 kybp, when the mass began increasing [*Huybrechts*, 1994].

1.1.2 Ice Sheet Mass Balance

The mass balance of the ice sheet is the result of gains by precipitation and losses from runoff of melt water, iceberg calving, basal melting, and surface water vapor loss by sublimation and evaporation. Moisture recycling in the form of redeposition of evaporated and sublimated snow adds to the mass balance. Some of the evaporated mass may also return in the form of solid precipitation. Analysis of the water vapor fluxes follows in detail, including a quantitative discussion on the mass balance implications of moisture recycling. About half of the mass loss is thought to be through melt and evaporation with most recent estimates for runoff of 2.37 x 10^{14} kg y^{-1} [*Warrick et al.*, 1996]. Recent estimates of the contribution of the surface water vapor flux to ice sheet mass balance have come from *Ohmura et al.*, [1999], who use general circulation models to estimate the surface water vapor flux leads to 13% of precipitation mass loss. The uncertainty in evaporation estimates are unknown as there is little model verification using in situ data. The other major component of mass loss is iceberg calving with estimates ranging from 2.39 x 10^{14} kg y^{-1} to 3.3 x 10^{14} kg y^{-1} [*Warrick et al.*, 1996].

Ice sheet mass balance is important for sea level change studies. Greenland's estimated contribution to present sea level change is not known to better than 25% uncertainty or +/- 0.4 mm y^{-1} global sea level change [*Warrick et al.*, 1996]. A 1° C temperature increase implies Greenland's contribution to sea level is +0.30 to +0.77 mm y^{-1} [*Warrick et al.*, 1996].

Efforts over the past decade have significantly improved our knowledge of the mass balance for the Greenland ice sheet. Using a satellite based altimeter, Zwally [1989] measured thickening of Greenland south of 72 degrees N with a large negative contribution to sea level change of 0.2 to 0.4 mm y^{-1}. Small but general thickening of 1 cm y^{-1} was estimated using a coupled ice sheet/climate model for Greenland [*Huybrechts*, 1994]. Thickening in the southern part of the ice sheet, however, could simply be a dynamic response to the ice sheet geometry that resulted from the last glacial transition [*Abe-Ouchi*, 1994]. Thinning in excess of 10 m over 5 years of Greenland's ice at low elevations has been measured by repeat laser altimeter surveys [*Krabill*, 2000]. Such a large surface height reduction cannot be explained by melting alone, but is rather due to the effect of ice dynamical variations such glacial surging. Greenland could also be thinning at low elevations in delayed response to warming since the Little Ice Age in Greenland, 1250 years ago to the mid 19th century [*Crowley*, 1991]. Repeat GPS measurements and mass conservation ice flow models are used by *Thomas et al.* [2000] to infer century-scale mass balance changes for individual drainage basins. Reanalysis of the satellite altimeter data of *Zwally* [1989] by *Davis* [1998] has shed light on radar sensitivities to changing snow properties which will aide in future radar studies.

1.1.3 Ice Sheet Climate

The surface climate of large ice masses is dominated by a temperature inversion that results from a net negative surface radiation balance. As a result of the air overlying a relatively cold surface, turbulent sensible

heat is almost continually being transferred to the surface. As the density of the surface air increases due to this isobaric cooling, the air begins to drain down slope. This katabatic wind undergoes adiabatic heating as it descends, allowing the air to contain more moisture. Thus, the evaporation of blowing snow is not self limiting as has been shown for a horizontal plane [*Déry et al.,* 1998]. The katabatic wind weakens in summer due to the reduced surface temperature inversion. Annual average wind speeds are some of the largest in the world, up to 7 m s^{-1} at 1150 m in western Greenland [*Steffen and Box,* in press]. Furthermore, the katabatic wind is effectively turned 45° to the right in the down-slope direction due to planetary rotation. Synoptic systems encounter Greenland and lead to variations in wind direction and wind speed as shown later in a case study. Invading synoptic systems are often characterized by up-slope winds, precipitation and the destruction of the temperature inversion by turbulent mixing and a neutralization of the surface radiation balance.

Summer input of solar radiation is the primary driver for energy fluxes at the surface of the ice sheet, greatly influencing melt extent and the intensity of turbulent fluxes of sensible and latent heat. The amplitude of temperature fluctuations in a changing climate is greatest over highly reflective surfaces such as snow and ice due to the ice-albedo feedback [*Budyko,* 1969]. During melt conditions the reduction in the surface albedo (α) from that of dry snow (α=0.9) to wet snow (α= 0.7) [*Oke,* 1987] leads to an increase in absorbed solar radiation by a factor of 3.

Large annual and diurnal temperature variations occur over the ice sheet up to 57° C and 25° C, respectively. The minimum recorded temperature is –64 ° C at Summit, at high elevation in northern Greenland [*Shuman et al.,* in press]. The maximum surface air temperature over ice is limited to 0° C. Excess heat goes into melting. It is worthy to mention that the Greenland ice sheet undergoes intense seasonal melting below 1000 m while the only melting in Antarctica is confined to a very small area in the dry valleys near sea level [*Warrick et al.,* 1996].

The planetary scale atmospheric circulation around Greenland is characterized by semi permanent low pressure systems in Baffin Bay and the North Atlantic near Iceland. In winter, these low pressure troughs are anchored by a high pressure ridge over Greenland and to the west over the Canadian archipelago [*Barlow,* 1997]. The ice sheet acts as a barrier to large-scale atmospheric circulation [*Barry and Kiladis,* 1982]. Cyclonic systems dominate winter circulation, characterized by predominant meridional flow [*Ohmura and Reeh,* 1991], and thus highlight the important role of Greenland in poleward heat transfer. Without the orographic barrier imposed by the Greenland ice sheet, mid to high latitude circulation would have a weaker meridional component.

Regions of maximum accumulation rate are located adjacent to cyclonic centers. Cyclonic storms force maritime air masses up-slope. The air mass undergoes cooling by orographic uplift, leading to cloud formation and the occurrence of precipitation. By an analysis of atmospheric model fields, *Calanca,* [1994] shows that the eddy component of moisture flux is greater than the mean component, meaning that the frequency of cyclones and the abundance of water vapor are therefore the major determinants of Greenland's precipitation budget. Cyclones from the Labrador Sea contribute more moisture to accumulation than do storm systems originating in the Icelandic sector [*Chen et al.,* 1997]. *Robasky and Bromwich* [1994] calculated the moisture budget of Greenland using rawinsonde data. There is net export of moisture from the northeastern sector of Greenland with the major entrance zones for moisture being the southeast and western coasts. There is not much exchange of moisture across the northern boundary of Greenland. Average precipitation for Greenland has been estimated to be 340 mm y^{-1} from 35 coastal meteorological stations [*Ohmura and Reeh,* 1991]. Annual accumulation is estimated to be 310 mm y^{-1} based on ice cores and snow pits collected from numerous scientific expeditions [*Ohmura and Reeh,* 1991]. A slightly lager estimate representing the later half of the 20th century has recently been made by *Ohmura et al.* [1999] after more scrutiny of the data, and addition of recently collected data. Annual precipitation averaged for the ice sheet is now estimated to be 340 mm y^{-1} (590 km^{-3} y^{-1}) and the mean annual accumulation is thought to be 297 mm y^{-1} (516 km^{-3} y^{-1}). Precipitation minus accumulation divided by precipitation implies 13% of the precipitation is lost by surface water vapor fluxes.

Recent analysis of the Greenland Climate Network observations indicates a 2° C temperature rise above 2000 m since 1951-1960 [*Steffen and Box,* submitted]. An increase in the melt extent is observed in the satellite passive microwave record from 1979 to 1994 with a short term reversal cooling linked with the eruption of Mt. Pinatubo in 1992 [*Abdalati,* 1997]. As the volcanic aerosols settled out of the atmosphere, the increasing temperatures trend continued. The region has emerged from a colder period in 1973 at Jakobshavn (Figure 1.1) on the west coast of Greenland. Upernavik to the north has a similar pattern with temperature minimum in the

early 1970s. In eastern Greenland, at Angmagssalik (65.6° N, 37.6° W), temperatures have been warming since the early 1980s, although not as much as in 1923-1947. During 1923-1936, a warm period also occurred in western Greenland.

Significant interdecadal variations appear in the precipitation measurement record [*Ohmura et al.*, 1999]. A decrease in coastal precipitation rates is observed from 1952 to minimum from 1962 to 1968. Precipitation rates then increased until 1990 and have since decreased, approaching the 1964 minimum. Precipitation rates produced by an atmospheric model forced with coastal observations and radio-sonde data exhibit a significant negative trend in ice sheet precipitation from 1960 to the present [*Bromwich et al.*, 1993]. The climate of the Greenland ice sheet is very dynamic, as indicated by the large observed interannual variability in precipitation and accumulation rates [*Ohmura et al.*, 1999].

2 Problem Statement and Objectives

2.1 Problem Statement

Determining ice sheet mass balance components is important because major changes in their dimensions affect climate and sea level throughout the world [*Patterson*, 1994; *Oerlemans*, 1993]. Variations in the surface water vapor flux on the Greenland ice sheet influence accumulation rates by removing snow and ice and by adding mass by deposition/condensation. Thus, the mass balance of the ice sheet is sensitive to water vapor fluxes. The magnitude of the net water vapor flux to and from the ice sheet surface, however, is relatively poorly known. Periods of *in-situ* evaporation measurements have spanned periods too short to derive an annual total surface water vapor flux . As a consequence, only modeling studies have attempted to map Greenland's surface water vapor flux [*Ohmura et al.*, 1999]. Fortunately, sufficient *in-situ* observations now exist from the Greenland Climate Network (GC-Net) [*Steffen et al.*, 1996] to quantify Greenland's surface net water vapor balance.

2.2 Defining Surface Water Vapor Flux Terminology

Before proceeding, it is useful to define *evaporation* and *sublimation*. Precise meaning of these terms depends on defining a convention. Water vapor exchanges to and from a snow/ice surface *during sub-freezing conditions* are called deposition and sublimation, respectively. Evaporation/condensation are also mass fluxes of water vapor but occur when the surface is at or above the melting point of ice, 0° C. Due to the fact that most of the water vapor mass fluxes on the Greenland ice sheet occur during sub-freezing conditions, the term sublimation is taken to refer generally to the process of evaporative mass transfer to and from the surface. The terms condensation or deposition and evaporation are still used in this thesis when the specific conditions in which they occur need to be described, i.e. water vapor mass transfer for temperatures above 0° C. Furthermore, the conditions that lead to vertical water vapor fluxes are sometimes ambiguous when characterized by a combination of sublimation and evaporation. Thus, the term evaporation is often used loosely, for example in *Ohmura et al.* [1999], to describe the water vapor exchanges for sites on the Greenland ice sheet where there is little or no melting. Thus, some flexibility must be granted in the use of the term evaporation or sublimation, as it should be apparent in the context to which specific process is being referred.

The sources of vertical water vapor exchange are not limited to the snow surface. Blowing snow is often associated with large atmospheric sublimation rates [*Schmidt*, 1972; *Schmidt*, 1982b; *Déry et al.*, 1998]. Furthermore, water vapor fluxes at the surface are contributed to by fluxes within the snow volume [*Albert*, 1996; *Colbeck*, 1997]. These important net surface sublimation components are discussed as part of this study.

2.3 Objectives

The principal goal of this study is to quantify net water vapor exchanges on the Greenland ice sheet and to assess their significance to the ice sheet mass balance. The steps taken in this pursuit are data collection, calibration, and quality control, evaluation of methods to gauge the surface water vapor flux, selection of methods, climatological analysis, water vapor flux mapping, estimates of blowing snow sublimation, and comparison of results with estimates from atmospheric models and other *in-situ* data.

Ultimate goals of this work are to enhance the accuracy of annual and sub-annual water vapor flux estimates for point locations and for the Greenland ice sheet as a whole. It is through large-scale synthesis of point measurements that the mass contribution of the surface water vapor flux can be assessed. Also of primary significance for this work is the ability to estimate the amount of precipitation that is lost by the surface water vapor flux.

The techniques to calculate the mass flux of water vapor are based on measurement of the latent heat flux using standard meteorological data. This method relies upon accurate measurement or simulation of vertical differences of temperature, humidity, and wind speed. Two types of aerodynamic profile methods are employed in this study. The first method uses humidity measurements at one level and assumes that the surface is saturated with respect to water vapor, i.e. 100% relative humidity. Evaporation schemes based on a saturated surface are

commonly used in general climate simulations for ocean and ice land surface types [*Piexoto and Oort,* 1992] because model simulations often lack the *in-situ* information to define the vertical humidity profiles in the lowest 10 m of the atmosphere. A second type of profile method used in this study measures the vertical moisture differences with humidity sensors at two levels above the surface. The differences in the resultant sublimation rates from one level and two level methods are evaluated. The preferred method is chosen by comparison with independent estimates of the surface water vapor flux. Discussion of the lesser method is included only where relevant. The results from 16 GC-Net locations are evaluated from mid 1995 to mid 2000. Then, based on the point estimates, a statistical model is developed to interpolate the water vapor fluxes for the entire ice sheet. Using the water vapor flux maps produced by the interpolation method, total water vapor flux estimates for the ice sheet are derived. The uncertainty of hourly, annual, and total ice sheet water vapor flux is another product of this work. The differences in results from one level and two level profile methods are discussed in the context of water vapor fluxes derived from general climate model results.

Sublimation of blowing snow is also important to quantify. Thus, this component of the surface water vapor balance is estimated using a model to determine the snow transport and the proportion of relocated precipitation. The results, when presented in context of observed precipitation and accumulation rates, yield a solution for the deposition component of the surface water vapor balance.

2.4 Overview of Greenland Surface Water Vapor Flux Estimates

Previously, sublimation and evaporation measurements have been made during a succession of spring and summer expeditions on the Greenland ice sheet. At 1000 m elevation, 70° N in western Greenland, careful micrometeorological measurements as part of the summer Expedition Glaciologique International au Groenland (E.G.I.G.) indicated evaporation rates of 18 mm per month [*Ambach,* 1963]. . *Ambach* [1977] concluded that evaporation calculated by the latent heat flux (Q_E) used 12% of the total energy available for melt with radiation being the predominant energy source. Near the same site, *Greuel* [1992] calculated 25 mm per month of evaporation for the 1990 melt season. *Lister* [1961] made detailed energy balance and ablation stake measurements in northeast Greenland during the 1953 ablation season. Evaporation rates in late summer were up to 3 mm d^{-1}, accounting for 34% of the available energy for melting. The surface water vapor flux was a small quantity in early summer and increased during windy periods of active melt. After the melt period, evaporation decreased to a small quantity. *Loewe* [1970] concluded that the transport of blowing snow off the ice sheet margin was a negligible quantity for the ice sheet mass balance. The Geological Survey of Greenland (GGU) made ablation measurements on the Nordbogletscher and Qamanarssup Sermia outlet glaciers during 1979-83 and 1980-86 [*Olesen and Braithwaite,* 1989] and *Braithwaite and Olesen* [1990] used the data to calculate ablation by the same approach as *Ambach* [1977]. They compared their results to stake measurements on the two glaciers. The latent heat flux values were near zero on average with substantial daily fluctuations between positive and negative flux values (evaporation and condensation, respectively). Surface energy balance measurements were made in southwestern Greenland in the ablation zone from within the tundra to a point 90 km from Sondrestrøm Fjord, near its equilibrium line altitude as part of the Dutch Greenland Ice Margin Experiment, GIMEX 1991 [*Oerlemans and Vugts,* 1993]. Based on the GIMEX data for a site at equilibrium line altitude in July, 1991, it was shown that evaporation dissipates 25% of the energy that would otherwise be available for melting [*Henneken et al.,* 1994; *Henneken et al.,* 1997]. At the ETH/CU 'Swiss Camp', located at the mean equilibrium line altitude in western Greenland (69° 34' 06" N, 49° 18' 57" W, 1149 m), the magnitude of the latent heat flux (6 W m^{-2}) corresponded to 19 mm water equivalence of water vapor loss from June 3 to August 13, 1991 [*Ohmura et al.,* 1994]. They state that the latent heat of vaporization of this magnitude corresponds to 140 mm of melt if used exclusively for the melt, which is common on most of the high arctic and alpine glaciers. Therefore, evaporation plays an important role for maintaining the ice sheet. *Bøggild et al.* [1994] measured and modeled the surface energy and mass balance on the Storstrømmen glacier, and determined that peak water vapor fluxes occurred on steeper slopes due to katabatic wind acceleration. At the ETH/CU camp, turbulent heat flux measurements throughout the onset of melt indicate that water vapor fluxes were largest at the onset of melt, with values up to 1 mm d^{-1} [*Steffen,* 1995]. Latent heat flux was again recognized as an important sink of sensible heat. In an effort to derive the precipitation rate for Greenland based on the spatial accumulation distribution, *Ohmura et al.* [1999] employed high resolution T106 global climate models ECHAM 3 and ECHAM 4 to estimate water vapor fluxes above 1500 m elevation with evaporation

below 1500 m was provided by the ECMWF model. They estimate the annual total evaporation from the Greenland ice sheet reduces the mass input from precipitation (590 km^3 y^{-1}) by 74 km^3 y^{-1} or 12.5%.

The Antarctic climate serves as an analogue of Greenland's climate in the context of sublimation. In the strong katabatic wind region of Antarctica at Mizuho Station, sublimation was important to the surface mass balance, according to one year of 12-hourly evaporation pan measurements [*Fujii and Kusunoki*, 1982]. Evaporation pan measurements at Dome Fuji, Antarctica also indicate that the water vapor flux to the surface is a significant accumulation mechanism [*Kameda et al.*, 1997]. Katabatic winds accelerate as the surface slope angle increases from the ice sheet plateau toward the coast. The divergence of the wind stream promotes the formation of blue ice regions in Antarctica due to sublimation [*Bintanja*, 1999]. Similar to *Ohmura et al.* [1999] with reference to Greenland, *Van-den-Broeke* [1997] used the T106 ECHAM3 general climate model to map Antarctica's sublimation. Sublimation was recognized as important to surface mass balance near the coast and in particular in blue ice zones where low surface albedo values provide more absorbed solar energy to drive sublimation. *Bintanja* [1998] modeled blowing snow sublimation along an elevation transect in Antarctica, and the results indicate that up to 170 mm y^{-1} of mass is lost from the blue ice zones.

3 Instruments and Data

3.1 Greenland Climate Network (GC-Net)

The principal data set used in this study is collected by a network of Automatic Weather Stations (AWSs) on the Greenland ice sheet (Figure 3.1). As of June 2000, this Greenland Climate Network (GC-Net) consisted of 20 AWSs [*Steffen et al.*, 1996] (Table 3.1, Figure 3.2). Data from 16 AWS sites are used in this study. The GC-Net is designed to provide the necessary parameters for mass and energy balance studies. Installation of the network began in 1995 with one to five AWS added each year during successive spring expeditions to Greenland. The majority of AWS are located near or above 2000 m elevation in the accumulation zone, to complement NASA's Greenland mass balance initiative entitled the Program for Arctic Regional Climate Assessment (PARCA) [*Thomas*, submitted]. The majority of GC-Net AWSs are located on the western slope of the ice sheet. The eastern slope is less desirable to situate an AWS for a number of reasons. East Greenland is relatively far from large airports, making it costly to visit. The eastern slope is smaller in area and has a larger slope which reduces large-scale representativity of the AWS. Accumulation rates are much greater in east Greenland south of 70° N. Hence, south east Greenland AWS sites require more frequent revisits than western sites. The number of lower elevation AWS sites has been augmented in recent years to assess accumulation and melt rates more accurately. The lowest elevation AWS site used in this study is JAR2, situated at 568 m above sea level. The AWS design is based on proven technology, refined from AWS installed in 1990 at the ETH/CU camp and from lessons learned on glaciers in Switzerland and on Arctic islands in Nunavut, Canada.

Table 3.1, GC-Net Site Information

Station Name	ID #	Latitude, Longitude	Elev. [m]	Activation Date	N years A*	N years B*	Data Link
Swiss Camp	1	69° 34’ 06” N, 49° 18’ 57” W	1149	1995.38	3.3	3.3	GOES
CP1	2	69° 52’ 47” N, 46° 59’ 12” W	2022	1995.39	2.1	3.2	GOES
NASA-U	3	73° 50’ 31” N, 49°, 29’ 54” W	2369	1995.41	3.1	3.9	ARGOS
GITS	4	77° 08’ 16” N, 61° 02’ 28” W	1887	1995.43	2.5	2.5	ARGOS
Humboldt	5	78° 31’ 36” N, 56° 49’ 50” W	1995	1995.47	3.3	4.3	ARGOS
Summit	6	72° 34’ 47” N, 38° 30’ 16” W	3254	1996.37	2.3	2.8	GOES
Tunu-N	7	78° 01’ 00” N, 33° 59’ 38” W	2113	1996.38	1.9	3.5	ARGOS
DYE-2	8	66° 28’ 48” N, 46° 16’ 44” W	2165	1996.4	3.8	4.2	GOES
JAR1	9	69° 29’ 54” N, 49° 40’ 54” W	962	1996.47	4.1	4.1	GOES
Saddle	10	66° 00’ 02” N, 44° 30’ 05” W	2559	1997.3	3.0	3.0	GOES
South Dome	11	63° 08’ 56” N, 44° 49’ 00” W	2922	1997.31	0.5	1.6	GOES
NASA-E	12	75° 00’ 00” N, 29° 59’ 59” W	2631	1997.34	1.8	2.0	ARGOS
CP2	13	69° 54’ 48” N, 46° 51’ 17” W	1990	1997.36	0.9	2.5	-
NGRIP	14	75° 05’ 59”N, 42° 19’ 57” W	2950	1997.52	2.0	2.0	ARGOS
NASA-SE	15	66° 28’ 52” N, 42° 19’ 20” W	2425	1998.3	1.8	1.8	-
JAR2	17	69° 25’ 12” N, 50° 03’ 27” W	568	1999.4	1.3	1.3	GOES

* A refers to the amount of time when two humidity measurement levels are available, B represents the time when at least one humidity measurement is available.

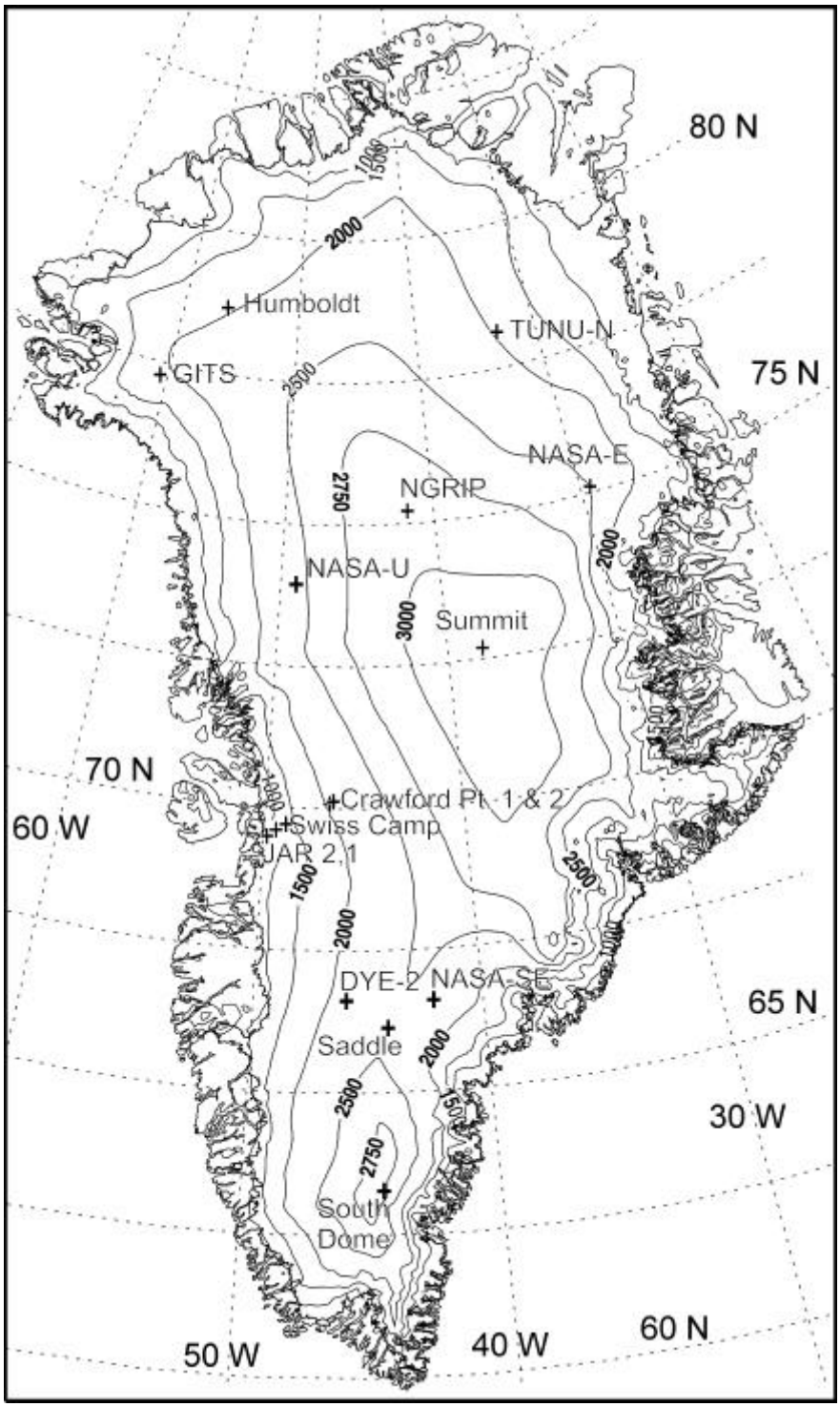

Figure 3.1, Location map of Greenland Climate Network locations referred to in the text

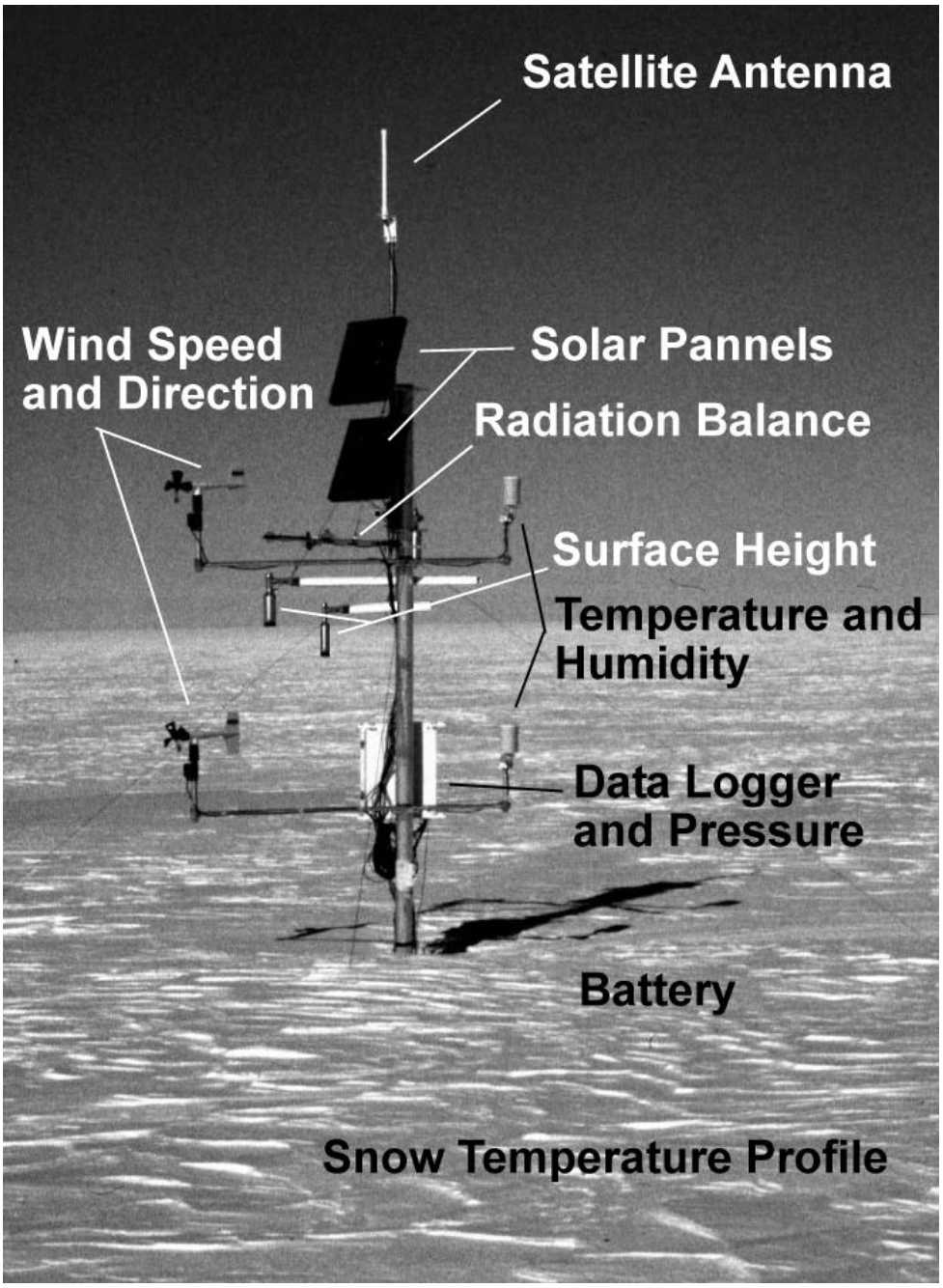

Figure 3.2, Photo of a GC-Net AWS featuring instrumentation

3.1.1 Instruments/Measurements

Instrument sampling intervals are set to represent the temporal variability in the meteorological parameters (Table 3.2) while conserving sufficient power to span the polar night. Measurements are stored locally in a Campbell Scientific CR10X data logger's 2 Mb memory. Older CR-10 data loggers still exist at the GITS and Humboldt sites. These are backed up by a Campbell Sci. SM-716 storage module. Data storage capacity is 3.6 years when 30 parameters are stored hourly.

Table 3.2, GC-Net Instrumentation Employed in this Study

Parameter	Instrument	Instrument Accuracy	Sample Interval	Number on site
Air Temperature	Vaisala 50YC (Campbell Sci. CS-500)	0.1 °C	60 s	2
Air Temperature	Type-E Thermocouple	0.1 °C.	15 s	2
Relative humidity	Vaisala INTERCAP or Vaisala HUMICAP 180	5% < 90% RH 3% > 90% RH	60 s	2
Wind Speed*	RM Young 05103	0.1 m s^{-1}	60 s*, 15 s	2
Station Pressure	Vaisala PTB101B	0.1 hPa	60 min	1
Surface Height Change	Campbell Sci. SR-50	1 mm	10 min	2
Multiplexer	Campbell Sci. AM-25T	-	-	1
Data Logger	Campbell Sci. CR-10/10X	-	-	1
Snow Temperature (initially -0.5 to –9.5 m each m)	Type-T Thermocouple	0.1 °	15 s	10
Incoming and reflected solar radiation flux (W m^{-2})	Li Cor Photodiode (400 μm – 1100 μm)	5-15%	15 s	1
Net Radiation	REBS Q* 7 or Kipp and Zonen NR-Lite**	5-50% 5-20%	15 s	1
GPS	Garmin (GPS25-LVS)	Approx. 15 m	4 s for 15 min each day	1
Solar Panel	Campbell Sci. / Solarex 20 W or 10 W	-	-	2

* Sampled each 15 sec after 1999 site visit, 2000 visit for NGRIP.

** NR-LITE instruments are located at Swiss Camp and Summit after mid 1999.

3.1.1.1 Data Problems

The latent heat flux formulation requires nine accurate input measurements, two temperatures (T_1 and T_2), two relative humidities (RH_1 and RH_2), two wind speeds (u_1 and u_2), two instrument heights (z_1 and z_2), and pressure (p). Due to the fact that sites may only be revisited each year, occasional instrument failures lead to extended gaps in the time series of measurements. Thus, gaps affect the monthly to annual statistics presented in later sections. To avoid statistical uncertainties in monthly and annual quantities associated with data gaps, only time periods with an acceptable fraction of missing data, usually 5% or 10%, are considered for scientific analysis. Most of the problems are related to the extreme cold encountered on the Greenland ice sheet. The major problems are summarized below.

- *Freezing of wind sensors* is observed to occur as the result of frost deposition on anemometers or melt water refreeze. The frequency of the frost problem is greatest at high elevation sites. The effect frost on anemometers is made worse by the lack of strong winds at high elevation sites to free the anemometers. Wind direction data are also susceptible to sticking. Wind direction measurements often become free before anemometer propellers. After an occasional lengthy time frozen, the wind data suddenly indicate a strong wind, usually between 8 m s^{-1} and 15 m s^{-1}, implying that it took such a high wind to free the propeller.
- *Air temperatures below -50° C* were not directly measured until a revised measurement routine was incorporated at sites visited in the spring of 2000. The frequency of air temperature below –50 is extremely small for all sites except Summit and NGRIP. Analysis of winter of 2000/2001 data indicate that the frequency of air temperature below -50° C occurs only a few percent of the year. Air

temperatures below -50° C are estimated, however, using a regression fit to the response of the humidity instruments below -40° C. The accuracy is usually within 1-2° C when the results of this method are compared over the -45° C to -50° C range when the air is saturated and the air temperature measurements were still functioning. A minimum temperature of -64° C is estimated to occur at the NGRIP using this method.

- Several *humidity instrument failures* have occurred, typically during extremely cold temperatures, i.e. below -40° C. The implications of this problem for one and two-level profile methods is discussed in section 5.8.
- A *software error* led to the duplication of the lower profile thermocouple temperature data over the level two thermocouple temperature data at three sites (JAR1 mid 1998-1999, Saddle, and South Some) from mid 1997-1999. The problem is now fixed. Two temperature measurement levels are necessary for stability corrections to the profile methods.
- *Temperature instrument overheating* occurs under conditions of solar radiation in excess of approximately 100 W m^{-2} combined with wind speed less than approximately 3 m s^{-1}. Biased air temperatures lead spurious water vapor flux estimates. In reality, maximum air temperature is usually limited to some value below 0° C due to the fact that excess heat goes into ice melt. As a means of limiting the effect of this problem on water vapor flux estimates, only cases for air temperature measurements below +0.5° C are selected for water vapor flux calculations. A temperature instrument overheating correction scheme is applied to AWS data for sites in the accumulation zone where surface albedo effects allow corrections to be made (see section 3.1.7 below).

3.1.2 AWS Power Supply

The AWS are powered by four 100 ah photovoltaic batteries. This power supply is divided equally in half between the data logger and data telemetry systems. Each battery pair is charged with two 10 W or 20 W solar panels. The batteries are housed in a sealed wooden crate buried in the snow to avoid extreme minimum temperatures encountered in the air. At low elevation AWS, the battery pack consists of two sets of three 18 ah batteries. Fewer batteries are needed at lower elevation sites owing to the increased battery performance in the warmer climate encountered there.

3.1.3 AWS Platform

The AWS tower is custom-fabricated from aluminum in the University of Colorado Cooperative Institute for Research in Environmental Sciences machine shop. Steel is less preferable being heavier and not corrosion resistant. The mast outside diameter is 10.16 cm (4 in.) with 0.635 cm (1/4 in.) wall thickness and has an initial total length of 7.315 m (24 feet). The mast is inserted 2 m to 5 m into a firn or ice borehole drilled with a hand auger. Deeper installations are made at low elevation sites to account for net surface ablation. Shallow installations are made for accumulation zone sites, where the AWS will be buried unless extended periodically. Instruments are placed on boom arms that extend on average 91 cm from the central mast. Wind sensors are placed at least 1.2 m from the mast while temperature/humidity instruments are no closer than 50 cm from the mast. Boom arms with wall thickness less than 0.635 cm have been found to be prone to vibration and deformation. Wall thickness of 1.27 cm (1/2 in.) is preferred for aluminum boom arms. Radiation and surface height instrument boom arms are stabilized with steel cable. Mounting hardware are preferably stainless steel owing the tendency of raw steel to rust and bind. Three steel cables are anchored with approximately 120° radial separation above the mid point of the AWS to stakes 2.54 cm (1 in.) OD approximately 1.8 m in length that are driven or drilled at least 1.6-1.8 m (3 m) into the firn or (ice), respectively. This AWS platform has proven to be without major problems over 5 years of continuous use.

3.1.4 GC-Net Instrument Height Characteristics

For the majority of GC-Net sites, net accumulation occurs throughout the year (except the JAR sites and Swiss Camp). Thus, instrument heights are set sufficiently high to not be buried within the expected time between installation and the next planned site revisit that includes mast extension. Site revisits are planned depending on the accumulation rate and site accessibility. So far, return-times have varied from 1 year to 3 years. Given a typical 1 year revisit schedule, instrument heights must be greater than the predicted surface

height change above the surface. The observed profile instrument heights and their annual minimum and maximum is given in Table 3.3. Total instrument height frequencies are given in Table 3.4. In three cases, the lower instrument profile has been buried by greater than expected accumulation, CP1 1997, NASA-SE 200, or by the inability to extend at Tunu-N 1999. During cases when instrument level 1 becomes negative, two level aerodynamic profile calculations are not made. The separation of the profile instruments 1 and 2 has been between 0.57 m and 8 m. Both extreme cases occurred for the Swiss Camp AWS. When extended gaps in Swiss Camp AWS record occurred, the gaps have been filled by the Swiss Camp 10 m tower data. The 10 m tower measurement heights are nominally 1.5 m and 10 m above the surface. At all other sites, the separation of profile instruments is between 1.0 m and 1.79 m. More recently, we have adopted a standard 1.2 m profile separation for less complicated intercomparison of profile results. The Swiss Camp AWS profile separation was also set to 1.2 m in 2000. The number 1.2 m is intended to be great enough to resolve vertical humidity *(dq)* and temperature *(dT)* differences within the instrument's precision while not too great to be dominated by a large change in height *(dz)*. A smaller profile separation (0.6 m to 1 m) would be preferable if the profile level 1 was always about 1 m above the surface. In this case, the vertical gradients in temperature, humidity, and wind speed would be stronger because the differences are greater near the surface. However, due to the fact that the accumulation has to be taken into account, a larger profile separation is required. Profile measurements above 2 m, for example, should be more widely spaced to account for instrument precision given that the vertical differences in temperature etc. are smaller.

Table 3.3, GC-Net Instrument Height Information [m]

Site		1995		1996		1997		1998		1999		2000	
		z_1	*Dz*	z_1	*Dz*	z_1	*Dz*	z_1	*Dz*	z_1	*Dz*	z_1	*Dz*
Swiss Camp	Min.	1.30	0.57	1.30	0.57	1.02	0.57	1.20	8.00	1.16	1.20	1.33	1.20
	Max.	2.00		2.14		2.42		2.00		2.91		2.29	
CP1	Min.	1.40	1.30	0.05	1.30	-0.28	1.00	0.66	1.13	2.72	1.21	1.82	1.21
	Max.	2.37		1.53		2.33		1.29		3.49		2.92	
NASA-U	Min.	2.05	1.35	1.51	1.35	1.55	1.75	0.87	1.75	0.55	1.30	1.51	1.30
	Max.	2.75		2.16		2.34		1.60		3.15		2.29	
GITS	Min.	1.29	1.56	0.94	1.10	0.76	1.07	*	*	-0.39	1.20	2.88	1.20
	Max.	2.19		1.86		2.19		*		4.17		3.56	
Humboldt	Min.	2.14	1.79	1.73	1.79	1.30	1.75	0.84	1.75	0.70	1.20	0.90	1.20
	Max.	2.35		2.35		1.83		1.51		1.90		1.53	
Summit	Min.	**	**	1.62	1.39	1.28	1.27	0.81	1.27	0.76	1.20	0.62	1.20
	Max.	**	**	2.15		1.80		1.37		1.80		0.99	
Tunu-N	Min.	**	**	1.48	1.27	0.98	1.27	0.98	1.27	0.51	1.29	0.15	1.29
	Max.	**	**	1.75		1.67		1.30		1.05		0.61	
DYE-2	Min.	**	**	1.46	1.47	0.52	1.47	0.24	1.47	0.43	1.12	0.11	1.12
	Max.	**	**	2.20		1.53		1.70		1.26		2.79	
JAR1	Min.	**	**	1.25	1.02	2.12	1.02	1.76	1.02	0.37	1.20	0.75	1.20
	Max.	**	**	3.11		3.86		4.01		3.53		2.39	
Saddle	Min.	**	**	**	**	1.68	1.23	1.26	1.10	1.04	1.18	1.70	1.18
	Max.	**	**	**	**	2.52		1.88		3.23		2.28	
South Dome	Min.	**	**	**	**	1.37	1.10	0.57	1.10	1.76	1.10	*	*
	Max.	**	**	**	**	2.56		3.23		3.44		*	
NASA-E	Min.	**	**	**	**	2.19	1.28	1.71	1.28	1.12	1.28	*	*
	Max.	**	**	**	**	2.55		2.29		1.83		*	
CP2	Min.	**	**	**	**	-0.01	1.28	0.95	1.28	0.52	1.20	0.16	1.19
	Max.	**	**	**	**	2.57		1.72		2.16		1.22	
NGRIP	Min.	**	**	**	**	1.77	1.48	1.29	1.48	0.00	1.30	0.85	1.39
	Max.	**	**	**	**	2.03		1.91		1.55		3.12	
NASA-SE	Min.	**	**	**	**	**	**	2.06	2.14	-0.32	1.22	-0.48	1.22
	Max.	**	**	**	**	**	**	3.11		2.08		0.59	
JAR2	Min.	**	**	**	**	**	**	**	**	0.20	1.2	0.53	1.20
	Max.	**	**	**	**	**	**	**	**	3.48		3.40	

*- insufficient data, ** - AWS not yet installed.

Table 3.4, GC-Net Instrument Height Frequencies [m]

Site	$Mean_1$	$Mean_2$	$Median_1$	$Median_2$	$Min._1$	$Min._2$	$Max._1$	$Max._2$	Years
Swiss Camp	3.15	2.00	1.87	5.36	1.01	1.59	2.91	10.00	6.0
CP1	2.97	1.80	1.69	2.83	-0.28	0.71	3.49	4.70	4.7
NASA-U	3.24	1.78	1.82	3.33	0.55	2.30	3.15	4.45	4.5
GITS	3.15	1.91	2.24	3.46	0.79	1.83	4.17	5.37	3.7
Humboldt	3.08	1.61	1.59	3.20	0.70	2.10	2.35	4.14	5.2
Summit	2.50	1.25	1.26	2.53	0.39	1.59	2.15	3.54	4.6
Tunu-N	2.42	1.13	1.09	2.37	0.15	1.44	1.75	3.02	4.3
DYE-2	2.53	1.22	1.30	2.57	0.11	1.23	2.79	3.93	4.6
JAR1	3.70	2.68	2.52	3.60	0.37	1.57	4.01	5.03	4.2
Saddle	3.15	1.96	2.00	3.06	1.04	1.81	3.23	4.41	3.1
South Dome	3.58	2.48	2.32	3.37	0.64	1.74	3.44	4.54	2.8
NASA-E	3.31	2.03	1.93	3.21	1.12	2.40	2.55	3.83	2.5
CP2	2.66	1.40	1.41	2.66	0.42	1.61	2.57	3.85	3.1
NGRIP	2.82	1.43	1.50	2.94	1.26	2.3	3.12	4.53	3.2
NASA-SE	2.96	1.67	1.61	3.28	-0.48	0.74	3.11	5.25	2.1
KAR	4.41	3.26	3.17	4.32	2.36	3.51	3.38	4.53	0.5
JAR2	4.30	3.18	2.79	3.95	0.61	1.71	3.48	4.68	1.6

3.1.5 Data Telemetry

The majority of GC-Net AWS are equipped with satellite data telemetry systems that serve to improve data collection success. Telemetry helps ensure getting the data with the potential of not being able to return or not being able to find the site. Telemetry also indicates if replacement instruments need to be brought for the next site visit in the event of evident instrument failure.

Two different telemetry systems built by Telonics Inc. of Arizona are employed. Data logger to transmitter interface modems are obtained from Campbell Scientific. AWS south of 73° N transmit during a specific minute in each hour to a US government Geostationary Operational Environmental Satellite (GOES East, 75° W). The elevation angle of the directional antenna is between 20° and 7° from the horizon, often operating near the limit of the line of sight capabilities of data transmission. The antenna azimuths range from 206° to 223°. For northern GC-Net AWS, the System-ARGOS commercial satellites are employed. These transmitters send 16 channels of data every 200 seconds to one of the two polar orbiting satellites, depending on which one is in the line of sight. Data transmission is effectively doubled by overriding a redundancy option, sending two different 16 channel blocks instead of the same 16 channel block twice. Overriding the redundancy option, although doubling bandwidth, results in an increase of missing hours due to occasional transmission error. Maximum missing hours correspond to upwards of 50% of the data volume and about 20% under normal operation. The factors associated with transmission are many and varied. Most transmission errors are due to physical failure of telemetry hardware or loss of temporal synchronization as in the case of GOES telemetry.

GPS circuitry was added to GC-Net AWS in 1999 and 2000 field seasons to synchronize the AWS clock leading to increased success in maintaining GOES telemetry synchronization. The new system actually reactivates the transmitter daily, whereas formerly activation was only possible during site revisits every 1-2 years. Clock drift has been typically about -15 minutes after one year without GPS clock synchronization. In some instances clock drift has been as long as 3 hours.

3.1.6 Quality Control

Statistical procedures are applied to the GC-Net data in effort to remove occasional spurious data values. Measurement errors exist in the data caused by frost/ice on sensors, tower obstruction of the wind sensors, instrument overheating bias and permanent instrument failure. Often the primary cause of spurious data is data transmission errors whereby some data values are scrambled yet still fall within possible limits. Various

quality control procedures have been developed and applied consistently to all of the data. The software is written in Interactive Data Language (IDL) code that are rerun on the data as procedures are refined. Periodically, when AWS data are brought up to date from recent transmissions or data collected on site in the field, the quality control program is rerun on the entire dataset to ensure consistent quality control.

The procedures include, firstly the rejection of impossible values. Secondly, a gradient threshold compares a measurement with the next sequential hourly measurement. If the change is greater than a specified threshold (Table 3.5, Table 3.6), the later point is rejected. Thirdly, a scanning statistics time-interval is run through the time series to identify and reject data beyond a specified variance threshold for a varying time intervals. The variance threshold and time interval is also tuned to represent a different parameter's variance characteristics. In some cases, a range of time intervals is employed to reject outliers. In general, the data that are rejected by these filters represent a minor proportion of the total data volume. Quality control is refined by iterations consisting of human inspection followed by a sequence of algorithms tuned until all obviously spurious data are filtered out.

A success rate defined by the availability of 12 critical parameters to the GC-Net as a function of time averages above 80% for all annual time periods and has been above 90% following the first two years of the GC-Net. Despite an increasing number of sites to manage, the success rate has remained above 90%.

Table 3.5, Thresholds for Data Rejection and Interpolation

Parameter	Gradient Threshold	Autocorrelation Threshold (hours)
Air Temperature	8 K – 12 K	10
Wind Speed	10 m s^{-1}	10
Relative humidity	15%	10
Pressure	3 hPa	48
Wind Direction	-	4
Solar Radiation	200 W m^{-2}	5
Net Radiation	120 W m^{-2}	5
Snow Temperature	2 K	160
Surface Height	30 cm	Linear interpolation not used

Table 3.6, List of Quality Control Procedures

IDL Procedure	Description
‘Fill Time Gaps‘	Inserts missing hourly data rows 999 in place of the missing data
‘Variance Filter’	Sets data beyond a standard deviation threshold for given search time interval to 999
‘Gradient Threshold’	Rejects data points in time series that are indicative of a hourly change greater than a realistic threshold.
Interpolation	Linearly interpolates gaps smaller than a user supplied autocorrelation threshold using the closest available values.
‘Last Fill’/’First Fill’	Fills in gaps in snow height with last good value.
‘Tower Wake Filter’	Flags wind speed data associated with wind directions indicative of tower obstruction of wind flow.
‘Negative wind speed difference’	Rejects wind speed profile data when vertical wind speed gradient is negative.
‘Instrument height’	Calculates instrument height based on surface height change measurements and initial instrument heights measured at site visits.
‘Coefficient’	Incorporates multipliers and offsets for pressure, radiation, and relative calibration coefficients.

These autocorrelation threshold values may in some cases be too liberal since the significance threshold sometimes falls off very rapidly. In the competing interest of data continuity, liberal thresholds have been selected to eliminate all but extended gaps. However, the data user may select only non-synthetic data if one needs to be conservative by using a quality identification code described below.

3.1.7 Correcting Overheating of Temperature Measurements

Under strong solar radiation conditions with little or no wind, overheating of temperature instruments occurs. Overheating bias in excess of 8° C was observed by comparison of air temperature measurements from actively ventilated and non-ventilated temperature sensors. The overheating observations were used to construct a correction factor *(C)* for temperature data as a function of wind speed and solar radiation measurements (Figure 3.3). The correction function is based on a 2nd order polynomial best fit to the data. The residuals of the fit are characterized by an route mean square error of 2° C. The correction factor is applied to all GC-Net data for sites above 1000 m elevation. The correction is therefore not applied to JAR1 or JAR2 data, where for most of the relevant period, low surface albedos lead to less overall solar overheating. The correction is applied for conditions when the greatest solar overheating is observed, i.e. wind speeds less than 5 m s^{-1} and solar radiation > 50 W m^{-2}. Implementation of the correction is made by summing C with the temperature data.

$$C= -(0.207-0.701*u+0.014*S+0.131u^2-0.002*u*S-4.743x10^{-6}*S^2) \qquad \text{Eq. 3.1}$$

where *u* is the wind speed measured by a Young model 05103 anemometer (m s^{-1}) and *S* is the incoming solar radiation measured by a Li Cor pyranometer (W m^{-2}).

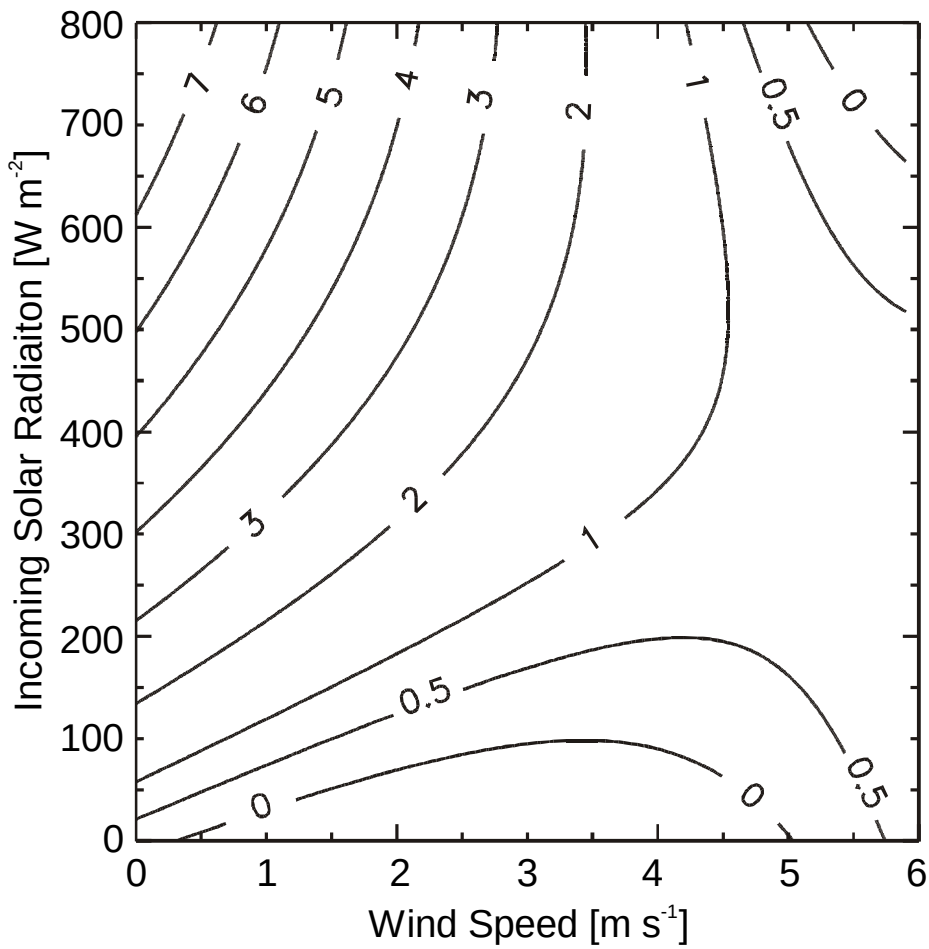

Figure 3.3, Temperature data solar overheating correction values

3.1.8 Input Data Filtering

Aerodynamic profile modeling poses certain requirements on input data for realistic output. Therefore, a set of input data selection criteria reduced the occurrence of spurious latent heat flux values that would contaminate monthly means and annual net surface water vapor flux. Occasional errors in the profile data occur as the result of rime ice on anemometers, solar overheating of passively aspirated temperature sensors, and electrostatic discharge. Only cases when wind speed increases with height were selected and fluxes are

calculated for wind speeds greater than 1 m s^{-1}. Such low wind speeds sometimes are associated with spurious wind speed profile differences that can result in unrealistically large profile-based turbulent flux estimates. Data gaps associated with these cases are interpolated linearly. The extremely small turbulent fluxes that occur at wind speeds less than 1 m s^{-1} nonetheless have an insignificant influence on monthly to annual net surface water vapor flux totals. Times when air temperature exceeded 0.5° C were omitted as they usually result from overheating of temperature sensors under low wind speed and high solar irradiance. Large spikes in the data caused by electrostatic discharge were removed using a variance threshold of 3 standard deviations from the daily mean of 24 hourly observations.

3.1.9 Quality Identification Scheme

The quality control procedures track the modification history of each data point. The codes enable the data user to identify modified and unmodified AWS readings (Table 3.7). Since interpolated values occasionally lead to spurious profile-based moisture flux estimates, only non-synthetic data are used in this study.

Table 3.7, GC-Net Quality Identification Code

Code	Description	Parameter
0	not currently used	-
1	un-synthesized data	All
2	linearly interpolated value	All
3	when a measurement is 'frozen' e.g. with wind direction when the anemometer is frosted over with the exact same value for more than 4 hours.	All
4	not currently used	-
5	cases when incoming shortwave radiation was less than reflected solar radiation. At this time, the cleaning code sets incoming to reflected and reflected to the new incoming * the last good albedo value	Solar Radiation
5	cases rejected because of shadowing by the tower. Azimuth ranges up to +/- 25 degrees are required to remove the direction-wind speed difference bias.	Wind Speed
6	corresponds to synthetic wind values. To simulate 2 wind speeds when only one is out, the logarithmic slope-intercept formula is used assuming a roughness length of 5 cm (average condition). For some annual data sets, this approach fills in up to 15% of wind data where one wind sensor is frozen. Some of the cases are obviously frozen wind sensors (when sensor 2 reads zero and sensor 1 is moving).	Wind Speed
7	corresponds to profile instruments that have had their order reversed, i.e. wind level 1 for 2 and 2 for 1. The reason for this switch is that not always the same order convention was used on AWS.	All
8	temperature < -50° C synthesized from RH instrument response at saturation. The standard error is less than 2° C.	Temperature
9	temperature values have been corrected for overheating when wind is less than 3 m s^{-1} and solar radiation is greater than 100 W m^{-2}.	Temperature

3.1.10 Relative Calibrations

GC-Net instruments come factory-calibrated. Nonetheless, on-site relative temperature, humidity and wind speed calibrations are made to verify the relative accuracy of profile measurements. Based on relative calibration results, the relative accuracy is often greater than the absolute accuracy. Field calibrations are set to represent the relative bias between the profile instruments over a range of local conditions. Relative calibration is performed by the following method. The mean deviation from one sensor to the another is adjusted to zero using the inverse of the percent mean deviation during a calibration period of 7 to 24 hours. The resultant corrections are all less than 1% for temperature sensors and 5% for humidity and wind speed sensors (Table 3.8). Relative calibrations have not been performed at the beginning of the measurement period at all AWS sites. Failure to make, or rejection of, relative calibrations at the time of AWS installation has resulted from insufficient time on-site or inappropriate meteorological conditions for calibration, i.e. very low wind speeds and/or fog depositing rime. Relative calibrations have been made during subsequent site visits. Other new sites such as JAR 2 and NASA-SE have not yet had relative calibrations performed. Therefore, at the time of this study, some time periods at AWS sites are not covered by relative calibrations. In such cases, the relative accuracy of the temperature and wind speed instruments is a function of the absolute calibration provided by the manufacturer. The humidity instrument relative accuracy is maintained by the procedure to offset humidity instruments with respect to their maximum output level discussed in section 3.1.11.

Table 3.8, Calibration Coefficients Used by GC-Net Profile Instruments

AWS	Year Initial	Time Initial	Year Final	Time Final	SW ↓	SW ↑	Net +	Net -	TC 1	CS/HMP 1	RH 1	Wind 1
1	1995	1.0	1996	168.6	**	**	**	**	*	*	*	*
1	1996	168.7	1996	367.0	**	**	**	**	0.99981	1.00035	1.02413	1.00046
1	1997	1.0	1998	145.7	**	**	9.29	11.62	0.99981	1.00035	1.02413	1.00046
1	1998	145.8	1999	90.0	100	100	9.29	11.62	0.99981	1.00035	1.02413	1.00046
1	1999	90.0	2000	140.5	200	77	80	80	1.00001	1.00054	1.03359	1.05179
1	1999	140.5	2000	366.0	200	77	80	80	1.00007	1.00048	1.04744	1.00091
2	1995	1.0	1999	147.7	200	200	9.43	11.77	*	*	*	*
2	1999	147.7	2000	366.0	200	200	9.43	11.77	1.00011	*	1.01858	*
3	1995	1.0	2000	366.0	200	200	9.08	11.36	1.00017	0.99954	0.97903	1.00761
4	1995	1.0	1999	148.7	200	200	9.35	11.66	1.00007	0.99941	1.02351	1.0302
4	1995	148.8	2000	366.0	200	200	9.35	11.66	1.00018	*	1.03526	1.0302
5	1995	1.0	1996	129.6	200	200	9.29	11.62	*	1.0003	0.9949	*
5	1996	129.6	2000	366.0	200	200	9.29	11.62	*	*	*	*
6	1995	1.0	1999	131.5	200	200	9.51	11.88	*	*	*	*
6	1999	131.6	2000	169.4	200	200	78.74	78.74	1.00058	*	1.10464	1.00495
6	1999	169.4	2000	366.0	200	200	78.74	78.74	0.99881	1.00132	0.93029	1.00185
7	1995	1.0	1998	139.0	200	200	9.43	11.66	0.999	*	1.01993	1.049
7	1998	139.0	2000	366.0	200	200	9.43	11.66	1.00012	0.99891	1.02595	0.9783
8	1995	1.0	1998	118.6	200	200	9.29	11.54	*	*	1.02861	1.18212
8	1998	118.7	2000	366.0	200	200	9.29	11.54	*	1.00034	1.0226	1.04372
9	1996	100.0	1999	153.9	200	200	9.29	11.53	*	*	*	*
9	1999	153.9	2000	366.0	200	200	9.29	11.53	1.00034	1.00029	0.98876	1.01533
10	1997	1.0	1999	106.3	83.63	76.19	9.29	11.7	*	*	*	*
10	1999	106.3	2000	366.0	83.63	76.19	9.29	11.7	*	1.00076	0.97868	*
11	1997	1.0	2000	366.0	62	72.79	9.29	11.7	*	*	*	*
12	1997	1.0	2000	366.0	71.43	70.75	9.29	11.7	0.99993	0.99802	0.99985	1.09206
13	1997	1.0	2000	366.0	71.43	70.07	9.3	11.45	1	1.00004	0.98804	1.00557
14	1997	1.0	1999	366.0	73.47	71.43	9.29	11.7	0.99963	0.99808	1.00412	1.00827
14	2000	1.0	2000	167.5	73.47	71.43	9.29	11.7	1.00024	1.02136	1.01539	0.99762
14	2000	167.0	2000	366.0	73.47	71.43	9.29	11.7	1.00827	1.00222	1.00827	0.99762
15	1998	1.0	2000	366.0	200	200	9.29	11.7	*	*	*	*
17	1999	1.0	2000	366.0	83.63	76.19	9.29	11.54	*	*	*	*

** - calibration coefficients applied already by K. Steffen

3.1.11 Scaling Humidity Sensors for Subfreezing Temperatures

The GC-Net measures relative humidity, expressed as percent saturation of the air with respect to pure liquid water (RH_{liq}), using a Vaisala INTERCAP 50YC temperature/humidity sensor (Vaisala, Oy, Finland). The instrument incorporates the INTERCAP in a capacitance bridge followed by both temperature compensation and linearization circuits to give a final output voltage proportional to relative humidity (RH) over a -40°C to 50°C temperature range. The INTERCAP humidity sensor measures relative humidity scaled with respect to liquid water. For meaningful humidity measurements at temperatures below 0° C, the raw data must be rescaled to reflect saturation with respect to ice. The theory to rescale RH_{liq} values for saturation with respect to ice (i.e. RH_{ice}) is reviewed by [*Anderson*, 1994] plus a correction scheme for individual instruments. The first step based on well known thermodynamics is to multiply each RH_{liq} reading by the ratio of saturation vapor pressure with respect to water over that with respect to ice at a given air temperature (Figure 3.4) given the relation.

$$RH_{ice} = RH_{liq} \frac{e_{s,ice}}{e_{s,liq}} \qquad \text{Eq. 3.3}$$

where $e_{s,ice}$ is the water vapor pressure at saturation for a given temperature < 0° C (hPa) and $e_{s,liq}$ is the water vapor pressure at saturation for a given temperature > 0° C (hPa).

The saturation vapor pressure *(e_s)* is expressed in the following after *Curry and Webster* [1999].

$$e_s = e_0 \exp R_v^{-1}\left((L + T_0\, b)\left(T_0^{-1} - T^{-1}\right) - \left(b \ln\left(T T_0^{-1}\right)\right)\right) \qquad \text{Eq. 3.4}$$

where e_0 is the water vapor pressure (hPa) at the melting/freezing point of H20, 0° C, R_v is the individual gas constant for water vapor (461.5 J kg^{-1} K^{-1}), and L is the latent heat of either vaporization or sublimation (J kg^{-1}). The difference between $e_{s,ice}$ and $e_{s,liq}$ is the latent heat of either vaporization or sublimation. Latent heat is further described in following sections. T_0 is the Kelvin temperature at the melting point of pure water (273.15 K), T is the temperature at which the saturation vapor pressure is desired, and *ß* is a constant equal to 2317.

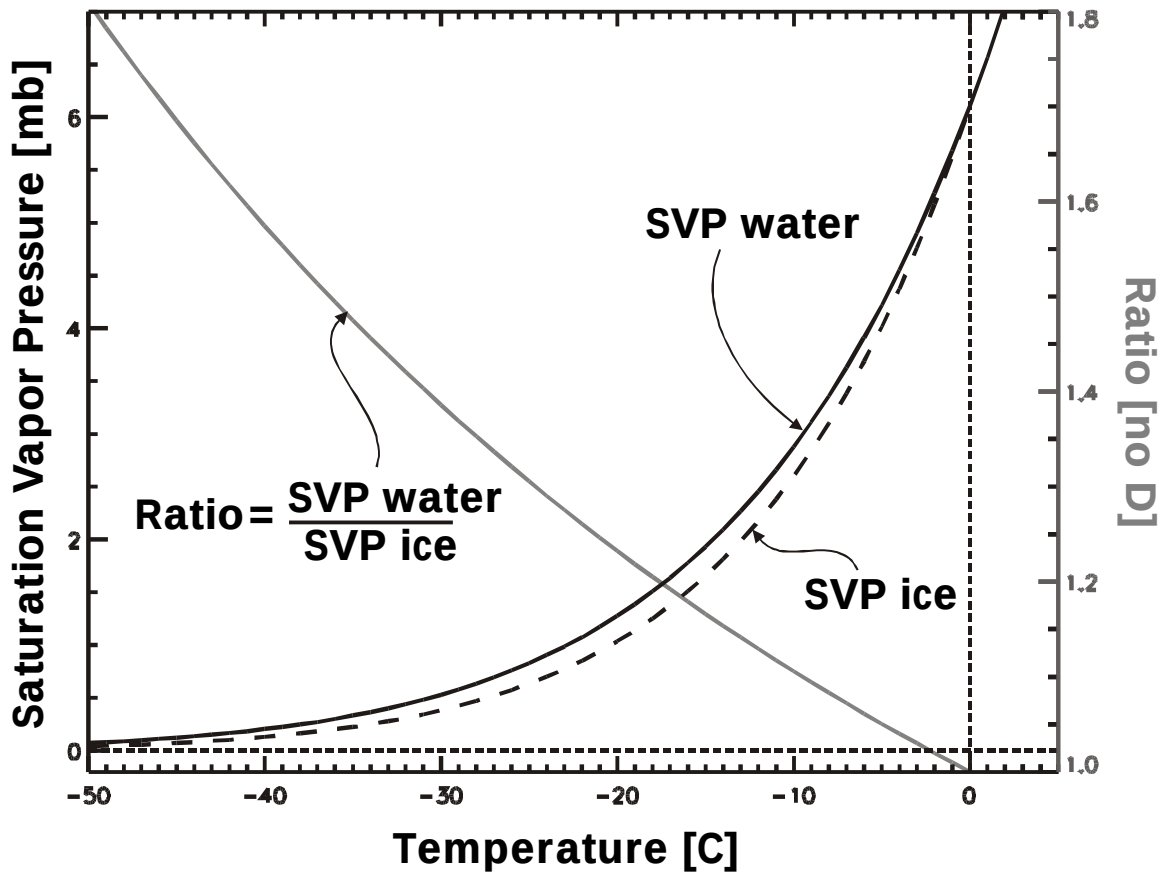

Figure 3.4, Saturation vapor pressure as a function of temperature with respect to a plane of pure ice and water surfaces. The ratio of the two vapor pressures is shown on the right axis.

The progression of this conversion is featured in Figure 3.5. Figure 3.6 shows the annual time series of hourly average relative humidity before and after scaling with respect to ice.

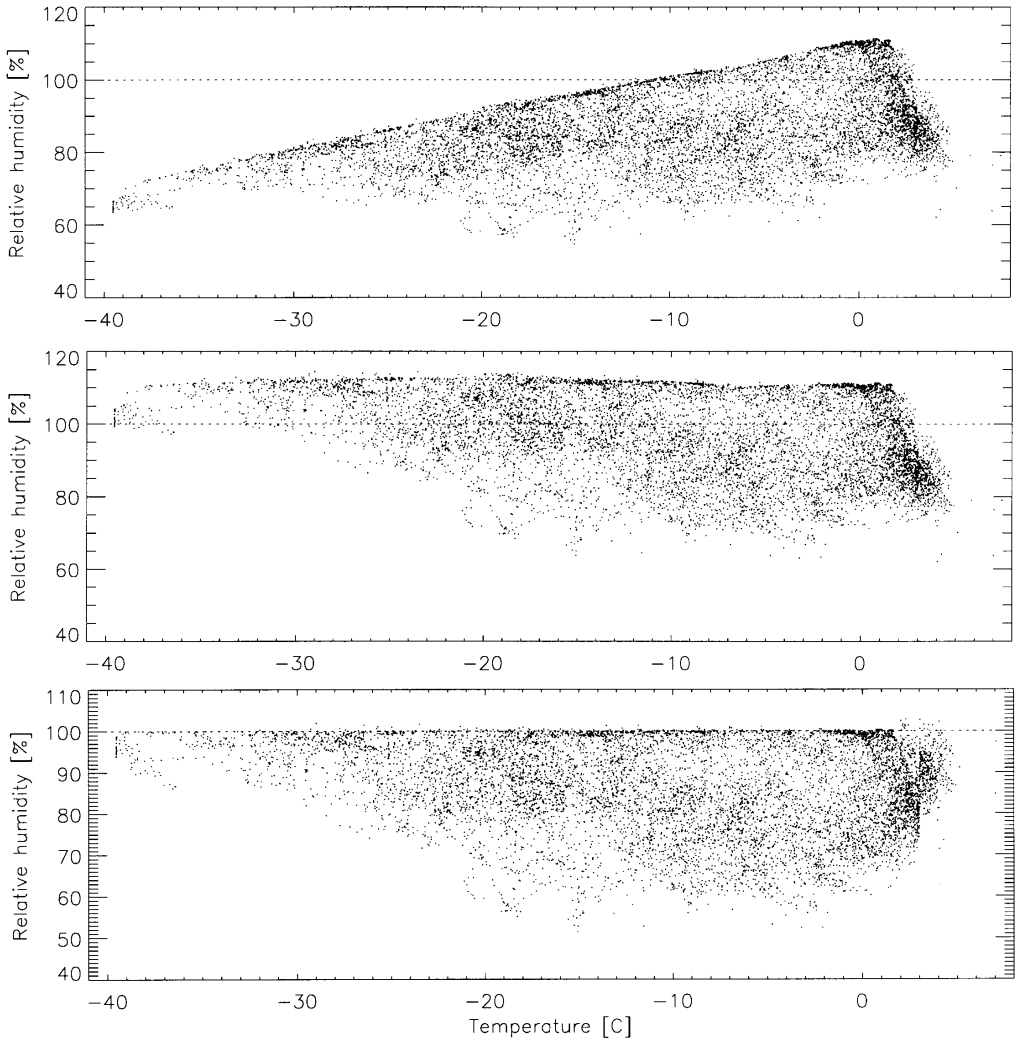

Figure 3.5, (Top graph) Relative humidity versus temperature, illustrating the need for rescaling with respect to the saturation limit of the instruments. (Middle graph) Relative humidity versus temperature after conversion to saturation over ice instead of saturation over liquid water. (Bottom graph) Relative humidity versus temperature after application of the temperature dependant offset with respect to saturation limit for the individual instrument.

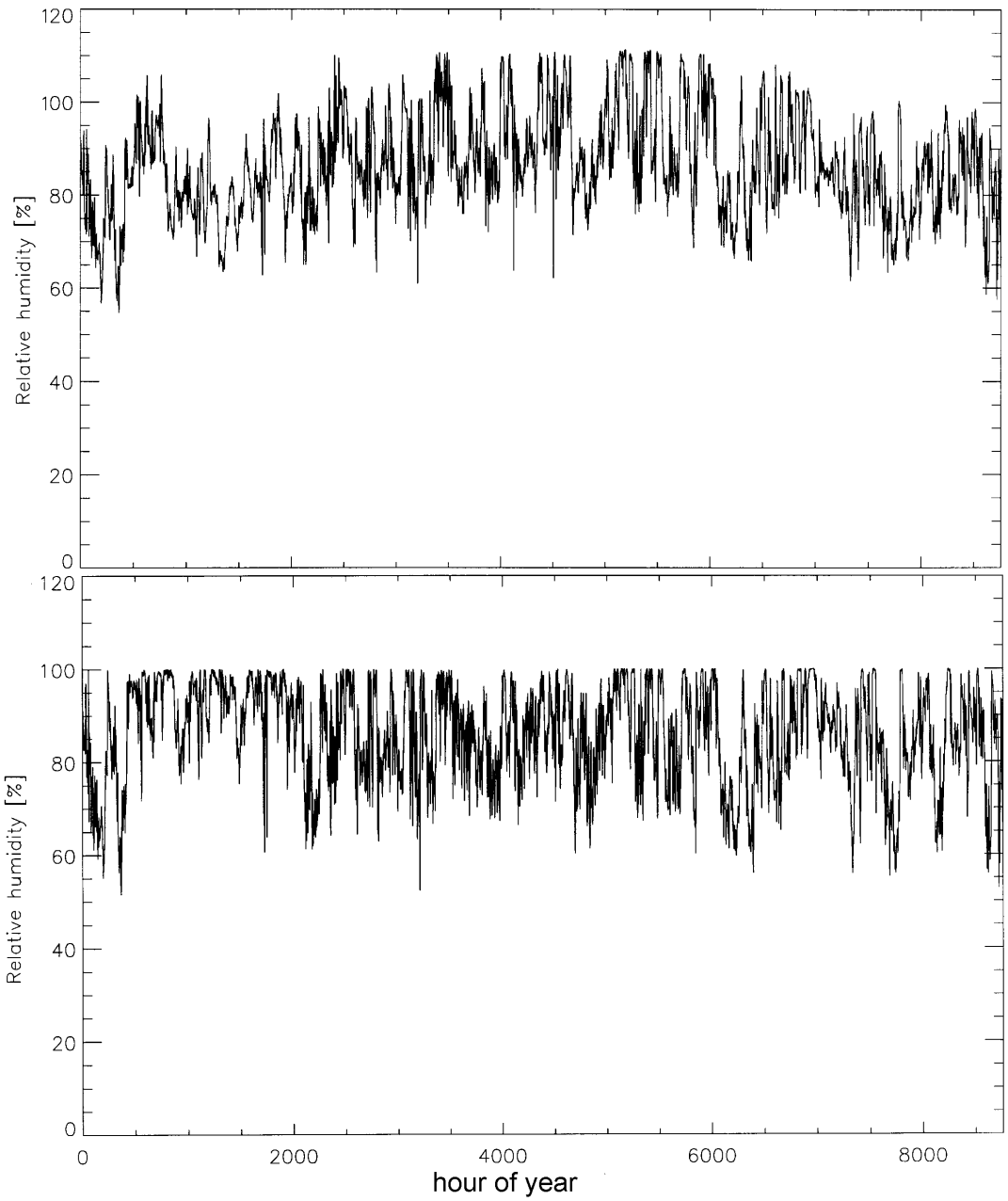

Figure 3.6 One year of relative humidity observations from the JAR 1 site in 1998 (top) raw data representing saturation over liquid water (bottom) the same data scaled with respect to saturation over ice.

A second step in the rescaling process that improves the relative accuracy of relative humidity measurements is now outlined. The humidity readings are offset with reference to the maximum output of the sensor for temperatures in 1 K intervals. The 98th percentile of each sorted bin is taken as the maximum output of the sensor because spuriously high readings can occasionally occur in the course of one-year for a given temperature. *Makkonen* [1996] pointed out that this theory neglects super saturation with respect to ice. Super saturation is ignored in this analysis owing to the instrument's inability to measure it and the rarity of its occurrence [*Anderson*, 1996]. During saturation at low temperatures (< -30° C), the range in *RH* values is no greater than 3%. The same range is taken as the instrument absolute accuracy after rescaling.

The effects of the RH conversion are investigated in how they change the measured vertical specific humidity gradient. The specific humidity gradient is found to be larger for uncorrected cases. Therefore, the correction serves to reduce the predicted surface water vapor flux.

3.1.12 Absolute Calibration of Humidity Sensors

The Yankee Environmental Systems MET-2010 Chilled Mirror Hygrometer (CMH) was deployed in Greenland for an absolute calibration experiment for AWS humidity sensors. Measurements were conducted at the ETH/CU Swiss Camp in the spring (May 18 – May 24) of 2000 at a nominal height of 1.8 m, corresponding with the upper measurement level on the AWS located 10 m away. The Met-2010 is actively ventilated to reduce thermal radiation errors and to supply the sensors with ambient air at 5 m s^{-1}. Ten minute averages are compared between the two sensor types. There is a strong positive correlation for the first 49 hours of observation, then a more noisy relation with negative bias occurs. Ice had developed over the CMH mirror leading to spuriously high humidity measurements. The use of this instrument seems to be restricted by the need to clean the mirror surface of ice regularly to prevent ice build up. No comparison data was obtained between the dew/frost point hygrometer and the newer Vaisala HUMICAP (HMP) sensors were deployed at the colder AWS sites starting in 2000.

The values of dew point temperature and ambient air temperature from the MET 2010 are combined to obtain relative humidity for comparison with AWS measurements using:

$$RH = \frac{e_s(T_d)}{e_s(T_a)} * 100\% \qquad \text{Eq. 3.5}$$

where e_s is the partial pressure of water vapor at saturation (hPa), T_a is the ambient temperature measured by the MET-2010 (K), T_d is the dew point or frost point temperature measured by the MET-2010 (K), L is the latent heat of vaporization or sublimation (J kg^{-1}), and R_v is the individual gas constant for water vapor (461.5 J kg^{-1} K^{-1}).

Linear regression between the two humidity measurements yields an explained variance of about 90% for Vaisala INTERCAP instruments (Table 3.9). However, 7% of the explained variance is lost by the $RH_{liq} \rightarrow RH_{ice}$ conversion as indicated by an increase in the standard deviation of the difference in RH values. In the conversion, the offsets between the two Vaisala INTERCAP instruments are brought from 3.64% to 0.44 % absolute difference. Vaisala INTERCAP RH_{ice} was on average 3.6% greater than the MET 2010 RH_{ice} (Figure 3.7). Also, there is less bias for RH_{ice} than RH_{liq}, so the conversion certainly helps. The two instruments calibrated by the instrument offset procedure (section 3.1.11) exhibit a much better relatively accuracy.

Table 3.9, Hourly Vaisala INTERCAP / Frost Point Hygrometer Comparison

	RH_{liq} Instrument 1	RH_{liq} Instrument 2	RH_{ice} Instrument 1	RH_{ice} Instrument 2
N Samples	59	59	59	59
r^2	0.97	0.97	0.89	0.91
slope	0.74	0.68	0.81	0.74
Mean difference	1.51	5.15	3.42	3.86
1 σ resid	1.88	2.35	1.81	2.05
1 σ Difference	2.17	2.15	2.97	2.69

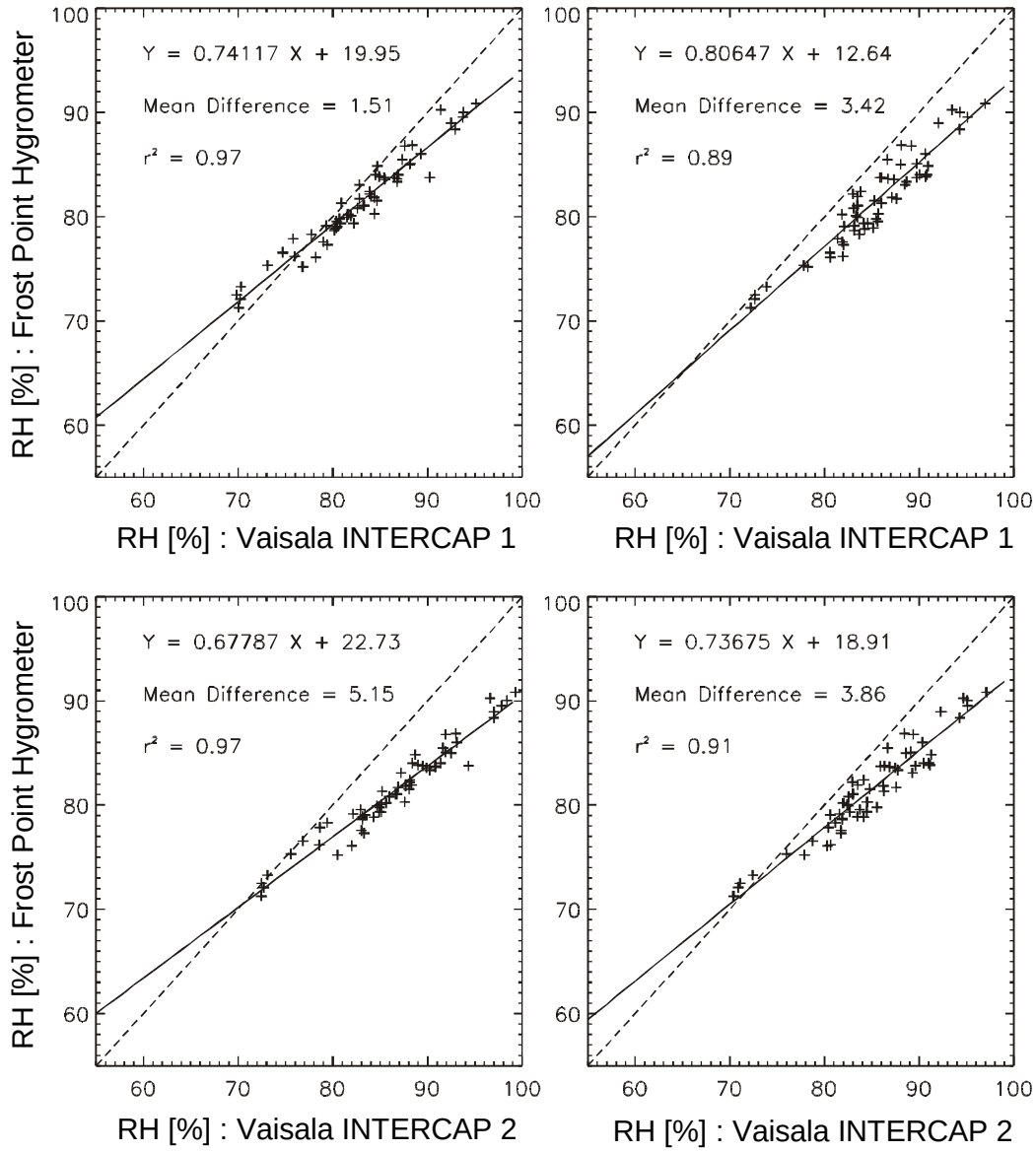

Figure 3.7, Relative humidity measured by capacitance versus chilled mirror sensors.

3.1.13 Uncertainty and Averaging

Knowledge of how instantaneous uncertainties change with averaging are crucial for gauging uncertainties in seasonal and annual water vapor flux quantities. Monthly and annual uncertainties are modeled with random Gaussian distributions. The distributions are scaled with respect to the uncertainties given by instrument specifications (Table 3.2) and relative calibration results (Table 3.8). To simulate the uncertainty for different averaging periods, the instantaneous uncertainty is applied to 240 samples (hourly average of 15 sec samples) averaged over one hour as with AWS data and then averaged over a range of time periods from one hour to one year. As the number of samples increases from 60 as with hourly averages to 5.256×10^5 for one year, the uncertainty decays steadily (Figure 3.8). According to the results, the uncertainty decreases to 50% of the original uncertainty when 60 samples are taken, representing one hourly average. Monthly uncertainties are 20% of the original uncertainty. Annual uncertainties are only 2% of the original uncertainty.

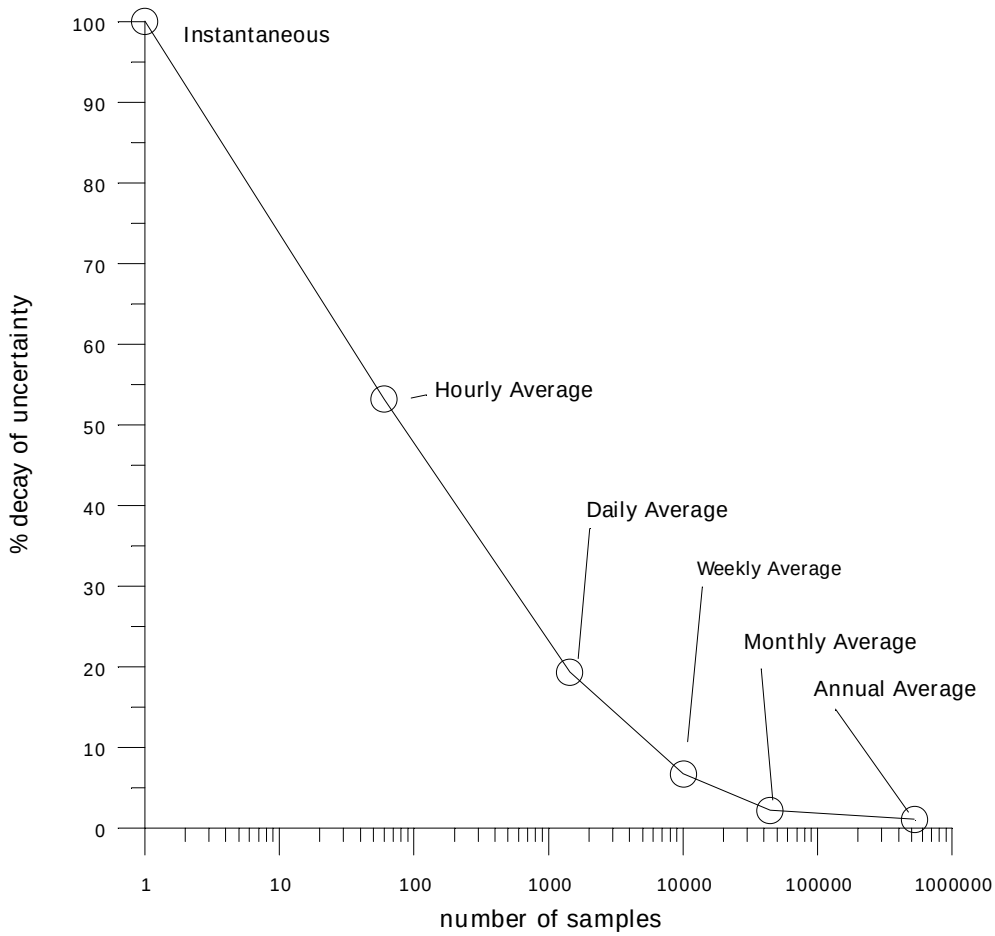

Figure 3.8, decay of uncertainty due to averaging.

3.2 Eddy Flux Correlation Measurements

The eddy flux correlation method (ECM) is a standard technique to directly sample atmospheric turbulent energy and mass fluxes [*Stull,* 1988]. Wind velocity is measured using speed of sound variations and air density changes with temperature. Air temperature variations are measured using a 0.08 mm chrome-constantan fine wire thermocouple. Humidity variations are measured using the KH20 instrument that relates water vapor concentration to its attenuation of ultraviolet radiation from a krypton gas light source. Vertical fluxes of latent and sensible heat are derived from the covariance of vertical wind velocity and that of heat or a chemical admixture, e. g. water vapor. The ECM is considered more accurate than techniques that relate averaged temperature, wind speed, and humidity profiles to turbulent heat fluxes [*Oke,* 1987]. Eddy correlation measurements used in this study have been made at the ETH/CU 'Swiss Camp' and Tunu-N (Table 3.1). The 3D and 1D measurements represent the same quantity, the vertical flux of latent heat associated with sublimation or evaporation. These experimental measurements are employed to validate latent and sensible heat flux estimates derived from GC-Net profile measurements. ECM data were filtered for times when wind direction caused measurement errors.

Table 3.10, Eddy Correlation Experiments

Site	Date	Campbell Scientific Instruments
TUNU-N	May 13 – May 31, 1996	1D CA-127 Sonic Anemometer KH-20 Hygrometer
ETH/CU Swiss Camp	May 24 – June 6, 1999 May 21 – June 8, 2000	3D CSAT Sonic Anemometer KH-20 Hygrometer

ECM uncertainties are assessed based on a relative calibration of two 3D eddy correlation measurements made June 22 2000 at Summit [*N. Cullen,* personal communication] (Table 3.11).

Table 3.11, Turbulent Fluxes for a Relative Calibration Period

Latent Heat Flux [W m^{-2}]	Mean	1 Standard Deviation	Range	Maximum	Minimum
System A	9.18	8.08	27.60	-3.82	23.79
System B	6.18	6.49	21.66	-4.20	17.46
Difference	33%	20%	21%	9%	27%

Based on this one day comparison of fluxes from the ECM, the bias is 33%, however. Confidence in an uncertainty based on only one day of measurements is not great. This bias is larger than expected. It does provide insight into the uncertainty in ECM data which are used to validate profile method results in chapter 5. More relative comparisons of the ECM would give more confidence, even if the uncertainty were still 33%.

3.3 Evaporation Pan Measurements

Evaporative mass transfer is directly inferred by measuring weight changes of an isolated volume of snow or solid ice [*Fujii and Kusunoki,* 1982; *Kaser,* 1982; *Kojima,* 1985; *Kameda et al.,* 1997]. In these studies, samples are contained by clear glass or plastic dishes with dimensions ranging from 4 cm to 9 cm in width and from 1 cm to 10 cm in depth. Only cases when there is no blowing snow or snowfall are considered as useful data points because this method assumes that all mass transfer into and out of the pan is by water vapor only. To eliminate confusion in the following discussion, sublimation and/or evaporation are referred to as ‘evaporation’.

The results of various field experiments help define the limits of naturally occurring evaporation rates

over snow surfaces. Evaporation rates varied from an extreme value of -0.18 mm h^{-1} for a 9 m s^{-1} wind in Moshiri, Hokkaido, Japan to typical monthly mean values of -0.16 mm day^{-1} for February and -0.22 mm day^{-1} for March [*Kojima,* 1985]. At 3030 m elevation on Hinterereisferner, Austria, the average evaporation rate for a 12-day period in summer was -0.25 mm day^{-1} [*Kaser,* 1982]. The daily variation displayed maximum evaporation before noon and condensation in the afternoon with maximum condensation commonly 2 hours after sunset. Maximum evaporation during this period was -2.0 mm d^{-1}. Evaporation values typical of the strong katabatic wind region in Antarctica at Mizuho Station, 2230 m elevation, are -0.7 mm day^{-1} in summer with a maximum of -0.92 mm d^{-1} observed on the summer solstice [*Fujii and Kusunoki*, 1982]. The annual cycle of water vapor flux based on one year of 12 h evaporation pan measurements resembled that of the solar radiation with wintertime values indicating a small amount of deposition (+6 mm). The annual net surface water vapor flux was large -54 mm compared to the net accumulation of only 58 mm. Evaporation pan measurements at Dome Fuji Antarctica, situated at a topographic peak on the ice sheet (3810 m) *Kameda et al.* [1997] indicated that during summer, evaporation of -3.9 mm occurred, while 5.5 mm net deposition occurred in winter. Thus evaporation pans are useful for measuring the net water vapor flux over snow and ice surfaces. In the following, an evaporation pan experiment at Swiss Camp by the author is described. The goal of this experiment was to determine if the eddy correlation accurately gauges evaporation.

From May 31 – June 8, 2000, surface water vapor flux was measured using 190 mm wide x 100 mm deep clear Pyrex glass pans containing snow samples. Samples were extracted from similar snow nearby with a steel cylindrical cutter. The sample then was slid into the slightly larger inside diameter pan. A void was extracted from snow at the measurement site, then the pan was set into the snow with its top level with the snow surface. The pan weights were measured twice daily. Measurements were obtained primarily during melt conditions characterized by strong winds, often greater than 8 m s^{-1} and air temperatures at or above the melting point. One nighttime measurement indicated net water vapor deposition to the surface, i.e. rime frost. Seven 12-hour observations for two evaporation pans were obtained (Table 3.12). Throughout the period, two simultaneous evaporation pan measurements were made. The results of this evaporation pan experiment are featured in comparison with eddy correlation in section 5.7.2.

Table 3.12, Evaporation Pan Data

Run	Date	UTC H	UTC min	Pan A (g)	Δm (g)	Density (kg m^{-3})	Pan C*	Δm (g)	Density (kg m^{-3})
1	31-May	13	20	1536		373.2	1296.5		286.71
	1-Jun	14	35	1529	-7.4		1294.0	-2.5	285.83
2	2-Jun	2	0	1524		369.0	1289.4		284.21
	2-Jun	12	20	1532	7.6		1290.0	0.6	
3	5-Jun	12	15	1504		361.6	1530.6		369.32
	5-Jun	20	30	1493	-11.0		1510.6	-20.0	
4	6-Jun	15	0	1671		420.8	1808.4		467.35
	6-Jun	1	0	1659	-12.4		1797.0	-11.4	
5	7-Jun	1	25	1549		377.7	1646.2		410.11
	7-Jun	14	20	1526	-23.0		1628.0	-18.2	403.69
6	7-Jun	14	20	1526		369.6	1628.0		403.69
	8-Jun	1	20	1516	-10.6		1618.0	-10.0	400.16
7	8-Jun	1	50	1682		424.7	1642.0		408.63
	8-Jun	12	30	1667	-15.4		1630.0	-12.0	

* Pan B was broken at the beginning of the experiment.

3.4 Accumulation Rates Derived from Ice Cores

A number of shallow ice cores have been collected in Greenland during several field expeditions (Table 3.13) [*Ohmura et al*, 1999; *Moseley-Thompson et al.*, submitted]. A main objective has been to derive accumulation rates, a critical parameter for glacier mass balance studies. Accumulation rates for sites without ice cores are estimated from the accumulation map of *Ohmura et al.* [1999].

Table 3.13, Ice Core-derived Accumulation Rates at GC-Net Sites

Site	Accumulation [mm y^{-1}]	Standard Deviation	Source
Swiss Camp	250	N/A	**
CP1	480	N/A	*
NASA-U	330	88	*
GITS	350	80	*
Humboldt	140	40	*
Summit	200	N/A	**
Tunu-N	100	N/A	*
DYE-2	300	N/A	**
Saddle	450	N/A	*
South Dome	670	130	*
NASA-E	150	48	*
CP2	672	N/A	***
NGRIP	170	N/A	**
NASA-SE	600	N/A	*
JAR2	225	N/A	**

* - [*Moseley-Thompson et al.*, submitted]
** [*Ohmura et al.*, 1999]
*** - based on surface height measurements (Appendix section C).

3.5 Precipitation Rates from a Regional Model

Precipitation is a relevant quantity to assess the importance of surface water vapor flux to accumulation. Precipitation data are available based on a diagnostic model of *Chen et al.*, [1997]. The model determines precipitation based on the vertical velocity component of atmospheric circulation via the generalized 'omega' equation. The vertical velocity is used to derive cloud development and subsequent precipitation for a three dimensional box in the atmosphere, assuming a lifting condensation level given by temperature and liquid or ice water content. The model further assumes that all condensed moisture falls to the surface, with a parameterization for evaporation of falling precipitation. Annual precipitation rates for individual years 1995-1999 were obtained for GC-Net sites from a recent 40 km horizontal resolution model reanalysis [*Bromwich et al.*, submitted]. Data were obtained from David Bromwich and John Cassano at the Byrd Polar Center, Ohio State University, Columbus, OH (Table 3.14).

Table 3.14, Precipitation at GC-Net Sites from a Diagnostic Model [mm w. e. y^{-1}]

AWS Site	1995	1996	1997	1998	1999	Average:
Swiss Camp	783	783	821	675	795	771
CP1	533	666	654	494	644	598
NASA-U	346	409	508	400	404	414
GITS	396	344	363	306	230	328
Humboldt	185	244	245	237	157	214
Summit	121	100	113	123	115	114
Tunu-N	164	128	151	155	176	155
DYE-2	434	507	460	476	530	482
JAR1	726	739	775	641	741	724
Saddle	219	388	332	298	426	333
South Dome	406	495	500	416	518	467
NASA-E	163	142	185	206	241	188
CP2	512	651	640	480	628	582
NGRIP	138	74	118	118	118	113
NASA-SE	503	597	485	384	533	501
JAR2	726	739	775	641	741	724

3.6 Snow Pit Density Measurements

Density profiles from snow pits measured at twelve GC-Net sites in 1999 (Table 3.15) are used to estimate the accumulation rate based on surface height change measurements. Samples were taken each 10 cm by the 'Kelly Cutter' sampler. This sampler has dimensions of 10 cm width, 20 cm length, and 10 cm height. Sample weights were measured by an Ohaus digital balance to 1 g accuracy. If ice layers were present, representative samples were taken. Using the density profiles obtained from the twelve snow pits, a general depth-density relationship for GC-Net sites was derived (Figure 3.9). Average density for the top 2 m of firn is estimated to be 346 kg m^{-3}. This value falls within the range of 300 kg m^{-3} – 400 kg m^{-3} given by *Benson* [1962] for Greenland ice sheet sites.

Table 3.15, Summary of 1999 Snow Pit Density Measurements

Site	Maximum Depth [m]	Date in 1999
Swiss Camp	0.7	Apr. 3
NASA-SE	1.7	Apr. 21
Saddle	1.9	Apr. 16
South Dome	1.6	Apr. 22
Crawford Pt. 1	1.2	Apr. 26
Summit	1.8	May 12
Humboldt Gl.	1.5	Apr. 5
GITS	2.0	Apr. 29
DYE-2	0.9	Apr. 18
NASA-U	2.0	May 13
CP-2	1.5	May 28
JAR	1.2	May 31

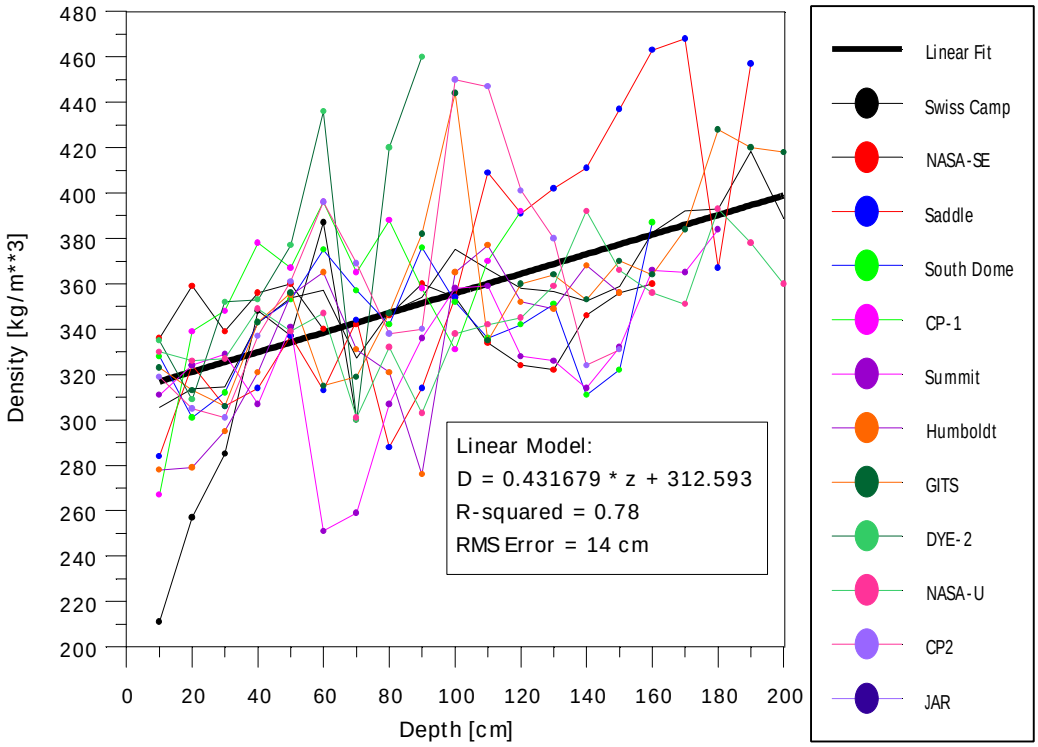

Figure 3.9, Empirically-derived depth density relationship based on average snow pits density profile from twelve pits collected in 1999. D is the density and z is the depth [cm].

4 Climatological Context for Surface Water Vapor Fluxes

4.1 Derived Parameters

The surface water vapor flux is calculated from meteorological state variables, temperature, humidity, and wind speed. Differences of these variables between two measurement levels is used to derive the vertical water vapor flux. The state variables often require conversion. Specific humidity and its variation with height, for example, is derived from relative humidity, temperature, pressure, and surface height change measurements. Analysis of the state variables in this section aims to clarify the context of surface water vapor flux on the Greenland ice sheet.

4.1.1 Specific humidity

Specific humidity *(q)* is the density of water vapor per unit volume divided by the unit density of the whole air volume given by:

$$q = e\,\frac{e}{p-(1-e)e} \qquad \text{Eq. 4.1}$$

where e is the ratio of the molecular mass of water vapor to that of dry air (0.622), *p* is the local barometric pressure (hPa), and *e* is the water vapor pressure (hPa). Specific humidity is expressed in units of g kg^{-1}. Taking an hourly temperature uncertainty of ± 0.1 K, ±3% for RH_{ice}, and ± 1 hPa in pressure, over a range of RH_{ice} and with temperature of -10° C, the maximum uncertainty in *q* is ± 0.07 g kg^{-1}. The ± 1 hPa pressure uncertainty has a negligible effect on *q* of about ± 0.0001 g kg^{-1}. On a monthly basis, with temperature uncertainty dropping to ± 0.01 K, and RH_{ice} uncertainty of ± 0.15 % the uncertainty in q is ± 0.004 g kg^{-1}.

4.1.2 Instrument Heights

For accurate profile simulation, temperature, humidity, and wind sensor heights *(z_1* and *z_2)* are calculated hourly using the average of the two surface height change measurements ($\Delta\bar{z}_{1,2}$) (Table 3.2), the instruments' initial height *(z_*)*, and a mast extension offset *(z')*.

$$z_i = z_* - \Delta\bar{z}_{1,2} + z' \qquad \text{Eq. 4.2}$$

Instrument height estimates are validated by measurements made during site visits (Figure 4.1). The one standard deviation route-mean-square error of instrument heights was ±4 cm with 95% of the cases within ±10 cm.

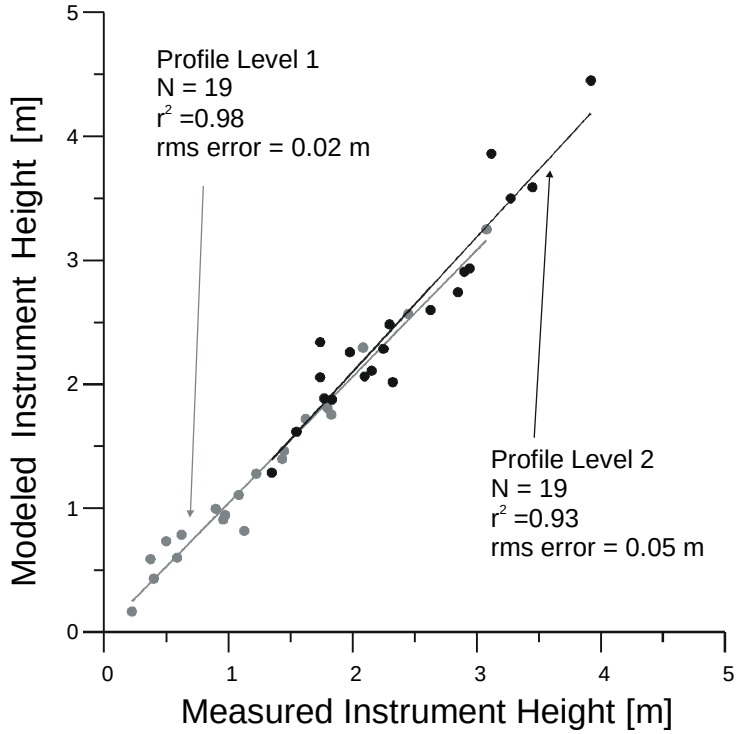

Figure 4.1, Validation of instrument height calculations.

4.2 Climatological Context

The climatological variations of temperature, specific humidity, and wind speed derived by GC-Net measurements are now presented. Discussion focuses on the annual cycle to determine the seasonal and geographic patterns of the state variables. Annual cycles of vertical profile differences are also presented and discussed in context of the surface water vapor flux potential.

4.2.1 Air Temperature

Air temperatures on the Greenland ice sheet are characterized by a large annual range. The range of monthly mean temperature in a mid-latitude maritime climate is often less than 10° C. Continental climates often have a range up to 25° C [*Henderson-Sellers*, 1986]. At GC-Net sites, the annual range of monthly mean temperature is up to 35° (Figure 4.2). The large amplitude of the annual temperature cycle is a function of the extreme variations in solar elevation angle that occur at high latitudes. The mid day (mid night) sun remains below (above) the horizon in winter (summer) for up to 3.7 months at the northernmost site (Humboldt: 78.5° N; 1995 m a s l). At the southernmost site (South Dome: 63.1° N; 2850 m a s l), all days of the year have some sunshine. Hence, at South Dome, the annual amplitude of monthly mean temperature is 10° C less than at Humboldt despite South Dome's higher elevation.

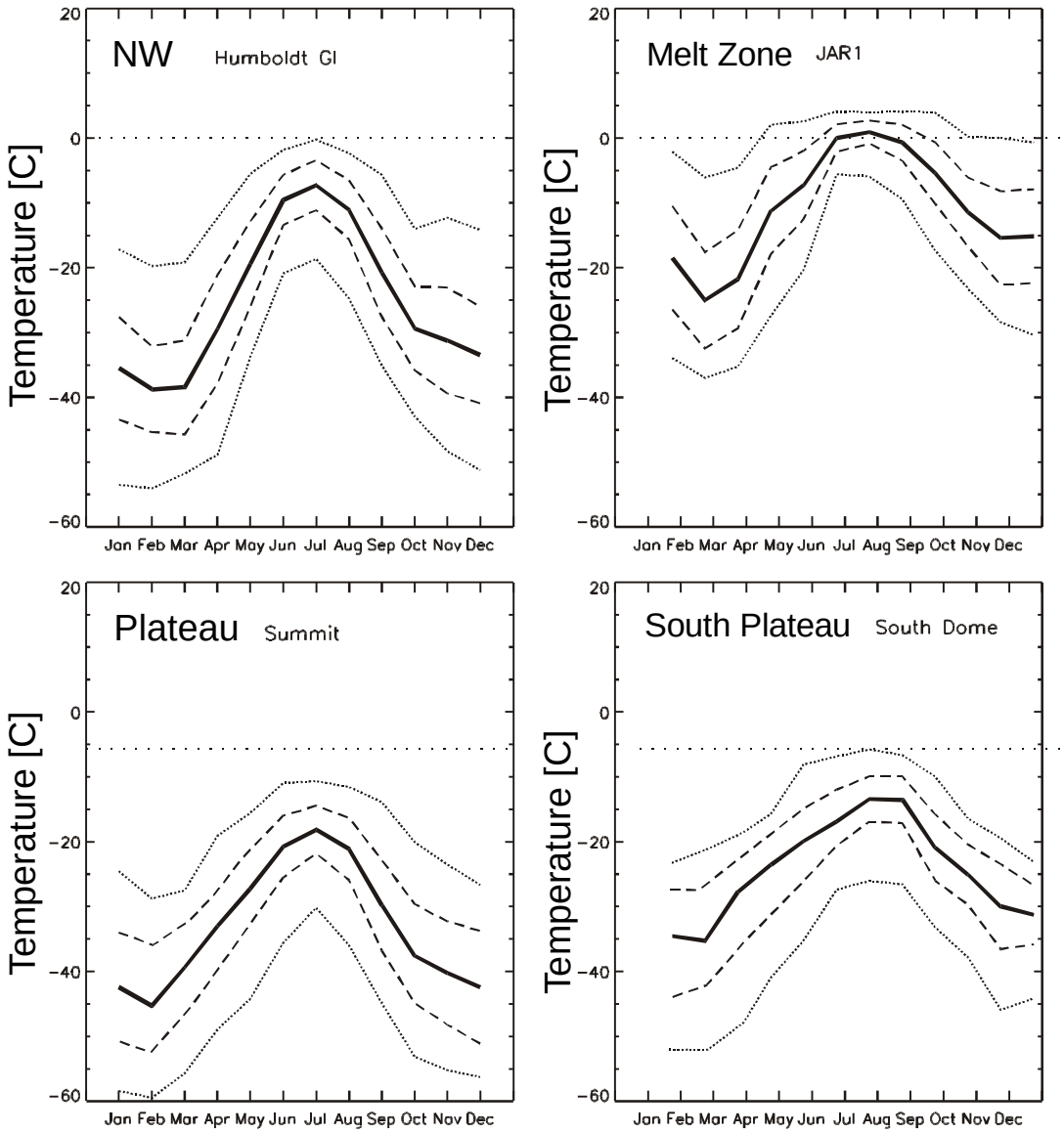

Figure 4.2, Annual variations of monthly mean temperature at representative GC-Net sites. The average of available measurements is represented by the solid line. The dashed lines represent one standard deviation of the monthly mean. The dotted lines represent the average maximum and minimum observed values for available data.

The duration of temperatures near the melting point will be an important determinant of the amount of potential surface water vapor flux. Melt event durations range from a few hours or days per year near 2000 m elevation to as long as 3 months at 500 m elevation at JAR 2. No melting is evident from temperature observations at the highest elevation and/or most northerly GC-Net sites (Summit, NGRIP, TUNU-N and NASA-E) (Table 4.1). At sites above 2000 m, the frequency of temperatures near the melting point is less than 1% with the exception of NASA-SE, located in the south. The frequency of melt is of interest to water vapor flux studies because when the surface is melting, less latent heat is required to extract an equivalent amount of moisture.

Table 4.1, Frequency of Air Temperature Above the Melting Point at GC-Net sites

Site	% of time $T_1 > 0°$ C 1998	% of time $T_1 > 0°$ C 1999
Swiss Camp	10.1	13.2
CP1	3.6	5.2
NASA-U	0.1	0.2
GITS	*	0.1
Humboldt	0.7	0.0
Summit	0.0	0.0
Tunu-N	0.1	0.0
DYE-2	3.3	4.8
JAR1	21.3	15.8
Saddle	0.6	0.8
South Dome	0.1	0.3
NASA-E	0.0	0.0
CP2	3.3	3.9
NGRIP	0.0	0.0
NASA-SE	*	1.4
JAR2	*	37.1**

* - insufficient data, **- calculated using 1999 and 2000 data

The ice sheet latitudinal temperature gradient ranges from –1.2° C per degree latitude in winter to -0.4° C in summer (Table 4.2). After the latitude gradient is subtracted from available GC-Net monthly means, the elevation gradient of temperature is well represented by a linear fit (r^2 = 0.79 to 0.89). Slope lapse rates over the ice sheet surface are largest in winter (~ 8.5° C km^{-1}) and smaller in summer (~6° C km^{-1}) (Table 4.2).

Table 4.2, Monthly Latitude and Elevation Gradients of Temperature

Month	Latitude Gradient [deg. C $deg.^{-1}$]	r^2	Elevation Gradient [deg. C km^{-1}]	r^2	N Obs.
Jan	-1.0	0.36	-8.6	0.84	34
Feb	-0.9	0.32	-7.1	0.81	31
Mar	-1.2	0.55	-7.0	0.86	39
Apr	-1.2	0.50	-6.9	0.72	39
May	-0.7	0.33	-6.3	0.79	35
Jun	-0.4	0.15	-6	0.81	50
Jul	-0.4	0.17	-5.7	0.89	55
Aug	-0.7	0.36	-5.7	0.84	49
Sep	-0.9	0.39	-7.4	0.89	44
Oct	-1.2	0.47	-8.1	0.83	43
Nov	-1.1	0.41	-8.2	0.89	37
Dec	-1.0	0.33	-8.5	0.86	34

4.2.1.1 Vertical Temperature Difference

The vertical temperature difference *(dT/dz)* near the surface of the Greenland ice sheet is predominantly positive throughout the year (Figure 4.3), indicative of a persistent surface temperature inversion. The inversion is strongest in winter, with monthly mean values often greater than 0.3 K m^{-1} at the colder sites (Humboldt, Summit, TUNU-N, Saddle, and NGRIP). Negative *dT/dz* values are also observed. These occur when weak winds allow the surface to be heated by absorption solar radiation to a temperature greater than the air just 1 m to 3 m above. Cold air advection over a relatively warm surface may also cause negative *dT/dz*. Negative *dT/dz* occurs most frequently during summer. The sign of *dT/dz* is important in determining the sign of *dq/dz* as the specific humidity calculation also responds to temperature.

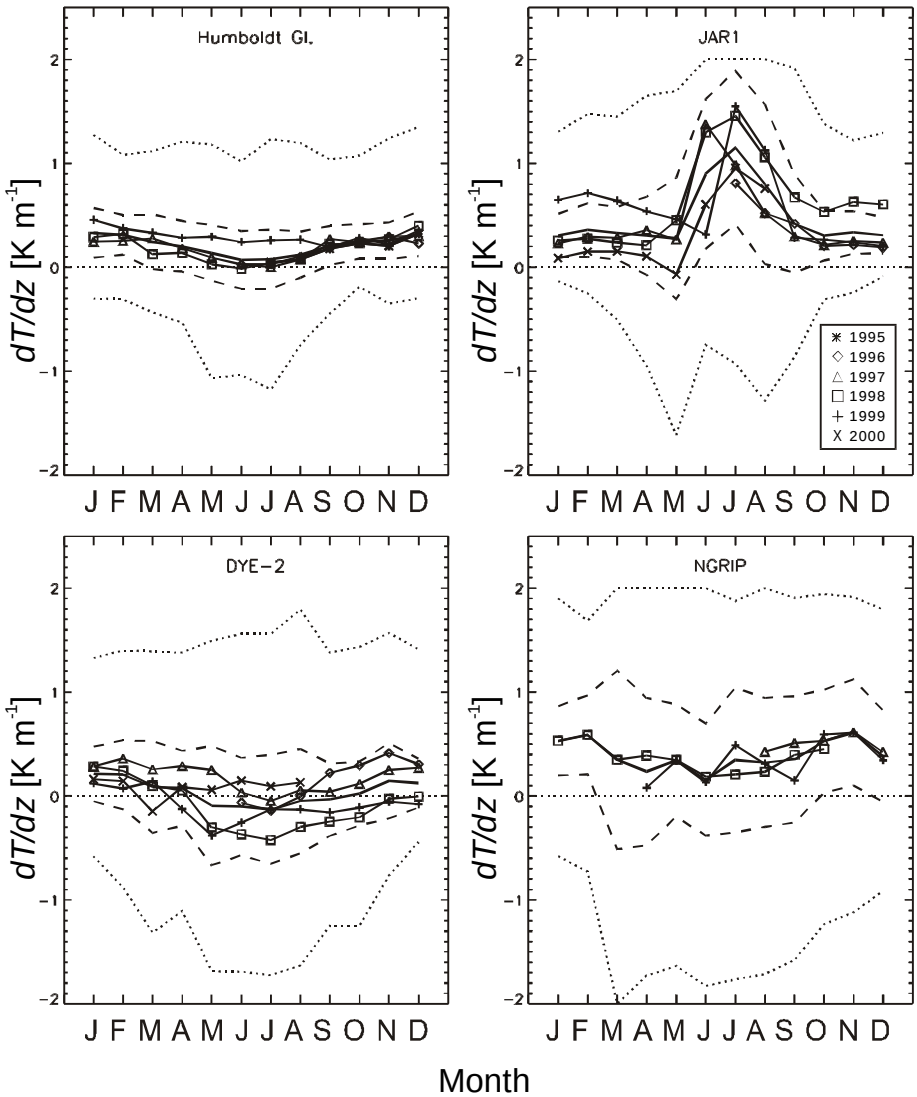

Figure 4.3, Annual variations of monthly mean vertical temperature difference at representative GC-Net sites The average of available measurements is represented by the solid line. The dashed lines represent one standard deviation of the monthly mean. The dotted lines represent the average maximum and minimum observed values for available data.

The *dT/dz* data from DYE-2 are somewhat suspect for errors. It seems impossible that the air nearer the surface is on average warmer than 1.2 m above. Monthly average cases in March or November when the surface heats the air are surprising. Negative *dT/dz* is observed most commonly in summer when intense solar heating of the surface is possible. Another possibility is persistent cold air advection. This instability may be an instrument relative calibration error. The vertical temperature differences are larger than can be explained by on-site

calibration results.

The cold air advection case poses an interesting scenario. A hypothesis for the DYE-2 instability in vertical temperature difference is that the air originating from upslope is colder. This may be the result of the greater melt rates at DYE-2 than are found upslope. Larger melt rates will lead to a more ice inclusions in the firn and hence a lower surface albedo than found upslope where melting is less extensive. The lower surface albedo will allow more solar heating of the surface, driving this instability.

4.2.2 Specific Humidity

A distinct annual cycle in specific humidity, consistent with other Arctic regions [*Serreze et al.*, 1995], is evident from GC-Net observations (Figure 4.4). Maximum specific humidity is found in summer, primarily in July, with hourly values as large as 7 g kg^{-1}. Minimum specific humidity is found in winter, particularly in February when air temperatures are usually at their minimum. For comparison, at coastal stations in Greenland, specific humidity often reaches 10 g kg^{-1} due to the relatively moist maritime climate and the ability of the warmer air to hold more moisture. In the mid latitudes, specific humidity peaks near 20 g kg^{-1} [*Piexoto and Oort*, 1992]. In winter, ice sheet humidity is as near zero as may be expected anywhere on the surface of the Earth (0.01 g kg^{-1}). On average, the minimum specific humidity at AWS sites above 2000 m is 0.05 g kg^{-1}, while at lower elevation sites (Swiss Camp and JAR), minimum specific humidity is noticeably larger (0.1 g kg^{-1}).

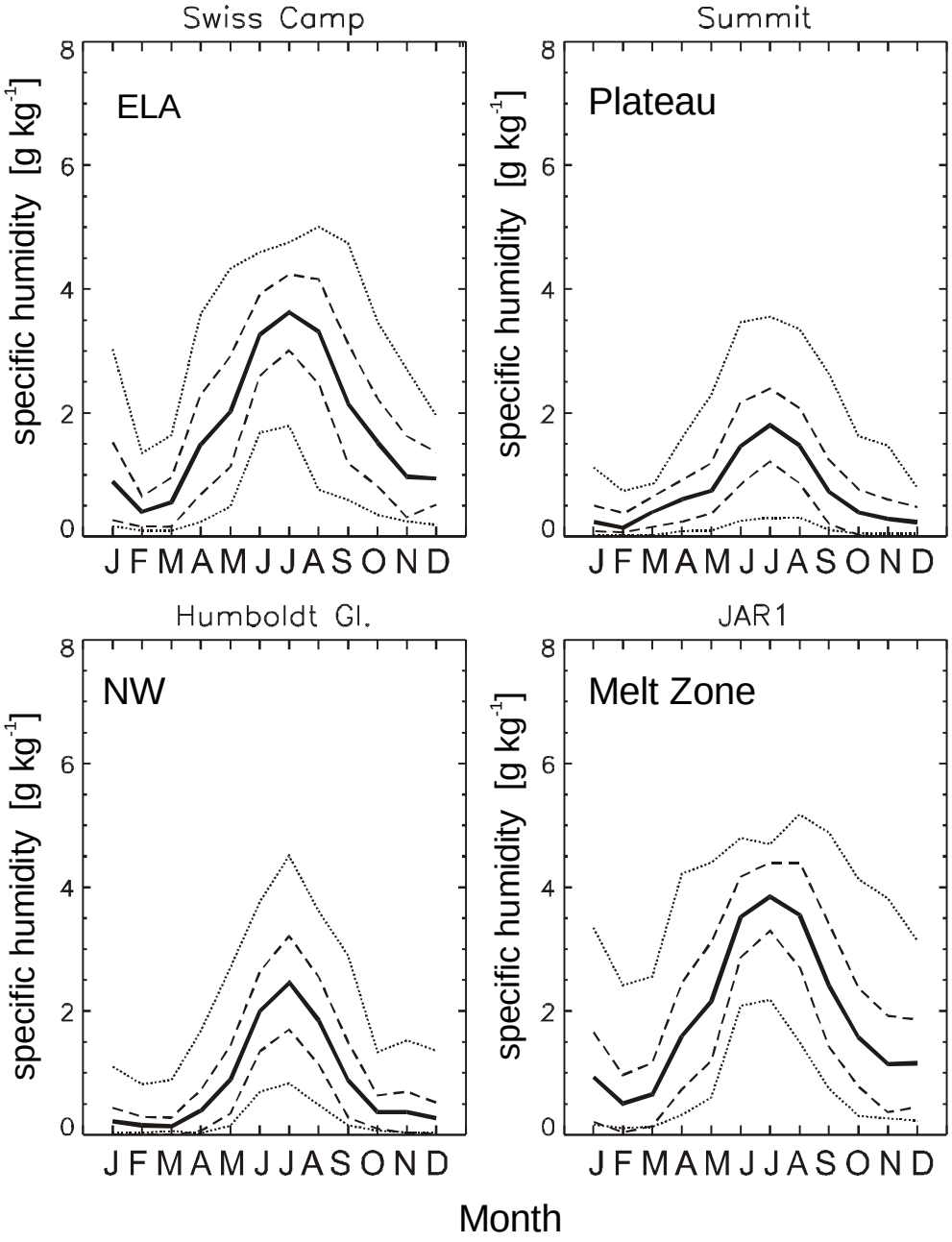

Figure 4.4, Annual variations of monthly mean specific humidity at representative GC-Net sites. The average of available measurements is represented by the solid line. The dashed lines represent one standard deviation of the monthly mean. The dotted lines represent the average maximum and minimum observed values for available data.

The annual range in specific humidity gets smaller with increasing elevation on the ice sheet. The annual temperature range is larger at high elevation sites. Orography and distance to the coast are major determinants in the amount of available moisture on the Greenland ice sheet. As higher elevations are reached, the distance to the coast increases and relatively few storms penetrate far inland because it precipitates out due to orographic uplift. Continentality is often expressed in terms of the annual temperature range and the difference in the heat capacity of oceans versus land [*Barry*, 1992]. A high degree of continentality is characteristic for Greenland, where the snow surface has a heat capacity 20 times smaller than water [*Oke*, 1987]. Given this fact, the surface air temperature is highly responsive to the annual cycle in net radiation.

Specific humidity decreases with elevation on the surface of the ice sheet (Table 4.3). Largest elevation gradients are observed in summer. There is also a notable latitude gradient in specific humidity. In winter, the elevation decrease of specific humidity is small because the amount of moisture is near zero over the entire ice sheet. Variability decreases with elevation in winter, as only the lower elevation sites have appreciable humidity amounts.

Table 4.3, Monthly Latitude and Elevation Gradients of Specific Humidity

Month	Latitude Gradient [g kg^{-1} deg.$^{-1}$]	r^2	Elevation Gradient [g kg^{-1} km^{-1}]	r^2	N Obs.
Jan	-0.04	0.35	-0.32	0.90	16
Feb	-0.03	0.58	-0.13	0.70	16
Mar	-0.04	0.63	-0.10	0.58	16
Apr	-0.06	0.35	-0.48	0.79	16
May	-0.07	0.37	-0.54	0.87	16
Jun	-0.06	0.07	-1.25	0.86	16
Jul	-0.07	0.16	-1.06	0.92	16
Aug	-0.11	0.43	-0.80	0.93	16
Sep	-0.07	0.32	-0.63	0.90	16
Oct	-0.07	0.42	-0.47	0.88	16
Nov	-0.04	0.28	-0.36	0.86	16
Dec	-0.04	0.28	-0.36	0.87	16

Broader annual cycles of specific humidity are found at the lower elevations and latitudes. However, at South Dome, the annual variation of specific humidity is broad despite the high elevation (2850 m). At lower latitudes, a lower amplitude annual variation in sun angle occurs. The annual specific humidity cycles are similar for the northern part of Greenland (Humboldt and TUNU-N) as compared to the plateau region (Summit and NGRIP).

4.2.2.1 Vertical Specific Humidity Difference

The annual variation of vertical specific humidity difference *(dq/dz)* indicates conditions that promote net loss of water vapor during the warmer half of the year ($dq/dz < 0$) with occasional deposition. Smaller amounts of water vapor deposition ($dq/dz > 0$) are favored during the winter period (Figure 4.5). Summertime loss of water vapor is favored at almost all sites. Deposition is favored particularly at sites above the equilibrium line altitude. For monthly averages, *dq/dz* favors water vapor loss throughout the winter at the ablation zone sites. Summertime *dq/dz* monthly means are as large as –0.1 mg kg^{-1} m^{-1}. The occurrence of mid-winter storms at lower elevation sites leads to a less distinct annual cycle in *dq/dz* at those sites. At northern sites, the season for potential water vapor loss is limited to a few months. During summer, deposition signals are common at ice sheet crest sites (Summit, NGRIP, and Saddle). Substantial elevational water vapor flux gradients occur in the ablation zone in summer and during winter when winds are strong and air temperatures approach 0° C.

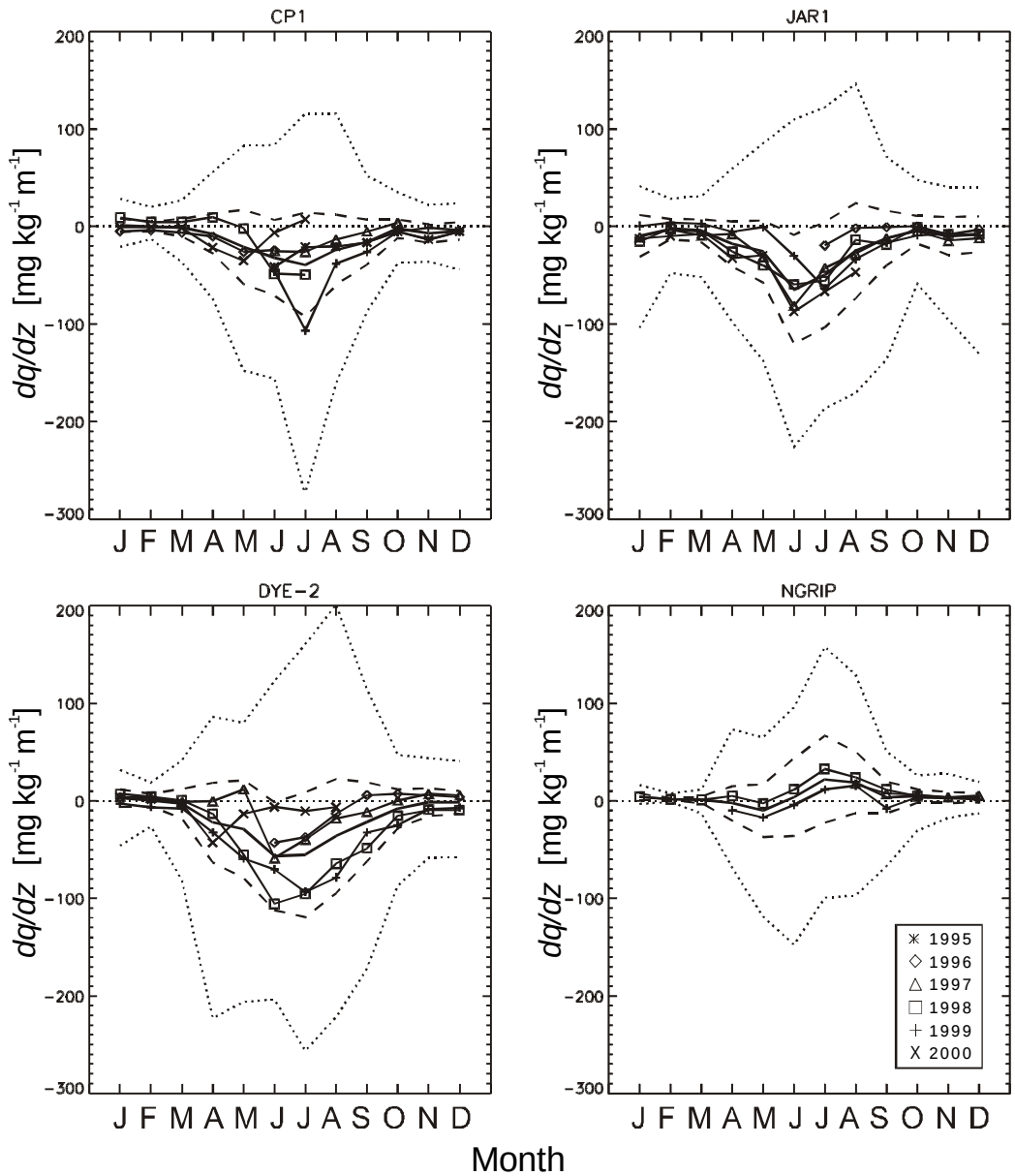

Figure 4.5, Annual variations of monthly mean vertical specific humidity difference at representative GC-Net sites. The average of available annual samples is represented by the solid line The dashed line represents one standard deviation of the monthly mean. The dotted line represents the average maximum and minimum observed values. The monthly means from individual years are also featured.

At NGRIP and Summit, an opposite pattern to most GC-Net sites is often observed. *dq/dz* remains positive, indicating the tendency for net deposition of water vapor mass throughout the year. Maximum deposition is favored in mid summer (Figure 4.5). The very small *dq/dz* occurring in winter, particularly at sites above ELA, cannot be measured within the uncertainty limits of the humidity instruments. Fortunately, this inaccuracy would not contribute to great errors in annual surface water vapor flux totals because wintertime humidity differences are on average so small ($|dq/dz| < 10$ mg kg^{-1} m^{-1}). *dq/dz* can be derived with sufficient accuracy during summer when largest values are expected.

4.2.3 Wind Speed

Surface winds drive turbulent heat transfers. Analysis of the GC-Net wind speed measurements at an average height of 1.5 m reveals that there is a distinct annual cycle in wind speed on the Greenland ice sheet.

Average wind speed peaks in winter, when the katabatic wind is most developed [*Bromwich et al.*, 1996] (Figure 4.6). Diurnal cycles of wind speed will be discussed in the review of hourly flux characteristics in the next chapter which summarizes water vapor flux calculations and results.

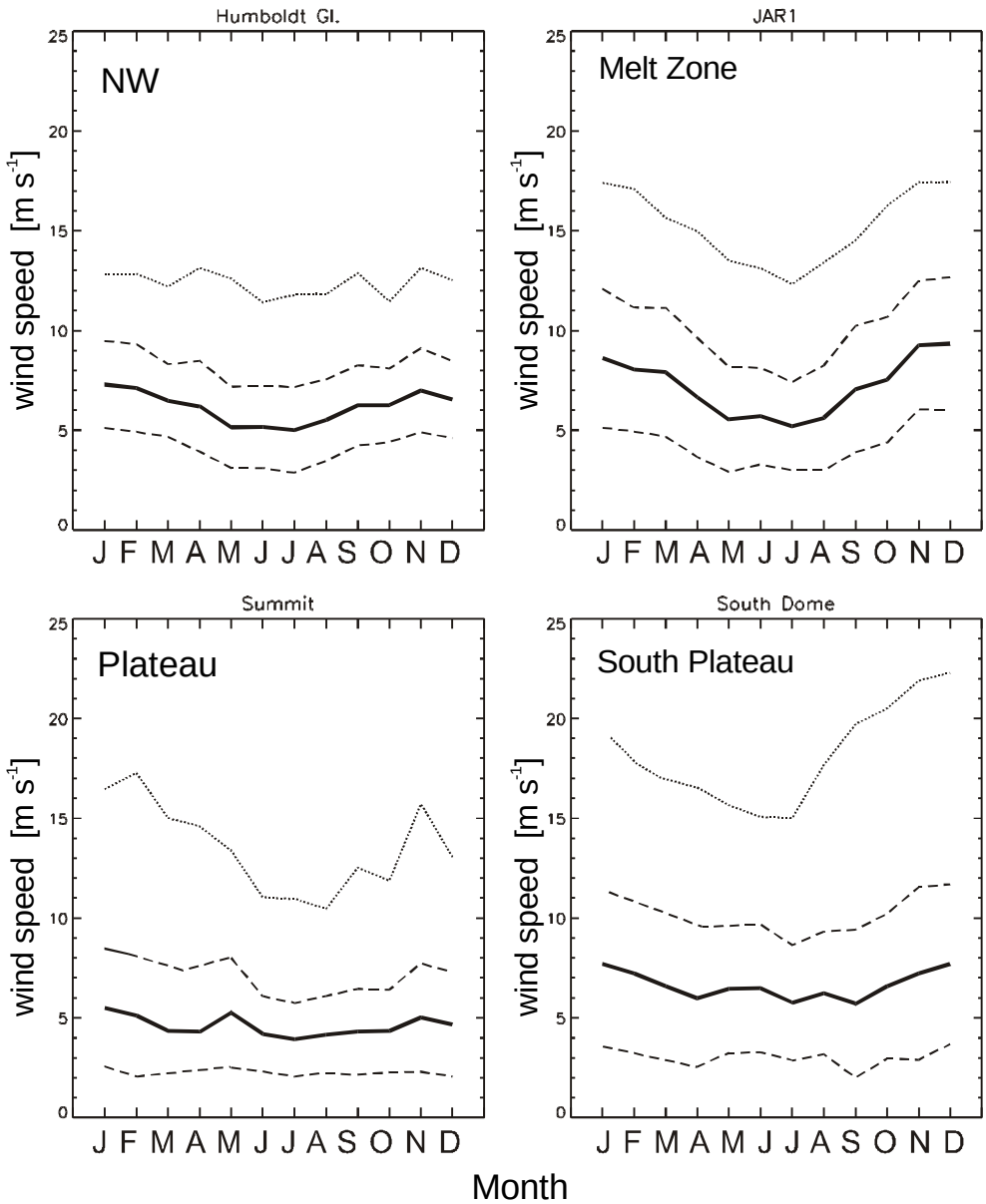

Figure 4.6, Annual variations of monthly wind speed at representative GC-Net sites. The average of available measurements is represented by the solid line. The dashed line represents one standard deviation of the monthly mean. The dotted line represents the average maximum and minimum observed values.

On a monthly basis, wind speeds decrease with elevation (Table 4.4). This pattern is not significant in all months. Observations from South Dome violate this generalization, as the South Dome climate indicates strong prevailing easterly winds which are synoptic in origin. There is no significant latitude gradient in wind speed on the ice sheet.

Table 4.4, Monthly Latitude and Elevation Gradients of Wind Speed

Month	Elevation Gradient [m s^{-1} km^{-1}]	r^2	Number of Observations
Jan	-0.67	0.18	16
Feb	-0.97	0.48	16
Mar	-1.2	0.60	16
Apr	-0.68	0.37	16
May	0.51	0.42	16
Jun	-0.33	0.11	16
Jul	-0.28	0.13	16
Aug	-0.16	0.03	16
Sep	-0.62	0.29	16
Oct	-0.82	0.43	16
Nov	-1.35	0.58	16
Dec	-1.47	0.58	16

4.2.3.1 Vertical Wind Speed Difference

The logarithmic wind speed profile is such that the vertical wind speed difference *(du/dz)* increases with wind speed. Thus, *du/dz* reaches its maximum in winter (Figure 4.7). *du/dz* is on average always less than 1 s^{-1} but also depends on the height of the profile relative to the surface. As the measurement profile nears the surface due to net accumulation, *du/dz* will increase. This effect is accounted for by the water vapor flux calculations which employ measurement heights.

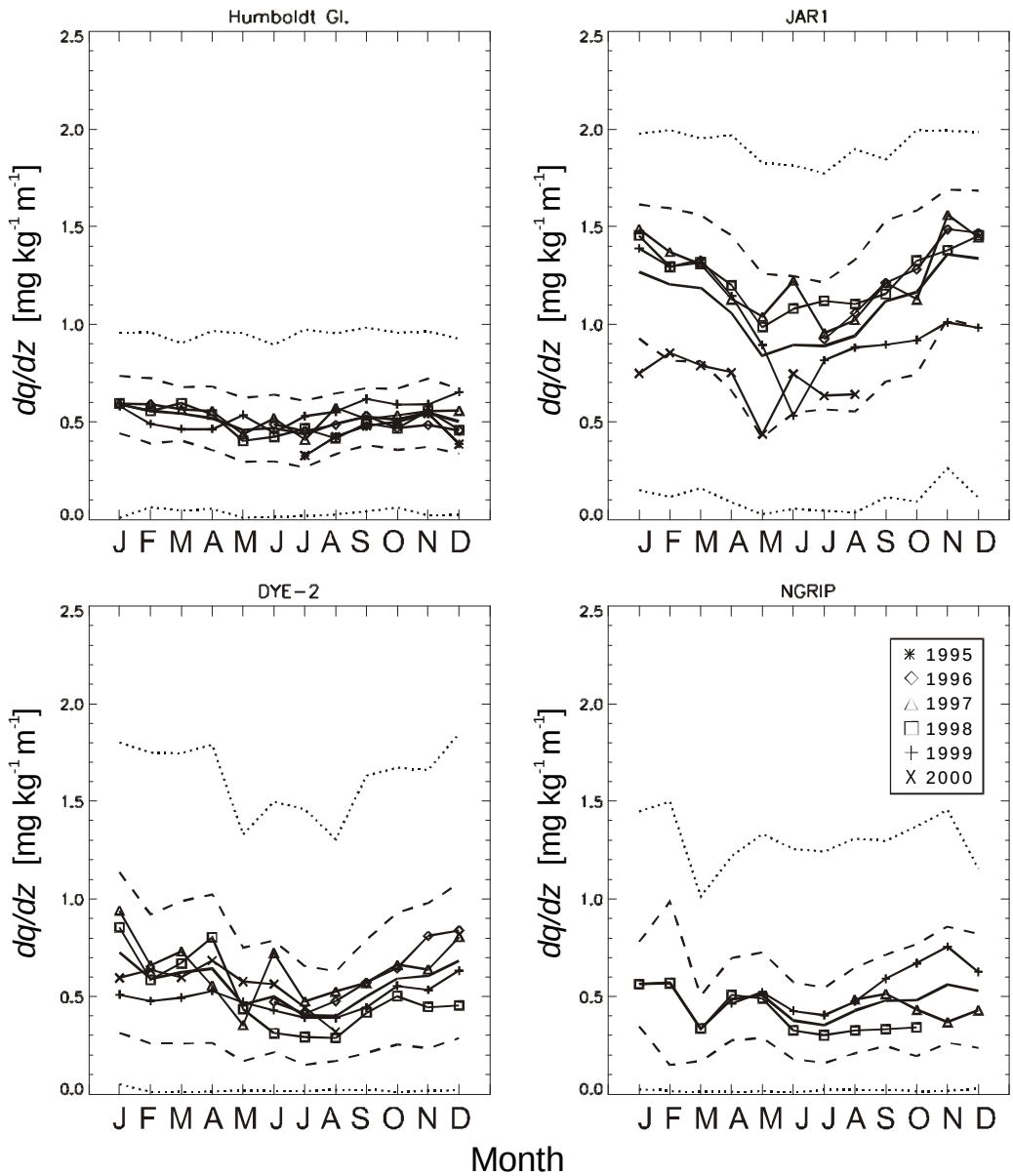

Figure 4.7, Annual variations of monthly mean vertical wind speed difference at representative GC-Net sites. The average of available measurements is represented by the solid line. The dashed line represents one standard deviation of the monthly mean. The dotted line represents the average maximum and minimum observed values.

4.3 Wind Direction

Wind direction at GC-Net sites is indicative of prevailing down-slope flow, implying transport of sublimated water vapor toward the ice margin (Table 4.5). Due to planetary rotation, winds are effectively deflected to the right of the slope up to 45° [*Steffen and Box*, in press]. At high elevation sites, the wind direction distribution is less constant because katabatic flow is not developed and the average wind shows the influence of synoptic systems. In comparison with the slope azimuth, the average Coriolis deflection is 50° to the right of the slope.

Table 4.5, Annual Modal Wind Direction and Surface Slope at GC-Net Sites

Site	Wind Direction [true degrees]	Slope Azimuth [true degrees]
Swiss Camp	132	60
CP1	142	50
NASA-U	140	90
GITS	135	70
Humboldt	193	150
Summit	168	160
Tunu-N	255	230
DYE-2	135	120
JAR1	125	60
Saddle	165	*
South Dome	168	*
NASA-E	260	220
CP2	144	50
NGRIP	173	150
NASA-SE	212	290
JAR2	125	60

* - no large scale slope

4.4 Conclusions

The spatial patterns of the climatological state variables temperature (*T*), specific humidity (*q*), and wind speed (*u*) indicate that water vapor fluxes are favored to be largest in summer when temperatures and vertical specific humidity differences are greatest. Despite larger vertical wind speed differences (*du/dz*) in winter, small water vapor fluxes are implied due to near zero vertical specific humidity (*dq/dz*) differences. In winter, the role of blowing snow sublimation may be more important than suggested here as blowing snow sublimation may occur above the profile measurements [*Mann et al.*, 2000]. Because summertime *dq/dz* is so much greater than in winter, the bulk of significant *dq/dz* signals are captured by GC-Net measurements.

There is a large annual cycle in the state variables. Thus, the presentation of the annual cycle in vertical surface water vapor flux is highly relevant to a climatological analysis. There are some cases, occurring commonly in winter, when the instrument specifications are insufficient to measure vertical humidity differences with certainty. Water vapor fluxes from sites where a small amount of deposition is favored will be associated with a larger uncertainty than lower elevation sites where the *dq/dz* is large.

5 Aerodynamic Profile Methods

The Greenland Climate Network (GC-Net) automatic weather station (AWS) is designed to meet the major aerodynamic profile theory requirements to facilitate water vapor flux calculations. The theory is described in detail below. In this section, it is shown that because results from the aerodynamic profile calculations compare sufficiently with independent methods such as eddy flux correlation and indirectly with evaporation pans, water vapor fluxes on the Greenland ice sheet can be measured with reasonable certainty using the GC-Net data.

5.1 Scientific Background: Aerodynamic Profile Theory

Early work in atmospheric turbulence was pioneered by *Reynolds* [1874] who explained the transfer of heat to a surface in terms of the rate at which a hotter fluid moves towards that surface while a cooler fluid moves in the opposite direction. In 1904, Prandtl discovered the boundary layer which adjoins a surface with moving air or water. In 1925, Prandtl proposed the law that describes the wind speed profile near the surface [*Prandtl,* 1925]. Based on this discovery, a theory for turbulent transfer of heat and chemical admixtures was developed based on vertical profiles of temperature, humidity, and wind speed [*Holzman,* 1939]. Vertical heat and moisture profiles are characterized with temperature, humidity, and wind speed measurements at two or more heights near the surface. Aerodynamic profile calculations are typically expressed one dimensionally with an assumption of horizontal homogeneity, i.e. that average turbulence characteristics do not vary significantly over local horizontal scales [*Stull,* 1988]. The homogeneity assumption is sufficiently met in the case of the Greenland ice sheet owing to very gradual slope gradients and a surface comprised of very small roughness elements. A number of contemporary text books review the current state of knowledge about aerodynamic profile theory, giving examples of diverse applications and experiments in surface boundary layer micrometeorology [*Munn,* 1966; *Brutsaert,* 1982; *Oke,* 1987; *Arya,* 1988; *Monteith and Unsworth,* 1990; *Garratt,* 1992], while *Patterson* [1994] states its application to glaciology.

Measurements are made in the 'constant flux layer' where diffusion is assumed constant with height. During field experiments at Mizuho Station in Antarctica, momentum flux decreased by only 2% between 2.5 and 30 m [*Inoue,* 1989]. Turbulence measurements at 2 m, 10 m, and 30 m above the surface at the mean equilibrium line altitude in western Greenland at the ETH/CU camp, also now referred to as 'Swiss Camp', indicate that the similarity assumptions are generally valid for moderately stable conditions [*Forrer and Rotach,* 1997]. However, within the blowing snow layer near the surface, the assumption of constant fluxes with height may be invalid due to internal sensible and latent heat flux sinks and sources [*Bintanja,* 2000b]. Fortunately, the height range where the majority of the heat flux divergence occurs, i.e. in the lowest 50 cm, where the greatest snow drift concentration occurs, is not within the layer sampled by the AWS profile measurements. The AWS profile is typically in the height range from 1.5 m to 3 m above the surface. Measurement error increases in significance the closer the profile sensors are. Frequency statistics of instrument heights are given in Table 3.4. The vertical water vapor flux is not sampled unless the moisture passes up or down through the measurement profile. Solid particles in suspension that are transported through the profile will not be accounted for in net surface water vapor flux estimates. Based on the results of four state of the art blowing snow models, the blowing snow sublimation rate above 3 m, once blowing snow is developed, represents only 10% to 20% of the total water vapor flux from the surface to 100 m height [*Xiao et al.,* 2000]. In the first minute of blowing snow development, the proportion of sublimation above 3 m is greater. However, the sublimation rates and particle concentration above 3 m in the first simulation minute are much less than at 60 minutes when the blowing snow is completely developed. This means that the proportion of missed water vapor flux that occurs above 3 m will be small the majority of time. Over the course of the 1 hour averaging of 15 sec samples by the AWS, net vertical moisture flux, including that due to blowing snow sublimation passing through the sensor profile, should be captured by the profile measurements. Furthermore, the thickness of the sampled layer is sufficiently small (0.6 m to 1.6 m) to assume a constant flux with height.

In order to determine water vapor fluxes from profile measurements, the direct relationship between the mass transfer of water vapor *(?m)* and the amount of latent heat transfer to the surface or atmosphere by the phase changes of H_2O is employed.

$$\Delta m = \frac{-Q_E \Delta t}{L r} \qquad \text{Eq. 5.1}$$

where Q_E is the latent heat flux (W m^{-2}), *?t* is the time interval (s), *?* is the density of liquid water (1000 kg m^{-3}), and *L* is the latent heat either for vaporization (L_v = 2.501 x 10^6 J kg^{-1}) or for sublimation (L_s), which is equal to sum of latent heat of fusion and vaporization (L_v = 2.834 x 10^6 J kg^{-1}). *?m* is presented in units of mm water equivalent depth. The latent heat constant depends on the air temperature and whether liquid water droplets are present. Liquid water droplets may exist below 0° C due to insufficient quantity of ice condensation nuclei [*Knight*, 1979]. The latent heat of sublimation is selected for temperatures below –12.5° C, based on a rough estimate of the availability of ice condensation nuclei. The sensitivity to a random ±7.5 K uncertainty is shown later. Following common convention, energy fluxes in the surface boundary layer are defined with reference to the atmosphere. Upward heat fluxes associated with the surface water vapor flux are taken as positive.

Two profile methods were selected after evaluating five in comparison with eddy flux correlation measurements. The two selected methods fall into separate categories based on whether they employ humidity and wind speed measurements at two-levels or at one-level. One-level methods (1LMs) are commonly used when only one humidity and wind speed measurement level are available. 1LMs simulate a second profile level by assuming the surface to be saturated with respect to ice or water, i.e. 100% relative humidity at the surface. Methods that employ the surface as a 'level' are referred to as 'bulk methods' [*Garratt*, 1992]. 1LMs still require temperature measurements on at least two levels to calculate atmospheric stability and to estimate the surface specific humidity. A surface roughness parameter is necessary for 1LMs to define the vertical wind speed profile. The selected 1LM is based on *Lettau* [1979] and *Stearns and Weidner* [1993] and defines the surface temperature by estimating the near surface turbulent sensible heat flux. The two other 1LMs are a bulk drag coefficient method after *Brutsaert* [1982] and a one humidity-level and two-level wind speed method used by *Ishikawa et al.*, [1992]. The three 1LM results were very similar. Therefore, the method of *Stearns and Weidner* [1993] was chosen for a comparison with their Antarctic results. The selected two level method (2LM) is the so-called 'K-theory' formulation [*Munn* 1966]. This K-theory is a simplified version of the 'bulk aerodynamic profile method' [*Oke*, 1987]. The latter method was evaluated but performed more erratically than the K-theory. In general, 2LMs are believed to be more accurate to calculate net surface water vapor flux because they sample the *in-situ* vertical moisture differences and do not depend on surface temperature, and surface humidity assumptions. Furthermore, the frequency of condensation or deposition occurrences is much greater for 2LMs than for 1LMs, because for the latter method, the lower profile level is forced to be saturated. The 1LMs only detect deposition in extreme temperature inversion cases when it is possible for specific humidity above the surface to exceed that at a saturated surface. It is commonly assumed that the relative humidity at a snow surface is 100%. This is probably the case for melting. However, in a sub-freezing conditions, observations indicate that undersaturation of the air near a snow/ice surface occurs [*Schmidt*, 1982b]. Both one level and two level method types are outlined in detail below. First, however, the fundamental stability quantity is defined.

5.2 Atmospheric Stability and Corrections to Turbulent Heat Fluxes

The surface stability variation has to be known for calculating latent heat flux from aerodynamic profile methods, because the basic theory applies to neutral stability conditions. When stability is either stable or unstable, *stability functions* for momentum and water vapor (Φ_M and Φ_E) must be applied for accurate turbulent flux estimates using profile methods. The so-called *gradient Richardson number (R_i)* is commonly used as a measure of the stability [*Garratt*, 1992].

$$R_i = \frac{g}{\overline{q_v}} \frac{\Delta \overline{q_v} \Delta z^{-1}}{\left(\Delta \overline{u} \Delta z^{-1}\right)^2} \qquad \text{Eq. 5.2}$$

where *g* is gravitational acceleration (9.81 m s^{-2}), $\overline{q_v}$ is the average virtual potential temperature between

instrument level 1 and 2 (K), Dq_v is the virtual potential temperature difference, level 2 minus level 1 (K), Dz is the difference in profile heights (m), and Du is the difference in wind speed (m s^{-1}). When warm air overlies cooler air, buoyant destruction $(dq/dz > 0)$ dominates turbulent shear production (du/dz), and the atmosphere is stable ($R_i > 0$). In stable conditions, the surface layer is resistant to turbulent transfer.

No analytic formulation currently exists for the effect of stability on turbulent fluxes. However, numerous stability function parameters have been derived empirically based on field experiments. *Garratt's* [1992] text provides a summary of the experimental results. Stability functions for stable and unstable conditions have been proposed by *Webb* [1970] and *Dyer and Hicks* [1970], respectively. The stability functions are $(1-bR_i)^{-1/2}$ and $(1-gR_i)^{-1/4}$ for unstable and stable conditions, respectively, where $g = 16$ and $b = 5$. The parameters g and b vary in the results from various experiments [*Garratt*, 1992]. However, recent values, for example [*Högström*, 1988], do not differ greatly from earlier values. The observations of *Forrer and Rotach* [1997] suggest that the use of stability functions from *Webb* [1970] and *Dyer and Hicks* [1970] with profile data alone, i.e. no complementary eddy correlation data, are sufficient to estimate the turbulent surface fluxes to an acceptable accuracy for the general conditions encountered during their 3.5 month spring/summer Greenland ice sheet experiment. In this study, another slightly different form of the stability functions is taken from *Steffen and DeMaria* [1996], where $g = 18$ and $b = 5.2$ and as Φ_M is often not equal to Φ_E [*Smeets et al.*, 1998], *Steffen and DeMaria* [1996] used $\Phi_M/1.3$ for extremely unstable cases ($R_i < -0.03$). The uncertainties associated with extremely unstable and stable conditions do not differ greatly for the majority of AWS sites and conditions encountered on the ice sheet because their frequency of occurrence is generally small (Table 5.1).

Table 5.1, Annual Stability Characteristics at GC-Net Sites for Complete Calendar Years

Site	Year	$R_i > 0$ %	$R_i < 0$ %	$\|R_i\| < 0.001$ %	$R_i > 0.1$ %	$R_i < -0.05$ %
Swiss Camp	1999	74	22	16	2	3
CP1	1999	72	23	31	1	1
NASA-U	1998	64	33	5	3	7
GITS	1996	52	46	5	3	6
Humboldt	1997	82	16	5	3	2
Humboldt	1998	78	21	3	4	4
Humboldt	1999	91	8	2	6	2
Summit	1999	83	17	1	20	5
Tunu-N	1997	97	3	1	11	1
Tunu-N	1998	89	10	5	5	1
Tunu-N	1999	75	23	7	2	3
DYE-2	1997	77	22	5	6	5
DYE-2	1998	41	57	4	3	22
DYE-2	1999	28	70	5	2	18
JAR1	1997	80	15	5	1	1
JAR1	1998	91	8	16	0	1
JAR1	1999	75	23	10	1	3
Saddle	1999	61	32	8	7	3
South Dome	1998	72	25	22	9	2
NASA-E	1998	76	21	10	18	4
CP2	1998	79	19	2	3	2
NGRIP	1998	85	14	11	18	7
NGRIP	1999	78	22	1	9	7
NASA-SE	1999	64	32	5	12	7

5.2.1 Stability Characteristics at GC-Net Sites

The stability characteristics of complete annual records for GC-Net sites are investigated. Stable conditions ($R_i > 0$) are predominant at GC-Net sites (Table 5.1, Figure 5.1). A greater frequency of stable conditions and extremely stable conditions ($R_i > 0.1$) is observed at higher elevation sites (Summit, NGRIP) and for sites on the eastern slope of the ice sheet (NASA-E and NASA-SE), where surface temperature inversions are more developed (section 4.2.1.1). Extremely stable conditions are further promoted by low temperatures.

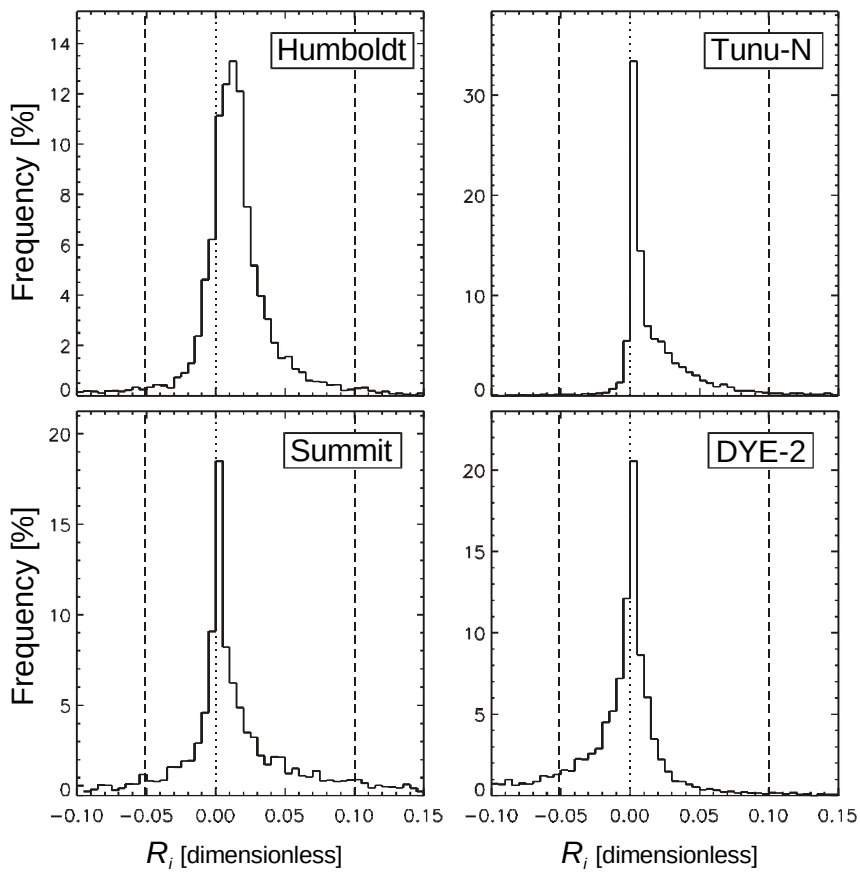

Figure 5.1, Annual histograms of stability (Ri) at representative GC-Net sites for 1998. Extreme values beyond dashed lines are cases in which stability functions are not well defined.

In the limit as R_i approaches 0.2, atmospheric turbulence becomes completely dampened by buoyant destruction [*Garratt*, 1992] and as a consequence, turbulent fluxes are effectively zero. Unstable conditions occur in summer due to absorption of solar energy by the surface and under low-level cloud conditions when longwave sky radiation can heat the surface [*Ohmura et al.*, 1994]. Unstable conditions are thus more commonly found during melt when the surface albedo is reduced. Unstable conditions also occur due to cold air advection over a relatively warm surface. This may occur as air originates from a cooler surface with higher albedo. Extremely unstable conditions ($R_i < -0.05$) occur in general between 0% and 4% of the year. Figure 5.1 illustrates annual frequency distributions of stability at representative GC-Net sites. The situation at Humboldt illustrates the common predominance of stable conditions at the majority of GC-Net sites. At Tunu-N at an equivalent elevation and latitude as Humboldt, unstable cases are almost nonexistent. This northeast slope site is colder and has more persistent high pressure and less precipitation [*Ohmura et al.*, 1999; *Bromwich et al.*, submitted]. The associated clearer skies at Tunu-N explain the stronger surface temperature inversion, lower air temperatures, and thus the greater frequency of stable conditions as compared to Humboldt. At Summit, the annual distribution is broader. This may be explained in the context of the weaker winds [*Steffen and Box*, in press] at this site as compared to other GC-Net sites. Without strong winds to mix the air in the surface boundary layer, extremely stable or unstable conditions may persist longer than at sites where greater winds provide an efficient turbulent mixing mechanism. A curious stability distribution is present for DYE-2. The annual distribution is

skewed toward negative values indicative of frequent unstable conditions. On-site instruments and calibration have been checked and the two pairs of temperature sensors (Table 3.2) imply that the instability is not instrument related. Solar overheating of the instruments is also not expected to be significant in early spring, when substantial instability is observed at DYE-2. It may be significant that DYE-2 is windier that normal for a site at this elevation as strong winds amplify R_i calculations. Furthermore, this site receives more intense solar irradiance that most of the other sites which are located to the north. Other GC-Net sites to the south (Saddle and South Dome) are at higher elevation and thus have a stability distribution more similar to Summit.

5.3 Logarithmic Wind Speed Profile

Vertical mass fluxes depend on the wind speed variation with height $u(z)$. Commonly, the wind speed profile closely obeys a logarithmic form in the turbulent boundary layer. This is particularly true over ice [*Andreas and Claffey,* 1995]. The vertical variation of wind near the surface is given by:

$$u(z) = \frac{u_*}{k} \ln\left(\frac{z}{z_0}\right) \qquad \text{Eq. 5.3}$$

where u_* is the friction velocity and k is the von Kármán constant (k @ 0.4) [*Arya,* 1988]. Values of k vary in the literature from 0.33 to 0.41 [*Andreas,* 1998] but for the case of neutral stratification, [*Högström,* 1988] showed that (k = 0.4±0.01) is a good approximation. z_0 is the surface roughness length. Variations of z_0 are linked with roughness element formation and destruction and short term changes in the wind orientation to the roughness features. Values between 10^{-5} and 10^{-3} are observed over snow covered surfaces [*Andreas and Claffey,* 1995].

To estimate wind speed at fixed heights when the surface roughness parameter is uncertain, the relationship of the wind speed at a reference height *(z)* to the wind speed at a fixed height *(z')* is given by:

$$u_{10} = u_z (z / z')^{-m} \qquad \text{Eq. 5.4}$$

where z is taken as that of profile level 2, z' is 10 m in this case, and m for fully turbulent flow over an aerodynamically smooth surfaces is 1/7 [*Arya,* 1988].

5.4 Profile Method Based on Two Humidity Measurement Levels

The following two-level profile formulation is based on the familiar *Thornthwaite and Holzman* [1939] flux-gradient theory, in which a first-order turbulence closure approximation is made. Simplification to the complete formulation is made assuming that the turbulent diffusion is represented sufficiently by the eddy diffusivities of the air [*Munn,* 1966; *Stull,* 1988]. This is the so-called K-theory.

$$Q_E = -rLu_*^2 K \left[\left(\frac{q_2 - q_1}{z_2 - z_1} \right) \Big/ \left(\frac{u_2 - u_1}{z_2 - z_1} \right) \right] \Phi_M \Phi_E \qquad \text{Eq. 5.5}$$

where *?* is the air density (kg m^{-3}), z_1 and z_2 are instrument heights increasing upwards (m), q is the specific humidity (kg kg^{-1}), u is the wind speed (m s^{-1}), and Φ_M and Φ_E are stability corrections described above. K is the ratio of eddy diffusivities for momentum and water vapor. There is some experimental evidence to suggest that for neutral conditions, this ratio is equal to 1.35 [*Stull,* 1988], and in fact this constant produces diurnal fluctuation amplitudes that agree with two eddy correlation experiments at Swiss Camp in 1999 and 2000, shown below.

Under blowing snow conditions in the Antarctic, *Budd et al.* [1966] found that the friction velocity (u_*, in m s^{-1}) was related to wind speed at 10 m height (u_{10}, in m s^{-1}) according to

$$u_* = \frac{u_{10}}{c} \qquad \text{Eq. 5.6}$$

where u_* has m s^{-1} units, u_{10} is the wind speed at 10 m above the surface (m s^{-1}) and c is a constant of proportionality (26.5). The roughness length (z_o) is implied in Eq. 5.6 according to an effective increase in z_0 with the wind speed over a surface where there is 'momentum extraction' due to saltation of ice particles near the surface [*McKenna and Nickling,* 1994]. The use of this parameterization does not lead to great uncertainties because of the observed good correlation of 2LM amplitude with eddy flux correlation measurements, particularly because blowing snow did not occur during most of the eddy correlation experiment. Furthermore, solving for the eddy diffusivity ratio is justified, rather than adjusting c, because Eq. 5.6 produced u_* values that agreed with those from 3D eddy correlation in terms of their regression slope (*Figure 5.2*). We use the observed comparison of the 2LM and 1LM methods with eddy correlation to illustrate the accuracy of this methodology in section 5.7.1, below.

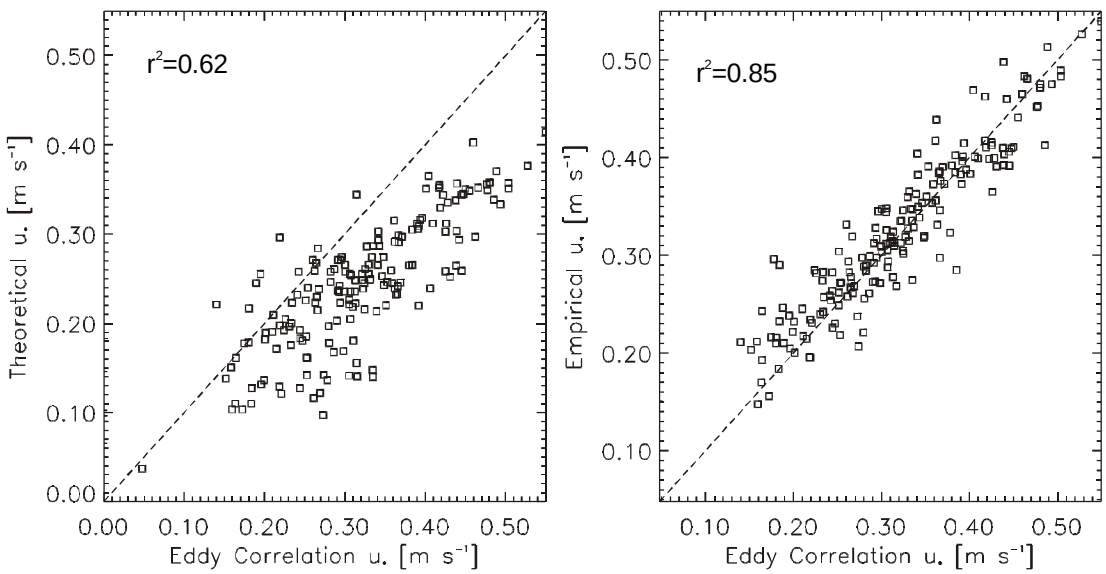

Figure 5.2, (Left) comparison of theoretical u_* with the 1999 eddy correlation measurements. (Right) comparison of empirical u_* with eddy correlation measurements.

5.5 Profile Methods Based on One Humidity Measurement Level

Lettau [1979] developed wind speed and temperature profile factors, (y_z) and (Y_z), respectively, to define the departure of the profiles from their neutral form depending on another atmospheric stability parameter *(?)* [*Monin and Obukhov,* 1954] for sites on the Antarctic ice sheet. *Stearns and Weidner* [1993] applied this theory as an iterative stability correction to derive latent and sensible heat fluxes for Antarctic AWS sites. Simplifications to the profile theory come in the form of a constant roughness length (z_0) assumption (5 x 10^{-4} m) given only one wind speed measurement level. This is certainly a poor assumption in the case of blowing snow. However, this constant roughness length value is adopted in this study for a more direct comparison of published Antarctic latent heat fluxes with that derived from GC-Net data.

As part of the iterative process, an initial u_* estimate is provided based on the parameterization described above (Eq. 5.6). Subsequent u_* values are based on the logarithmic wind speed equation and wind speed profile departures from neutral derived by the iteration. Thus the stability correction for momentum is implicit in the final value of u_*. The logarithmic wind speed profile is therefore:

$$u(z) = u_* k^{-1}\left[\ln\left(z / z_0\right) - y_z\right] \qquad \text{Eq. 5.7}$$

Lettau [1979] provides the lengthy set of *(y_z)* and *(Y_z)* functions not listed here. Errors in the presentation of the profile corrections were found in *Stearns and Weidner* [1993]. Lettau's 1979 functions are used here. The wind speed profile departure from neutral *(y_z)*, is greater than zero for stable conditions and thus reduces the wind speed profile curvature. u_* is solved by rearranging the above equation. In the initial case, $y_z = 0$. To derive the temperature profile curvature *(Y_z)* and ultimately the surface temperature, u_* is used to calculate the sensible heat flux *(Q_H)*.

$$Q_H = -rC_p u_* k \frac{(q_2 - q_1)}{\ln z_2 / z_1^{-1} - \Psi_2 + \Psi_1} \qquad \text{Eq. 5.8}$$

where C_p is the specific heat of the air (1005 J kg^{-1} K^{-1}), $?_1$ and $?_2$ are the potential temperature (K) at levels z_1 and z_2, and Y_1 and Y_2 are the diabatic adjustments to the temperature profile developed from the iteration of Q_H and surface temperature $?(z_0)$. Y_1 and Y_2 are not applied in the first iteration. The input parameter for Y_z and y_z is the Monin-Obukhov non-dimensional stability parameter *($?_z$)*.

$$z_z = -gkzQ_h \left(rC_p T_z u_*^3 \right)^{-1} \qquad \text{Eq. 5.9}$$

where T is the air temperature (K). As with Φ_M and Φ_E, Lettau's stability corrections vary between stable and unstable conditions, $\zeta > 0$ and $\zeta < 0$, respectively. The process to calculate u_* and then Q_H is repeated until the incremental change in Q_H is less than 0.01 W m^{-2} (Figure 5.3).

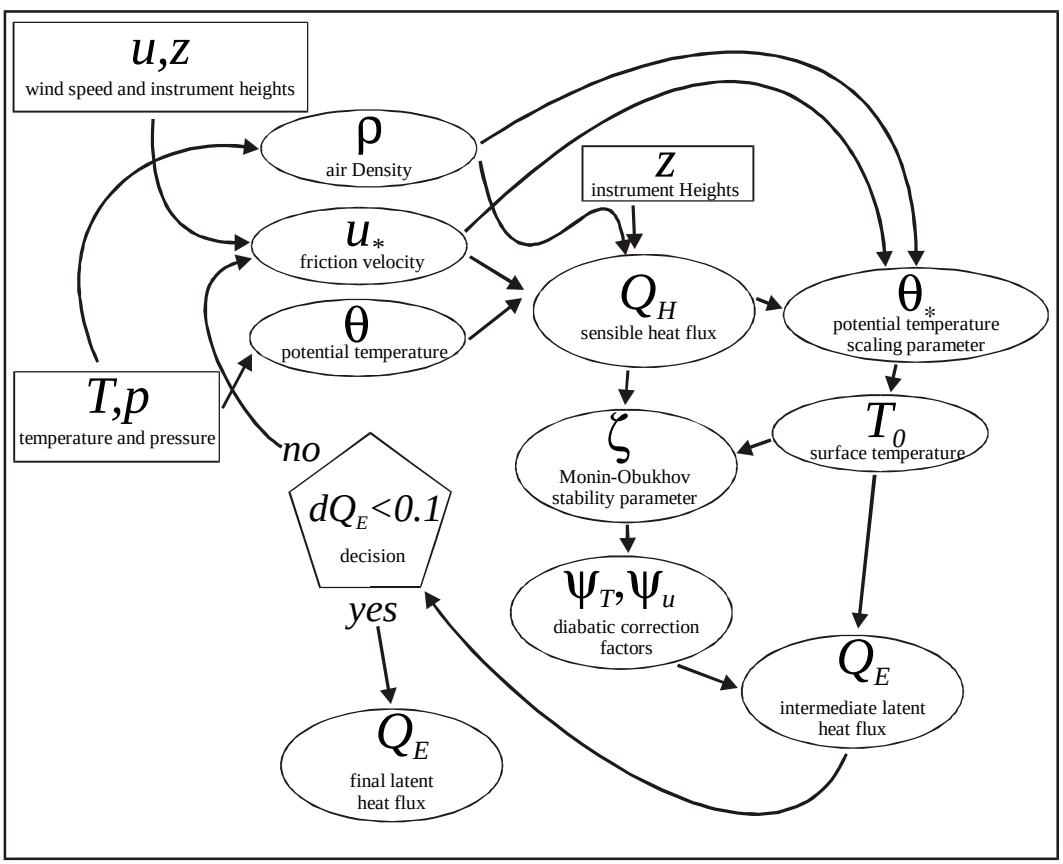

Figure 5.3, Flowchart of steps in iterative calculation of latent heat flux [Stearns and Weidner, 1993] based on Lettau [1979].

For winds above 6 m s^{-1}, usually only one iteration is required. As the wind speed decreases to 3 m s^{-1}, up to 10 iterations are required. The iterations serve to decrease (increase) the friction velocity during stable (unstable) conditions, resulting in a decrease (increase) in the latent or sensible heat flux, respectively. Figure 5.4 illustrates the effect of the iterative stability corrections for a moderately unstable case (R_i = -0.005).

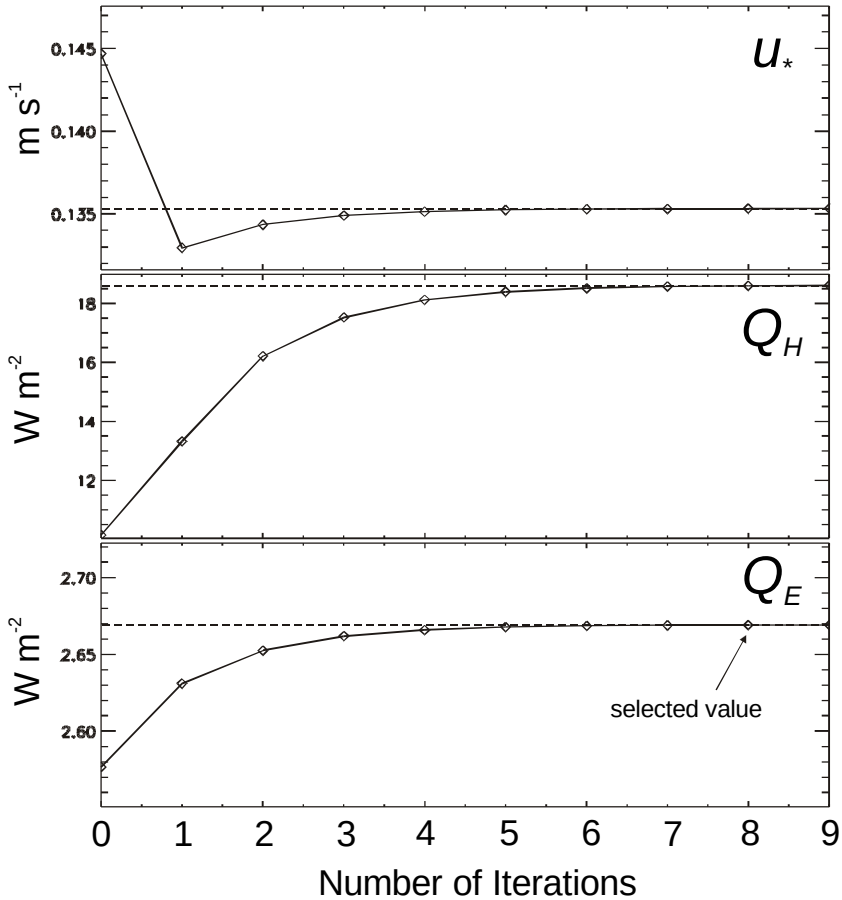

Figure 5.4, Example of iteration results of the SM1 method of Stearns and Weidner [1993] for friction velocity (u_*), sensible heat flux (Q_H) and the latent heat flux (Q_E) for a moderately unstable case (R_i = -0.005).

The iteration and heat flux was not calculated for cases of extreme stability (z > 0.2) because the iteration resulted in ever increasing sensible heat flux values because of an increase in the stability function in this open limit.

The temperature profile is represented by:

$$q(z) - q(z_0) = -q_* k^{-1}\left[\ln\left(z / z_0\right) - \Psi_z\right] \qquad \text{Eq. 5.10}$$

The scaling parameter for temperature (q_*) is calculated using the sensible heat flux and the friction velocity.

$$q_* = Q_H\left(rC_p u_*\right)^{-1} \qquad \text{Eq. 5.11}$$

Finally, the surface temperature estimate is given by combining Eq. 5.10 and Eq. 5.11. The surface

temperature is used to define the surface saturation vapor pressure and in turn the specific humidity needed for the bulk one level method latent heat flux *(Q_E)*.

$$Q_E = -ru_*^2 L[q_z - q_0]u_z^{-1} \qquad \text{Eq. 5.12}$$

where q_z and q_0 (kg kg^{-1}) are the average specific humidities at height z and adjacent to the surface, respectively. No stability correction is apparent in the above equation because the correction is accomplished by the iterative process described above.

5.6 Sensitivity Analysis

Uncertainty limits for vertical water vapor flux calculations are quantified in simulations that represent a range in instrument errors. The latent heat flux formulations based on two humidity measurement levels require nine accurate input measurements, two temperatures (T_1 and T_2), two relative humidities (RH_1 and RH_2), two wind speeds (u_1 and u_2), two instrument heights *(z_1* and *z_2)*, and pressure *(p)*. Formulations based on one humidity measurement level require one wind speed, humidity, and instrument height estimate. Two temperature measurement levels are required for both method-types. More than one error analysis is undertaken due to the complex nature of the multi-input latent heat flux formulation. The first analysis featured here determines accuracy limits of the vertical specific humidity difference measured between two instrument levels.

5.6.1 Precision of Vertical Specific Humidity Difference

Specific humidity is derived using relative humidity, temperature, and air pressure data. Assuming a uncertainty in relative humidity difference between profile level one and level two of 3% based on relative calibrations (sections 3.1.10 and 3.1.11), 0.06 K for the temperature profile difference, and 1 hPa in pressure, the instrument profile should be unable to accurately sense specific humidity gradients smaller than 0.14 g kg^{-1}. Given these uncertainties, a 0.1 K temperature difference in the temperature profile, and 0.1 ms^{-1} in wind speed difference, the extreme range of two-level method latent fluxes (section 5.4) is 35%. The one level method (section 5.5) is not as sensitive to instrument error. The one level method benefits from a relative large humidity difference typical of the surface to some height typically greater than 1 m above the surface. Taking the manufacturer's specifications, the absolute accuracy of relative humidity measurements (10%) and 1 m instrument height, the extreme range of one level method latent heat fluxes is 25%.

5.6.2 Uncertainty Estimates by Monte Carlo Approaches

The sensitivity of profile theory based latent heat flux calculations to measurement uncertainty is explored using a Monte Carlo technique. Instrument differences based on relative calibrations exhibit a normal distribution. Hence, Gaussian distributions of random samples are scaled to represent the instrument uncertainty (ε) such that 95% of the samples fall within the assumed uncertainty. Absolute instrument uncertainties are quoted from the manufacturer (Table 3.2) and the *relative accuracy* is assessed from on site relative calibrations (Table 3.8). In the case of instrument height or pressure measurements, the uncertainty is taken as the *absolute accuracy*. Simulating uncertainties by this approach allows the isolation of the uncertainty in the latent heat flux due to individual input parameters and to estimate the ensemble uncertainty due to all parameters, including feedbacks. A series of uncertainty simulations are made to represent the changing uncertainty over the range of environmental conditions. To simulate the GC-Net measurement routine, hourly averages of randomly-perturbed 15 sec interval data are generated. These data are input into the two and one-level latent heat flux calculations described in sections 5.4 and 5.5, respectively. Figure 5.5 illustrates an example of such a simulation for the two level profile method. The results show that relative humidity is the parameter that introduces the most uncertainty (25%) in the two level latent heat flux calculation. This is followed by temperature (15%), instrument height (4.5%), and wind speed (4%). Selection of the latent heat of sublimation or vaporization by an air temperature threshold of –12.5° C (section 5.1) results in an uncertainty of less than 1%. Pressure exerts an insignificant influence on the latent heat flux, as long as it is within 20 hPa. A low pressure bias results in smaller latent heat fluxes via a smaller specific humidity. The combination of variables

indicates a 35% uncertainty for the two level method. The results from a range of simulations is featured after the one level method uncertainties are analyzed.

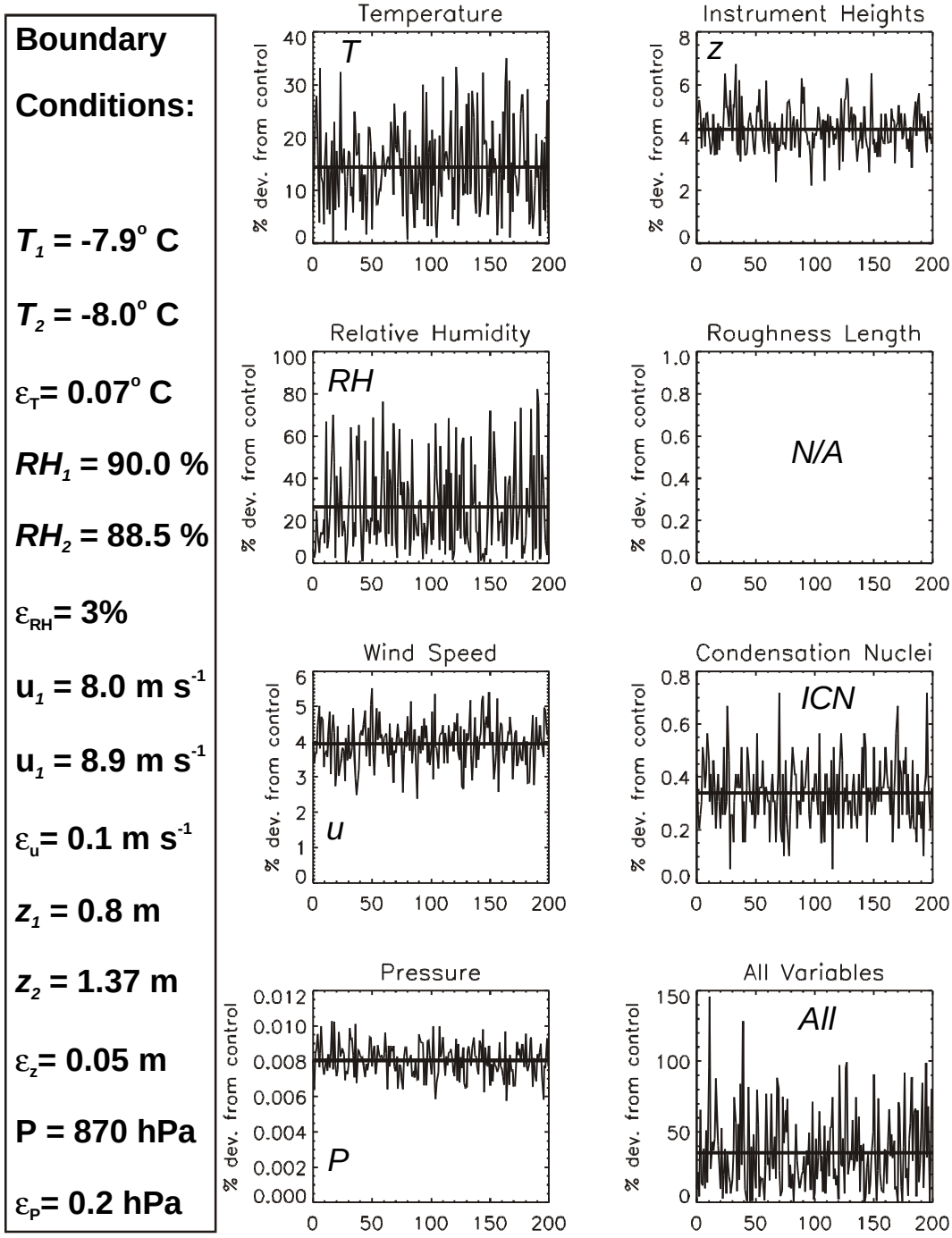

Figure 5.5, Example of results from a multivariate Monte Carlo uncertainty simulation of two level method latent heat flux calculations.

The Monte Carlo simulation is also applied to the iterative one level method (section 5.5). The results indicate that a general order of magnitude uncertainty in the roughness length assumption dominate the uncertainty (70%) (Figure 5.6). Temperature errors are responsible for 25% uncertainty in the latent heat flux. Relative humidity is not responsible for much uncertainty due to the relatively large specific humidity difference between the surface and 0.8 m, 2.5 g kg^{-1} in this case. Instrument height errors lead to a smaller uncertainty than with the 2 level method because only one level can have errors. Pressure exerts an even smaller uncertainty for the one level method because it is input into only one specific humidity value. The surface specific humidity is determined by temperature alone. The ensemble uncertainty in the one level latent heat flux for this example is 80%.

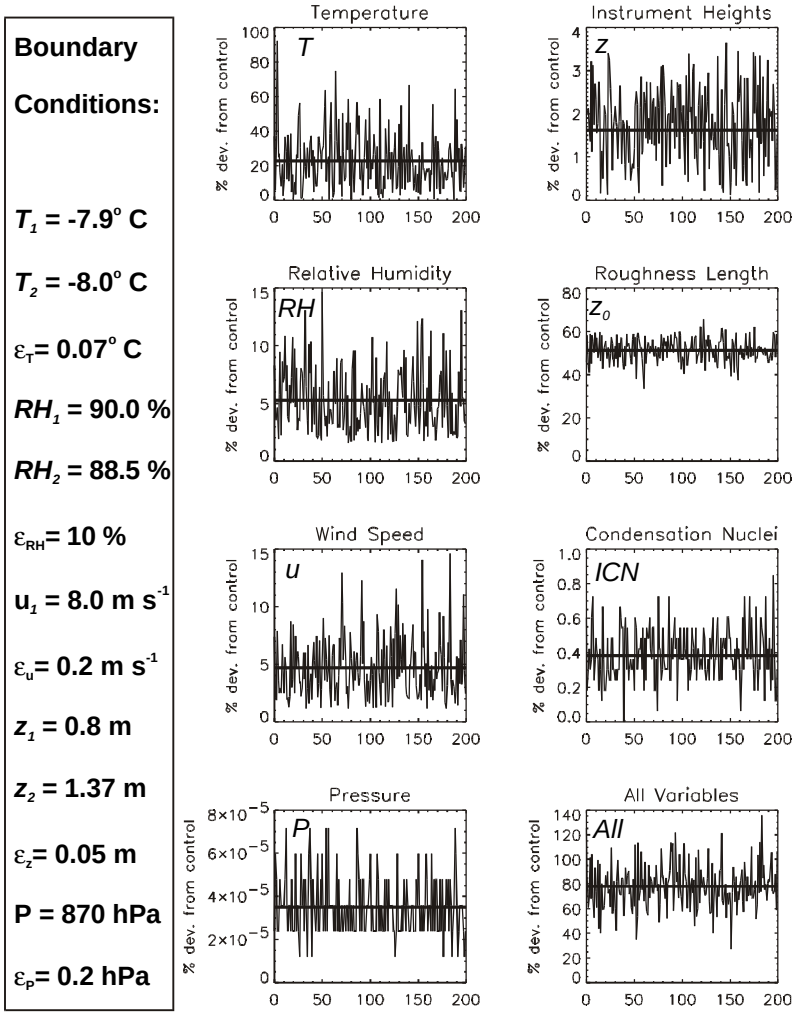

Figure 5.6, Example of results from a multivariate Monte Carlo uncertainty simulation of one level method latent heat flux calculations.

Because the values may fluctuate around zero for near neutral conditions, the difference in latent heat fluxes is used to measure uncertainty. This is shown below by a series of uncertainty simulations that focus on the range in the difference of perturbed and non-perturbed latent heat flux in the following. Figure 5.7 represents the results from a number of simulations in which a range in vertical humidity and temperature difference are varied while the random uncertainty is included for all other parameters. The range of uncertainty in the latent heat flux for small negative temperature differences illustrates the effect of the stability function to amplify uncertainties. For larger negative temperature differences, the stability function does not amplify the calculation as much because the stability function is divided by 1.3 for $R_i < -0.03$ (section 5.2). The range is small for large positive temperature differences because the stability function dampens the latent heat flux. The right graph illustrates the small difference that instrument spacing has for a range of humidity differences.

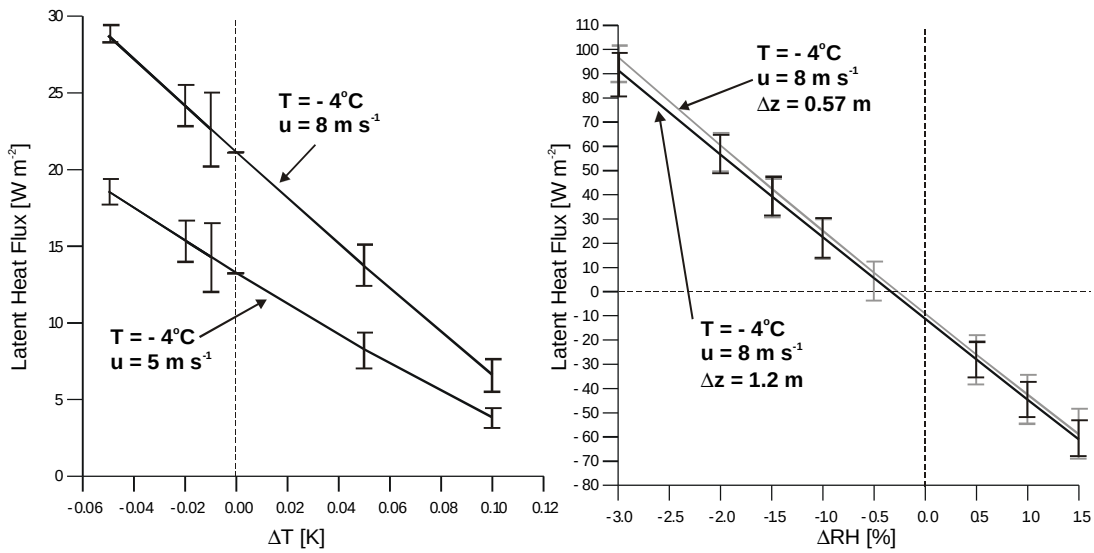

Figure 5.7, Range of latent heat fluxes based on an all-parameter Monte Carlo simulation of latent heat fluxes over a range of vertical temperature (left) and humidity differences (right).

5.7 Validation of Profile Methods

The latent heat flux calculated from the profile methods described above is compared with measurements by eddy flux correlation (ECM) instrumentation (Table 3.10). The ECM data are in turn compared with evaporation pan measurement for a qualitative confirmation that the ECM does measure evaporation. Evaporation pan measurements are described in section 3.3. Results of this validation effort are presented below.

5.7.1 Validation of Profile Methods with Eddy Correlation

Three two-week periods of ECM latent heat flux *(Q_E)* measurements made during springtime Greenland expeditions (Table 3.10) are compared with Q_E calculated from the two profile methods types, the one level method (1LM) and the two level method (2LM). The first comparison is with 3D ECM measurements taken in 1999 and 2000 at Swiss Camp. An rather large uncertainty estimate of 33% for ECM data was derived using a one day comparison of two simultaneous CSAT-3 latent heat flux measurements taken at Summit on June 22, 2000 (Table 3.11) [*N. Cullen,* personal communication]. A second comparison is with 1D ECM measurements taken at TUNU-N in 1996 [*K. Steffen,* personal communication]. During the Tunu-N experiment, temperatures were lower and stable conditions predominated. The comparisons yield encouraging results at Swiss Camp and more grave implications for Tunu-N.

During the 2000 ECM experiment at Swiss Camp, the 1.5 m air temperature fluctuated between -19° C and +2.5° C. The latent heat flux responded to the strong wind speed variations, vertical humidity and temperature differences (Figure 5.8). Given air temperatures above the melting point and strong winds, this comparison represents extremely large water vapor flux conditions. The AWS measurements of vertical temperature and humidity difference variations, *dT/dz* and *dq/dz* , respectively, illustrate the proper functioning

of the profile measurements. The positive and negative vertical heat and moisture fluxes based on the eddy correlation correspond well with the vertical temperature and humidity differences. As a result, the profile methods yield latent heat fluxes that track the eddy correlation fluxes well. The 2LM compares better with ECM data for condensation cases. The 1LM rarely indicates condensation and when it does, the value is too small. Linear regression results imply that the latent heat flux is overestimated by both profile methods (Figure 5.9). Averages over the comparison period indicate an 19% overestimation of the latent heat flux by the 1LM and a 12% underestimation by the 2LM for the 2000 comparison (Table 5.2). For 1999, the average difference corresponds to 25% overestimation for the 1LM and 6% for the 2LM. The slope of the regression lines suggest that the 2LM performs better than the 1LM. The average differences of the profile methods to the ECM results are within the uncertainty of the profile methods, given the 33% uncertainty estimate of the ECM stated in section 3.2.

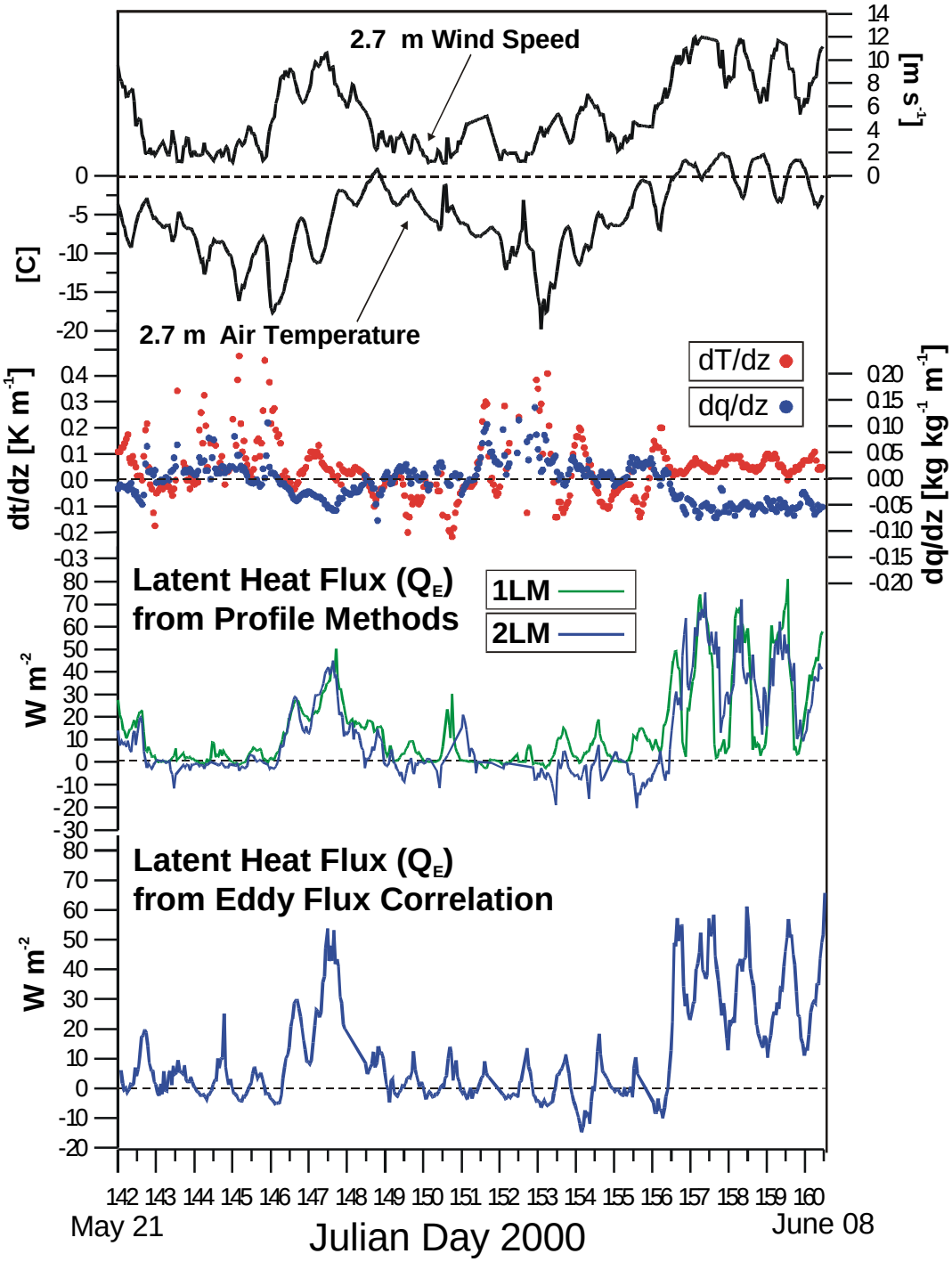

Figure 5.8, Time series of AWS profile measurements and latent heat fluxes derived by aerodynamic profile methods and eddy flux correlation at Swiss Camp.

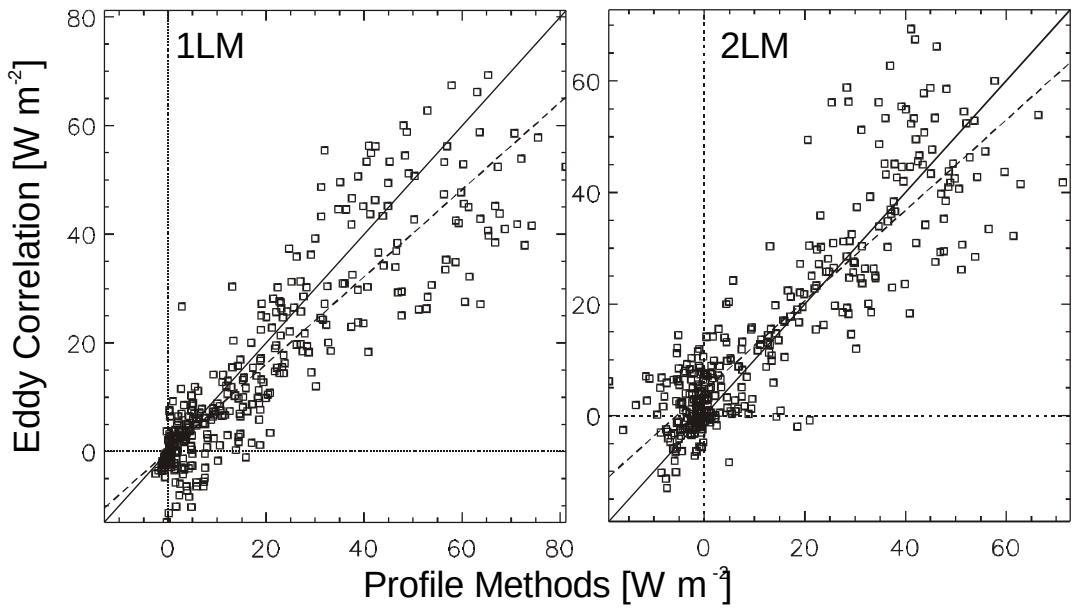

Figure 5.9, Scatter plots of the latent heat flux from one level and two level profile methods versus eddy flux correlation measurements from Swiss Camp 2000.

Table 5.2, Comparison of Q_E from Profile Methods with Eddy Correlation

Site	Tunu-N	Swiss	Camp	Tunu-N	Swiss	Camp
Year	1996	1999	2000	1996	1999	2000
Method-type	1LM	1LM	1LM	2LM	2LM	2LM
Number of hourly samples	206	244	357	206	244	357
Explained variance (r^2)	0.23	0.69	0.80	0.15	0.56	0.75
Regression slope	0.64	1.4	0.80	0.78	1.1	0.81
Average Q_E (Profile)	3	25	19	2	19	13
Average Q_E (ECM)	0	20	15	0	21	15
Difference (Q_E)	3	5.3	3.7	2	-1.1	-1.9

The comparison of profile method results with 1D eddy correlation from the Tunu-N 1996 experiment was not nearly as encouraging as the Swiss Camp comparison. However, the identification of certain cases yield useful information regarding profile method validation (Figure 5.10). Case A and F represent occasions when both the 2LM and the ECM detect deposition. However, during such cases, the 2LM overestimates the negative latent heat flux. Case B represents times when the 1LM overestimates the latent heat flux, as may be expected given its assumption of surface saturation. Case C represents the expected occasions when the 1LM detects some deposition, yet underestimates it as in the Swiss Camp comparison. Case D represents times when the 2LM and ECM agree well for deposition cases and Case E represents occasions the 1LM tracks the diurnal fluctuations of the latent heat flux well, matching the ECM daytime maximum. The predominant anticorrelation between the ECM and the profile methods for this site comparison can be somewhat clarified in context of the small fluxes involved. That much precision cannot be expected from hourly profile methods results given such a small flux. Large fluxes do not truly occur for the low average temperature (-16° C), unless by extreme wind cases. Average air temperature was -5° C at Swiss Camp during the 1999 experiment and -7° C at Swiss Camp in 2000. There may also have be greater errors in the 1D sonic anemometer used as compared with the 3D sonic anemometer used for the Swiss Camp experiments (Table 3.10). The 1D measurements may have been biased by frost deposition that would have occurred associated with the substantial frequency of observed negative latent heat fluxes. Profile measurements may have been biased by the likelihood of frost on relative humidity

sensors instruments or shields. The Swiss Camp comparison was more favorable in large part due to the greater ventilation and large water vapor fluxes involved. Note the clustering of values near zero in the scatter plot (Figure 5.9). If it were not for the larger flux values, the explained variance would certainly be lower. The performance of the profile methods at Tunu-N is a reminder, as initially understood by the uncertainty simulation in section 5.6, that the profile methods are more certain where vertical humidity differences are largest on average (Figure 4.4).

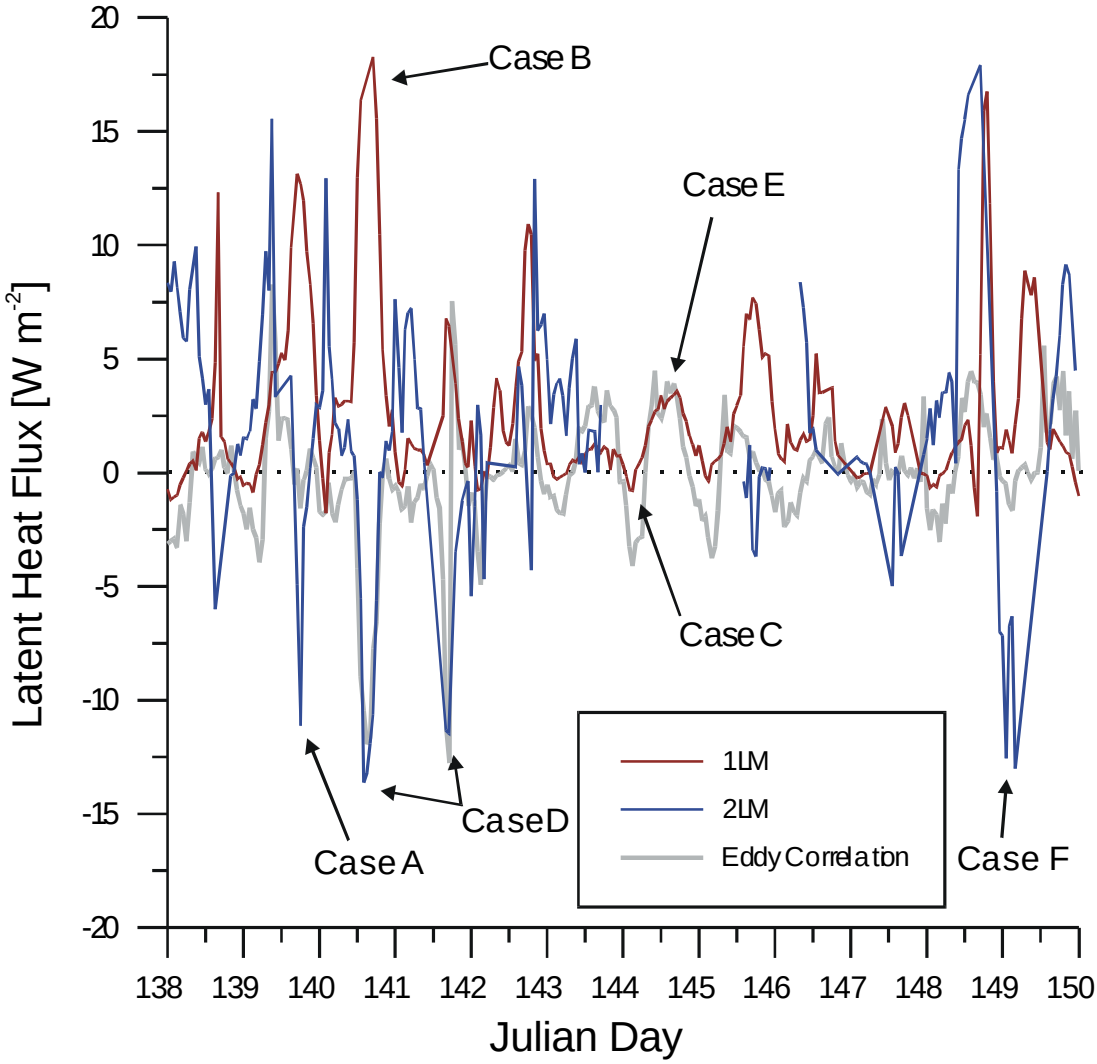

Figure 5.10, Time series comparison of latent heat flux measured by eddy flux correlation and by profile methods at Tunu-N in 1996.

5.7.2 Validation of Eddy Correlation with Evaporation Pans

Evaporation pan weight changes, in comparison with vertical water vapor flux measured by the eddy flux correlation, verifies the ability of eddy correlation to gauge surface water vapor flux (Figure 5.11). Maximum weight change of -23 ± 4.8 g indicates a maximum 12-hour average latent heat flux of 75 W m^{-2} (-0.6 mm), while over this 12 hour period, the ECM average flux was 81 W m^{-2} (-0.65 mm). Uncertainties due to snow sampling errors, voids in the sample or compaction of the sample, solar heating of the glass, and reduced snow ventilation due to pan sides, prevent the use of these data for absolute calibration of the eddy correlation. It would then seem that uncertainties due to solar overheating of the glass are not as suspect as uncertainties due to reduced ventilation of the sample by the pan walls. Largest differences in simultaneous evaporation pan measurements correspond to 0.6 mm d^{-1}. Uncertainties in Figure 5.11 are shown as the difference in values from the two simultaneous side by side pan results and a rough 33% uncertainty in eddy flux measurements from a one-day side by side comparison of two 3D ECM instruments [*N. Cullen*, personal communication]. The comparison of evaporation pan results with ECM results is encouraging.

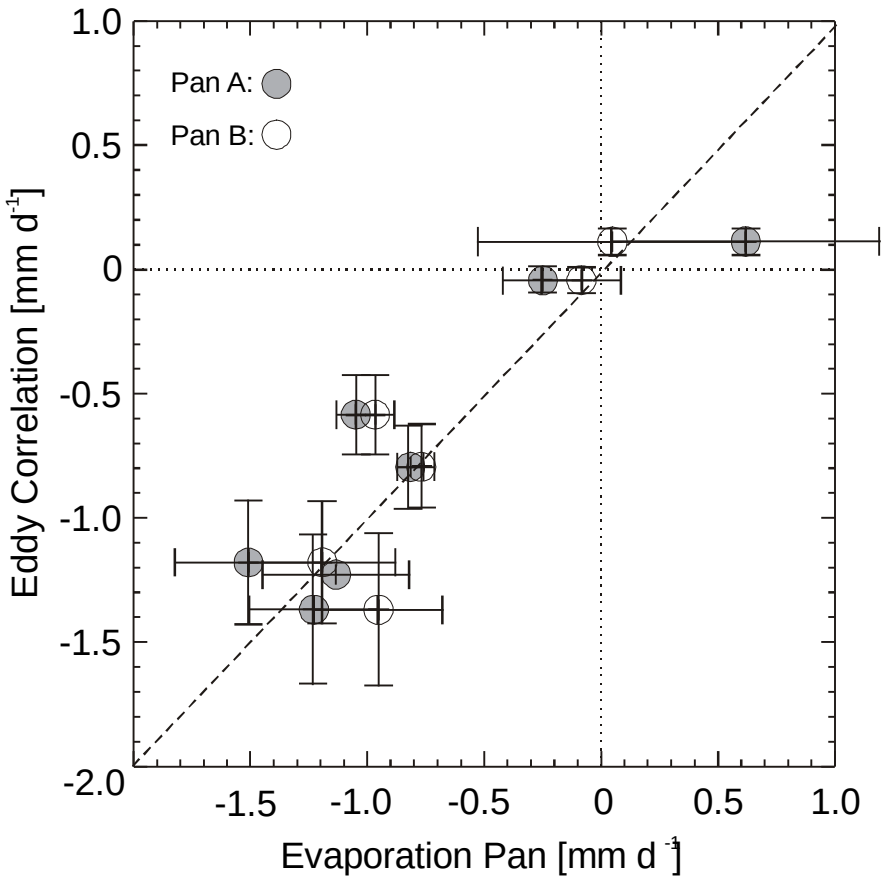

Figure 5.11, Comparison of evaporation measured with evaporation pans and derived with the eddy correlation method

5.8 Conclusions

The two profile methods presented in this chapter represent the application of averaged meteorological measurements applied to a calculation of the turbulent latent heat flux. For daily and longer term averages, the aerodynamic profile methods perform sufficiently well to provide useful surface water vapor flux estimates for Greenland ice sheet surface climatology. Independent measurements of the vertical water vapor flux from eddy flux correlation and evaporation pans indicate a general agreement with profile methods.

Of the utmost importance to the objectives of this study is whether the profile methods produce realistic average latent heat fluxes. At Tunu-N, the average of eddy correlation measurements is –0.08 W m^{-2}, for the one level profile method the average is 2.5 W m^{-2} and for the two level method, 2.0 W m^{-2}. Given the large

uncertainties in the Tunu-N comparison, the only encouraging conclusion is that the fluxes are so small that the uncertainties are insignificant. At Swiss Camp, the average latent heat flux from the ECM was 20.5 W m^{-2} in 1999 and 13.5 W m^{-2} in 2000, while the 1LM gave 25 W m^{-2} and 19 W m^{-2}, respectively, and the two level method gave 25 W m^{-2} and 15 W m^{-2}. Thus, the conclusion is that the two level method gives more reliable results, the latter method having been identified to produce a bias due to the inability of the 1LM to gauge deposition. Because temperature inversions are stronger at higher elevations (Figure 4.3), larger deposition rates are expected there. Thus, more confidence is placed in the two level method results despite the more erratic behavior of this method due to vertical temperature and wind profile sensitivities. The fact that validation measurements are only featured at two sites is a potential weakness of this methodology. Future work will be concerned with making eddy correlation measurements at other sites in order to account for potential elevation or region-dependant parameters in aerodynamic profile methods, the eddy diffusivity for example. Results from 1LM are followed through this study to compare with climate model results [*Ohmura et al.*, 1999; *Van-den-Broeke*, 1997] and with results from Antarctic AWS measurements [*Stearns and Weidner*, 1993].

There are competing advantages and disadvantages of the two profile method types. By underestimating negative latent heat fluxes, one level profile methods seem to overestimate net water vapor flux. The two level methods are more sensitive to profile difference errors. Two level methods exhibit a more erratic behavior, as measured by generally lower explained variances in comparison to eddy correlation than one level methods. Two level methods are also limited by the fact that two humidity measurements are required. Due to the fact that several humidity instruments have failed at GC-Net sites, there are 18% fewer useful hourly cases in the GC-Net database for two level methods to be applied (Table 3.1). Despite the more robust nature of the one level method, its inherent positive bias still makes two level methods more attractive for climatological evaluation of the net surface water vapor flux on the Greenland ice sheet. As is shown later, the frequency of negative latent heat fluxes increases with elevation.

6 Water Vapor Fluxes at GC-Net Sites Based on Profile Methods

Monthly and annual surface water vapor flux totals at GC-Net sites are presented in this section based on a two level aerodynamic profile method described in chapter 5. Analysis focuses on characterizing the diurnal and annual cycles of latent heat fluxes which are in turn directly related to surface water vapor fluxes. The physical processes that promote the surface water vapor flux are explained and the regional patterns are discussed. Hourly case examples of latent heat flux variations during melt and snowfall cases are presented and discussed. Annual surface water vapor flux is further compared with temperature and wind speed anomalies in an effort to determine if there is a detectable sensitivity of the surface water vapor flux to climate fluctuations. Greenland ice sheet latent heat fluxes are compared with those in Antarctica as some similarity in the climate is expected between these two ice sheets. Finally, net surface water vapor flux is added to the observed accumulation from ice cores for GC-Net sites with no runoff for an estimate of precipitation to compare with that from a model.

6.1 Hourly Surface Water Vapor Fluxes

Winds in the presence of absorbed solar radiation, radiative cooling, and warm or cold air advection promote vertical fluxes of water vapor. Surface water vapor fluxes occur as a result of vertical specific humidity differences modulated by vertical temperature differences. In winter, atmospheric moisture is basically unavailable as shown in section 4.1.1, thus despite large temperature inversions in winter, vertical water vapor fluxes are small. Large vertical temperature differences do not persist without a heat source that provides energy to maintain a significant vertical heat differential. Largest surface water vapor fluxes occur when melting reduces the surface albedo, allowing increased solar radiation absorption to drive a vertical humidity differential. As is often the case when snowfall begins, warm moist air advection over the cold ice sheet surface sets up a vertical humidity concentration gradient directed toward the surface, associated with a flux of latent heat to the surface. The surface water vapor flux variations during a snow storm case is shown in section 6.2.1.

Summertime maximum values of hourly latent heat flux calculated by the profile methods are rarely greater than 100 W m^{-2} (0.13 mm $hour^{-1}$ sublimation/evaporation). Largest surface water vapor flux occurs at ablation zone sites (JAR1, JAR2, and Swiss Camp) during warm windy conditions. The largest hourly average latent heat flux measured by eddy flux correlation was 93 W m^{-2} in 1999 at Swiss Camp. Hourly latent heat fluxes are no larger than 40 W m^{-2} at sites above 2000 m elevation with the exception of a handful of cases associated with high wind speeds. Largest deposition rates of +0.04 mm h^{-1} (-35 W m^{-2}), associated with the onset of snowfall are observed at low elevation sites. Such cases lasted for no more than a few hours. Extended periods of slight deposition occur throughout the winter. These are between +0.9 mm per month to +4.7 mm per month or -1 W m^{-2} to -5 W m^{-2} latent heat fluxes, respectively.

Surface water vapor fluxes exhibit a distinct diurnal cycle in summer during clear-sky conditions due to surface heating and cooling driven by the cosine effect of diurnal sun angle variations and the associated positive and negative net irradiance fluctuations. There is a degree of cancellation of daily mean latent heat fluxes i.e. latent heat fluxes fluctuating positive and negative over the course of the day. It is often the case in summer that some of the sublimated water vapor returns to the surface at night.

The annual cycle of surface water vapor flux rate is similar to that for temperature and solar radiation because solar radiation provides the energy to heat the surface (Figure 6.1). Peaks in the latent heat flux are caused by relatively large wind speeds, temperatures, and of course vertical moisture gradients.

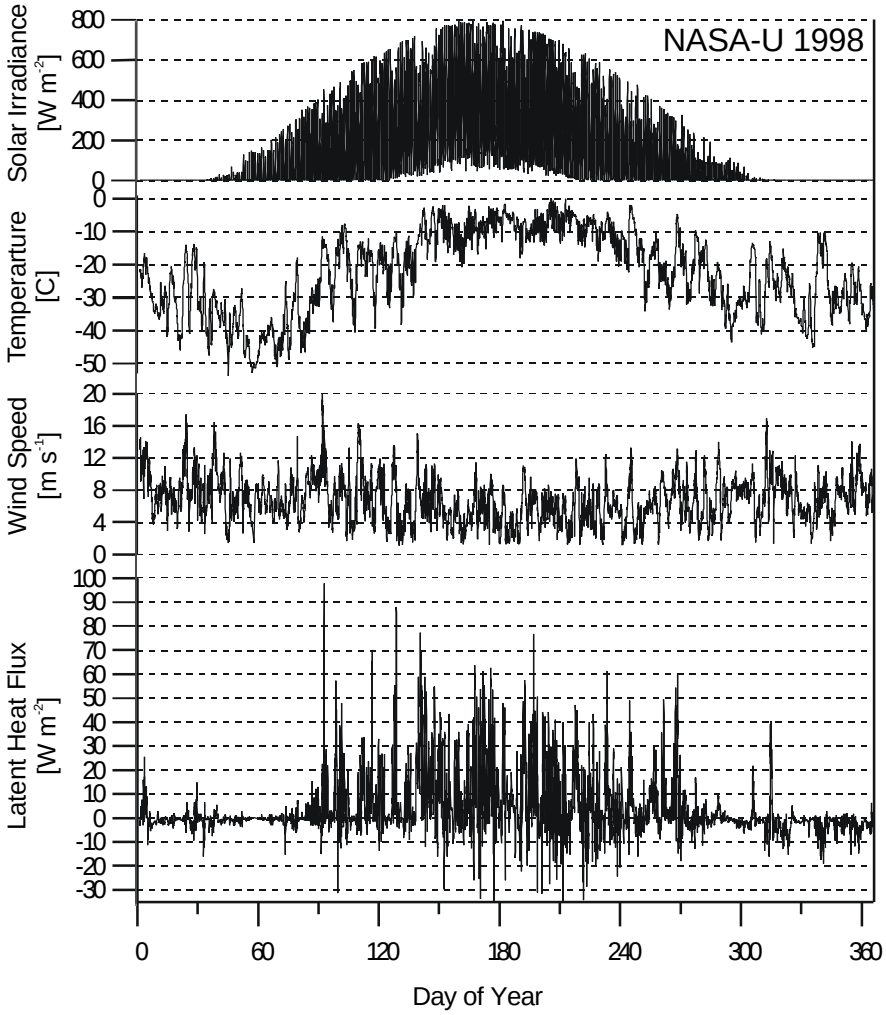

Figure 6.1, Annual cycle of hourly solar radiation, ~2 m temperature, ~2 m wind speed and latent heat flux.

6.2 Seasonal Variations in Surface Water Vapor Flux

There is a distinct seasonal variation of surface water vapor flux on the Greenland ice sheet. This was illustrated above by the annual cycle of hourly values (Figure 6.1). Now, the annual cycle of monthly mean latent heat flux and surface water vapor flux is provided for representative GC-Net sites (Figure 6.2). Fluxes from multiple years are included in the figures to illustrate the extent of interannual variability, which is largest at the lower elevation sites where peak surface water vapor fluxes are found. Interannual variability in the latent heat fluxes is less significant to the surface water vapor flux at sites at or above 2000 m because the fluxes are small. Monthly average latent heat fluxes are as great as 17.0 W m^{-2} (-16 mm per month) for June at the mean equilibrium line altitude at Swiss Camp (Table 6.1). Down glacier from Swiss Camp, at JAR1, the June mean latent heat flux in 2000 was 35 W m^{-2} (-33 mm per month). In other years, monthly fluxes are around 15 W m^{-2} (-12 mm per month). At DYE-2 where substantial atmospheric instability is observed (Table 5.1), monthly mean fluxes peak in excess of 40 W m^{-2} (-41 mm per month). The reason for the instability observed at DYE-2 is discussed in section 4.2.1.1.

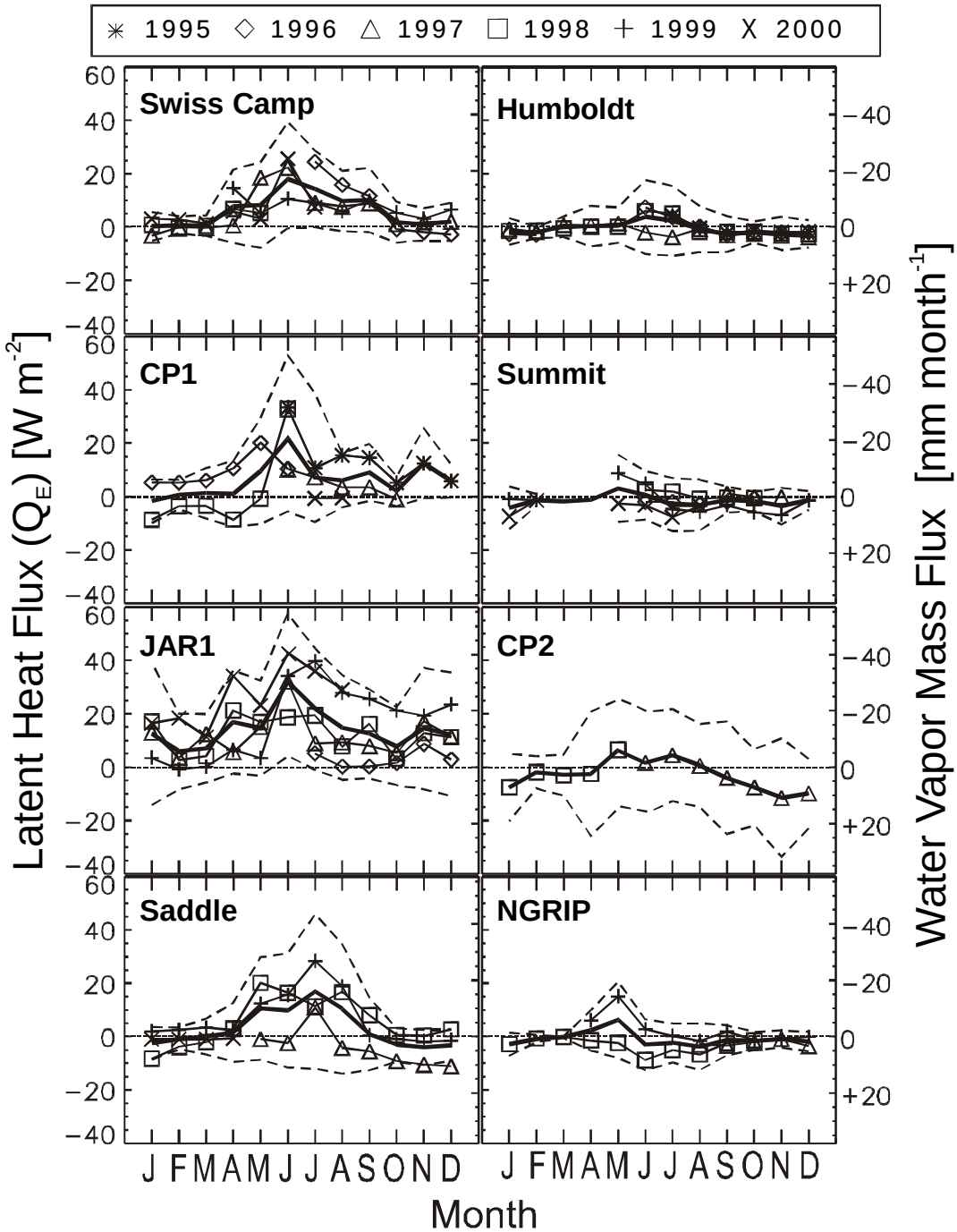

Figure 6.2, Annual cycle of latent heat flux (left axis) and corresponding surface water vapor flux (right axis) for representative GC-Net AWS sites based on the two level method. The dotted line indicates ± one standard deviation of hourly data in the monthly mean

At Summit and NGRIP, high on the ice sheet plateau where surface melting is effectively nonexistent, monthly fluxes are less than 15 W m^{-2} (-14 mm per month) in all years. At 2631 m, high on the eastern plateau at NASA-E, the annual range of latent heat fluxes is the smallest for the GC-Net with all monthly values less than 3 W m^{-2}. At NGRIP, and to a limited extent at Summit, monthly latent heat fluxes are indicative of net water vapor deposition, not only in winter but occasionally for summer totals. Monthly net deposition is curious because net radiation is most positive at this time. The only explanation is an augmented moisture source, such as from atmospheric subsidence associated with prevailing high pressure over the Greenland ice sheet. Based on

personal observation from camping for weeks at Summit, it is apparent that small amounts of condensation occur many days in spring, as evidenced by a rime frost on tents, ropes, and the surface each morning. Net deposition therefore contributes to the accumulation at plateau sites such as Summit or NGRIP. The mass input from deposition accounts for roughly 15% and 4% of the accumulation at NGRIP and Summit, respectively, when compared to accumulation rates from ice cores (Table 3.13). The result of net annual deposition of water vapor at the topographic summit of the Greenland ice sheet is consistent with results from Antarctica. Snow stake and evaporation pan measurements made at Dome Fuji, situated high on the Antarctic ice sheet at 3810 m elevation indicate that net annual water vapor deposition does occur (+1.6 mm y^{-1}) [*Kameda et al.,* 1997]. The contribution to the accumulation is 5% at Dome Fuji. Net deposition is also evident at high elevation sites in the north in some years at Humboldt and Tunu-N. At these sites, deposition contributes approximately 4% and 28% to the accumulation, respectively. The relatively large value derived for Tunu-N is the result of relatively large deposition values promoted by a strong temperature inversion in winter and a low average accumulation rate of roughly 100 mm y^{-1} [*Moseley-Thompson et al.,* submitted].

The standard deviation of monthly latent heat flux is often as large as the mean, indicating the highly variable nature of the combined humidity, wind speed, and temperature factors. At high elevation sites, there is little significance of the winter variability to annual net surface water vapor flux because their averages are always nearly zero. At the low elevation sites, wintertime variability in surface water vapor flux is significant because of storm activity. A single storm can greatly influence a monthly mean. Therefore, a case study of a wintertime storm is analyzed in the following section.

The results from the profile method validation in section 5.7 lead to the conclusion that the one-level method is not useful in evaluating the water vapor flux climate of the Greenland ice sheet. Results from the one-level method are included in the appendix (section A) for comparative purposes because atmospheric models and an Antarctic study employ this approach. One-level method results are useful to illustrate the bias in general climate model data obtained for ice sheets.

Table 6.1, Monthly Latent Heat Fluxes and the Corresponding Annual Surface Water Vapor Flux for Individual Years at GC-Net Sites Based on the Two Level Profile Method

Site	W m^{-2}	Jan.	Feb.	Mar.	Apr.	May.	Jun.	Jul.	Aug.	Sep.	Oct.	Nov.	Dec.	*Dm* [mm]	Year
Swiss Camp	mean 1	0.5	-1.6	4.1	0.5	15.5	17.0	7.7	7.7	6.9	0.5	7.3	9.0	-74	1997
	σ	7.4	2.0	5.4	10.4	20.5	13.2	10.5	9.8	8.8	5.2	11.3	13.7		
CP1	mean 1	-6.7	-1.6	-3.5	-1.0	-3.4	10.3	7.3	3.4	3.5	-1.2	-3.6	-8.7	5	1997.5 :
	σ	8.9	5.8	8.2	12.4	19.4	12.9	13.8	12.4	9.6	5.9	5.8	8.9		1998.4
NASA-U	mean 1	-0.1	-0.5	0.4	9.8	16.7	18.9	17.1	11.1	7.5	0.0	-0.9	-2.7	-73	1998
	σ	3.8	1.5	3.4	17.7	23.0	21.6	18.6	16.1	13.4	3.4	6.5	3.1		
GITS	mean 1	1.8	-1.0	3.2	1.7	11.3	19.9	14.0	21.0	2.4	0.0	0.7	0.0	-71	1996
	σ	5.2	5.4	6.0	5.4	16.3	18.3	17.8	37.2	6.8	5.9	6.4	12.3		
Humboldt	mean 1	-1.0	-1.1	-0.2	0.4	0.2	4.9	4.0	-1.3	-1.4	-1.3	-1.7	-1.9	0	1998
	σ	6.8	1.2	2.6	12.9	4.4	10.7	9.5	7.3	11.5	5.9	7.2	2.6		
Summit	mean 1	-4.2	-1.4	-1.8	-1.1	3.1	2.2	2.8	-0.1	-0.2	-0.4	-3.6	-1.4	6	1996.4 :
	σ	8.0	2.3	3.8	4.7	12.7	7.1	9.1	4.6	3.0	1.4	6.9	3.5		1999.5
Tunu-N	mean 1	-1.6	-0.9	-0.7	-3.8	-2.8	4.3	6.5	0.0	-9.0	-5.7	-2.8	-4.7	20	1997 :
	σ	5.6	1.0	0.7	3.8	4.7	9.4	11.0	6.9	17.3	6.9	4.0	4.7		1998
DYE-2	mean 1	-6.0	-1.7	2.2	4.2	10.0	47.5	17.8	10.2	9.3	0.9	-2.7	-4.5	-82	1997
	σ	16.2	1.6	9.5	14.5	10.1	36.6	29.2	27.2	18.9	10.9	8.4	10.2		
JAR1	mean 1	11.6	3.1	10.1	4.3	10.4	5.0	1.6	4.0	5.6	4.8	14.3	11.1	-82	1997
	σ	29.9	8.3	19.0	9.2	10.5	5.7	3.0	6.7	12.3	10.2	25.3	23.1		
JAR1	mean 1	15.5	2.1	3.5	16.7	8.7	5.3	4.5	1.0	9.1	3.1	11.2	10.1	-87	1998
	σ	30.1	6.9	6.9	21.5	10.5	5.7	9.2	6.5	13.1	10.7	18.6	18.2		
Saddle	mean 1	-6.4	-2.7	-1.7	5.0	17.0	13.1	8.4	13.2	6.6	0.4	0.8	2.6	-53	1998
	σ	5.8	3.5	7.4	19.9	26.4	22.2	24.3	26.7	16.8	3.8	2.7	5.6		
Saddle	mean 1	1.5	1.9	3.4	2.2	11.3	13.4	24.5	16.4	0.6	-0.7	-1.2	-1.1	-68	1999
	σ	3.1	4.9	8.2	7.4	20.8	18.5	28.1	21.5	9.7	3.4	2.3	1.8		
South Dome	mean 1	*	*	*	*	12.6	7.2	-7.8	6.6	-1.4	7.0	*	*	*	1999
	σ					23.9	22.5	24.8	29.1	13.4	12.3				
NASA-E	mean 1	-0.3	-0.1	0.3	-0.8	-0.6	2.4	0.6	-2.7	-1.8	-1.0	-0.5	-1.7	6	1997.4 :
	σ	0.3	0.2	1.1	0.4	2.5	6.9	5.2	11.5	3.2	2.4	0.5	2.6		1998.5
CP2	mean 1	-7.6	-3.6	-3.0	-2.5	0.6	1.6	4.6	0.6	-4.0	-7.6	-11.4	-9.9	40	1997.4 :
	σ	12.7	6.0	7.7	23.2	18.5	19.0	17.2	15.6	21.1	14.3	22.2	13.0		1998.5
NGRIP	mean 1	-2.4	-0.7	-0.1	-4.1	-4.1	-6.7	-4.0	-5.4	-2.3	-1.2	-0.8	-1.9	32	1998
	σ	3.7	1.2	0.5	4.3	3.7	6.8	4.6	6.5	4.0	2.5	3.2	3.7		
NASA-SE	mean 1	-3.3	-3.1	-0.8	-3.9	-7.5	-4.5	3.6	4.5	1.1	-0.3	-1.1	-1.1	15	1999
	σ	8.0	6.2	4.5	8.3	15.7	15.3	14.3	18.8	9.9	3.6	6.0	1.4		
JAR2	mean 1	1.7	1.5	1.5	4.1	3.4	23.0	3.2	6.8	7.3	4.3	1.4	3.2	-61	1999.8 :
	σ	4.7	6.8	6.4	10.4	8.3	21.4	5.7	9.3	12.3	8.7	6.7	8.7		2000.7

* - insufficient data.

6.2.1 Case Example: Winter Water Vapor Fluxes at Low Elevations

Distinct variations in the surface water vapor flux occur at lower elevation AWS sites in winter. These events introduce variability into winter month averages that is not observed for high elevation sites (Figure 6.2). Along the JAR transect (JAR 2, JAR 1, and Swiss Camp), a frontal passage has a notable effect on the latent heat flux (Figure 6.3). Over the 18 hours of frontal passage, the pressure falls 15 hPa, wind direction veers from predominantly down-slope to predominantly upslope, wind speed increases from 2 m s^{-1} to 10 m s^{-1} and temperatures dramatically increase from -20° C to +1° C. The relative humidity decreases from 100% to 87% toward the point when peak temperature is reached, indicating a drying of the air simply by dew point depression. Following this undersaturation, wind speed, and temperature, surface water vapor fluxes increase. Relative humidity then approaches 100% again at the point that instrument height begins to decrease indicating accumulating snow fall. During the initial phase of accumulation, the latent heat flux indicates water vapor deposition to the surface. Similar variations of micrometeorological parameters are observed for this case, up-glacier at Swiss Camp and down glacier from JAR1 at JAR2. At JAR2, however, there was no detectable surface height increase from snowfall. From the observed 3° C air temperature at JAR2, it is evident that it was raining instead of snowing.

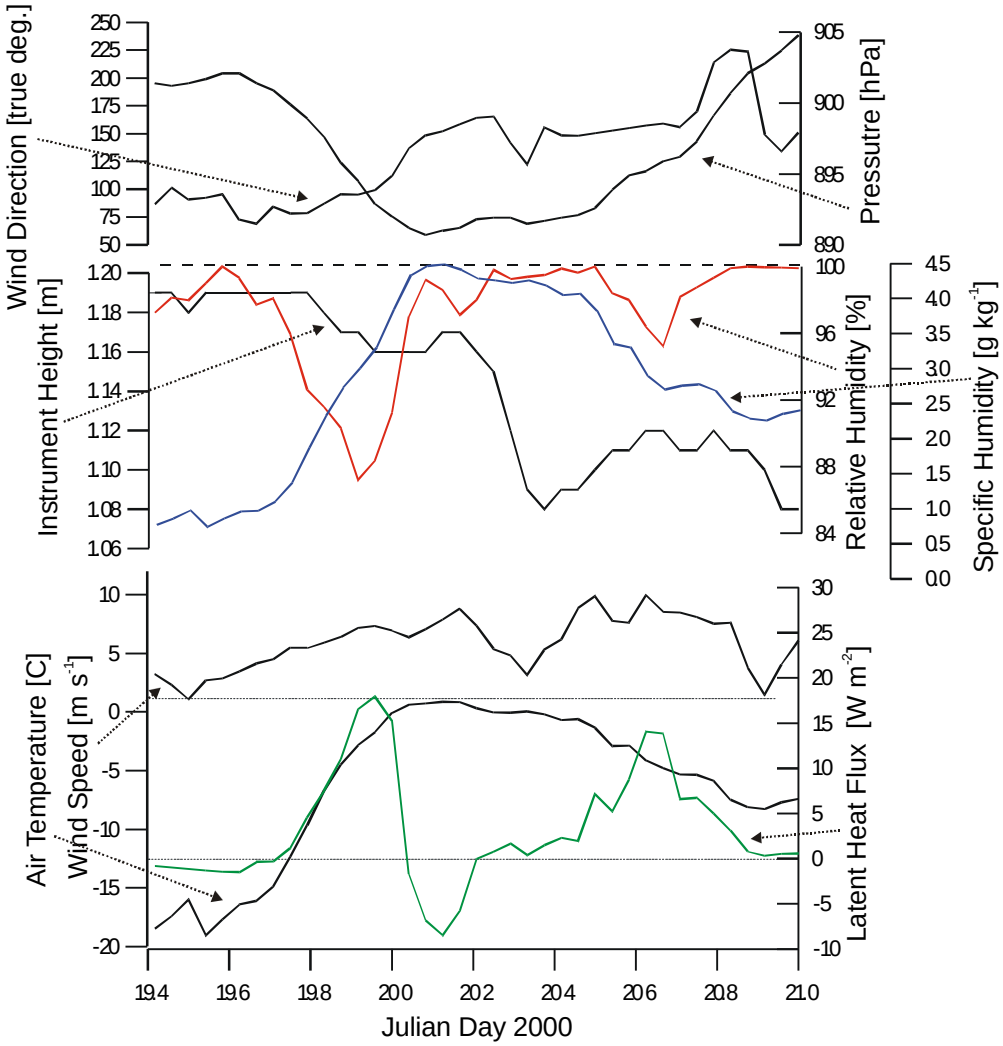

Figure 6.3, A case example of the meteorological conditions associated with the surface water vapor fluxes occurring during a wintertime snow storm at the JAR1 AWS.

6.2.2 Case Example: Melt and Strong Winds

During the 2000 field season at Swiss Camp, energy balance measurements coincided with conditions that promote large evaporation rates. These were characterized by winds above 8 m s^{-1} and daytime air temperatures at 0° C. Evaporation rates peaked near mid day owing to the heating of the surface by solar radiation absorption (Figure 6.4). Evaporation rates decrease after midday due to the surface radiation balance becoming negative. However, the evaporation continued through the night, as the warm foehn-type wind blew over the surface, supplying sensible heat, as indicated by positive latent heat fluxes. During this case, the sensible heat flux is basically equal and opposite to the latent heat flux, showing that both the sensible heat and radiation fluxes are sunk into evaporation, not snow melt. The evaporation pan measurement results featured in Figure 5.11 coincided with this period. Daily evaporation rates during this period were between 1.1 mm d^{-1} and 1.3 mm d^{-1}, some of the largest evaporation rates of the ablation season.

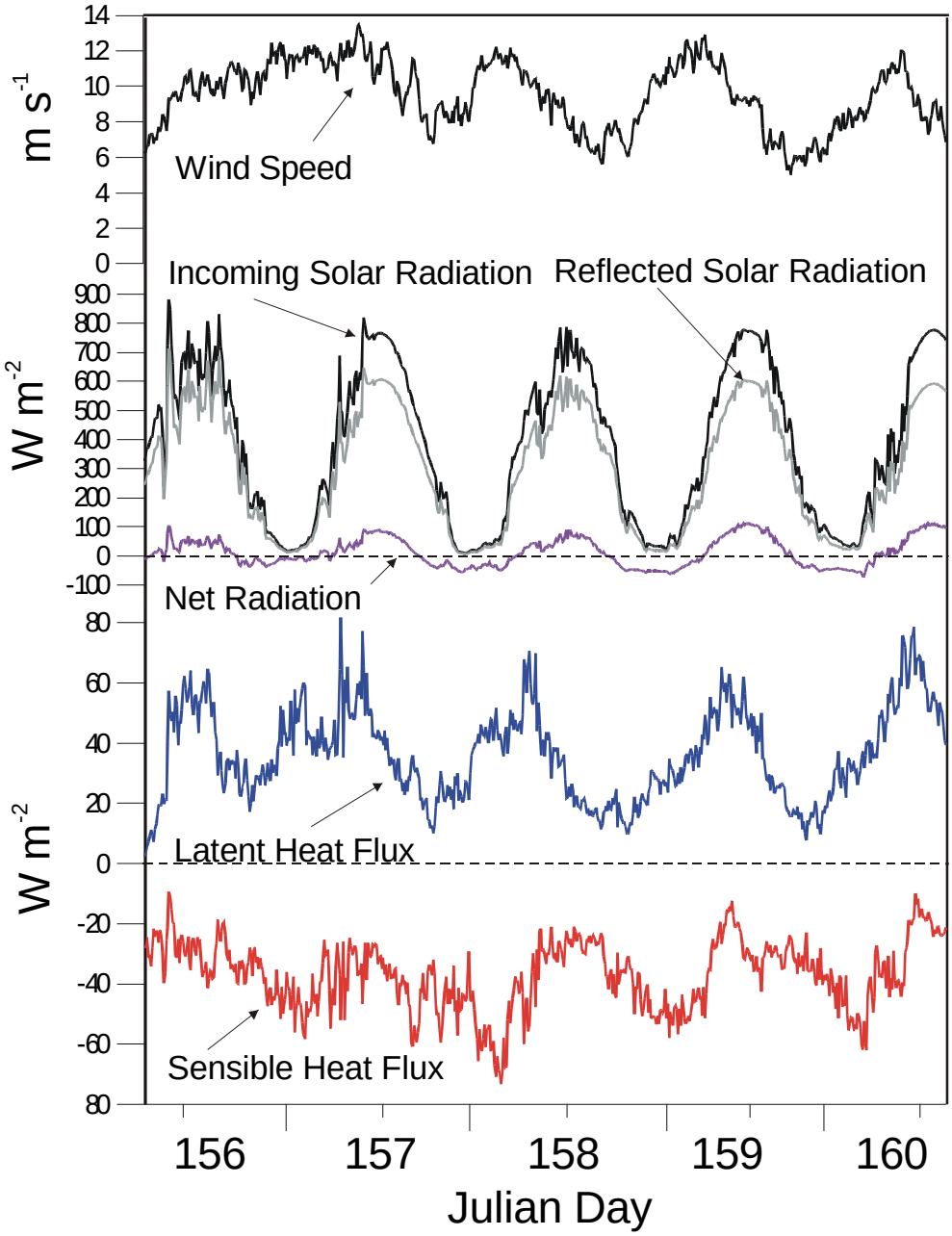

Figure 6.4, Evaporation as a major component of the surface energy balance during windy melt conditions at Swiss Camp in 2000

6.3 Sublimation Variability between an Undulation Crest and Trough

Surface water vapor fluxes vary substantially from one undulation crest site to its adjacent trough, 30 m lower in elevation and 6 km up-glacier, AWS CP1 and CP2, respectively (Figure 6.5). At the undulation trough, monthly latent heat fluxes more often indicate a net water vapor flux to the surface, while at the undulation crest, the latent heat fluxes are more often indicative of water vapor loss to the atmosphere. Some of the largest negative hourly latent heat fluxes in the GC-Net data, -55 W m^{-2}, are observed in January at CP2. The January 1998 average is –7.6 W m^{-2} (+ 7.2 mm) (Table 6.1). The large negative latent heat fluxes result in an annual net deposition at CP2 of 40 mm. Surface height measurements show that accumulation rates are roughly 40% higher at the trough site compared with the crest site. The difference in annual surface water vapor flux explains roughly 18% of the ~190 mm difference in accumulation between the two sites. The remaining difference in accumulation is thought to result from snow drift deposition in the undulation trough. The slope gradient is 1.8:100 based on the altimeter data. The comparison is complicated by the fact that CP1 is not directly downwind of CP2. Nonetheless, large spatial variability in surface climate is observed between these two sites. Much of the difference is explained in context of undulations.

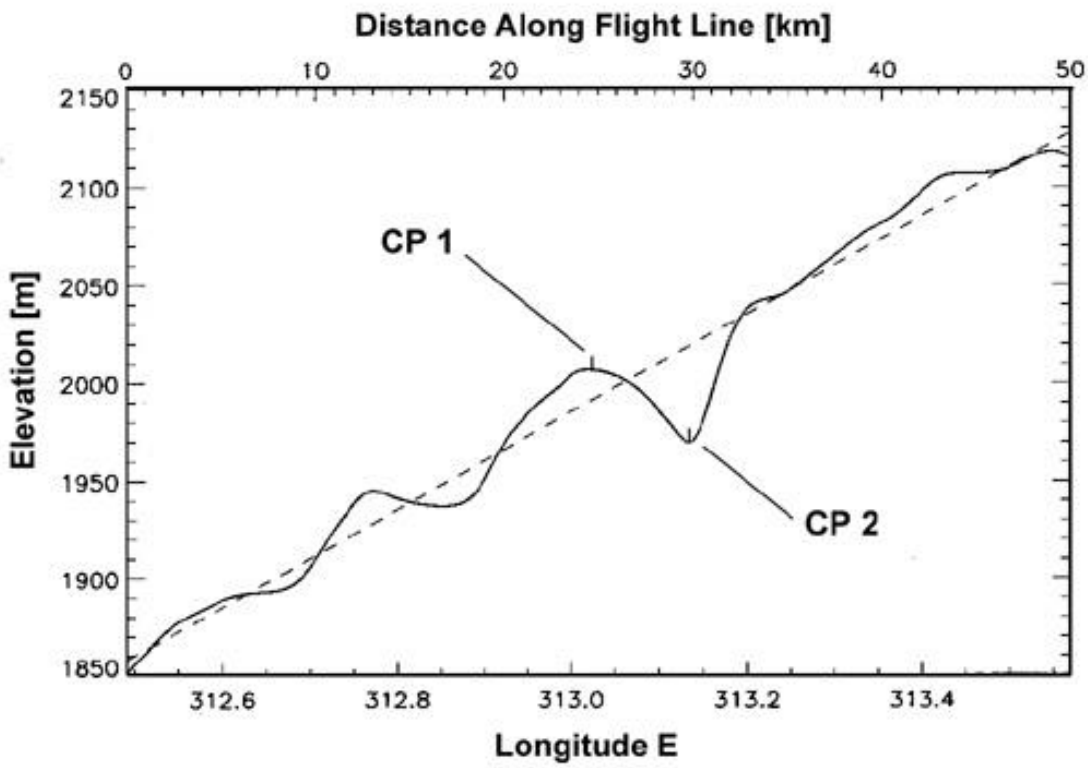

Figure 6.5, Laser altimeter-derived elevation transect between CP1 and CP2 along the flow line of the ice sheet, roughly 40° to the right of the modal wind direction.

During snowfall at the CP1 and CP2, the vertical specific humidity gradient and latent heat flux again indicates significant deposition at CP2 Julian day 177.5 while at CP1, there is no large deposition signal (Figure 6.7). The accumulation is greater at CP2. CP1 catches up in accumulation 24 hours later. This may be the result of snow deposition at CP1 from the upwind fetch.

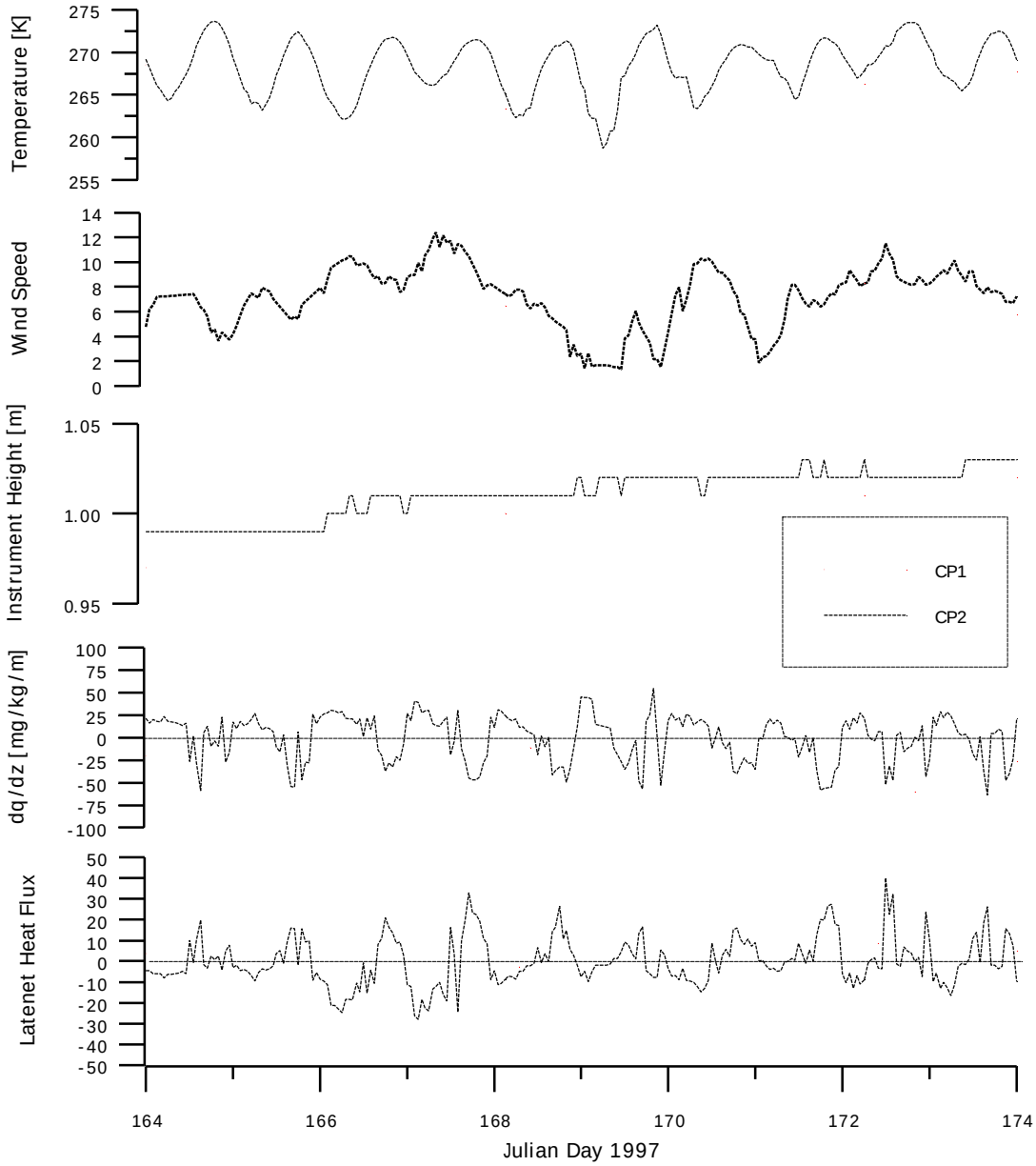

Figure 6.6, Time series of micrometeorological parameters between CP1 and CP2 for melt conditions indicating greater vertical specific humidity gradient (dq/dz) at the undulation trough site.

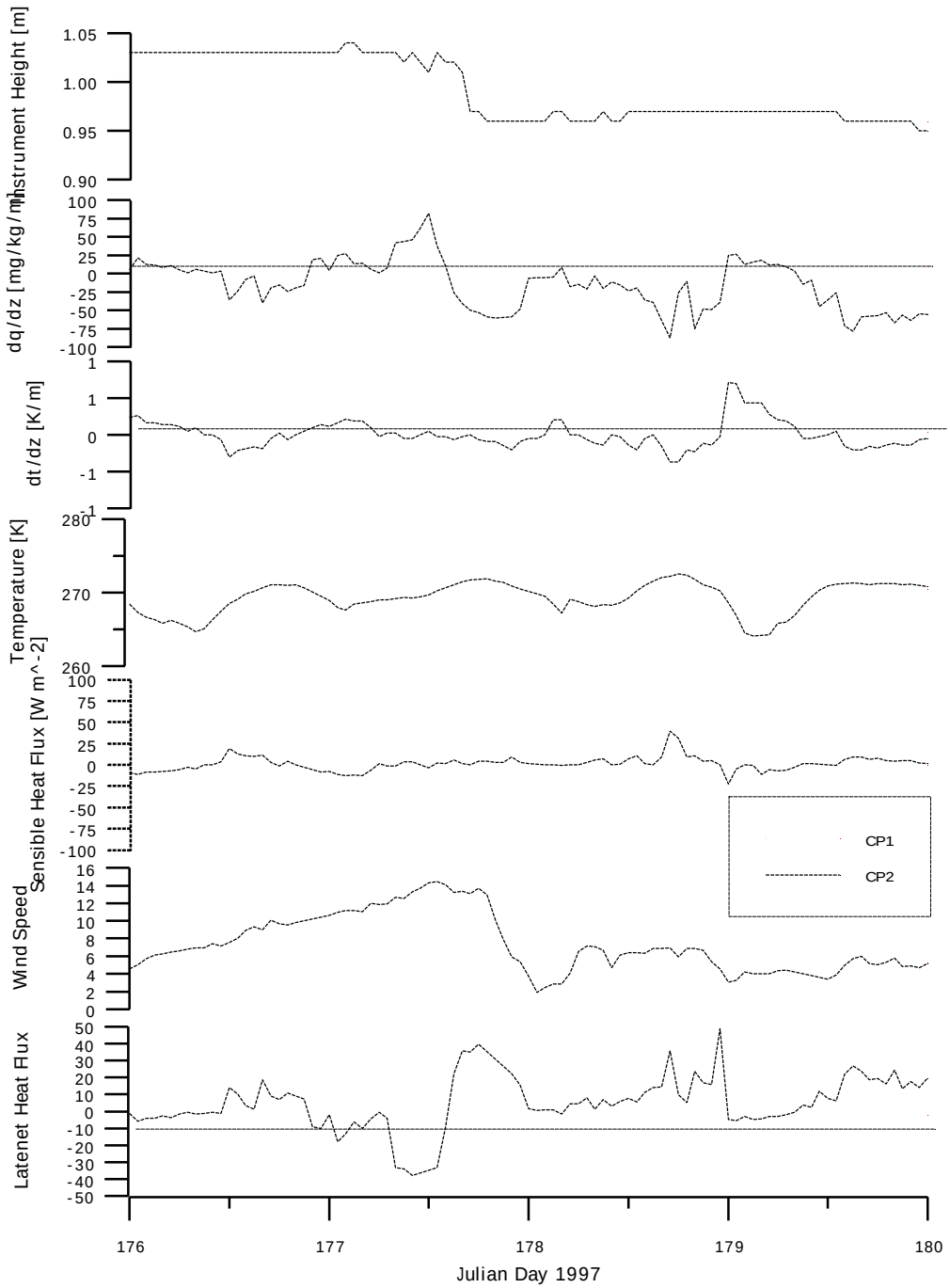

Figure 6.7, Time series of micrometeorological parameters between CP1 and CP2 during a snow event illustrating the greater deposition rate (negative latent heat fluxes) at the undulation trough site (CP2).

In winter, there are distinct deposition signals at CP2 and much smaller ones at CP1 (Figure 6.8). In this case, the vertical temperature gradients are very similar between the sites.

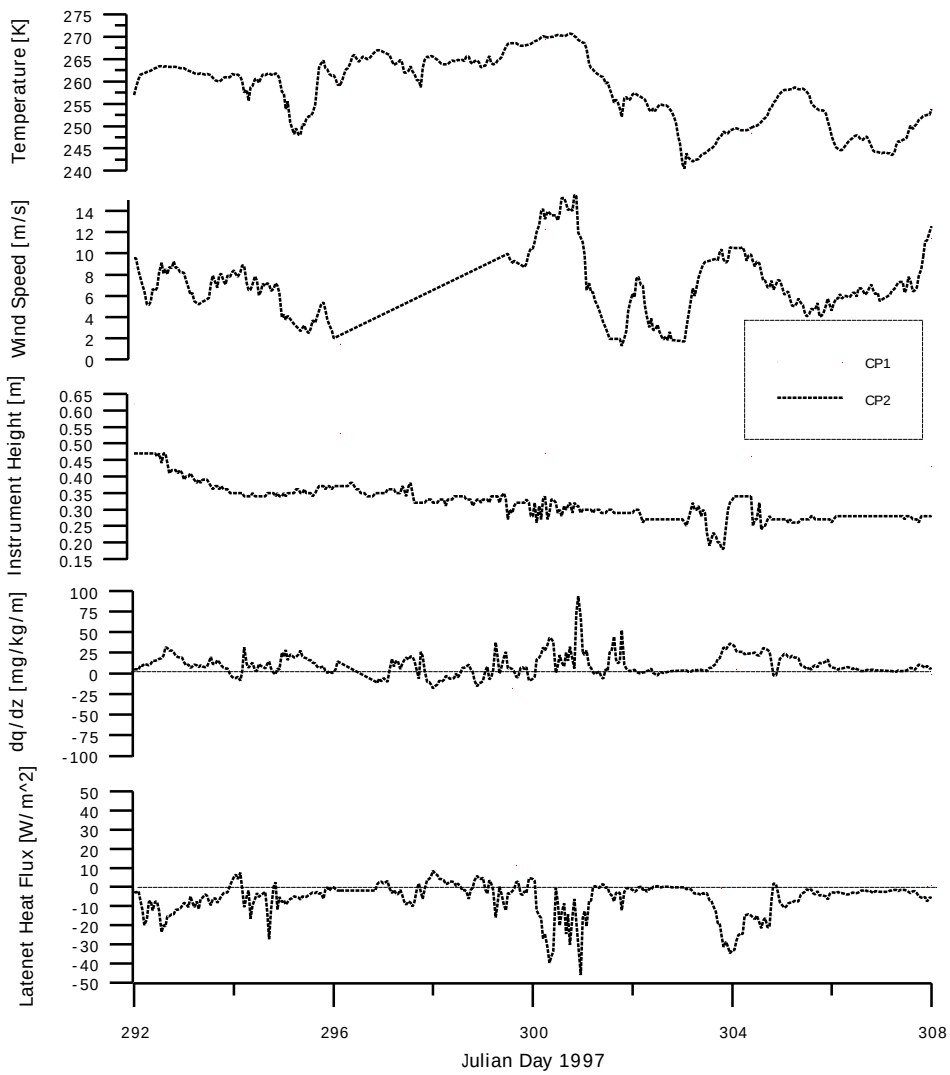

Figure 6.8, Time series of micrometeorological parameters between CP1 and CP2 during winter indicating the greater tendency for deposition at the undulation trough site (CP2).

Thus, there are distinct differences in vertical water vapor fluxes between CP1 and CP2, located only 6km apart. The sites are on sloping surfaces that contribute to significant surface water vapor flux variations which help to explain the accumulation rate differences between these sites.

6.4 Comparison of Antarctic and Greenland Surface Water Vapor Fluxes

Comparison with Antarctic results from *Dalrymple et al.* [1966]; *Stearns and Weidner* [1993]; *Van-den-Broeke* [1997]; and *Kameda et al.* [1997] indicate a very similar regional pattern of surface water vapor flux as on the Greenland ice sheet. Maximum Antarctic monthly mean latent heat fluxes based on a one level method are between 10 W m^{-2} and 30 W m^{-2} (Appendix Table A). The largest negative monthly mean Q_E is reported to be -5 W m^{-2} [*Stearns and Weidner,* 1993], although, larger negative Q_E would probably be detected using a two level method of this study. The annual cycle of latent heat fluxes, exhibiting a summer peak in net water vapor flux from the surface to the atmosphere and the tendency for a small net water vapor deposition throughout winter, is equivalent between Antarctic and Greenland results. As with GC-Net sites, net surface water vapor loss increases toward lower elevations and latitudes and particularly during summer resulting primarily from elevation-temperature relationships, as temperature is an important driver for surface water vapor flux. Maximum annual net surface water vapor flux was estimated to be -70 mm water equivalent on the Ross Ice Shelf at AWS Elaine [*Stearns and Weidner,* 1993]. Latent heat flux measurements as part of a 1958 South Pole

micrometeorological program by a two-level profile technique indicate 2.5 mm deposition to the surface from autumn through spring [*Dalrymple et al.,* 1966]. This study does not, however, include midsummer surface water vapor flux which would reduce the implied annual net water vapor flux. Cumulative surface water vapor flux for 1986 from the South Pole AWS data for an 11 month period using the one level method followed in this study, was –33 mm according to *Stearns and Weidner* [1993]. The difference is largely attributed to the use of the 1LM which underestimates the bulk deposition amount. Using output of a 1.1° horizontal resolution general circulation model (ECHAM-3 T106), the annual cycle in surface water vapor flux is well reproduced in comparison with this 1LM AWS-based data [*Van-den-Broeke,* 1997]. However, deposition in the model is underestimated in winter as compared to the one level method results. It should restated that the surface water vapor flux estimates based on the one level method are probably too high because of its inherent underestimation of water vapor flux to the surface. The ECHAM results suggest that 10-15% of the annual precipitation over Antarctica is lost through surface water vapor flux, an equivalent result to that of *Ohmura et al.* [1999] for Greenland. *Van-den-Broeke* [1997] notes that the ECHAM-3 model seems to underestimate deposition.

The comparison of Antarctic surface water vapor flux with Greenland ice sheet estimates is complicated by the fact that there is little overlap in latitude. Also, apparently because of lacking continuity of data, results based on Antarctic AWS are only presented for 4 low elevation sites on the Ross ice shelf or Ross Island (elevations below 75 m) and a 10 month series for the South Pole (2855 m) that does not include the summer months. No surface water vapor flux estimates are presented for the 20 other Antarctic AWS sites lying between 240 m and 3280 m elevation. GC-Net sites currently do not exist below 300 m, hence there is no elevation overlap with Antarctic sites in *Stearns and Weidner* [1993].

Latent heat flux measurements, as part of a 1958 South Pole micrometeorological program by a two-level profile technique, indicate 2.5 mm w. e. deposition to the surface from autumn through spring [*Dalrymple et al.,* 1966]. This study does not, however, include midsummer estimates which may reduce the positive surface water vapor flux as relatively large sublimation losses may occur in summer. Cumulative surface water vapor flux for the Patrick AWS for the same 11 months based on the one level method was –3.3 cm for 1986 [*Stearns and Weidner,* 1993]. The difference is largely attributed to the different methods used.

6.5 Precipitation from Water Vapor Fluxes and Accumulation

An estimate of precipitation is made for sites without runoff by the sum of the net surface water vapor flux with the observed accumulation. At sites where the surface water vapor flux augments accumulation, the surface water vapor flux value is subtracted from the accumulation to imply the precipitation. Greenland precipitation from the diagnostic model of *Chen et al*. [1997] is on average about 15% smaller than that precipitation rate implied by the surface water vapor flux estimates from profile methods and accumulation from ice cores at GC-Net sites [*Moseley-Thompson et al.,* submitted]. In a recent reanalysis using the same diagnostic model, but with a more accurate topographic dataset [*Bromwich et al.,* submitted], the modeled precipitation rates for Greenland sites have generally increased. The difference in implied versus modeled precipitation estimates is now much smaller (5%). It should be noted, however, that snow redistribution by the wind may also be a source of accumulation in ice core data that is neglected by this comparison. The only site where blowing snow is certainly thought to contribute to accumulation is discussed in the next section.

6.6 Conclusions

Vertical water vapor fluxes are greatest in summer at low elevation sites (10 mm to 20 mm per month). The magnitude of the moisture flux is greatest in summer, leading to net annual water vapor loss from the surface of the ice sheet. During melt, evaporation rates as great as 1.5 mm day^{-1} are observed at Swiss Camp and are explained by surface energy balance measurements. In winter, small amounts of deposition in association with strong surface temperature inversions are observed (1 mm to 5 mm per month). At plateau sites (Summit and NGRIP) and sites in the north (Tunu-N and Humboldt) annual net deposition is observed. Occasional net deposition in summer is observed for high elevation sites in summer at Summit and NGRIP. In other years, net water vapor loss is evident. The surface water vapor flux at high elevations are very small and are associated with a much greater uncertainty than the large fluxes observed at ablation zone sites JAR1 and JAR2. Wintertime variability in surface water vapor flux at low elevation sites is the result of winter advective storm

activity and is significant to net annual surface water vapor flux. The diurnal cycle of surface water vapor flux is similar to the annual cycle. During mid-day surface water vapor losses are at their maximum. At night, deposition is favored, as the surface cools radiatively.

Annual surface water vapor flux as great at -87±30 mm were calculated for ablation zone AWS sites (JAR 1 and JAR 2). At equilibrium line altitude (Swiss Camp), annual net surface water vapor flux is -74±26 mm. At intermediate elevation sites (NASA-U, CP1 and CP2), annual surface water vapor fluxes are smaller, exhibiting values between +15±5 mm and -68±24 mm. At some sites, particularly those at high elevations (Summit and NGRIP) and those in the far north (Humboldt and TUNU-N), annual deposition is evident , i.e. more water vapor mass is deposited to the surface over the course of the year than is lost.

There are distinct geographical variations of net surface water vapor flux that depend primarily on available energy. Surface water vapor fluxes are greatest at lower elevations and lower latitudes. The increase of surface water vapor flux toward lower elevations is linked not only with greater temperatures but also more developed katabatic wind speeds. The simple geographic gradients of surface water vapor flux make it possible to construct maps to determine the total net surface water vapor flux for the entire Greenland ice sheet. Surface water vapor flux mapping is featured in section 8.

The pattern of net surface water vapor loss at lower elevations and surface water vapor flux gain at high elevations is consistent with the atmospheric circulation patterns set up by the surface radiation balance.

Temperature and wind speed anomalies from 2-3 year records were compared to latent heat fluxes rates in an effort too determine if annual surface water vapor fluxes correlate with temperature and wind speed anomalies. Inconsistent changes of surface water vapor flux with temperature anomaly are found. The profile method results indicate increasing surface water vapor fluxes with increasing wind speed, although there are exceptions associated with factors other than wind speed, such as temperature and vertical water vapor concentrations. Thus, analysis of anomalies is not presented in this thesis. Longer records are must be awaited to make confident conclusions.

Surface water vapor losses are greater at an undulation crest site (+5 mm y^{-1} at CP1) than at an undulation trough site (+ 40 mm y^{-1} at CP2). In windy summer melt conditions, continuous evaporation is observed at the undulation crest site. At the trough site, only at mid-day does evaporation dominate the surface water vapor balance. It is hypothesized that some water vapor that sublimates upstream and is supplied on top of the surface layer contributes to a smaller upward moisture gradient. At night, deposition rates are generally greater at the undulation trough site. The difference in surface water vapor flux explains roughly 18% of the 40% difference in accumulation between the two sites. Another likely mechanism, redistribution of snow by the wind, is the main factor. This result implies that some of the mass that is lost from undulation crests may be deposited in undulation troughs. This has very important implications for the question of surface water vapor fluxes over the Greenland ice sheet because undulations are found all over the ice sheet. The western slope is much smoother than the eastern slope. Furthermore, these results raise an important issue in the placement of point measurements such as AWS and ice cores, given that large scale representativity is desirable. Consulting a high resolution elevation map for prior knowledge of local slope angles may be a useful approach in determining representative sites.

The direct comparison of surface water vapor fluxes between Greenland and Antarctica was complicated because of no overlap in elevation and latitude. Results from the literature, i.e. [*Stearns and Weidner,* 1993; *Van-den-Broeke,* 1997; *Dalrymple et al.,* 1966] do, however, indicate a similar environment for surface water vapor fluxes on the Antarctic ice sheet. The potential for surface water vapor loss is greatest in summer months and net water vapor flux to the surface occurs at high elevation on the Antarctic ice sheet [*Kameda et al.,* 1997].

7 Comparison With a Regional Climate Model

7.1 Introduction

Confidence can be taken in the results of climate change experiments only if the model produces a good simulation of the present climate [*Dethloff et al.*, 1996]. In the interest of providing insight into the validation of climate models, the *in-situ* derived latent heat fluxes of this study are compared with output from a state of the art regional model described below. Values from the nearest model grid cells are compared (Table 7.1).

Table 7.1, PSU / NCAR MM5 grid locations nearest to GC-Net locations

Site Name	Grid *i–1* value	Grid *j–1* value	Distance to AWS [km]	Grid Latitude deg. N	Grid Longitude deg. W
Swiss Camp	10	28	14	69.47	49.54
CP1	13	28	20	69.81	46.47
NASA-U	14	39	4	73.86	49.41
GITS	11	50	12	77.18	60.62
Humboldt	15	52	20	78.58	55.94
Summit	21	34	17	72.68	38.89
Tunu-N	26	48	18	78.17	33.72
DYE-2	11	19	19	66.39	45.89
JAR1	10	28	6	69.47	49.54
Saddle	12	18	18	66.13	44.76
South Dome	10	10	8	63.11	44.68
NASA-E	28	40	16	75.15	30.00
CP2	13	28	18	69.81	46.47
NGRIP	20	41	15	75.21	41.97
NASA-SE	15	18	21	66.39	42.08
KAR	25	26	18	69.84	33.26
JAR2	10	28	6	69.47	49.54

7.2 NCAR MM5 Modeled Evaporation Rates

The model output compared in this section comes from the Penn State / National Center for Atmospheric Research (NCAR) Mesoscale Model version 5 (MM5) [Dudhia, 1993; Grell, 1994] Polar version [*Cassano et al.*, in press]. The model is forced by European Center for Medium Range Weather Forecasting (ECMWF) analyses. MM5 surface-heat fluxes are defined by air density and potential temperature at the lowest model layer and exchange coefficients [*Cassano et al.*, 2001]. The lowest two model levels are 0 m to 14 m. Given the ability of the model to resolve the large temperature, moisture, and wind speed gradients in the lowest 5 meters above the surface, accurate exchange parameterization are crucial. The surface momentum flux is determined as a function of a drag coefficient, air density, and the wind velocity [*Nelson*, 1998]. The surface moisture flux is defined by a moisture availability parameter, which varies from 1 for a wet surface to 0 for a surface with no evaporation potential. For the ice sheet, a moisture parameter has a fixed value of 1 and thus the surface is taken to be saturated with respect to water or ice. The MM5 does not represent liquid water on the surface of the ice sheet, and so would significantly underestimate the latent heat flux if liquid water were present. Description of the model applied to the Greenland domain is found in *Cassano et al.* [in press]. In this paper, a comparison with GC-Net measurements indicates a negative model bias in temperature, wind speed, pressure, humidity, and net radiation. MM5 latent heat flux data (Table 7.2) nearest to GC-Net sites (Table 7.1) was extracted from the

35 x 69 grid. Model output were obtained from J. Cassano at the Byrd Polar Research Center, Ohio State University, Columbus, OH, USA.

Table 7.2, Monthly MM5 Latent Heat Flux Estimates [W m^{-2}]

Site	Jan. 1998	Feb. 1998	Mar. 1998	Apr. 1997	May. 1997	Jun. 1997	Jul. 1997	Aug. 1997	Sep. 1997	Oct. 1997	Nov. 1997	Dec. 1997
Swiss Camp	10.30	2.09	1.97	3.31	12.75	10.52	3.17	2.49	7.62	6.01	15.03	11.83
CP1	0.07	-0.61	-0.82	-0.53	2.80	7.41	8.83	1.35	0.52	-1.37	-0.22	-0.99
NASA-U	-1.24	-0.77	-0.87	-0.83	1.74	5.79	4.57	0.40	-0.88	-1.61	-1.94	-2.26
GITS	-1.84	-0.88	-0.99	-0.51	1.88	8.31	6.25	2.40	-2.45	-1.71	-2.01	-2.38
Humboldt	-1.55	-0.72	-0.87	-0.47	1.14	6.03	5.32	0.37	-1.52	-2.07	-1.91	-1.82
Summit	-1.46	-0.63	-0.95	-0.96	-0.16	2.53	2.15	-0.36	-1.96	-1.90	-1.41	-1.69
Tunu-N	-1.39	-0.54	-0.47	-0.59	-0.27	3.88	2.66	-1.01	-0.90	-1.93	-1.94	-1.73
DYE-2	-1.93	-1.11	-0.50	0.63	3.44	7.98	8.41	0.77	-0.33	-1.29	-2.63	-2.70
JAR1	10.30	2.09	1.97	3.31	12.75	10.52	3.17	2.49	7.62	6.01	15.03	11.83
Saddle	-3.08	-1.17	-1.08	0.22	2.42	7.74	8.28	0.67	-1.27	-2.24	-3.14	-4.17
South Dome	-1.97	-1.68	-1.86	0.16	4.93	7.38	7.85	1.83	-0.19	-2.52	-2.19	-1.98
NASA-E	-1.76	-0.63	-0.66	-1.43	-0.89	3.37	2.28	-0.61	-1.89	-2.23	-1.66	-2.00
CP2	0.07	-0.61	-0.82	-0.53	2.80	7.41	8.83	1.35	0.52	-1.37	-0.22	-0.99
NGRIP	-1.61	-0.49	-0.60	-0.95	-0.20	1.27	1.23	-1.10	-1.93	-1.99	-1.40	-2.10
NASA-SE	-1.92	-1.03	-1.32	0.29	1.90	7.80	7.33	1.63	-1.60	-2.11	-2.33	-2.75
JAR2	10.30	2.09	1.97	3.31	12.75	10.52	3.17	2.49	7.62	6.01	15.03	11.83

7.3 Results and Discussion

The annual cycle of MM5 latent heat fluxes is similar to those derived from GC-Net data. Maximum positive latent heat fluxes occur in summer and small negative latent heat fluxes occur in winter (Figure 7.1). The comparison is favorable for Humboldt, NASA-E, and NGRIP, where the fluxes are small. The MM5 and 2LM indicate a net flux of water vapor from the atmosphere to the surface at NGRIP in all months except June. There is better agreement between the model and the 1LM than the 2LM probably due to the fact that the MM5 employs a saturation-based evaporation scheme [*Nelson*, 1998]. Better agreement for the 1LM comparison may also be due to the fact that the 1LM is dominated by temperature effects.

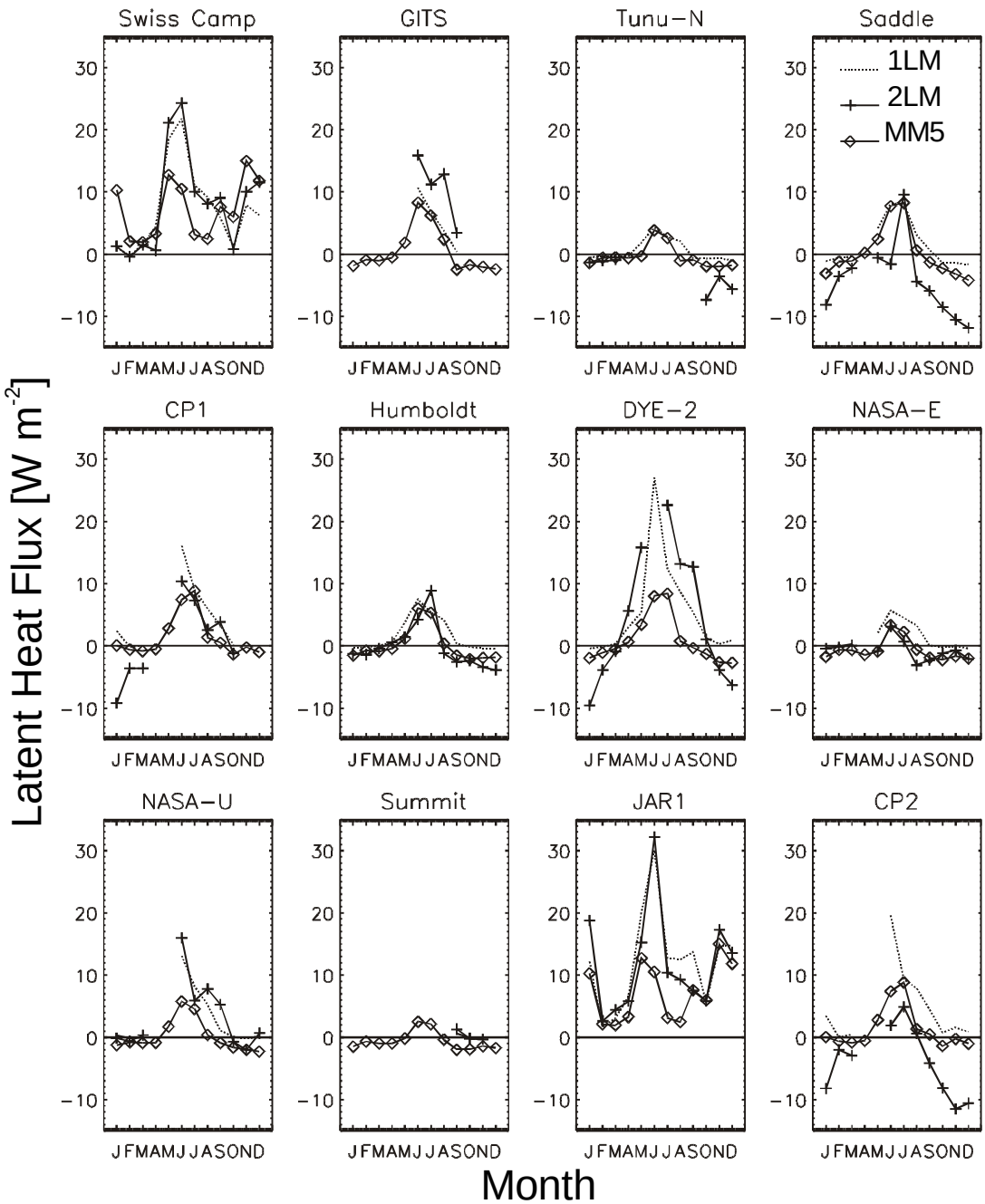

Figure 7.1, Comparison of latent heat fluxes from the GC-Net with those from the nearest grid points from the NCAR MM5 climate model output (April 1997 - March 1998).

A negative bias in the magnitude of MM5 fluxes is found in comparison with the one level method (1LM) and two level method (2LM) results by station through one annual cycle. Despite the bias, the explained variance (r^2) is between 30% and 97% (

Table 7.3). Thus, the model captures the month to month variability reasonably well. However, the underestimation of the latent heat flux by the MM5 is as great as 200%. The average bias ranges from -0.1 W m^{-2} to -5 W m^{-2} based on the 1LM comparison and +/- 5 W m^{-2} for the 2LM comparison. A monthly comparison of available data indicate that the bias is greatest in summer when fluxes are largest (Table 7.4). The negative wind speed, temperature, and moisture bias identified in *Cassano et al.*, [in press] would lead to a general underestimation of the latent heat flux. The slope of the linear regression indicates that the MM5 underestimates the 1LM latent heat flux on average by 80% in June, July, and August. In winter, the MM5 yields about 30%

more deposition than the 1LM but still about 40% less than the 2LM results. Comparison of the model turbulent flux parameterizations with in-situ observations at Halley, Antarctica, verified that the model underestimates the momentum flux [*Cassano et al.*, 2001]. The model agreed within acceptable limits by artificially increasing the surface roughness.

When AWS below 1200 m elevation are excluded from the comparison, the residual error is smaller due to the fact that the three lower elevation AWS, JAR2, JAR1, and Swiss Camp, exhibit a strong elevation gradient of latent heat flux (> 7 W m^{-2} 1000 m^{-1}), yet are nearest the same MM5 grid location. A similar increase in explained variance occurs if both CP1 and CP2 data are omitted because they too are nearest the same MM5 grid location.

Table 7.3, Regression Results for a Comparison of one Annual Cycle of Monthly Latent Heat Fluxes from the Polar NCAR MM5 versus GC-Net data from April 1997-March 1998

Site	Mean Bias (GC-Net - MM5)	% bias	r^2	Number of months
1LM				
Swiss Camp	-0.13	-2	0.38	12
CP1	-2.69	-58	0.78	8
NASA-U	-2.68	-96	0.93	10
Humboldt	-1.52	-90	0.88	12
Tunu-N	-0.92	-162	0.75	12
DYE-2	-4.45	-83	0.74	12
JAR1	-5.05	-41	0.42	12
Saddle	-1.36	-83	0.97	11
NASA-E	-1.96	-145	0.83	11
CP2	-3.45	-71	0.72	10
2LM				
Swiss Camp	-0.92	-11	0.34	12
CP1	1.11	137	0.63	8
NASA-U	-3.15	-96	0.72	10
Humboldt	0.29	-221	0.83	12
Tunu-N	1.95	-59	0.63	6
DYE-2	-3.96	-94	0.75	11
JAR1	-4.66	-39	0.47	12
Saddle	4.59	-106	0.74	11
NASA-E	0.03	-5	0.61	11
CP2	5.42	-135	0.6	10

Table 7.4, Regression Results for Comparison of Monthly MM5 Polar Version Latent Heat Fluxes versus GC-Net data from April 1997-March 1998

	1LM				2LM			
Month	Std. of Residuals [W m^{-2}]	r^2	Regression Slope	Count	Std. of Residuals [W m^{-2}]	r^2	Regression Slope	count
Jan	0.37	0.51	0.90	11	4.54	0.51	0.43	11
Feb	0.19	0.44	1.32	11	1.05	0.51	0.44	11
Mar	0.01	0.81	0.99	11	1.31	0.62	0.40	11
Apr	0.89	0.90	0.68	6	2.60	0.03	0.12	4
May	2.84	0.83	0.63	8	4.78	0.70	0.51	6
Jun	6.96	0.61	0.21	11	19.23	0.21	0.05	10
Jul	2.31	0.11	0.28	11	6.59	0.10	0.11	10
Aug	2.40	0.55	0.28	12	5.75	0.43	0.12	11
Sep	1.08	0.74	0.73	13	4.02	0.28	0.32	12
Oct	0.63	0.62	1.36	12	2.32	0.37	0.45	12
Nov	1.60	0.90	1.33	11	2.31	0.75	0.72	11
Dec	0.39	0.82	1.08	10	3.03	0.82	0.64	10

7.4 Conclusions

A number of conclusions may be made based on the comparisons of the GC-Net derived latent heat flux with simulated values from the MM5 regional climate model.

- Net surface water vapor loss decreases as elevation and latitude increase in the MM5, consistent with GC-Net derived values. This result is not surprising because elevation and latitude are major controls of temperature, a dominant parameter in the surface water vapor flux potential.
- The MM5 model underestimates the amplitude of the annual cycle in latent heat fluxes as compared to the fluxes derived for GC-Net sites. Largest biases are found in summer when latent heat fluxes are largest. In winter, the MM5 gives some deposition, about 30% more than the one level method but still about 40% less than the preferred two level method results. The negative bias is attributable to the negative wind speed, temperature, and moisture bias identified in *Cassano et al.* [in press] and to negative bias in the surface momentum flux [*Cassano et al.,* 2001].
- The steep elevation gradients of surface water vapor flux near the ice sheet margin are not resolved at 40 km model grid resolution. This problem is illustrated by the fact that the three ablation zone AWS: JAR2, JAR1, and Swiss Camp, all lie nearest to the same model grid location, while there is a 600 m elevation difference between the lowest and highest GC-Net location (JAR 2 to Swiss Camp). Along this elevation transect, a large gradient in the latent heat flux is evident, -7 W m^{-2} per 1000 m elevation increase.
- A 'climatology' of available monthly mean GC-Net net surface water vapor flux values does not compare as well with the model values as values from specific years. This lends confidence to the skill in capturing year-specific surface water vapor flux variability by both model and GC-Net measurements.
- At high elevation sites, particularly in winter months, net deposition is simulated by the MM5 model, consistent with GC-Net derived values. However, the MM5 tends to underestimate deposition. A similar result was obtained for a comparison of the ECHAM-3 over Antarctica [*Van-den-Broeke,* 1997].
- A fixed surface albedo is used in the model. A dynamic albedo that is reduced after temperature reaches melting would be a great improvement for the model. The effect of surface melting on albedo reduction would lead to greater surface air temperatures and an increased latent heat fluxes.
- The distance from AWS to model grid points is variable and will introduce some variance in the

comparison, even reducing the explained variance between the model results and GC-Net derived values. Thus, the model grid data should be interpolated to GC-Net coordinates by using the values from surrounding grid points.

- Based on this comparison, it seems that the MM5 model would provide the capability of accurately simulating the surface water vapor flux of the Greenland ice sheet if the known model negative biases in temperature, wind speed, moisture, radiation balance [*Cassano et al.*, in press], and the surface momentum exchange [*Cassano et al.*, 2001] can be corrected.

8 Mapping Surface Water Vapor Flux

Monthly and annual maps of net surface water vapor flux at the surface of the Greenland ice sheet are presented in this section. Maps are created by interpolating the observed spatial distribution of surface water vapor flux. Interpolation is achieved using trend-surface regression of monthly latent heat flux averages in terms of temperature, elevation, and latitude. Both linear and non-linear regressions are investigated. A digital elevation model of the ice sheet is then used to provide inputs for the resultant regression equations. Besides using elevation and latitude alone, a second, more physically-based method is used to produce net surface water vapor flux maps in terms of the latitude-adjusted slope lapse rate in temperature. Monthly temperature maps for the Greenland ice sheet are produced as a by-product. Based on the spatial distribution of surface water vapor flux on the equal area grid, monthly, seasonal, and annual water vapor transfer is derived for the Greenland ice sheet for both one level and two level aerodynamic profile method results. Greenland temperature distribution data obtained from earlier expeditions are used to create temperature maps for the 1950 to 1960 decade. The correlation of the latent heat flux with temperature is then used to produce water vapor flux maps representative of this earlier period. Hence, a suggestion of the change in net total and regional water vapor flux is derived, with implications for the mass balance of the ice sheet.

8.1 Digital Elevation Model as Input for Mapping

A grid based on the Danish mapping center Kort & Matrikelstyrelsen (KMS) digital elevation model (DEM) [*Ekholm*, 1996; *Bamber et al.*, submitted] is used for surface water vapor flux mapping. The DEM horizontal resolution is 1 km and the vertical accuracy is 1 m on relatively flat slopes and decreases to about 10 m on the relatively steep slopes found in the lower elevations. The DEM was obtained in latitude-longitude coordinates. The number of data points increased with latitude. To derive the net surface water vapor flux with respect to a finite area, the latitude-longitude grid was interpolated to a 13.7 km x 13.7 km equal area grid. Using a land mask available from KMS, mapping the surface water vapor flux can be performed as a simple function of elevation and latitude given by the DEM.

8.2 Two Component Trend Surface Sublimation Mapping

The observed elevation *(E)* and latitude *(L)* gradients of annual net surface water vapor flux are derived by linear regression (Table 8.1, Table 8.2). The regression coefficients are employed to map the net surface water vapor flux using the DEM. Surface water vapor flux mapping is pursued in an effort to quantify the total and regional net water vapor mass transfer at the Greenland ice sheet surface. This is achieved by effectively interpolating the surface water vapor flux between GC-Net sites and extrapolating to lower elevations where GC-Net observations are unavailable. Resultant surface water vapor flux *(DM)* functions are expressed as:

$$\Delta M_{i,j} = b_E E_{i,j} + E_0 + b_L L_{i,j} + L_0 \qquad \text{Eq. 8.1}$$

where b_E is the elevation gradient of net surface water vapor flux, $E_{i,j}$ is the elevation (m) at the grid point *i*, *j*, E_0 is the abscissa intercept of the elevation gradient, b_L is the latitude gradient of net surface water vapor flux, $L_{i,j}$ is the latitude at rectangular grid point *i*, *j*, and L_o is the abscissa intercept of the latitude gradient. Similar to temperature trend surface regression in section 4.2.1, subtracting the latitude component from the elevation regression results in an increase in the explained variance (r^2) of the regression in terms of elevation.

Table 8.1, Latitude and Elevation Surface Water Vapor Flux Gradients from One-level Profile Method Results

Month	Latitude Gradient b_L [mm deg.$^{-1}$]	Intercept L_0 [mm]	r^2	Elevation Gradient b_E [mm km^{-1}]	Intercept E_0 [mm]	r^2	Count	1 σ of Residuals [mm]
Jan	0.170	-13.30	0.09	2.364	-4.84	0.56	15	1.5
Feb	0.150	-11.62	0.09	2.152	-4.41	0.58	15	1.3
Mar	0.097	-8.06	0.06	2.512	-5.08	0.83	15	0.8
Apr	0.510	-40.72	0.17	6.154	-12.91	0.73	16	2.7
May	0.387	-33.54	0.19	4.516	-9.48	0.78	16	1.7
Jun	0.625	-56.43	0.12	10.276	-21.56	0.89	16	2.6
Jul	0.478	-44.55	0.13	7.683	-16.12	0.91	16	1.7
Aug	0.359	-31.99	0.14	5.356	-11.24	0.89	16	1.4
Sep	0.447	-36.61	0.13	6.774	-14.21	0.82	16	2.3
Oct	0.175	-14.19	0.06	3.868	-8.12	0.69	16	1.9
Nov	0.141	-11.47	0.05	3.314	-6.95	0.71	16	1.5
Dec	0.152	-12.22	0.05	3.539	-7.42	0.69	16	1.7

Table 8.2, Latitude and Elevation Surface Water Vapor Flux Gradients from 2-Level Profile Method Results

Month	Latitude Gradient b_L [mm deg.$^{-1}$]	Intercept L_0 [mm]	r^2	Elevation Gradient b_E [mm km^{-1}]	Intercept E_0 [mm]	r^2	Count	1 σ of Residuals [mm]
Jan	0.072	-4.94	0.01	3.067	-6.28	0.35	15	3.0
Feb	0.139	-9.87	0.12	1.165	-2.39	0.28	15	1.3
Mar	0.108	-8.72	0.05	1.392	-2.73	0.20	14	1.8
Apr	0.525	-40.80	0.14	2.278	-4.47	0.07	14	5.5
May	0.745	-59.24	0.13	0.651	-1.37	0.00	15	9.1
Jun	0.767	-64.00	0.12	8.083	-16.96	0.35	16	7.9
Jul	0.426	-36.26	0.07	4.200	-8.81	0.16	16	6.8
Aug	0.810	-62.94	0.26	2.792	-5.86	0.10	16	6.1
Sep	0.605	-45.78	0.18	3.315	-6.96	0.16	16	5.5
Oct	0.415	-30.26	0.26	1.442	-3.03	0.10	16	3.1
Nov	0.342	-25.25	0.08	2.567	-5.26	0.15	15	4.4
Dec	0.406	-29.63	0.15	2.532	-5.19	0.19	15	3.7

The standard deviation of the residual differences of the observations to the trend surface regression model ranged from 0.8 mm per month to 2.7 mm per month for the one level method and from 3.0 mm per month to 9 mm per month for the two level method. Two times these residual values represents 95% of the range in residuals. Regression results indicate a weak fit to the preferred two level method data. The residual uncertainty is on average nearly 50%. Combining the uncertainty of hourly two level method calculations averaged over one month plus the uncertainty due to trend surface residuals leads to an uncertainty estimate of 60% for the two level method mapping results. Despite the better explained variance for the 1LM results, the linear model overshoots the surface water vapor flux, resulting in lower than expected sublimation at high elevations. Small amounts of net deposition is observed in the 1LM data for winter months. However,

summertime sublimation dominates the net annual surface water vapor flux. A non-linear model was investigated to fit the 1LM data more accurately at high elevations. Making a regression with *ln(E)* instead of *E*, takes into account the non-linear variation of surface water vapor flux with elevation better than *E* alone for high elevations. However, this fit overestimates surface water vapor loss at low elevations (*Figure 8.1*). Nevertheless, the 1LM regression results do not indicate a large deposition rate at high elevations.

Using the regression coefficients as is, the DEM grid is input to yield monthly grids. The grid makes possible estimates for the ice sheet total net surface water vapor flux. Monthly, seasonal, and annual totals are made. The results are converted into mass transfers in kg (Table 8.3). Extreme positive and negative surface water vapor flux grid values based on the grid are also quoted.

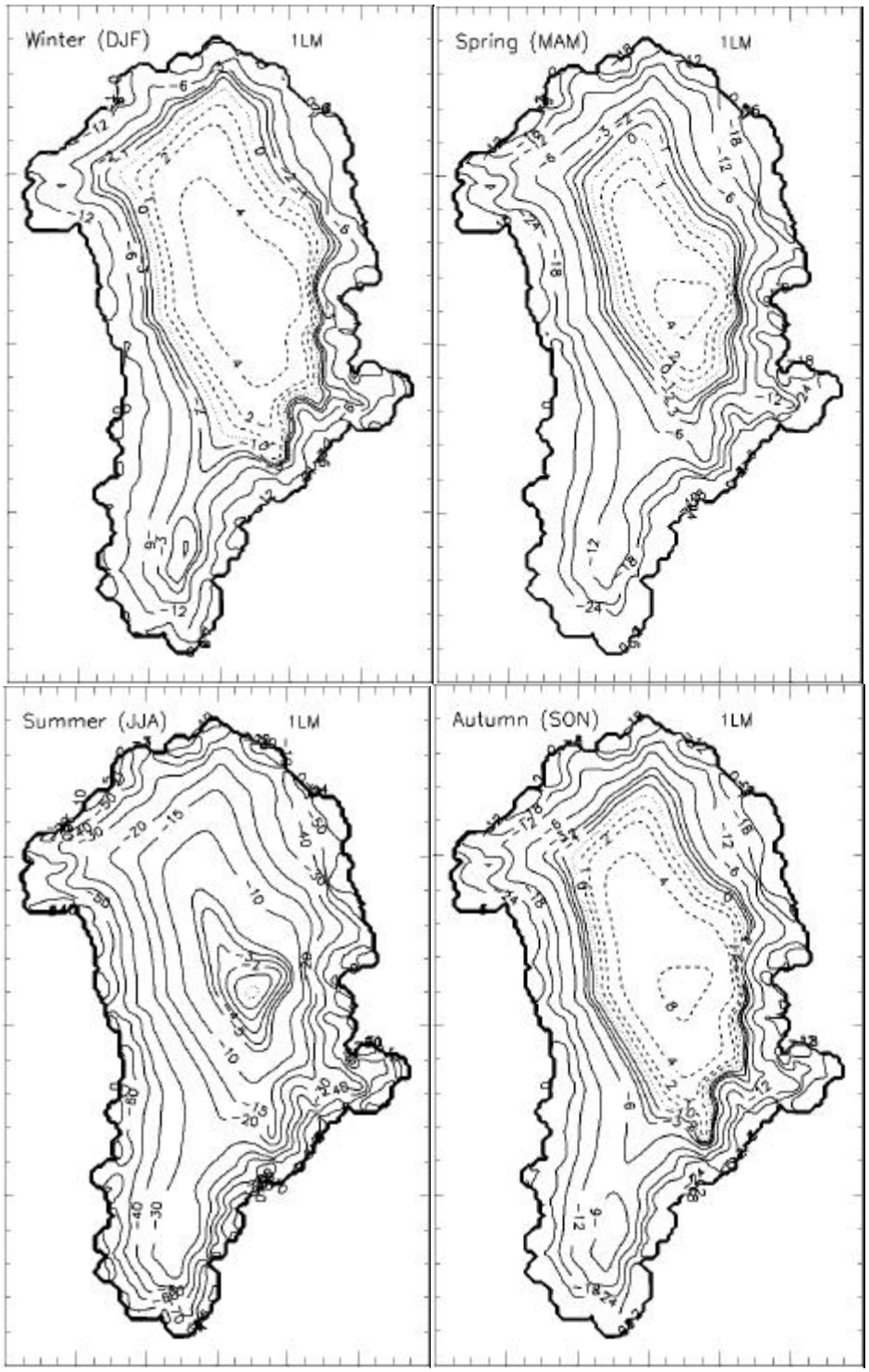

Figure 8.1, Seasonal surface water vapor flux maps based on elevation and latitude trend surface fits of monthly 1LM results. Values are in mm water equivalence. Areas of deposition are represented by dashed lines.

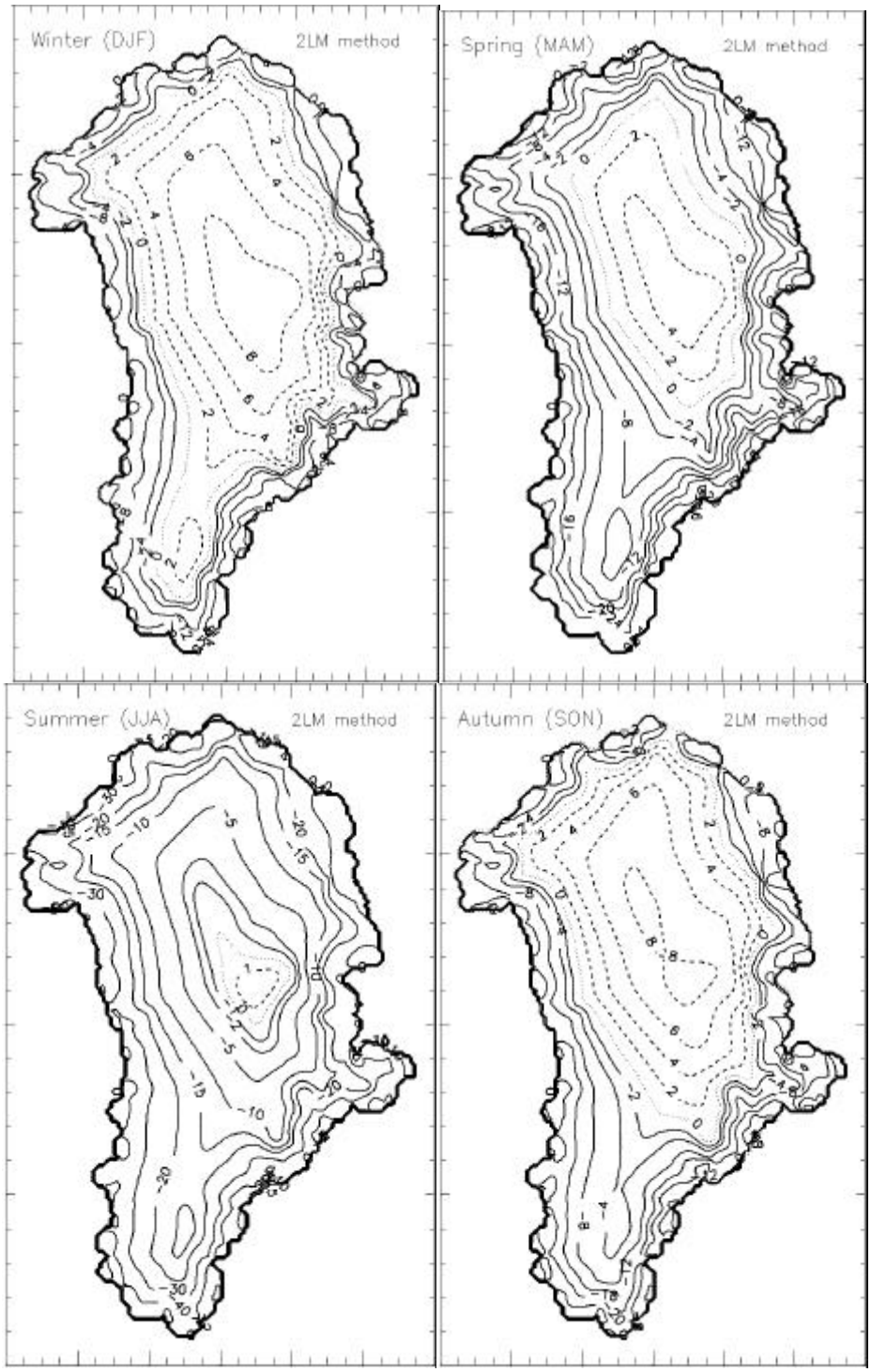

Figure 8.2, Seasonal surface water vapor flux maps based on elevation and latitude trend surface fits of monthly 2LM results. Values are in mm water equivalence. Areas of deposition are represented by dashed lines.

Seasonal and annual net surface water vapor fluxes are featured based on the regression models applied to the ice sheet elevation grid (*Table 8.3*). Values quoted as some number times 10^{12} kg y^{-1} are equivalent with Giga tons (Gt). The spatial pattern of surface water vapor flux is similar between one and two level method results, despite the poor explained variance of the two level method regression results. The pattern is very similar for winter and summer. Net surface water vapor flux values for sites below 500 m, 3% of the ice sheet area are extrapolated values. This uncertain region represents between 10% and 15% of the total surface water

vapor flux.

Table 8.3, Seasonal and Annual Total Greenland Ice Sheet Water Vapor Mass Transfer Based on One Level Method and Two Level Method and Trend Surface Fits

Time Period	Profile Method	Net Total Mass Transfer $\sum \Delta M$ [x 10^{12} kg y^{-1}]	Grid Maximum $\Delta M < 0$ [mm]	Grid Maximum $\Delta M > 0$ [mm]
Winter (DJF)	1LM	-8.5±4.3	-20.8	6.6
Spring (MAM)	1LM	-26.1±13.1	-43.5	5.2
Summer (JJA)	1LM	-65.7±32.9	-84.6	0.5
Autumn (SON)	1LM	-19.4±9.7	-39.5	9.4
Winter (DJF)	2LM	-0.7±0.4	-16.8	9.7
Spring (MAM)	2LM	-17.2±10.3	-33.7	5.6
Summer (JJA)	2LM	-38.3±23.0	-53.1	1.8
Autumn (SON)	2LM	-5.7±3.4	-25.8	8.6
Annual	1LM	-119.7±59.9	-188.4	21.8
Annual	2LM	-61.9±37.1	-128.4	25.6

8.3 Three Component Trend Surface Sublimation Mapping

Because temperature is an important control on potential evaporation [*Brutsaert*, 1982], the latent heat flux is compared with temperature measurements in an effort to map the net surface water vapor flux using observed slope lapse rates in temperature. The 1LM results (Table 8.4) correlate better with temperature than the 2LM results (Table 8.5). Residual differences of the observations to the slope lapse-rate-based trend surface fit ranged from 2 mm per month to 8 mm per month for the one level profile method and from 3 mm per month to 10 mm per month for the one level profile method.

Table 8.4, Surface Water Vapor Flux versus Temperature for the One-level Profile Method Results

Month	Gradient [mm K^{-1}]	Intercept [K]	R^2	N	1 σ Residuals [mm]
Jan	-0.259	61.96	0.63	15	2.4
Feb	-0.237	55.93	0.59	15	2.1
Mar	-0.160	37.73	0.40	15	1.9
Apr	-0.715	176.47	0.80	16	5.7
May	-0.699	174.30	0.81	16	4.1
Jun	-1.729	445.95	0.94	16	8.4
Jul	-1.378	357.64	0.92	16	6.2
Aug	-0.772	198.26	0.85	16	4.4
Sep	-0.799	200.54	0.82	16	5.8
Oct	-0.331	81.08	0.56	16	3.4
Nov	-0.314	76.15	0.60	16	2.9
Dec	-0.351	84.81	0.68	16	3.1

Table 8.5, Surface Water Vapor Flux versus Temperature for the Two-level Profile Method Results

Month	Gradient [mm K^{-1}]	Intercept [K]	r^2	N	1 σ Residuals [mm]
Jan	-0.247	60.37	0.23	15	3.7
Feb	-0.127	30.46	0.27	15	1.7
Mar	-0.156	36.70	0.29	14	2.1
Apr	-0.346	84.35	0.18	14	6.1
May	-0.452	110.47	0.16	15	9.8
Jun	-1.419	366.36	0.41	16	10.4
Jul	-0.864	224.99	0.23	16	7.7
Aug	-0.722	186.04	0.26	16	7.4
Sep	-0.570	143.93	0.32	16	6.6
Oct	-0.255	63.05	0.28	16	3.8
Nov	-0.356	87.04	0.27	15	5.0
Dec	-0.339	82.67	0.33	15	4.5

Given the observed latitude-adjusted slope lapse rate in temperature and the correlation of surface water vapor flux with temperature (Table 8.6), the water vapor flux may be mapped using temperature maps. The ability of the regression to reproduce the spatial temperature distribution is indicated by the standard deviation of the residual difference between the monthly temperatures and the regression best fit. Residuals are between 1.7° and 2.5°. Examples of the temperature maps produced by this method are shown in Figure 8.3.

Table 8.6, Monthly Latitude and Elevation Gradients of Temperature (Same as Table 4.2 but with intercepts and residuals)

Month	Latitude Gradient [K deg.$^{-1}$]	Latitude Intercept	r^2	Elevation Gradient [K km^{-1}]	Elevation Intercept	r^2	N Obs.	1 σ Residuals [C]
Jan	-1.00	42.1	0.36	-8.53	17.4	0.83	34	2.5
Feb	-0.86	27.3	0.32	-7.04	14.3	0.81	31	2.3
Mar	-1.23	54.5	0.55	-6.91	14.7	0.86	39	1.9
Apr	-1.20	64.2	0.50	-6.84	14.5	0.72	39	2.9
May	-0.71	34.5	0.33	-6.26	13.5	0.79	35	2.2
Jun	-0.42	21.2	0.15	-5.88	12.4	0.81	50	1.9
Jul	-0.41	22.5	0.17	-5.61	11.9	0.90	55	1.3
Aug	-0.71	41.9	0.36	-5.62	12.1	0.84	49	1.7
Sep	-0.92	48.3	0.39	-7.22	15.7	0.88	44	1.7
Oct	-1.24	65.2	0.47	-7.92	17.1	0.82	43	2.5
Nov	-1.06	48.3	0.41	-8.11	16.9	0.89	37	1.9
Dec	-0.98	42.2	0.33	-8.37	17.3	0.85	34	2.4

Using the observed correlation of monthly surface water vapor flux with temperature given in Table 8.4 and the observed surface lapse rate in monthly mean temperature, surface water vapor flux maps are produced for both one level and two level method results (Figure 8.4 and Figure 8.5, respectively).

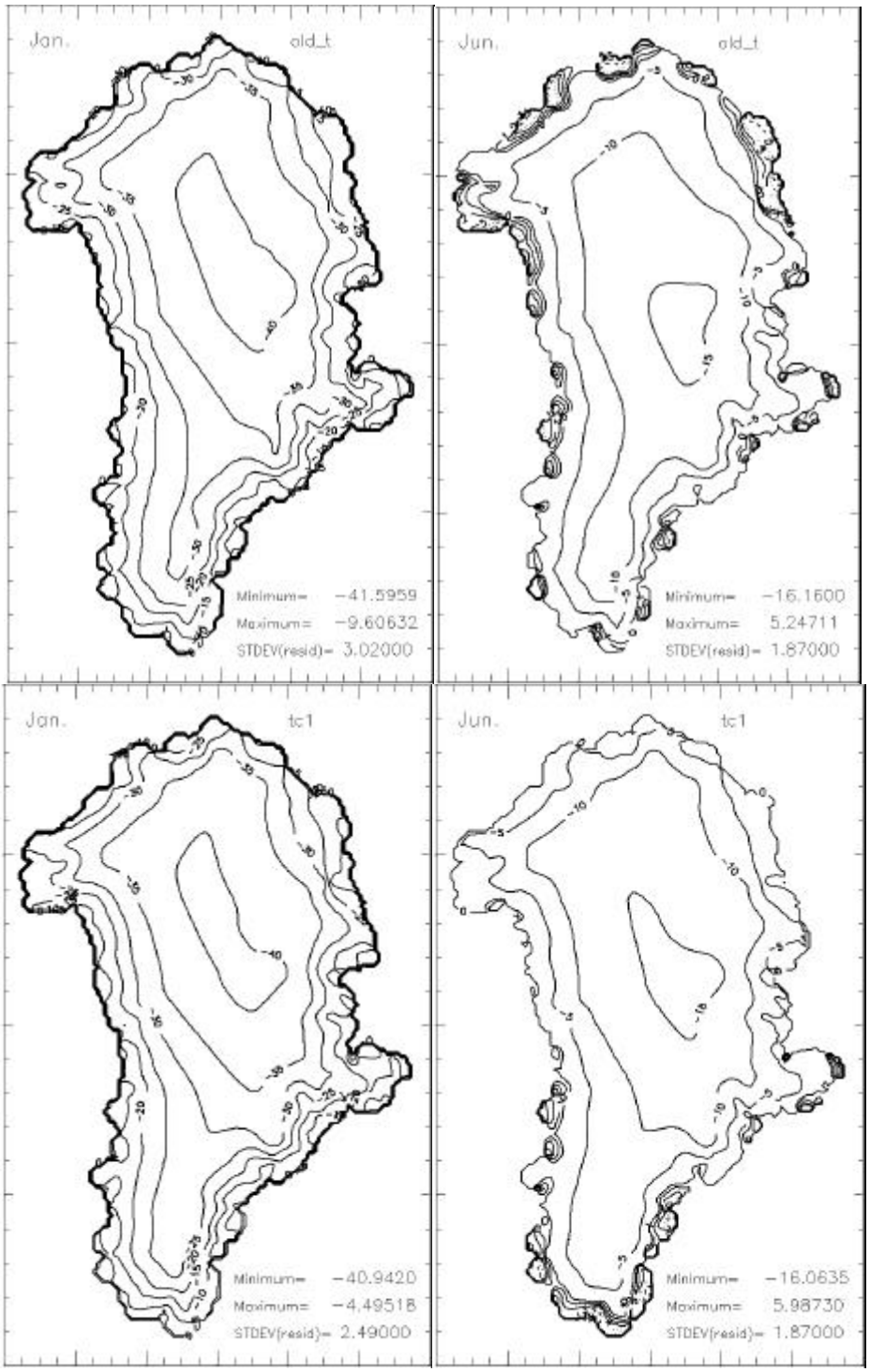

Figure 8.3,(Top row) Monthly mean temperature distribution maps based on values tabulated in Ohmura [1987] for 1950 - 1960. (Bottom row) Monthly mean temperature distribution maps based on GC-Net monthly temperatures for mid 1995 to mid 2000.

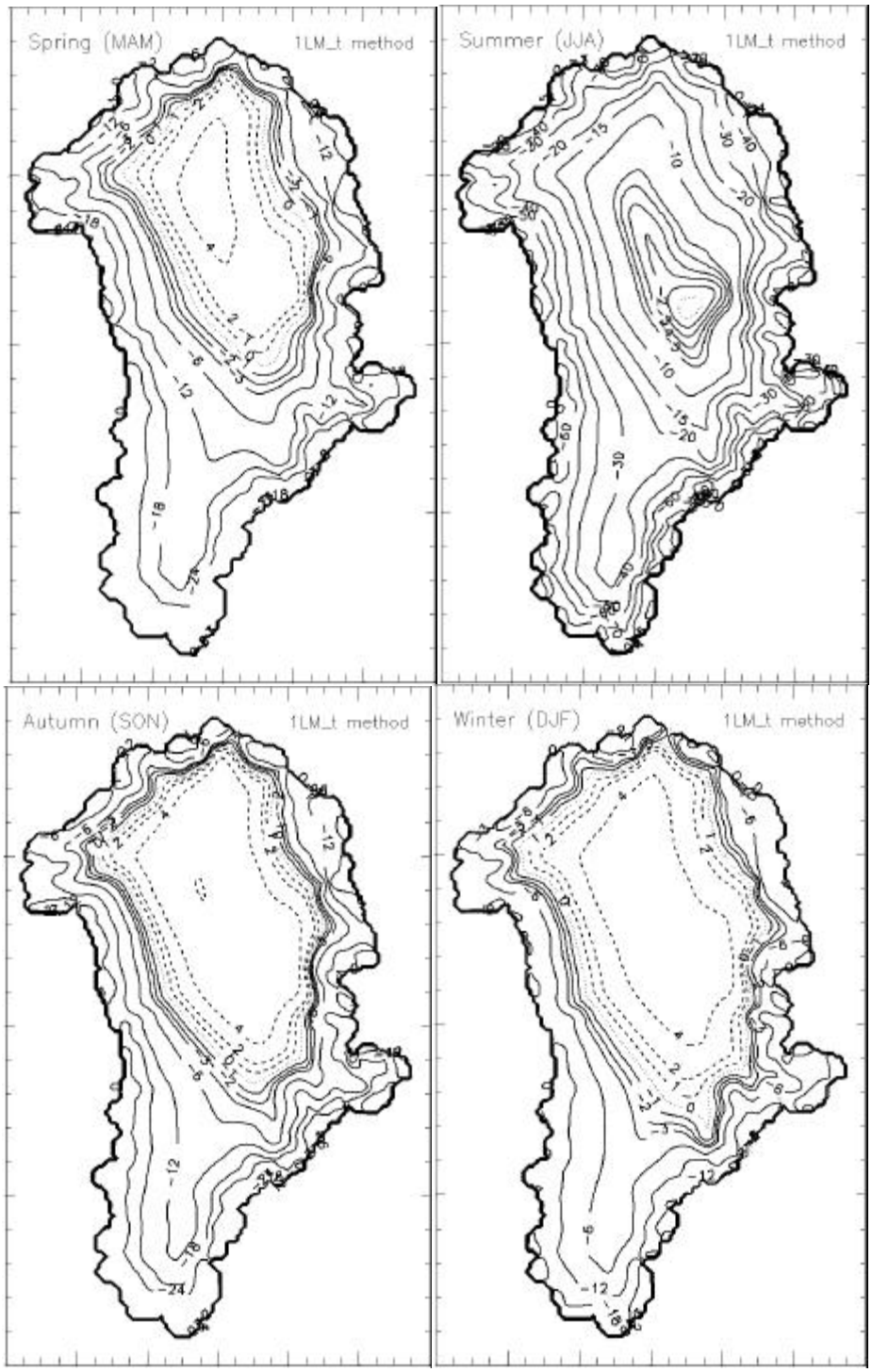

Figure 8.4, Seasonal surface water vapor flux maps based on monthly latitude-adjusted temperature lapse rate with elevation trend surface fits of monthly 1LM results. Values are in mm water equivalence. Areas of deposition are represented by dashed lines.

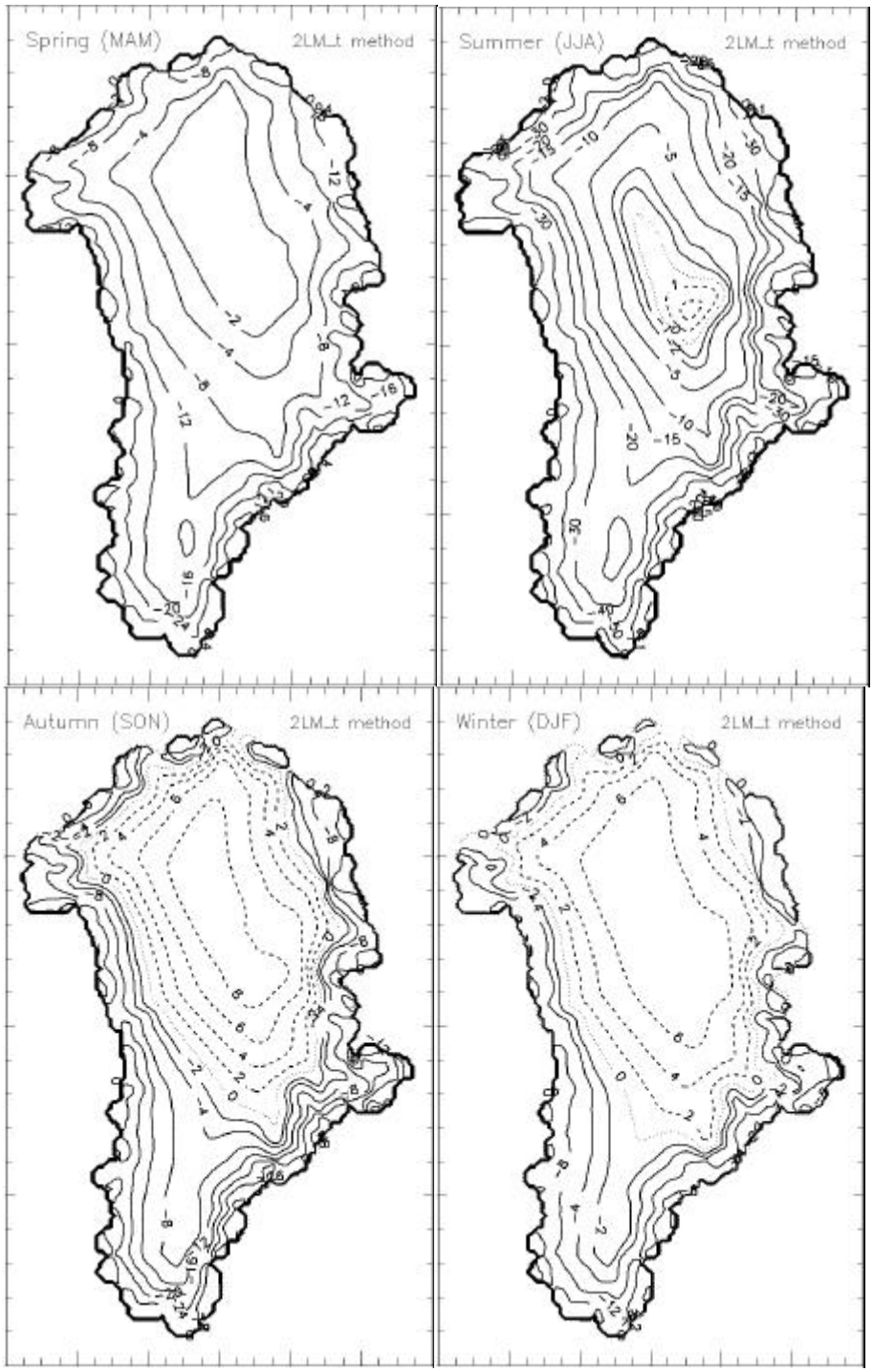

Figure 8.5, Seasonal surface water vapor flux maps based on monthly latitude-adjusted temperature lapse rate with elevation trend surface fits of monthly 2LM results. Values are in mm water equivalence. Areas of deposition are represented by dashed lines.

The seasonal and annual total water vapor flux is given now for the 3-component trend surface fit (*Table* 8.7). Using the correlation of surface water vapor flux with temperature and temperature distribution grids based on data tabulated in *Ohmura*, [1987], net water vapor flux grids for the 1950-1960 decade were produced. Assuming a good correspondence between the temperature measurements made as part of multiple Greenland scientific expeditions, the annual water vapor loss has decreased by 8.7% for the 2LM correspondence or by 39% according to the 1LM results. The decrease in water vapor loss from 1950 to 1960 as compared with mid

1995 to mid 2000 is associated with an observed increase of the area of water vapor deposition in the recent record. This increase in deposition is implied by an annual warming from 1950-1960 to mid 1995 to mid 2000.

Table 8.7, Seasonal And Annual Total Greenland Ice Sheet Water Vapor Mass Transfer Based on 1LM and 2LM and Temperature Lapse Rate Relationship

Time Period	Profile Method	Net Total Mass Transfer $\sum \Delta M$ [x 10^{12} kg y^{-1}]	Grid Maximum $\Delta M < 0$ [mm]	Grid Maximum $\Delta M > 0$ [mm]
Winter (DJF)	1LM	-6.9±3.5	-23	6.1
Spring (MAM)	1LM	-22.1±11.05	-44.5	5.0
Summer (JJA)	1LM	-63.3±31.7	-85.1	0.5
Autumn (SON)	1LM	-16.0±8.0	-41.6	8.0
Winter (DJF)	2LM	-0.4±2	-17.1	7.8
Spring (MAM)	2LM	-20.3±10.2	-30.1	0
Summer (JJA)	2LM	-45.0±7.0	-64.5	2.3
Autumn (SON)	2LM	-7.6±3.8	-31.7	9.2
Annual	1LM	-108.2±54.1	-194.2	18.1
Annual	2LM	-73.4±44.0	-143.3	18.0
Based on *Ohmura*, [1987]				
Annual	1LM	-178.0±106.8	169.0	15.6
Annual	2LM	-80.4±48.2	124.3	16.4

The annual net surface water vapor flux maps using the temperature lapse rate trend surfaces are constructed. Values of surface water vapor flux over the southern half of the ice sheet are about 50% greater in the one level method map (Figure 8.6). Otherwise, there is general agreement at high elevations. The regions of deposition at high elevations are similar despite the divergence of the two method-types at high elevations. The one level-derived maps give greater surface water vapor loss at lower elevations. As a result of these differences, primarily those at low elevations, the annual water vapor loss for the one level method maps are more than 30% greater than for the two level method results. Despite the uncertainty of a relatively poor regression fit to the two level method data, these results are consistent with the conclusions drawn about these method types in chapters 5 and 6.

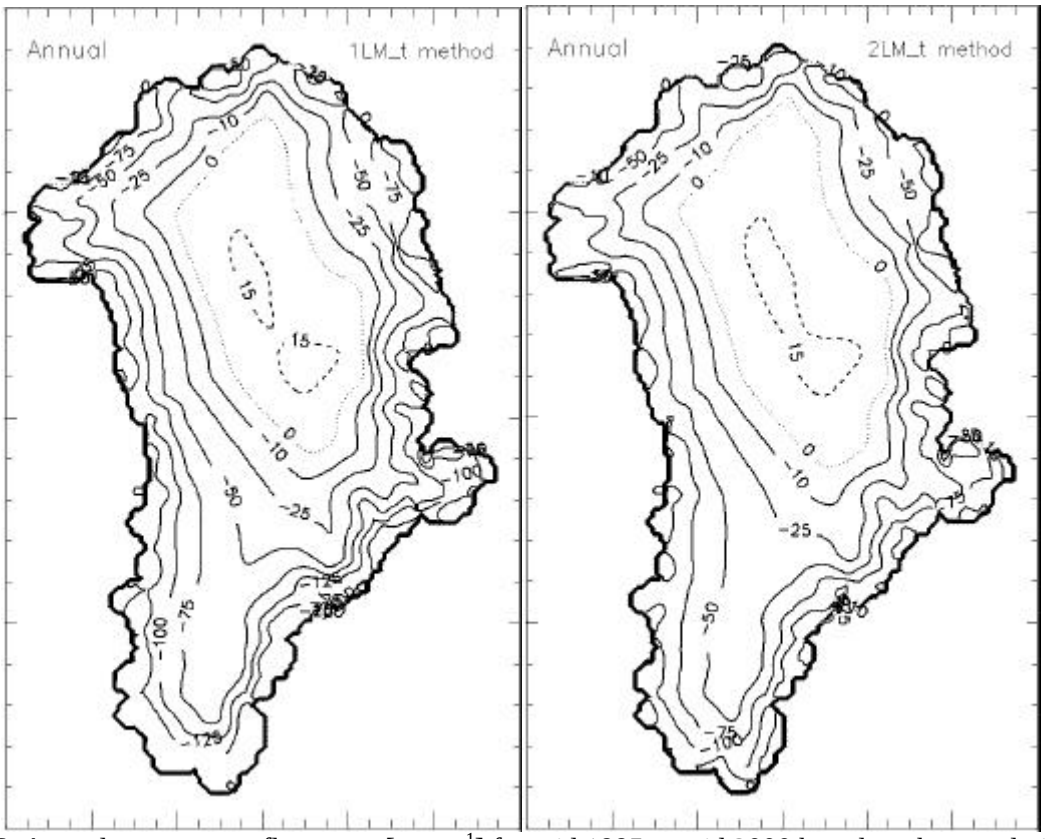

Figure 8.6, Annual water vapor flux maps [mm y^{-1}] for mid 1995 to mid 2000 based on the correlation of the vertical water vapor mass-flux with temperature, elevation, and latitude for 1LM results (left) and 2LM results (right). Areas of deposition are inside dashed lines.

Annual water vapor flux maps for the 1950-1960 period are constructed using the correlation of the water vapor flux with temperature. Temperature data from this period are taken from the tabulated values in *Ohmura*, [1987] adjusted to this specific decade. According to the two level method results fit with temperature, the 1950-1960 maps (*Figure 8.8*) imply that the water vapor flux loss has decreased by 8.7% as compared to recent period. The one level methods imply that the water vapor flux has increased by 60% over this time interval. The divergence is related to the fact that the two level method has a negative correlation with temperature anomalies. The one level method results are a direct function of temperature (Table 8.4) combined with the observation of a general warming, up to 6° C warming of over the southern half of the ice sheet, over this time interval.

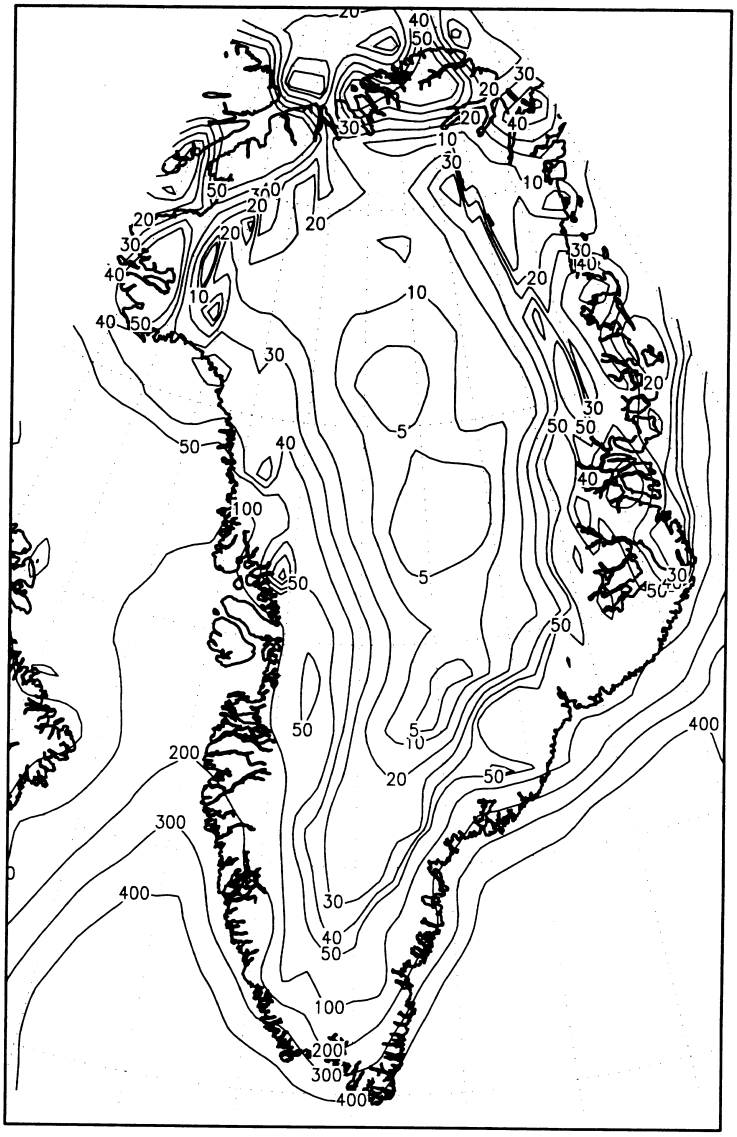

Figure 8.7, Annual evaporation from the ECMWF model re-Analysis (below 1500 m elevation) and the ECHAM3 atmospheric model (above 1500 m) from Ohmura et al. [1999]. Values are in mm water equivalence.

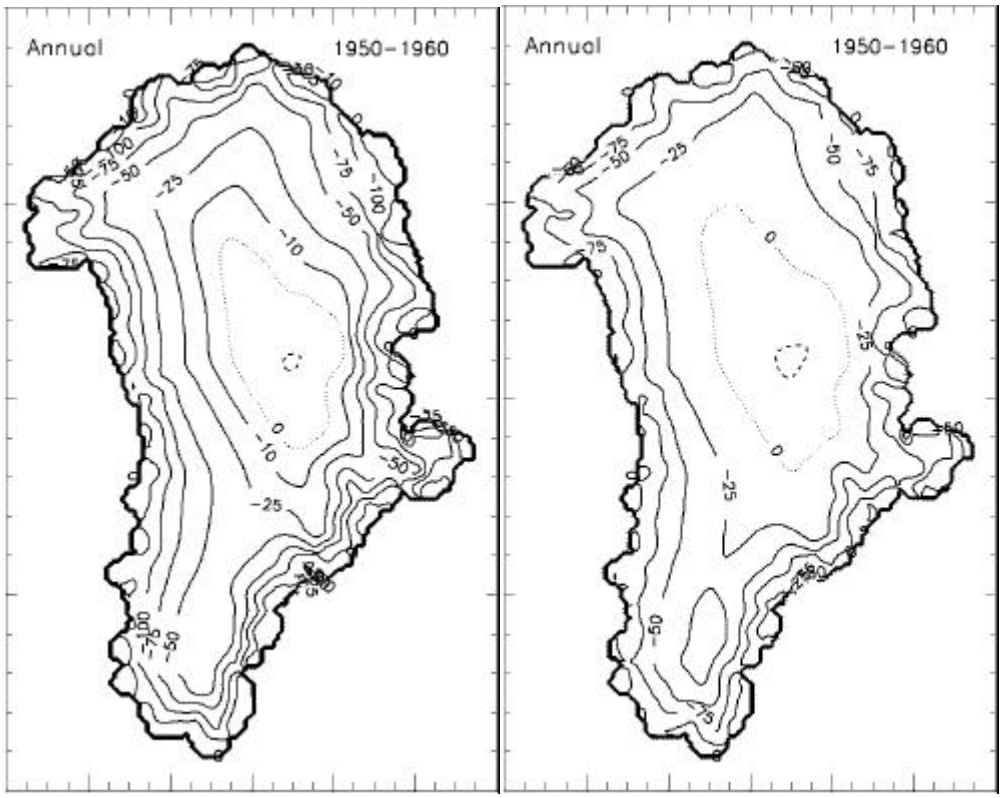

Figure 8.8, Annual water vapor flux maps for the 1950-1960 period based on the correlation of water vapor flux with temperature, elevation, and latitude from 1LM results (left) and 2LM results (right). Values are in mm water equivalence.

8.4 Results and Discussion

The most realistic estimate of the annual total net water vapor flux for the Greenland ice sheet is that based on the two level aerodynamic profile method results as a function of the slope lapse rate in temperature (–7.34±4.4 x 10^{13} kg y^{-1}). The residual uncertainty is however lower for the simpler trend surface to the two level profile method results not including the slope lapse rate in temperature (–6.19±3.1 x 10^{13} kg y^{-1}). The totals for one level methods indicate a greater loss of water vapor for the ice sheet, –1.08±0.5 x 10^{14} kg y^{-1} for the three component trend surface fit and –1.20±0.7 x 10^{14} kg y^{-1} for the two component fit. These total ice sheet surface water vapor flux estimates are similar to the result of –6.18 x 10^{13} kg y^{-1} in *Ohmura et al.* [1999] based on atmospheric modeling. Given an ice sheet total accumulation estimate of 5.90 x 10^{14} kg y^{-1} [*Ohmura et al.,* 1999], the precipitation loss is estimated to be 14% based on the most realistic estimate. Based on the residuals in surface water vapor flux and estimates for the hourly uncertainty of the two profile method-types, uncertainties for the total water vapor flux for the Greenland ice sheet are roughly 60% based on two level method data and 50% based on one level method data. The net surface water vapor flux for Greenland in this study, according to the two level method, is almost identical with the result from *Ohmura et al.,* [1999]. However, the spatial distribution of surface water vapor flux in the two maps is quite different. Greater water vapor losses are found below 1000 m in the two level maps as compared to the *Ohmura et al.,* [1999] map.

Given estimates for the total mass exchange with the ice sheet by precipitation (+5.90 x 10^{14} kg y^{-1}) [*Ohmura et al.,* 1999], melt runoff (-2.44 x 10^{14} kg y^{-1}) [*Ohmura et al.,* 1999], direct runoff of rainfall (-0.13 x 10^{14} kg y^{-1}) [*Ohmura et al.,* 1999], iceberg discharge (-3.16 x 10^{14} kg y^{-1}) [*Reeh,* 1994], and net surface water vapor flux (-0.73 x 10^{14} kg y^{-1}), the mass balance of the Greenland ice sheet is -0.56 x 10^{14} kg y^{-1}. This negative balance may be expressed as a 9% y^{-1} decrease of the precipitation input. A modeling study by [*Huybrechts,* 1994] concludes that the Greenland ice sheet is at present in a state of slight growth (2%). The uncertainties in these estimates are on the order of the currently observed sea level change [*Reeh,* 1999] and therefore needs to be further constrained to gauge the ice sheet's contribution to global sea level change.

The three-component surface water vapor flux maps produced similar results to the two component maps but with added realism at the extreme elevation limits, despite discouragingly low explained variance values. The one and two level-based total ice sheet water vapor flux estimates converged to within 30%, a difference less than the uncertainty limits of either estimate.

Assuming a good correspondence between the temperature measurements made as part of multiple Greenland scientific expeditions from 1930 to 1980, reduced to a standard decade 1950 to 1960 [*Ohmura,* 1987], the annual surface water vapor flux has decreased by 8.7% for the two level method correspondence or by 39% according to the one level method results. The decrease in net mass loss from 1950 – 1960 to mid 1995 to mid 2000 is associated with an increase of the area of net water vapor flux to the surface in the recent record implied by a warming implied by comparison of the temperature grids. This warming has been noted recently by *Steffen and Box,* [in press].

8.5 Conclusions

The net surface water vapor flux for Greenland in this study, according to the two level method, is nearly equal to that from *Ohmura et al.,* [1999] based on the ECMWF Re-analysis and the ECHAM-3. However, the spatial distribution of surface water vapor flux in the two maps is quite different. Greater surface water vapor flux are found below 1000 m in the two level method map as compared to the *Ohmura et al.* [1999] map. Note that the one level method surface water vapor flux map includes a region of net deposition at the highest elevations of the ice sheet. The linear trend surface fit overshot into negative latent heat fluxes. This is despite the fact that the annual total surface water vapor flux based on monthly mean one level method latent heat fluxes was always positive. The surface water vapor flux based on the temperature lapse rate does not include as large of a region of net deposition in the one level map. Thus, the lapse-rate-based method is more realistic, despite lower explained variation. The two-step process of regression of surface water vapor flux with temperature and then temperature with elevation explains the lower statistical skill of fit. The evaporation map in *Ohmura et al.* [1999] (Figure 8.7) does not exhibit a region of net deposition. This result is consistent with a conclusion of *Van den Broeke,* [1997] that the ECHAM-3 model underestimates deposition for Antarctica, even when compared to the one level method Antarctic one level method results from *Stearns and Weidner,* [1993] which probably also underestimate deposition according to the two level method results in this study (section 5.4). If the NCAR MM5 model data were used to map the surface water vapor flux, there would be a region of slight deposition in the interior of the ice sheet, as this model seems to more realistically parameterize deposition over the ice sheet at high elevations.

Surface water vapor flux values below 500 m may actually be lower than estimated in this study. Greater cloud amount near the ice margin associated with marine cloudiness of the adjacent seas would reduce the evaporation potential at the low elevations. Increasing cloudiness toward lower elevations is observed over Iceland's largest ice cap [*Oerlemans et al.,* 1999]. The same has been observed by the author in western Greenland. The katabatic wind may also become decoupled from the surface at the lowest elevations on the ice sheet as it does in east Antarctica [*Bintanja,* 1998] because the flow cannot follow the rapidly steepening surface near the ice edge. Thus, the surface water vapor loss at lower elevations may be overestimated by this mapping procedure and this in turn the total ice sheet surface water vapor loss may be an overestimate. This potential error will affect 10% to 15% of the bulk estimate over 5% of the ice sheet area below 500 m elevation.

Longitude would have been chosen as an additional factor to include in the mapping methodology were it not for insufficient information concerning the eastern slope temperature and surface water vapor flux lapse rates. The longitude component may be added in the future as more AWS data become available. More AWS data will also make possible a more robust interannual variability analysis. Higher resolution DEMs may make it possible to include undulation-scale effects which have been shown to be significant in chapter 6. Other interpolation methods such as kriging or optimal interpolation may be pursued. However, given the intuitive nature of expressing the trend surface in elevation and latitude, this effort represents a good start.

9 Blowing Snow Sublimation

9.1 Introduction

The importance of processes associated with wind blown snow in the hydrologic cycle of snow-covered areas around the world has long been recognized [*Dyunin,* 1959; *Kobayashi,* 1972; *Tabler,* 1994; *Pomeroy and Gray,* 1995]. However, the significance of surface water vapor flux for the Greenland ice sheet has not received much attention. *Loewe* [1970] concluded that the loss of solid mass of the ice margin was insignificant to the mass balance. This really is the point. Large amounts of blowing snow do not arrive at the ice margin despite last seen heading that direction because of the large losses to evaporation in transit [*Schmidt,* 1972, *Tabler,* 1975]. Thus, this chapter attempts to gauge the blowing snow lost by sublimation for sites on the Greenland ice sheet. Firstly, estimates of annual potential snow transport by the wind are derived using an empirically-derived bulk formula. Subsequently, the sublimation of blowing snow is estimated using a conceptual model that assumes all transported snow evaporates for sites with surface topography in equilibrium with snow drift deposition. Precipitation rates and accumulation are important parameters in this effort to gauge the relative magnitude of blowing snow loss. Blowing snow conversion to water vapor estimated from the conceptual model, when subtracted from the precipitation, also implies the accumulation rate for sites where snow drift is in equilibrium with the surrounding topography. Keeping in mind the large uncertainties in the potential snow transport, model-derived precipitation, and surface height-derived accumulation, the results of this chapter are useful only as a first approximation of the importance of blowing snow sublimation and serve to identify where future work is needed. This model development begins with a definition of relevant terms.

9.2 Snow transport

Snow transport here refers to snow that is moved by the wind by three transport modes, *saltation*, *turbulent diffusion* , and *creep*. The three transport modes combined constitute the total snow transport discussed below in section 9.4.1. Saltation occurs as particles bounce along a snow surface, often dislodging other particles as they impact the surface. Saltating particles follow a parabolic trajectory [*Kobayashi,* 1972], reaching maximum heights that are a function of the wind speed but are virtually always below 10 cm [*Pomeroy and Gray,* 1993]. Turbulent diffusion, hereafter referred to as suspension, is characterized by ice particles being held aloft by upward eddy drag forces imposed on the particle that exceed the gravitational forces which would have the particle return to the surface [*Pomeroy and Gray,* 1995]. The speed of snow particles in suspension at a given height closely approximates the average wind speed [*Schmidt,* 1982b]. Suspension cannot begin until a wind speed threshold for suspension is exceeded and saltation has already begun, because the snow in suspension originates from the saltation layer. Suspended particles are typically smaller than those in saltation. For a constant wind speed above the suspension threshold, relatively large snow particles eroded in saltation may eventually ablate until they become light enough to be held in suspension. The mass concentration of suspended snow reaches a maximum just above the saltation layer and decreases with height at a rate that depends on the wind speed. The maximum concentration of blowing snow transport occurs in the layer within 10 cm of the surface. The relative contribution of saltation and suspension to the total snow transport depends on the wind speed, with suspension dominating the transport during high winds [*Pomeroy and Gray,* 1995]. The vertical concentration of transported snow is therefore generally decreasing exponentially from the surface. Creep is a snow drift transport mode characterized by grains rolling or sliding along the surface. These particles are too large to be ejected into saltation or suspension. Creep may be associated with migrating snow barchan dunes or waves. Dune migration occurs by a process of many thousands of particles being eroded from the windward face of a dune and deposited in the lee. Dune migration rates of 5 m h^{-1} for 10 m winds of 8 m s^{-1} have been observed [*Tabler et al.,* 1990b] in which approximately 45 kg of snow per hour per meter across the wind are implied. Snow creep usually comprises a very small proportion of the total transport. Other terms of significance to this model development are defined below.

9.3 Scientific Background for Sublimation of Blowing Snow

Sublimation from blowing snow can be much greater than from snow at rest [*Thorpe and Mason,* 1966; *Schmidt,* 1972; *Wu,* 1974; *Schmidt,* 1982b; *Gosink,* 1989; *Mann et al.,* 2000]. This is due to the greatly enhanced exposure of snow grains to atmospheric turbulent diffusion. A theory of blowing snow sublimation for individual ice spheres was first published by *Schmidt* [1972]. Factors that determine sublimation rates from ice particles in turbulent suspension are particle size, humidity, air temperature, solar radiation, wind speed, and atmospheric pressure. Ice particles sublimate at an increasing rate as they decrease in size because of the increasing surface area to volume ratio. Development of increasingly sophisticated numerical models followed Schmidt's theoretical framework [*Lee,* 1975; *Pomeroy,* 1988; *Pomeroy and Gray,* 1993; *Schmidt,* 1972; *Déry et al.,* 1998; *Mann,* 1998; *Bintanja,* 2000a]. The models compare reasonably well with direct measurements [*Schmidt,* 1982b; *Pomeroy and Essery,* 1999] but are fraught with uncertainties in boundary conditions such as eddy diffusivity and other environmental factors [*Xiao et al.,* 2000]. Blowing snow sublimation is estimated to return 10-50% of snowfall to the atmosphere in prairie environments [*Pomeroy and Essery,* 1999]. As the occurrence of blowing snow on the Greenland ice sheet is common [*Benson,* 1962], blowing snow is expected to be an important component of sublimation at the surface.

As bulk formulations perform reasonably well in comparison with observations [*Tabler,* 1994] and the development of a numerical model for application to GC-Net data is beyond the scope of this thesis, estimates of blowing snow sublimation at GC-Net sites are derived using a bulk method based on *Budd et al.,* [1966], *Tabler* [1975], and *Tabler* [1991]. It begins with calculation of the amount of potential blowing snow transport above an empirically defined threshold in wind speed in which blowing snow begins. The potential transport is the maximum transport expected for a given wind speed with an unlimited supply of snow. Then, the annual amount of blowing snow sublimation is estimated based on assumptions of snow transport distance, surface conditions, and precipitation. Discussion of the results is given in the context of profile methods (chapter 5).

9.4 Blowing Snow Transport from Bulk Formulae

9.4.1 Bulk Snow Transport by the Wind

Physical blowing snow models provide the necessary insight to develop a simplified method for estimating blowing snow transport [*Tabler,* 1994]. Numerous empirical equations have been proposed to estimate blowing snow transport given wind speed. *Tabler et al.* [1990] provide a review of nine bulk transport equations published from several previous studies. Bulk transport equations often require wind speed at a fixed height. To estimate wind speed at fixed heights when the surface roughness parameter is uncertain, it can be assumed for blowing snow conditions that the wind speed at some height, *z*, is related to that at some other height, *z'*, according to:

$$u_{10} = u_z \left(z'/z\right)^m \qquad \text{Eq. 9.1}$$

where *z* is taken as that of profile level 2 and *m* for aerodynamically smooth surfaces is 1/7 [*Arya,* 1988]. For compatibility with the following blowing snow sublimation conceptual model, a transport equation based on the Antarctic blowing snow data of *Mellor and Radok* [1960] and *Budd et al.* [1966] is selected from *Tabler* [1991].

$$Q_{0\ pot}^{10} = {u_{10}}^{3.93} \big/ 290951 \qquad \text{Eq. 9.2}$$

where $Q_{0\ pot}^{10}$ is the potential blowing snow transport across an orthogonal unit length per unit time (kg m^{-1} s^{-1}) for the vertical range from 0 to 10 m [*Tabler,* 1991], and u_{10} is the ten meter wind speed (m s^{-1}). The determination of the actual snow transport below is based on this potential snow transport calculation.

Snow transport rarely occurs for wind speeds less than about 7 m s^{-1} [*Schmidt,* 1982a]. This fact is incorporated for transport estimates using an empirically defined wind speed threshold (u_T) [*Li and Pomeroy,* 1997]. The function is derived from a large dataset of meteorological station reports of blowing snow

occurrence from human observers and is correlated to air temperature to represent, at least partially, the complex snow availability factors.

$$u_T = 9.43 + 0.18T + 0.0033T^2 \qquad \text{Eq. 9.3}$$

where u_T is the 10 m wind speed entrainment threshold (m s^{-1}) and T is the 2 m air temperature (C). The quadratic nature of the parameterization results in an unrealistic increase in U_T for temperatures below -27° C (Figure 9.1) because of too few data points below -27° C. To alleviate this problem, a constant wind speed threshold of 7 m s^{-1} was used for temperatures below -27° C. Blowing snow was not allowed in this model for air temperatures above 0° C because melting snow cohesion limits snow drift. The use of this u_T estimate may overestimate snow transport because other factors are not taken into account, such as how wind speed thresholds increase after the development of surface crust, after a sunny day or from condensation [*Schmidt*, 1982a]. Thus, u_T may not be very accurate. Modeling u_T to include other snow availability factors will be associated with other large uncertainties. Deriving an estimate for the *actual snow transport* is crucial in gauging sublimation of transported snow. A model for snow availability is introduced in section 9.4.4 to estimate the actual snow transport after the potential snow transport is assessed.

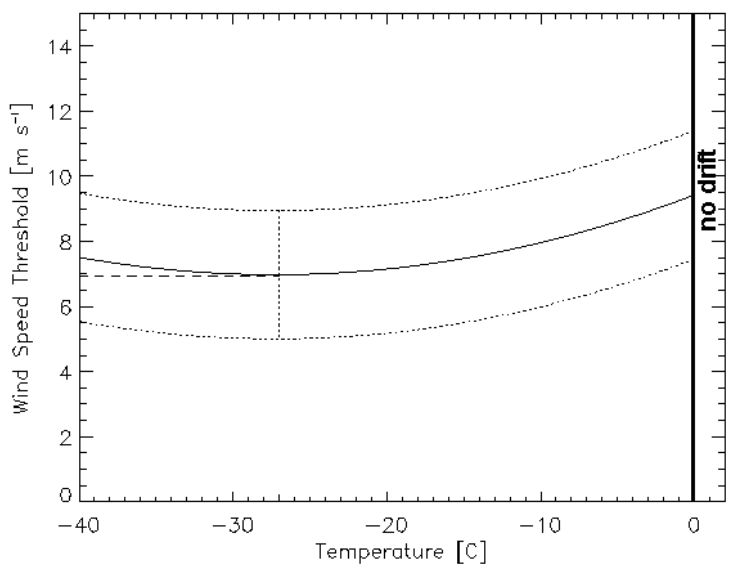

Figure 9.1, Ten meter wind speed threshold for snow drift, ± one standard deviation from observations [Li and Pomeroy, 1997]. The dashed line represents the constant u_T taken for temperature less than -27°C.

Potential snow transport rates based on Eqs. 9.2 and 9.3 are totaled for wind speed and direction intervals. An example of an azimuth-velocity distribution of transport at a GC-Net site (Swiss Camp 1999) is given in Table 9.1.

Table 9.1, Annual Potential Blowing Snow Transport (t m^{-1}) at Swiss Camp in 1999

Azimuth	Range	10 m Wind Speed Class [m s^{-1}]							
True	Deg.	6-9	9-12	12-15	15-18	18-21	21-24	18-21	**Total**
0	10	0.6	6.6	7.8	0.0	0.0	0.0	0.0	**15.0**
10	20	0.4	3.5	2.4	0.0	0.0	0.0	0.0	**6.3**
20	30	0.1	3.1	3.1	0.0	0.0	0.0	0.0	**6.3**
30	40	0.2	1.3	0.2	0.0	0.0	0.0	0.0	**1.8**
40	50	0.2	0.7	0.0	0.0	0.0	0.0	0.0	**0.9**
50	60	0.2	0.1	0.0	0.0	0.0	0.0	0.0	**0.4**
60	70	0.3	0.2	0.0	0.0	0.0	0.0	0.0	**0.5**
70	80	1.1	1.5	0.6	0.0	0.0	0.0	0.0	**3.2**
80	90	6.7	31.7	28.8	11.6	0.0	0.0	0.0	**78.8**
90	100	5.7	30.5	52.6	32.7	5.3	3.1	0.0	**129.9**
100	110	5.8	36.6	52.4	35.2	9.9	2.2	0.0	**142.2**
110	120	6.2	39.9	42.5	52.2	16.1	2.4	0.0	**159.2**
120	130	8.5	28.2	32.3	27.8	19.9	18.0	8.3	**143.0**
130	140	4.9	16.4	19.6	30.1	28.9	3.2	0.0	**103.0**
140	150	2.8	9.6	13.7	4.3	10.2	0.0	0.0	**40.6**
150	160	1.3	5.9	5.0	1.2	7.4	8.3	0.0	**28.9**
160	170	0.8	5.7	5.1	2.5	1.4	0.0	0.0	**15.4**
170	180	0.4	3.1	4.6	0.8	2.7	0.0	0.0	**11.6**
180	190	0.6	4.7	6.3	1.9	0.0	0.0	0.0	**13.6**
190	200	0.6	5.2	2.7	0.5	0.0	0.0	0.0	**9.0**
200	210	0.3	0.8	0.2	0.0	0.0	0.0	0.0	**1.3**
210	220	0.0	0.1	0.0	0.0	0.0	0.0	0.0	**0.1**
220	230	0.1	0.0	0.0	0.0	0.0	0.0	0.0	**0.1**
230	240	0.0	0.0	0.0	0.0	0.0	0.0	0.0	**0.0**
240	250	0.0	0.0	0.0	0.0	0.0	0.0	0.0	**0.0**
250	260	0.0	0.0	0.0	0.0	0.0	0.0	0.0	**0.0**
260	270	0.0	0.0	0.0	0.0	0.0	0.0	0.0	**0.0**
270	280	0.1	0.1	0.0	0.0	0.0	0.0	0.0	**0.1**
280	290	0.0	0.0	0.0	0.0	0.0	0.0	0.0	**0.0**
290	300	0.0	0.0	0.0	0.0	0.0	0.0	0.0	**0.0**
300	310	0.0	0.2	0.0	0.0	0.0	0.0	0.0	**0.2**
310	320	0.3	0.1	0.0	0.0	0.0	0.0	0.0	**0.5**
320	330	0.8	1.7	0.0	0.0	0.0	0.0	0.0	**2.5**
330	340	0.8	4.8	2.2	0.0	0.0	0.0	0.0	**7.8**
340	350	0.5	3.6	2.7	0.0	0.0	0.0	0.0	**0.0**
350	360	1.4	5.7	7.8	1.1	0.0	0.0	0.0	**0.0**
	Total	**51.6**	**251.6**	**292.5**	**202.0**	**101.8**	**37.2**	**8.3**	**945.0**

Largest annual transport at Swiss Camp occurred in the range of wind speeds from 12 m s^{-1} to 15 m s^{-1}. Maximum transport direction coincides with the prevailing katabatic wind direction (110° - 120°). A range from 90° to 140° in wind direction comprises 75% of the transport. In the 1997 snow transport distribution, there is a secondary peak in potential snow transport associated with southerly storms. However, the potential transport in the storm direction (180° - 190°) represents 100 times less than the annual transport in the prevailing 10° wind direction interval. Other sites exhibit the same tendency for transport in the prevailing katabatic wind direction. Based on this and personal observation of the immense drift in the lee of Swiss Camp, DYE-2, and drifts leeward of fuel drums left at Tunu-N and CP1 for 1 year, *Benson's* [1962] claim that larger snow drifts form in alignment with the prevailing storm direction than in the katabatic wind direction is inaccurate. Only 8% of the total potential transport would occur in the prevailing storm direction at Swiss Camp (160° – 220°). Less than 1% of the total snow transport was estimated to occur in the 230° to 70° range in 1997 (totals less than 1000 kg m^{-1} y^{-1}) while in 1999 3% of the transport came from northerly wind directions (310° - 50°).

Largest values for annual potential blowing snow transport are found at South Dome and Swiss Camp. Swiss Camp exhibits larger annual average wind speed than South Dome [*Steffen and Box,* in press]; however, South Dome does not have a melt season to limit transport during summer. Smallest potential transport values are found for relatively high elevation sites where the katabatic winds are weak (Table 9.2).

Table 9.2, Annual Potential Snow Transport at GC-Net sites

Site	Year	Q_{pot} [t m^{-1} y^{-1}]
CP1	1996	1059
GITS	1996	701
Humboldt	1996	550
Swiss Camp	1997	1714
Humboldt	1997	769
Summit	1997	613
Tunu-N	1997	719
DYE-2	1997	1842
JAR1	1997	1289
NASA-U	1998	932
Humboldt	1998	567
Tunu-N	1998	401
DYE-2	1998	1639
JAR1	1998	1193
Saddle	1998	1370
South Dome	1998	1839
NASA-E	1998	220
CP2	1998	1456
NGRIP	1998	290
NASA-U	1999	665
Humboldt	1999	494
Summit	1999	359
Tunu-N	1999	523
DYE-2	1999	1420
JAR1	1999	851
Saddle	1999	1055
South Dome	1999	1047
CP2	1999	1014
NGRIP	1999	226
Swiss Camp	2000	1355

Annual potential snow transport estimates range from 226 t m^{-1} y^{-1} at NGRIP to1714 t m^{-1} y^{-1} at Swiss Camp. Estimates for the potential blowing snow transport at Swiss Camp are up to eight times greater than the value for NGRIP or Summit, located 2000 m higher in elevation. The reason for the elevation gradient is that katabatic winds are less developed at high elevations [*Bromwich et al.,* 1996; *Steffen and Box,* in press]. South Dome, Saddle, CP1 and CP2 are an exceptions, having large potential transport rates (> 1000 t m^{-1} y^{-1}). At South Dome and Saddle, strong winds result from the interaction of the ice sheet crest with large scale atmospheric circulation. The prevailing wind direction at South Dome and Saddle is easterly, consistent with the predominant circulation associated with the Icelandic Low [*Serreze et al.,* 1993]. The annual potential transport values in Table 9.2 are greater than observed for sites in Wyoming and Alaska [*Tabler and Schmidt,* 1972; *Tabler et al.,* 1990a] as a result of the year-round potential for blowing snow on the Greenland ice sheet as compared to seasonally snow covered regions in the mid-latitudes.

9.4.2 Sublimation of Transported Snow

A conceptual model for blowing snow sublimation based on the theoretical maximum transport distance of an average sized snow particle transported by the wind was developed by *Tabler* [1975]. The concept is applied to GC-Net data assuming that the conditions at GC-Net sites are consistent with a uniform surface and uninterrupted upwind fetch. Anomalous results in comparison with precipitation and accumulation rates may imply that some or all sites violate these fetch assumptions. The following derivation of blowing snow sublimation is taken practically verbatim from Tabler [1975]. Theory shows that the instantaneous sublimation rate *(dm/dt)* of a spherical ice particle at time *t* is proportional to the 3/2 or 1.5 power of its diameter *(x) [Schmidt, 1972]*. Using *Lee's* [1975] turbulence model and the environmental conditions observed for a site at 2600 m elevation in Wyoming [*Tabler and Schmidt*, 1972], this relationship was found to be approximated by

$$dm/dt = kx^{1.4} \qquad \text{Eq. 9.4}$$

over the diameter range 0 to 0.5 mm, and where *k* is a negative constant.

Since particle mass *(m)* is proportional to the cube of the diameter, Eq. 9.4 may be written as

$$dm/dt = kk_1^{-0.47} m^{0.47} \qquad \text{Eq. 9.5}$$

where k_1 is $r p/6$. r is the ice particle density (1 g cm^{-3}). Integrating by separation of variables yields

$$1.887 m^{0.53} = kk_1^{-0.47} t + c \qquad \text{Eq. 9.6}$$

The constant *c* can be evaluated by setting time $t = 0$. Then solving for the residual mass *m* at time *t*, the above equation becomes, for a particle with initial mass m_0

$$m = \left(0.53 kk_1^{-0.47} t + m_0^{0.53}\right)^{1.89} \qquad \text{Eq. 9.7}$$

For a reference particle with initial diameter x_{01} and mass m_{01}, there is a corresponding time t_{s1} required for complete sublimation. Solving the above equation for t_{s1} gives

$$t_{s1} = -1.89\left(k_1 / k\right) x_{01}^{1.6} \qquad \text{Eq. 9.8}$$

Substituting Eq. 9.8 in Eq. 9.7 gives an expression for the residual mass at time $t=t_{sl}$ for any particle with initial diameter $x_{0i} \geq x_{01}$.

$$m_i = k_1\left(x_{0i}^{1.6} - x_{01}^{1.6}\right)^{1.89} \quad , x_{0i} \geq x_{01}. \qquad \text{Eq. 9.9}$$

9.4.2.1 Residual Mass Fraction and Particle Diameter

Determining blowing snow sublimation for a host of particles is accomplished by integration of sublimation rates from a distribution of particle sizes. If some function, *f(x)*, describes the frequency distribution of nominal particle diameters in a unit volume of air-snow mixture, then the number of particles with diameters in the range *x* to *x+dz* is *Nf(x)dx*, where *N* is the total number of particles. With the understanding that only initial diameters are involved, total residual mass *M* of all particles in the unit volume at time t_{s1} is then given by

$$M = Nk_1 \int_{x_1}^{\infty} \left(x^{1.6} - x_1^{1.6}\right)^{1.89} f(x)dx \qquad \text{Eq. 9.10}$$

Dividing by total initial mass, M_0, gives the proportion of the initial mass remaining after an interval of time, t_{s1}, just sufficient for complete sublimation of the reference particle with initial diameter x_1

$$M / M_0 = \frac{\int_{x_1}^{\infty} \left(x^{1.6} - x_1^{1.6}\right)^{1.89} f(x)dx}{\int_0^{\infty} x^3 f(x)dx} \qquad \text{Eq. 9.11}$$

The size distribution function *f(x)* for actively blowing snow has been observed to be represented by a two-parameter gamma distribution [*Budd et al.*, 1966; *Schmidt*, 1982a; *Pomeroy and Male*, 1988]. Despite the fact that none strictly treat a size distribution for particles newly dislodged from a snow cover previously undisturbed by wind, i.e. in this model at time *t=0*, *Tabler* [1975] took a gamma probability density function for this derivation.

$$f(x) = \frac{1}{b^a \Gamma(a)} e^{-x/B} x^{a-1} \qquad \text{for } 0 < x < \infty \qquad \text{Eq. 9.12}$$

where a and b are parameters such that $a\,b$ equals the mean particle diameter *(m)*, and *G(a)=(a-1)!*. Using Budds' results, a is taken as 15 throughout the following development, x is in cm units and $b=u/a$.

As a final step, let all diameters be expressed relative to the mean *m* using a new variable *(y)*

$$y=x/m \qquad \text{Eq. 9.13}$$

substituting Eq. 9.12 and Eq. 9.13 into Eq. 9.11 gives

$$M / M_0 = \frac{\int_{y_1}^{\infty} \left(y^{1.6} - y_1^{1.6}\right)^{1.89} e^{-ay} x^{a-1} dy}{\int_0^{\infty} y^{a+2} e^{-ay} dy} \qquad \text{Eq. 9.14}$$

9.4.2.2 Residual Mass Fraction and Transport Distance

A useful application of Eq. 9.14 is to determine the transport distance *(R)* for a particle with initial diameter x_0 and traveling at some average speed $\overline{u}_p$, given by

$$R_x = \overline{u_p} t_s \qquad \text{Eq. 9.15}$$

where t_s is the time for complete sublimation for an average sized particle. Particle speed is assumed independent of particle diameter and equal to the average wind speed as confirmed by *Schmidt* [1982b]. Then from Eq. 9.8,

$$R_x = k_2 x_0^{1.6} \qquad \text{Eq. 9.16}$$

$k_2 = -u_p[1.89(k_1/k)]$, where u_p is average particle speed, assumed equal to average wind speed. Given this function, numerically integrating Eq. 9.14 for parametric values of R_x/R_m shows that residual mass is about the residual mass is about 39, 11, and 0.4 percent of the initial mass after transport over distances of R_x/R_m equal to 0.5, 1, and 2, where R_μ is the maximum transport distance for an average sized particle. Considering the assumptions to develop Eq. 9.14 a more tractable function can be used as an approximation to facilitate calculation:

$$M / M_0 = e^{-2(R/R_m)} \qquad \text{Eq. 9.17}$$

9.4.2.3 Using the Residual Mass Fraction as a Weighting Factor

The final step in this development consists of using Eq. 9.17 to weight the relative importance of each increment of distance *(dR)* with respect to its contribution to the total amount of blowing snow passing some point down wind. For this purpose, *dQ* is defined as the volume of blowing snow (water-equivalent per unit width perpendicular to the wind) contributed by the elemental length, *dR*. located at distance *R* upwind of the point. Then, since volume equals mass divided by density, Eq. 9.17 may be written as

$$dQ = dQ_0 e^{-2(R/R_m)} \qquad \text{Eq. 9.18}$$

where dQ_0 is the initial volume of snow blown off the length *dR*, and is thus given by

$$dQ_0 = P_r dr \qquad \text{Eq. 9.19}$$

where P_r is the water equivalent precipitation swept off *dR* by the wind. For calculating the annual transport, P_r is the total precipitation less that amount retained by the surface and by snow melting in place before relocation. Substituting Eq. 9.19 in Eq. 9.18 gives

$$dQ = P_r e^{-2(R/R_m)} dr = P_r 0.14^{R/Rm} dr \qquad \text{Eq. 9.20}$$

In Eq. 9.20 and all others that follow, for snow transport or evaporation in cubic meters water-equivalent per meter of width, P_r, R, and R_m are in meters. If appropriate values are used for P_r and R_m, all equations developed here should apply to annual totals.

The total snow transport volume ($Q_{R_2-R_1}$) contributed by some finite distance $DR = R_2 - R_1$ would then be

$$Q_{R_2} - Q_{R_1} = \int_{R_1}^{R_2} P_r 0.14^{(R/R_m)} dr \qquad \text{Eq. 9.21}$$

The assumption of an unlimited fetch is reasonable for the Greenland ice sheet. The surface is almost flat and no major upwind obstacles exist at GC-Net sites, with the exception of ablation zone sites JAR1 and JAR2 where local undulations > 50 m in height occur within 2 km. No upwind barriers to snow drift exist at accumulation zone sites because after thousands of years, topographic features such as undulations ought to be in equilibrium with snow drift. This does not mean that there is no snow redistribution, only that the fetch is unlimited. Thus, selecting $DR=R_m$ so that P_r and the factors affecting evaporation are taken to be uniform over this distance, integration of Eq. 9.21 yields the total relocated precipitation *(Q_r)* in units of snow water equivalence across a perpendicular unit length.

$$Q_r = \frac{P_r R_m}{2}\left(1 - 0.14^{(R/R_m)}\right) \qquad \text{Eq. 9.22}$$

Over the annual scale, an average value for R_m, was found to be 3000 m for sites in Wyoming near 2000 m elevation [*Tabler*, 1994]. Engineering applications of Eq. 9.22 have shown R_m to be approximately 3000 m over a wide range of locations throughout the US, including Alaska [*Tabler*, 1994]. R_m varies with the relative humidity, air temperature, wind speed of an individual storm and in response to other environmental conditions. Thus, derivation of R_m is pursued for GC-Net data, made possible by the assumption of infinite fetch described below.

9.4.2.4 Resultant Equation for the Conceptual Model

The annual sublimation for a site with unlimited fetch *(Q_{evap})* in units of kg m^{-2} or mm water equivalence is given by the difference of Q_r from all precipitation relocated.

$$Q_{evap} = 1000 P_r F - 500 P_r R_m \left(1 - 0.14^{F/R_m}\right) \qquad \text{Eq. 9.23}$$

where F is the fetch (m) and P_r is the relocated precipitation (m w. e.). Below, a simplification is incorporated where the fetch is taken to be the maximum transport distance R_μ. Precipitation *(P)* is taken from an atmospheric model [*Chen et al.*, 1997; *Bromwich et al.* submitted]. Table 3.14 features annual precipitation values for model grid locations nearest GC-Net sites. Modeled precipitation is believed to be fairly accurate because the sum of net surface water vapor flux based on profile methods (section 6) and accumulation agrees with the precipitation on average to within 5% (section 6.5). Section 3.5 includes a description of the model used to derive precipitation. The proportion of relocated precipitation to the total precipitation is referred to as the *relocation coefficient (q)*. Thus, the relocated precipitation is:

$$P_r = qP \qquad \text{Eq. 9.24}$$

The water equivalent depth of evaporated blowing snow is the actual blowing snow transport divided by the fetch, assuming an infinite fetch. With this assumption, the second term of Eq. 9.23 goes to zero. Infinity cancels from the denominator of both sides of the equation. Thus, blowing snow evaporation over an infinite fetch is equivalent to the relocated precipitation:

$$Q_{evap} \cong P_r \qquad \text{Eq. 9.25}$$

This should not be too surprising given the results of *Schmidt* [1972]; *Tabler and Schmidt* [1972]; and *Schmidt and Gluns* [1992] that show individual ice particle lifetime not exceeding 10 minutes in turbulent suspension. Blowing snow events detected by GC-Net hourly means will all last six times the sublimation time of an average particle. This formulation does not necessitate an R_m estimate. However, R_m is then calculated to evaluate Q_{evap} estimates. It should also be noted that this estimate for blowing snow sublimation represents a loss-only term in the surface net water vapor balance. The missing term in the balance, the gain-only component by water vapor deposition, may be solved for as a residual in two ways using estimates of accumulation, precipitation, blowing snow sublimation, and the net surface water vapor balance from profile methods. This analysis follows the blowing snow sublimation results in section 9.4.5.

9.4.3 Relocation Coefficient Based on Surface Height Measurement

GC-Net surface height measurements provide an independent estimate of the relocation coefficient. Surface height measurements indicate the net effect of accumulation due to snowfall, snow compaction, and importantly, the erosion effect of the snow surface by the wind. Following snowfall accumulation events at GC-Net sites, peaks in wind speed above 8 m s^{-1} -10 m s^{-1} are often associated with surface height reduction. This reduction is taken to be the result of surface erosion by the wind. A model for snow compaction should take into account compaction due to wind packing. Two such surface erosion cases are illustrated in Figure 9.2. Relative humidity also peaks at the onset of surface height increase signifying that these are not sastrugi development events.

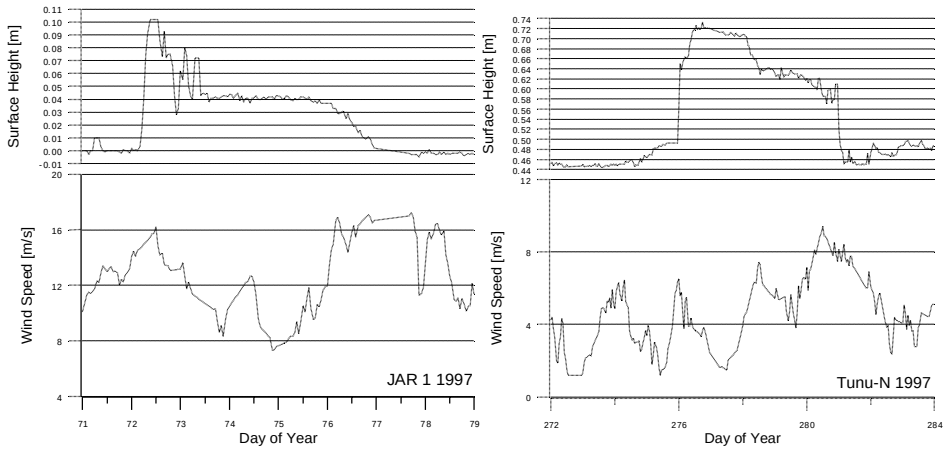

Figure 9.2, Two examples of surface erosion due to the wind at GC-Net sites

Decomposing the surface height time series data into positive and negative components gives direct information of accumulation, surface erosion, and compaction. The ratio of the cumulative sum of negative and positive surface height changes indicate the proportion of surface height change that is caused by erosion plus compaction of snowfall accumulation (Figure 9.3).

$$q = \left(\sum \left|(\Delta h / \Delta t)_{<0}\right|\right) - w^{-}C \Big/ \left(\sum (\Delta h / \Delta t)_{>0}\right) + w^{+}C \qquad \text{Eq. 9.26}$$

where Δh is the daily change in surface height and Δt is time change in days. The effect of firn compaction is removed from q by subtracting the compaction *(C)* from the numerator and adding *C* to the denominator of Eq. 9.26. *C* is weighted by the annual fraction of days with accumulation (w^{+}) or surface lowering (w^{-}). The model to estimate compaction is featured in the Appendix, section B. Correcting for compaction leads to a 5% to 10% decrease in q because not all surface height reduction is due to erosion by the wind. Incidentally, the weighting fractions indicate that there is a greater frequency of negative surface height change days than positive ones. Accumulation is observed to occur in short time intervals while the greater proportion of the year is composed of days in between snow events that are characterized by surface height reduction. Daily averages of surface height measurements are used to eliminate the effect of hour to hour surface roughness changes which may result from the migration of sastrugi and snow barchans in the field of view of the surface height sensors. A weakness of this method is that sastrugi formation occurs on a time scale less than one day. This method neglects the potential for a depression to form within the field of view of surface height instruments caused by the AWS mast. Such a 'moat' if found at AWS sites, is usually small enough that the range of surface height instruments from the mast is far enough that it is not a problem. Negative surface height changes were not totaled if associated with melt as estimated by daily mean air temperatures above –1.5° C. At GC-Net sites above 1150 m, the frequency of temperatures above –1.5° C is less than one tenth of one percent, thus this thresholding technique will not lead to great uncertainties. This methodology assumes that blowing snow is not a source of accumulation. Whether or not this is true may emerge when the final blowing snow sublimation results are tabulated and analyzed in the residual of the surface mass balance.

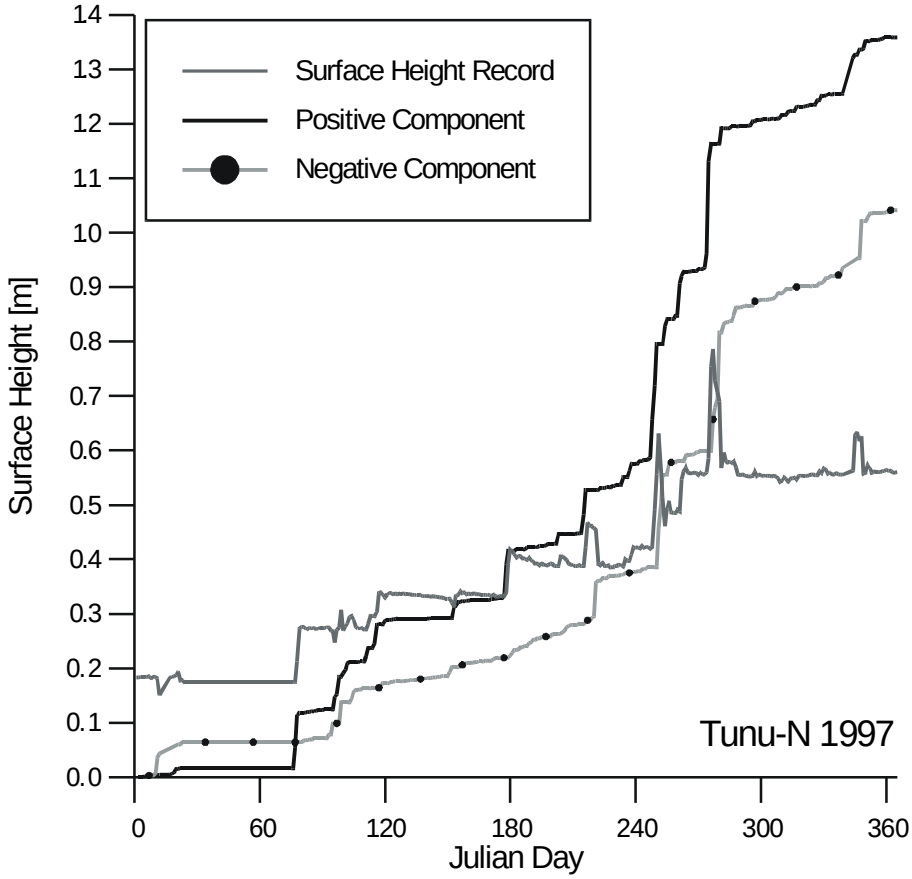

Figure 9.3, Positive and negative components of an annual surface height time series indicating the ability to separate accumulation and erosion.

Relocation coefficients based on GC-Net surface height data are given in Table 9.3. Maximum q values are at the Tunu-N site where the highest number of wind induced surface erosion cases are observed in the surface height record. Lowest q values are generally found at sites with relatively large accumulation rate, NASA-SE and GITS for example. Studies in Siberia and Wyoming show that even on flat areas with low-growing vegetation, winter q seldom exceeds 0.7 [*Tabler*, 1994]. No q values are featured for 1995 because the measurements began in the late spring and thus annual values are not possible to calculate.

Table 9.3, Relocation Coefficient *(q)* at GC-Net Sites Based on Surface Height Measurements

Site	1996	1997	1998	1999	2000
Swiss Camp	**	0.49	**	**	0.49
CP1	0.52	0.47	0.42	0.38	0.31
NASA-U	0.55	0.49	0.49	0.44	0.49
GITS	0.45	0.27	**	0.47	0.40
Humboldt Gl.	0.71	0.50	0.52	0.45	0.35
Summit	**	0.65	0.53	0.59	0.66
TUNU-N	**	0.74	0.57	0.58	0.63
DYE-2	**	0.46	0.47	0.41	0.34
JAR1	**	0.37	0.46	0.42	0.48
Saddle	*	0.40	0.43	0.40	0.32

South Dome	*	0.41	0.42	0.44	0.40
NASA-E	*	0.58	0.57	0.44	**
CP2	*	0.41	0.46	0.51	0.30
NGRIP	*	0.41	0.60	0.64	0.55
NASA-SE	*	*	0.34	0.43	0.35
JAR2	*	*	**	0.57	0.52

* - AWS not yet activated, ** - insufficient data

9.4.4 Model for Blowing Snow Availability

The actual blowing snow transport *(Q_{act})* is estimated by modeling the snow cohesion factors that restrict snow transport. The model is set up as follows. Snow availability is assumed to be unlimited when snow is freshly deposited. Availability is set to decay with time from snow events detected by peaks in the positive component of the surface height measurement time series. This snow availability factor *(SAF)* may be expressed as:

$$SAF = \left(1.038 + 0.03758t - 0.00014349t^2 + (1.911315e-7)t^3\right)^{-1} \qquad \text{Eq. 9.27}$$

where *t* is time in hours after a snowfall event. After 12 days (288 hours), *SAF* decays to a value of 0.22 that is then held constant (Figure 9.5). The constant value is proportional to the force of 4.5 times the force required to disaggregate bonds between freshly deposited snow particles measured by *Jellinek* [1957].

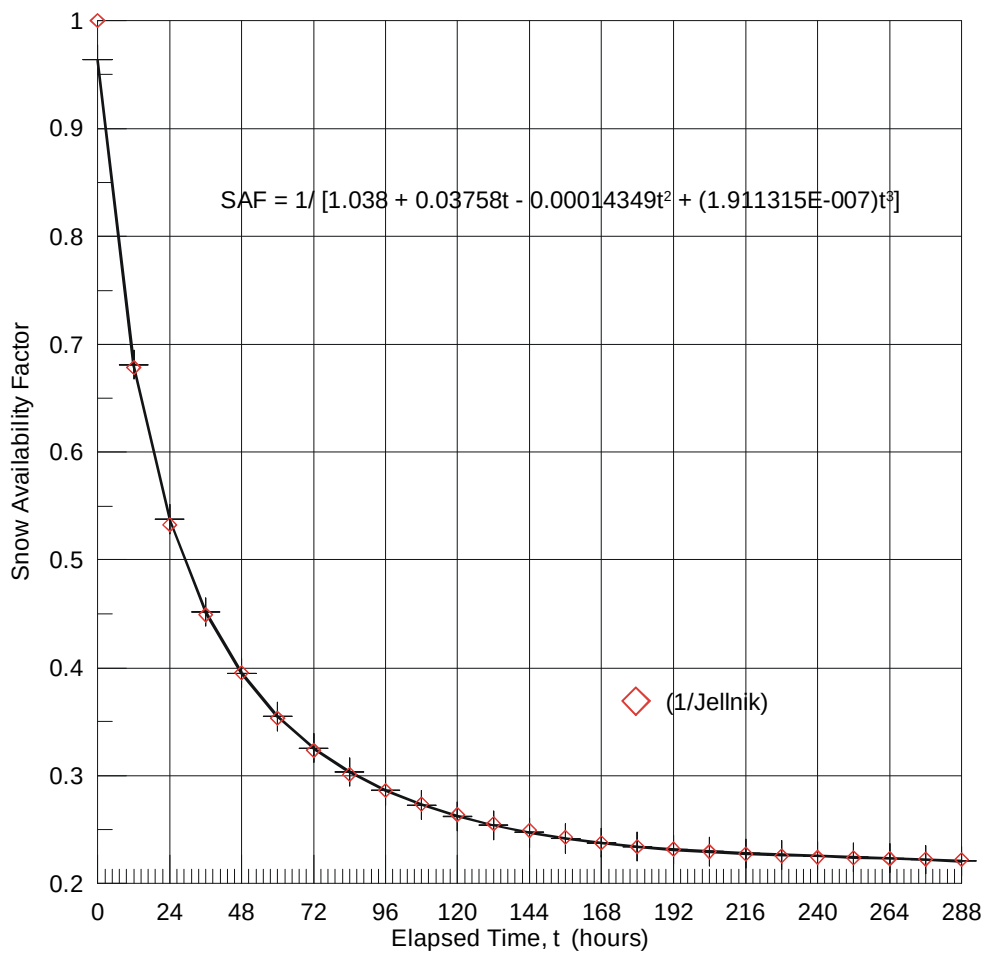

Figure 9.4, Snow Availability Factor as a function of time (Plot provided by R. Tabler)

Factors that reduce snow availability, surface hardening by the sun, wind, frost, rain, and temperature fluctuations are grouped into this single decay term. In reality, the decay of snow availability with time will fluctuate due to these factors. Simulating the effects due to the individual factors may be the subject of future work, because they require validation from field measurements not currently available. Snow events are detected at GC-Net sites when the hourly surface height increases by more than 3 cm. Thresholds less than 3 cm lead to spurious snow event detection due to surface roughness variations. The actual snow transport *(Q_{act})* is estimated by multiplying hourly values of Q_{pot} by *SAF*. The means to validate the *SAF* is the use of photoelectric particle counters or indirect techniques such as snow fence accumulations to measure Q_{act}. The logic behind this particular *SAF* function could be refined, for example to have λ that is also a function of solar radiation because a large solar radiation flux would cause a more rapid decay of *SAF* with time. Figure 9.5 illustrates the components of this model for a snow event and subsequent erosion captured by AWS observations at Tunu-N in 1997.

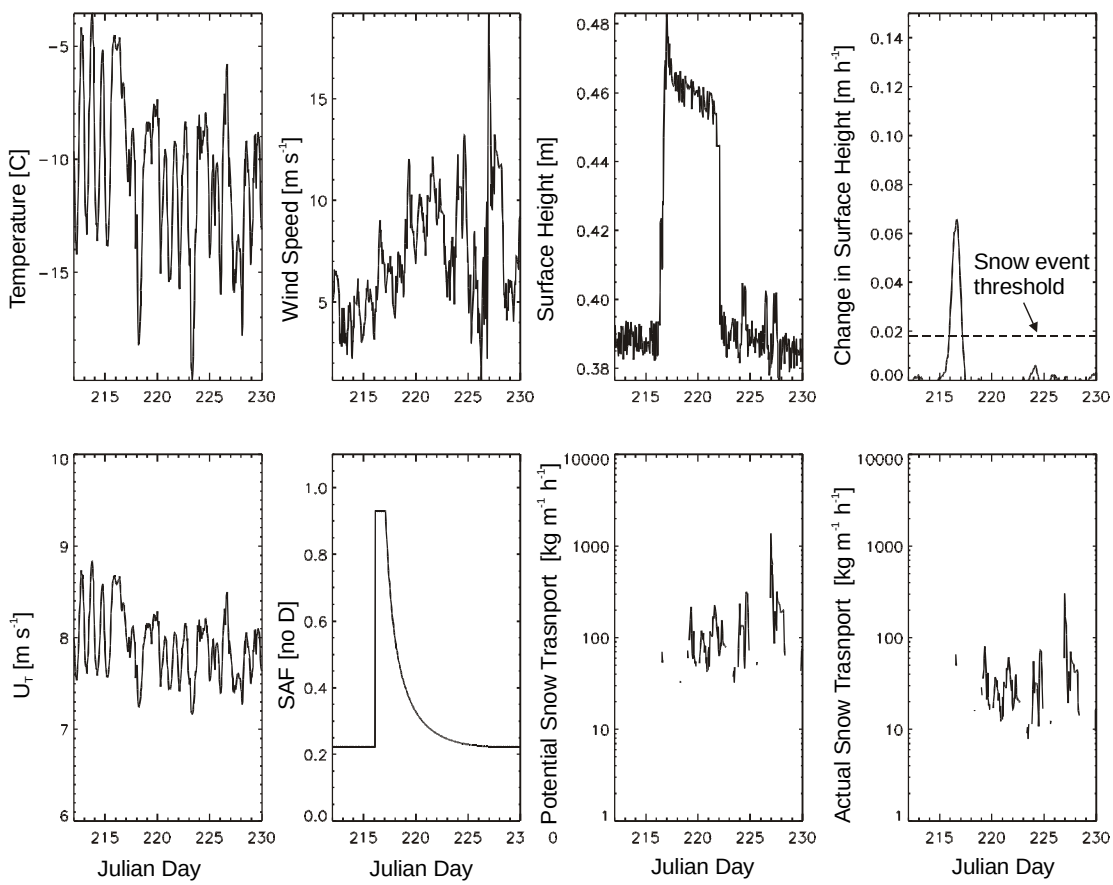

Figure 9.5, Example of the factors included in the simulation actual blowing snow transport for a case observed at Tunu-N in 1997.

The maximum transport distance *(R_m)* is of use in diagnosing whether blowing snow sublimation estimates are reasonable. R_m may be solved for given an estimate for the annual precipitation, relocation coefficient, and the assumption of infinite fetch.

$$R_m = Q_{act} / 0.5P_r \qquad \text{Eq. 9.28}$$

The results are featured below in context of Q_{act} and other relevant parameters of this exercise.

9.4.5 Blowing Snow Sublimation and Surface Mass Balance

Using the estimates of the relocation coefficient *(q)*, actual blowing snow transport *(Q_{act})*, precipitation *(P)*, and accumulation *(A)*, the contribution of blowing snow sublimation to the mass balance may be assessed (Table 9.4). Potential blowing snow transport *(Q_{pot})* values are given in *Table 9.2*. Annual Q_{act} tends to be about one third of Q_{pot} with values ranging from 89 t m^{-1} y^{-1} at NASA-E due to the relatively low wind speeds and up to 1197 t m^{-1} y at South Dome where there is a high accumulation rate, no melt to restrict blowing snow entrainment, and where relatively strong winds are observed. South Dome data yield a larger estimate for Q_{act} than Swiss Camp, despite the latter having larger Q_{pot}. Swiss Camp exhibits melt conditions that do not allow blowing snow in this model for up to 10% of the year.

Blowing snow sublimation *(Q_{evap})* estimates are in the range of 68 mm y^{-1} to 71 mm y^{-1} for sites with little wind (Summit and NGRIP) to 500 mm y^{-1} at Swiss Camp where wind speeds are relatively high. South Dome Q_{evap} is relatively small due to the effect of the large accumulation rate. This is despite the very large Q_{pot} and Q_{act} for South Dome. These numbers are much larger than the net surface water vapor flux derived from the aerodynamic profile methods in chapter 5. One test for the Q_{evap} estimates is whether or not the observed and implied accumulations agree. The implied accumulation *(A_i)* is calculated as the precipitation minus the blowing snow sublimation. A_i values are generally lower than observed accumulation *(A_o)* calculated using AWS surface height measurements. There are errors in both accumulation measurements, modeled precipitation, and blowing snow. Thus, the comparison is not conclusive. This would imply that Q_{evap} is too high, as a result of Q_{pot} or *SAF* that is still too high, that the modeled precipitation is too low, or that water vapor redeposition is not accounted for. Given that Q_{evap} is really a loss-only term, the latter implication is further investigated below.

Table 9.4, Blowing Snow Sublimation Estimated from Tabler's Conceptual Model Using an Estimate of the Actual Snow Transport

Site	Year	Q_{pot} t m^{-1} y^{-1}	Q_{act} t m^{-1} y^{-1}	P mm y^{-1}	q	Q_{evap} mm y^{-1}	Implied Accum mm y^{-1}	AWS derived Accum. mm y^{-1}	R_μ	N. of Snow Events y^{-1} > 3 cm
CP1	1996	1059	559	666	0.52	346	319	519	3229	48
GITS	1996	701	313	344	0.45	155	189	406	4045	33
Humboldt	1996	550	171	244	0.71	173	71	218	1970	25
Swiss Camp	1997	1714	542	821	0.49	402	419	*	2694	36
Humboldt	1997	769	221	245	0.50	122	122	191	3601	13
Summit	1997	613	191	113	0.65	73	40	216	5200	22
Tunu-N	1997	719	200	151	0.74	112	39	162	3585	15
DYE-2	1997	1842	667	460	0.46	212	248	339	6300	26
JAR1	1997	1289	474	775	0.37	287	488	*	3302	36
NASA-U	1998	932	294	400	0.49	196	204	243	2995	17
Humboldt	1998	567	164	237	0.52	123	114	203	2662	13
Tunu-N	1998	401	116	155	0.57	88	66	155	2640	10
DYE-2	1998	1639	493	476	0.47	224	252	233	4406	22
JAR1	1998	1193	478	641	0.46	295	346	*	3241	40
Saddle	1998	1370	467	298	0.43	128	170	309	7283	21
South Dome	1998	1839	896	416	0.42	175	241	517	10252	25
NASA-E	1998	220	68	206	0.57	118	89	204	1154	13
CP2	1998	1456	506	480	0.46	221	259	322	4585	26
NGRIP	1998	290	120	118	0.60	71	47	188	3402	16
NASA-U	1999	665	239	404	0.44	178	226	470	2685	27
Humboldt	1999	494	142	157	0.45	71	86	174	4020	10
Summit	1999	359	161	115	0.59	68	47	271	4742	21
Tunu-N	1999	523	224	176	0.58	102	74	205	4381	22
DYE-2	1999	1420	466	530	0.41	217	313	**	4286	20
JAR1	1999	851	348	741	0.42	311	430	*	2234	39
Saddle	1999	1055	409	426	0.40	170	256	363	4801	23
South Dome	1999	1047	482	518	0.44	228	290	456	4226	33
CP2	1999	1014	420	628	0.51	320	307	**	2624	34
NGRIP	1999	226	67	118	0.64	75	42	103	1792	12
Swiss Camp	2000	1355	501	771	0.49	378	393	*	2652	41
CP1	2000	932	367	598	0.31	185	413	411	3959	37
Summit	2000	286	94	114	0.66	75	39	126	2485	13
DYE-2	2000	1583	601	482	0.34	164	318	275	7337	19

* - impossible to calculate accumulation with surface height data alone. ** - insufficient data.

Estimates of the maximum blowing snow transport distance ($R\mu$) are equal to or larger than the value of 3000 m observed for mid latitude sites. Sites with $R\mu$ values less than 4500 m are those near 2000 m in elevation and Swiss Camp. Other sites such as South Dome and DYE-2 have larger values. South Dome 1998 value is in excess of 10000 m, implying that the estimate for Q_{act} is may be too high or the relocated precipitation estimate

is too low.

The number of blowing snow events is in the range of 10 at a low accumulation site such as Humboldt and as great as 30-40 at South Dome, CP1 and CP2, sites with a relatively large accumulation rates.

9.4.6 Implied Water Vapor Deposition

Water vapor recycling at the surface of the Greenland ice sheet is implied by a mass gain term needed for the accumulation to balance with Q_{evap}. The water vapor deposition gain *(D)* may be calculated in two ways. One solution uses the profile method net annual water vapor balance (ΔM) from chapter 5. The surface water vapor balance can be expressed by gains due to water vapor deposition *(D)* and losses by blowing snow sublimation (Q_{evap}) and the water vapor flux from the static surface (Q_{stat}).

$$\Delta M = D - \left(Q_{evap} + Q_{stat}\right) \qquad \text{Eq. 9.29}$$

Thus, the net water vapor deposition *(D)* is

$$D = \Delta M + \left(Q_{evap} + Q_{stat}\right) \qquad \text{Eq. 9.30}$$

Unfortunately, Q_{stat} may not be calculated directly from GC-Net measurements because the humidity profile measures the net effect of both upward and downward fluxes of moisture, simultaneously. Given that annual Q_{stat} is probably much smaller than Q_{evap}, particularly for sites without melt and that Q_{stat} would add to Q_{evap}, making D even larger. A rough estimate of D can be obtained by neglecting Q_{stat}.

However, it is possible to define another solution for the water vapor deposition term (D_2), one that employs Q_{evap} accumulation *(A)* precipitation *(P)* and does not rely on the net surface water vapor balance derived from profile methods (ΔM).

$$D_2 = \left(Q_{evap} + Q_{stat}\right) - A + P \qquad \text{Eq. 9.31}$$

The gain-only term of annual water vapor deposition (D and D_2) required to balance ΔM with precipitation and accumulation is in the range of 76 mm y^{-1} for Summit and up to 400 mm y^{-1} or 500 mm y^{-1} in the case of CP2, NASA-U, and DYE-2 Table 9.5. Because including Q_{stat} would increase D, the actual value for D must be larger than the estimated derived here. This bias should be small, however because the sublimation rate from blowing snow is much greater from snow at rest and the difference between the gain and loss terms is usually less than 100 mm y^{-1}. Thus, the water vapor flux from a static surface is probably less than 100 mm y^{-1}. The two water vapor deposition estimates D_1 and D_2 are of similar magnitude.

Table 9.5, Water Vapor Deposition as the Residual of Two Water Vapor Balance Equations

Site	Year	Precip. [mm y^{-1}]	Bl. Sn. Subl. [mm y^{-1}]	AWS derived Accum [mm y^{-1}]	ΔM	D_2	D
CP1	1996	666	346	519	*5*	493	351
GITS	1996	344	155	406	-71	93	84
Humboldt	1996	244	173	218	*0*	199	173
Humboldt	1997	245	122	191	*0*	176	122
Summit	1997	113	73	216	*6*	-30	79
Tunu-N	1997	151	112	162	20	101	132
DYE-2	1997	460	212	339	-82	333	130
NASA-U	1998	400	196	243	-73	353	123
Humboldt	1998	237	123	203	0	157	123
Tunu-N	1998	155	88	155	*20*	88	108
DYE-2	1998	476	224	233	*-82*	467	142
Saddle	1998	298	128	309	-53	117	75
South Dome	1998	416	175	517	*	74	*
NASA-E	1998	206	118	204	6	120	124
CP2	1998	480	221	322	40	379	261
NGRIP	1998	118	71	188	*32*	1	103
NASA-U	1999	404	178	470	*-73*	112	105
Humboldt	1999	157	71	174	*0*	54	71
Summit	1999	115	68	271	*6*	-88	74
Tunu-N	1999	176	102	205	*20*	73	122
DYE-2	1999	530	217	*300*	*-82*	447	135
Saddle	1999	426	170	363	-68	233	102
South Dome	1999	518	228	456	*	290	*
CP2	1999	628	320	*670*	*40*	278	360
NGRIP	1999	118	75	103	*32*	90	107
CP1	2000	598	185	411	*5*	372	190
Summit	2000	114	75	126	*6*	63	81
DYE-2	2000	482	164	275	*-82*	371	82

* - insufficient data

9.5 Conclusions

Previous experiments and studies show that the sublimation from blowing snow is much greater than from snow at rest. The special conditions found over the majority of the Greenland ice sheet allow the development of a conceptual model to estimate the amount of blowing snow sublimation. Simplification to the complex blowing snow sublimation problem are based on the assumption that the surface topography of the ice sheet is in equilibrium with snow drift from thousands of years of blowing snow. The water vapor mass loss from individual ice particle transported by the wind is so rapid that it is shown that virtually all transported snow sublimates.

Using the conceptual model, blowing snow sublimation is estimated to be a large component of the net surface water vapor balance over the Greenland ice sheet. It is only by a slightly smaller flux of evaporated blowing snow back to the surface (+70 mm y^{-1} to + 400 mm y^{-1}) that the observed accumulation rate and precipitation balance. Sites with large blowing snow sublimation require a redeposition of almost as much that is lost to balance with the observed net surface water vapor balance measured by the aerodynamic profile methods (section 5). It is well known that at any one time, the mass flux of water vapor to and from a surface may be large even when the surface is in equilibrium [*Brutsaert*, 1982]. Two estimates of moisture recycling, one using the net water vapor flux based on aerodynamic profile methods and another relying on precipitation and accumulation estimates, are in general agreement. These estimates may be too small because they neglect sublimation or evaporation from the static surface. This bias should be small, however, because the sublimation rate from blowing snow is much greater than from snow at rest and the difference between the gain and loss terms is usually less than 100 mm y^{-1}. Thus, the water vapor flux from a static surface is probably less than 100 mm y^{-1}.

Precise blowing snow sublimation estimates are open to large uncertainty due to the extremely complex nature of the phenomenon. For example, large uncertainties exist in the bulk model for blowing snow transport, given insufficient data to represent snow availability. Substantial uncertainties also exist for accumulation rates, model precipitation, and other parameters such as the proportion of relocated precipitation estimated from surface height records. The availability of snow depends on the surface hardness [*Schmidt*, 1982a], a factor that itself is approximated by a bulk formula such as *SAF* (Eq. 9.24). The uncertainty of implied deposition rates is large due to the compounded errors in modeled precipitation, blowing snow sublimation, and the high annual and spatial variability of ice core accumulation rates [*Anklin et al.*, 1998]. Sophisticated numerical models of blowing snow sublimation are themselves fraught with uncertainties [*Xiao et al.*, 2000]. Although precise quantitative estimates of blowing snow evaporation are not yet possible, there is little doubt that in-transit evaporation is a major component of the mass balance of the ice sheet.

10 Summary of Results and Conclusions

Over 50 station years of Greenland Climate Network automatic weather station data are used to estimate the surface water vapor mass fluxes on the Greenland ice sheet. Results are presented for point locations and in the form of maps. The primary justification to construct the maps is to estimate the total net surface water vapor mass flux for the ice sheet. There is an obvious geographical pattern of surface water vapor flux with decreasing annual loss with increasing elevation that results from the temperature dependence of sublimation and evaporation potential [*Brutsaert*, 1982]. Methods that employ one or two humidity measurements levels are validated using eddy flux correlation measurements and evaporation pans. Methods that employ only one humidity measurement level are shown to underestimate deposition and have greater hourly uncertainty than two level methods, 80% and 35%, respectively. The uncertainty of monthly means is about 10% of the hourly value, assuming normally distributed errors. One-level methods are consistent with that used in global and regional climate simulations. Therefore, the climate models are susceptible to the same bias and uncertainty. Mapping sublimation by trend surface regression leads to an increase in uncertainty due to residuals of 50% for the two level method data and 60% for the one level method data.

10.1 Treatment of Humidity data

The rescaling of humidity data with respect to liquid water to an ice surface described in section 3.1.11 greatly increased the accuracy of the latent heat flux values calculated by the profile methods in chapter 5. This conclusion was reached not only by comparing the relative humidity from AWS instruments with chilled mirror hygrometer measurements before and after rescaling (Figure 3.7), but in the resultant latent heat fluxes in comparison with eddy correlation data. Formerly, the rescaling of humidity data to the sensor's maximum output was only performed for temperatures below melting. The extreme evaporation values encountered at Swiss Camp in 2000 were associated with temperatures above the melting point. Latent heat fluxes for these cases were unrealistic until the rescaling procedure was revised to include temperatures above the melting point. Even after making substantial conversions, more confidence may be taken in the converted humidity data than the raw data.

10.2 Validation of Profile Methods

The surface water vapor flux is gauged by the latent heat flux measured by AWS profile methods or during experiments using eddy flux correlation instrumentation. The eddy flux data are taken to be more accurate than the profile method results because eddy correlation instruments directly sample atmospheric turbulence heat fluxes. Profile methods appear to represent the turbulent latent heat flux reasonable well when compared with eddy flux correlation measurements, in particular the two level profile method and certainly for daily average periods. The one level method, although providing accurate positive latent heat fluxes, cannot accurately gauge the negative latent heat fluxes associated with condensation or deposition. Thus, the two level method results are taken in evaluating the surface water vapor flux climatology of the Greenland ice sheet. Further validation of the eddy correlation results should be done, for its uncertainty is not confidently gauged in the literature or this thesis.

Uncertainties associated with hourly 1LM and 2LM results are substantial, 80% and 35%, respectively. Longer term figures, such as monthly means and annual net surface water vapor fluxes will suffer less from uncertainty. The weakest link of our preferred two level method is probably the assumption of the constant ratio of the eddy diffusivities.

10.3 Climatology of Water Vapor Fluxes on the Greenland Ice Sheet

A climatology of surface water vapor flux is described, based on the Greenland climate Network (GC-Net) AWS measurements. For a given time of the year, from one to five years of data are currently available. A distinct annual cycle of surface water vapor flux is observed. Greatest surface water vapor fluxes occur in

summer when solar heating of the surface drives a specific humidity gradient from the surface to the atmosphere. Thus the predominant flux is a loss of water vapor. Winter months are typically indicative of water vapor deposition to the surface. Deposition rates in winter are much smaller than the surface water vapor flux in summer. At high elevation sites, however, the predominance of a strong temperature inversion promotes deposition through the greater specific humidity at measurement level two than at level one, nearer the surface. During summer at high elevations, a high surface albedo and weaker winds leads to small surface water vapor fluxes. Due to a greater frequency of monthly net deposition, annual net water vapor exchanges at high elevation sites is sometimes positive. Thus, deposition apparently provides an additional mass input to precipitation. The proportion of deposited water vapor to accumulation by snowfall is apparently small, between roughly 4% and 18% at Summit and NGRIP, respectively.

Annual net surface water vapor flux at GC-Net sites according to the two level method is as great as -87 ±30 mm water equivalent at 960 m elevation in the Jakobshavn ablation region, -74 ±26 mm up-glacier at equilibrium line altitude (1150 m), and from +40 ±14 mm to –82 ±29 mm in the zone between 1150 m and 2200 m. On the ice sheet plateau, above 2200 m annual net water vapor flux is often toward the surface with a maximum value of +18 ±6 mm found at Summit.

10.4 Sublimation Variability between an Undulation Crest and Trough

Surface water vapor fluxes are greater at an undulation crest site relative to an adjacent trough site. At the undulation trough, monthly latent heat fluxes indicate condensation, while, at the undulation crest, water vapor flux to the atmosphere is predominant. Some of the largest negative hourly latent heat fluxes in the GC-Net data, -55 W m-2, are observed in January at CP2. The January 1998 average is –7.6 W m-2 (+ 7.2 mm). Surface height measurements show that accumulation rates are 40% greater at the trough site than the crest site [*Steffen and Box,* in press]. The difference in surface water vapor flux explains approximately 18% of the difference, while the remainder is thought to result from snow drift deposition into the undulation trough.

These results raise a serious issue as to the placement of point measurements such as AWS instruments and ice cores, given the common assumption that ice sheet point measurements are representative of a large scale. Therefore, care must be taken in the selection of a site for ice sheet point measurements. Consulting a high resolution (0.1-1 km) digital elevation model for prior knowledge of local slope angles may be a useful approach in determining representative sites.

10.5 Water Vapor Fluxes in a Climate Model

Surface water vapor fluxes inferred from latent heat fluxes produced by the NCAR Mesoscale Model (MM5) 'Polar version' [*Cassano et al.,* in press] exhibit a very similar annual cycle as GC-Net derived values. However, the amplitude of this seasonal cycle is 50% to 200% smaller than that derived by the in-situ GC-Net measurements. The negative bias is attributable to the negative wind speed, temperature, and moisture bias identified in *Cassano et al.* [in press] and to negative bias in the surface momentum flux [*Cassano et al.,* 2001]. Based on this comparison, it seems that the MM5 model would provide the capability of accurately simulating the surface water vapor flux of the Greenland ice sheet if the known model negative biases in temperature, wind speed, moisture, radiation balance [*Cassano et al.,* in press], and the surface momentum exchange [*Cassano et al.,* 2001] can be corrected.

10.6 Surface Water Vapor Flux Mapping

Surface water vapor flux maps for the Greenland ice sheet were produced from trend-surface regression of latent heat fluxes from profile methods with three components, the slope lapse rate in temperature, the elevation, and latitude. The residual differences of the observations to the trend surface indicate a general 60% uncertainty for the one level method and a 50% uncertainty for the two level method. Temperature is a dominant factor for the surface water vapor flux according to the regression of temperature with the latent heat flux.

The most realistic estimate of the annual total net water vapor flux for the Greenland ice sheet is that based on the two level aerodynamic profile method results as a function of the slope lapse rate in temperature (–

7.34±4.4 x 10^{13} kg y^{-1}). The residual uncertainty is however lower for the simpler trend surface to the two level profile method results not including the slope lapse rate in temperature (–6.19±3.1 x 10^{13} kg y^{-1}). The totals for one level methods indicate a greater loss of water vapor, –1.08±0.5 x 10^{14} kg y^{-1} for the three component trend surface fit and –1.20±0.7 x 10^{14} kg y^{-1} for the two component fit. These total ice sheet surface water vapor flux estimates are similar to the result of –6.18 x 10^{13} kg y^{-1} in *Ohmura et al.* [1999] based on atmospheric modeling. Given an ice sheet total accumulation estimate of 5.90 x 10^{14} kg y^{-1} [*Ohmura et al.,* 1999], the precipitation loss is estimated to be 14% based on the most realistic estimate. Based on the residuals in surface water vapor flux and estimates for the hourly uncertainty of the two profile method-types, uncertainties for the total water vapor flux for the Greenland ice sheet are roughly 60% based on two level method data and 50% based on one level method data.

Assuming a good correspondence between the temperature measurements made as part of multiple Greenland scientific expeditions from 1930 to 1980, reduced to a standard decade 1950 to 1960 [*Ohmura,* 1987], the annual surface water vapor flux has decreased by 8.7% for the two level method correspondence or by 39% according to the one level method results. The decrease in net mass loss from 1950 – 1960 to mid 1995 to mid 2000 is associated with an increase of the area of net water vapor flux to the surface in the recent record implied by a warming implied by comparison of the temperature grids. This warming has been noted recently by *Steffen and Box,* [in press].

The mapping functions also provided surface water vapor flux estimates for low elevation locations and sites far from GC-Net measurements. The largest annual surface water vapor flux implied by the mapping results are 194 mm for one level methods and 143 mm for two level methods based on the correlation with temperature, while for the fit to the observations with the correlation to temperature only implicit in the elevation and latitude components, maximum annual surface water vapor flux was -188 mm and -128 mm, respectively. Given the inherent elevation and latitude pattern assumed by these functions, maximum surface water vapor fluxes are found at the lowest elevations of the lowest latitudes. This may not be far from the truth, however, the assumption neglects the likelihood of increased cloudiness where the ice sheet meets the ocean at many low elevation locations. The more maritime climate of the low elevation areas has been shown to be associated with greater cloudiness and thus lower magnitudes of absorbed solar radiation on the Vatnajökull, Iceland's largest ice cap [*Oerlemans et al.,* 1999].

10.7 Blowing Snow Sublimation

Blowing snow sublimation rates was estimated to a sufficient accuracy to conclude that it is a very important component of the net surface water vapor exchange of the Greenland ice sheet. Even taking conservative estimates of blowing snow sublimation, there must be a substantial downward flux of water vapor (at least 100 mm water equivalent y^{-1} at most sites) to balance the observed accumulation rates with precipitation. Thus, aerodynamic profile methods gauge the difference of two large quantities, simultaneous sublimation and deposition. Blowing snow models are highly sensitive and depend crucially on accurate inputs, which really are not adequately provided by unattended automatic weather stations. Nonetheless, further insight into the blowing snow problem can be achieved by application of the GC-Net data to blowing snow studies, including annual potential and actual snow transport estimates.

A model for snow availability for blowing snow transport was developed using GC-Net surface height measurements. Snow availability is taken to be unlimited when snow is freshly deposited and is set to decay with time after a snow event. Snow events are detected by peaks in the positive component of the surface measurement series. Actual snow transport was derived from potential blowing snow estimates based on wind speed records and bulk snow transport formulae. Estimates for annual actual blowing snow transport range from 89 t m^{-1} at high elevation sites with little wind (NASA-E in this case) to 1197 t m^{-1} at South Dome where there is a large accumulation rate and thus a high degree of snow availability, no summer melting to reduce potential transport and it is relatively windy. Given the special conditions of uninterrupted upwind fetch and based on the assumption that blowing snow transport is in equilibrium with the surface topography after thousands of years, the assumption that virtually all transported snow sublimates is not unreasonable. A well established theory for the sublimation of ice particles in turbulent suspension supports this assumption. Thus, given estimates for actual snow transport by the wind and the proportion of relocated precipitation based on surface height measurements and model derived precipitation rates, blowing snow sublimation is calculated. Blowing snow

sublimation estimates range from 70 mm y^{-1} at the NGRIP and Humboldt sites to 500 mm y^{-1} at Swiss Camp. To balance accumulation rates, there must be a significant flux of water vapor to the surface, implying the amount of moisture recycling on a local scale. Water vapor deposition rates required to balance the observed accumulation are in the range of 100 mm y^{-1} to 400 mm y^{-1}. The deposition estimates are, however, associated with a large uncertainty as they are calculated as the residual of the several quantities tied to the surface water vapor balance. Thus, the exercise to estimate blowing snow sublimation has shed light on the potential magnitudes of positive and negative surface water vapor fluxes, potential and actual rates of blowing snow transport, the amount of precipitation reduction, and moisture recycling.

11 Future Work

Some questions were answered by this effort, other questions were raised. Major questions that were answered are addressed by the following statements:

- The GC-Net automatic weather station instrumentation can be successfully used to gauge net surface water vapor fluxes. This is provided that a good relative calibration of humidity instruments is made. Fortunately, the process of rescaling the humidity data to reflect saturation over ice instead of liquid water, and the subsequent readjustment of the humidity data with respect to the maximum output of each individual sensor, achieved a relative calibration that is shown to produce latent heat fluxes that agree in amplitude and sign with eddy flux correlation measurements.
- Two-level aerodynamic profile methods provide more realistic net water vapor exchange estimates than one-level methods. One level methods, although apparently functioning well during melt conditions at the lowest elevations on the ice sheet, underestimate deposition.
- Estimates of the net total surface water vapor flux for the Greenland ice sheet were made using aerodynamic profile methods GC-Net data.
- Insight into 5-10 km undulation-scale surface water vapor flux variability by comparison of CP1 and CP2 data.
- Potential snow transport rates at GC-Net sites have been defined. Blowing snow sublimation is implied to be a large component of the surface water vapor budget that must be offset by significant deposition rates to balance with observed accumulation rates from ice cores and surface height measurements.
- Accumulation rates from surface height measurements have been estimated. Future efforts will address comparing snow water equivalence from snow density measurements with accumulation derived from surface height measurements on a snow event basis.
- Compaction rates necessary for correcting annual surface height change totals at GC-Net sites have been estimated.
- Elevation gradients of temperature, humidity, and wind speed are determined for each month of the year. Temperature, humidity, or wind distribution maps are easily generated at this point.

Major questions raised in this thesis that were beyond its scope constitute a list of items that should be addressed by future work.

11.1 Model Intercomparisons

This work would proceed by furthering an intercomparison of surface energy and mass fluxes derived from in-situ Greenland Climate Network (GC-Net) measurements and those output from regional climate models, i.e. the PSU/NCAR Mesoscale Atmospheric Model (MM5) Polar version [*Cassano et al.*, in press], and the Hamburg High Resolution Atmospheric Model (HIRHAM) [*Rinke et al.*, 1999]. Much of the data are already in hand. An efficient data exchange has already been established with Dr. Annette Rinke at the Alfred Wegener Institute (AWI) in Germany. I have been invited to AWI for 2 weeks in September, 2001 to begin writing a paper. By comparing the surface energy flux parameterizations from more than one state of the art models with in-situ measurements made by GC-Net automatic weather stations and other experiments in Greenland, insight into improving glacial energy and mass balance models will be gained. Given the present availability of in-situ surface energy and mass balance measurements combined with state of the art atmospheric models, the contribution of ice sheet mass balance changes to sea level and ocean circulation changes will be gauged to an unprecedented level of accuracy. An ultimate goal of this research is publication of the results, emphasizing the large scale implications of Greenland ice sheet mass balance for use by the broad scientific community and environmental policy makers.

11.2 Accuracy Assessment of Eddy Flux Correlation Instrumentation

Future work should be concerned with deriving relative and absolute uncertainty estimates for eddy flux correlation instrumentation. While it is useful to estimate the relative accuracy of the eddy flux correlation

instrumentation from side by side comparisons of latent or sensible heat fluxes, the question of absolute calibration is also of crucial importance. One method to perform absolute calibration may be to conduct very precise evaporation pan studies. However, evaporation pans are associated with large uncertainties mentioned in section 3.3. Another issue that comes to mind is the absolute accuracy of humidity readings from the Campbell Scientific fast-response hygrometer (KH-20). The KH-20 is calibrated with reference to a chilled mirror hygrometer. The laboratory calibration indicates small deviations of up to 1.3% in absolute humidity over a range of 1.7 g m^{-3} to 19 g m^{-3}. Information regarding the calibration of the ultrasonic anemometer (CA-27 or CSAT3D), is not indicated in the manufacturer's specifications. Thus we should obtain this information from Campbell Scientific and given this information make an analytical derivation of the uncertainty.

11.3 Portable Eddy Correlation System

The fact that validation measurements are only available from two sites is a potential weakness of this methodology. Future work will be concerned with making eddy correlation measurements at other sites in order to account for potential elevation or region-dependant parameters in aerodynamic profile methods. However, taking eddy flux measurements next to the AWS for only a few hours, in the rapid deployment sense, may not be worth the effort. We need to characterize the skill of the profile methods under different conditions, e.g. blowing snow, melt, snowfall. Getting useful data under certain conditions is a big challenge. Comparisons of profile methods with eddy correlation should last at least one day. Multi-day comparisons are much more preferable.

11.4 Eddy Correlation Measurements During Blowing Snow

To verify that profile methods give appropriate results during blowing snow conditions, it is important to obtain eddy flux correlation measurements during blowing snow conditions. Coincident with the eddy flux measurements should be an AWS with a robust relative calibration dataset to ensure sufficient insight into relative instrument biases and uncertainties are also fully understood.

11.5 Antarctic Surface Water Vapor Fluxes

The comparison of GC-Net results with Antarctic data produced results that fell within the expected range for the one level profile methods. The Antarctic surface water vapor flux has been simulated by a state of the art atmospheric model, the ECHAM-3 [*Van-den-Broeke,* 1997]. However, only the evaporation pan results of *Fujii and Kusunoki* [1982] and *Kameda et al.* [1997] speak to the deposition rates not gauged by one level methods. It would be interesting to analyze vertical humidity profiles over the Antarctic ice sheet to asses the importance of deposition in Antarctica. A similar climate to the Greenland ice sheet should be expected. Sufficient profile measurements at 2 to 5 levels have been made in Antarctica at station Halley, situated on the Brunt ice shelf [*Mann,* 1998]. Of further interest would be to investigate vertical humidity variations along an elevation transect, i.e. that from Dumont d'Urville to Dome C [*Bintanja,* 1998]. However, at these sites humidity is not measured at more than one level. Therefore, either we may persuade those involved with this AWS transect to include an additional humidity measurement level, or we accept the challenge to install AWSs in Antarctica.

11.6 Total Boundary Layer Surface Water Vapor Flux

The use of sondes to derive a vertical profile of water vapor fluxes in the lowest 500 m to 1000 m is key in assessing the net water vapor flux of the entire surface boundary layer. Tether-sondes or kites can be set up to continuously sample the vertical profiles. Of particular interest is the vertical profile of water vapor fluxes occurring during blowing snow. The boundary layer may be saturated in the lowest 5 m, making it impossible for humidity profile measurements below 5 m to gauge vertical water vapor fluxes, while aloft, there is a significant water vapor exchange. Monitoring the moisture exchange near the temperature inversion would certainly provide insight into the importance of the upper part of the surface boundary layer. How much

moisture is exchanged at the top of the boundary layer with the synoptically-driven atmosphere would be an important problem to investigate with such measurements.

11.7 Greenland Moisture Budget

Where does the surface sublimated water vapor go? Answering this question would require analysis of a network of upper air observations over Greenland. This work has begun. In a study of European Center for Medium-Range Weather Forecasts (ECMWF) analysis fields, strong water vapor flux divergence over northeastern Greenland indicate loss of water vapor across the northeast boundary [*Calanca,* 1994]. Another atmospheric moisture budget based on radio-sondes by *Robasky and Bromwich* [1994] confirms the northeastern boundary of Greenland to be the only major water vapor exit region. There was very little moisture exchange along the northern and northwestern perimeters of Greenland in both studies. The south eastern and western boundaries are the entrance regions of water vapor that comprise the precipitation input Greenland. The degree of moisture recycling within the boundaries of the Greenland ice sheet is not directly indicated by these studies. Thus, the question is open for sites in the south, for example. The work of *Trenberth,* [1999] will be useful in defining methods to estimate the proportion of recycled water vapor mass on the continental ice sheet scale.

11.8 Partitioning of Net Surface Water Vapor Flux Components

The question of how much water vapor comes directly from the surface and how much comes from depth in the snow is another partitioning of the net surface water vapor flux that is not addressed in this study. The AWS profile measurements do not partition the vertical components of the water vapor flux. They represent the net effect of upward and downward water vapor pressures.

The extent of moisture transport within the snow is beginning to be understood by modeling studies that to this point simulate the effect of forced convection and molecular diffusion within the snow pack [*Albert,* 1996; *Colbeck,* 1997]. Measurements of wind velocity and humidity in the snow are prohibitive because probes disturb the medium. Mary Albert has indirectly measured air transport within the snow by tracer gas analysis. The work of S. Colbeck is useful for the theoretical and numerical modeling which may contribute to an understanding of the partitioning of net surface water vapor flux components. It would be useful to collaborate with one of these investigators, given GC-Net data as an input, to begin addressing how much water vapor is extracted from the snow pack and how much can be safely assumed to originate from the surface layer of snow directly exposed to the atmosphere.

11.9 East Greenland AWS Transect

Surface water vapor flux and temperature mapping neglects potential east versus west slope differences. The eastern slope is steeper and with greater undulations, so a significant difference in lapse rates may be expected. Thus, future work may be best complemented by more AWSs in east Greenland. Due to the remoteness of East Greenland as compared with West Greenland, efforts may be best concentrated on maintaining an elevation transect in one basin instead of installing more AWSs near the same elevation. As the task of maintaining more and more AWSs requires the efforts of an increasing number of people. An alternative exists to analyze existing east Greenland ice sheet climate data. Data are available from projects as the GGU Storstrømmen AWS transect [*Bøggild et al.,* 1994] or possibly even older sources such as the British North Greenland Expedition [*Simpson,* 1957] or the British Arctic Air Route Expedition [*Chapman,* 1932]. These data do lack consistency with the GC-Net data, however, so more GC-Net stations would be preferred. The best approach may be to investigate existing data first, evaluate if it can be used to construct an eastern-slope lapse rate, hopefully one that varied by month through the annual cycle. If the existing data are insufficient to derive the necessary information, they at least may help in site selection of an east Greenland GC-Net transect.

11.10 Refined Quality Control Procedures

The quality control procedures may be further refined for more realistic measurement correction and

interpolation. An example of a correction improvement is a instrument overheating correction that varies with surface albedo. Conditions of lower surface albedo at JAR1 and JAR2, associated with bare ice and during melt and melt ponding, are associated with less overall overheating. Thus, the overheating correction derived at Swiss Camp overcorrects the air temperature. Other instrument corrections may be derived in the future, for example the effect of wind speed on ventilation of net radiation or humidity measurements. Interpolation may be improved by the use of non-linear interpolation.. Interpolation is problematic, especially for profile measurements. Synthetic values often result in spurious profile differences. For some variables, such as pressure, a spline or polynomial interpolation may produce more accurate results. Different interpolation methods may be tested by comparing synthetic values with artificially removed values. Thus, refinement of quality control procedures will be the focus of future work.

11.11 Energy Balance Modeling using GC-Net Data

Other surface water vapor flux models may be developed for which the GC-Net data provide useful inputs. These may include more accurate profile methods, if for example a parameter such as the eddy diffusivity may be better defined. Yet other profile methods exist that could be evaluated. A reviewer to *Box and Steffen* [submitted] asked why we did not perform a surface energy balance study to determine the net surface water vapor flux. Our reply was that we did not want errors and uncertainties in the other energy balance terms to contaminate our latent heat flux only basis for surface water vapor flux estimates. At this point, it would be worth doing some energy balance modeling, starting with one site, and even one week when humans are on-site to check the instruments. This time period could also include eddy flux correlation measurements, infrared thermometer measurements of surface temperature, and more accurate radiometry. In fact, these data already exist from previous Swiss Camp experiments. Thus, following an approach similar to *Greuel* [1992], surface water vapor fluxes may be estimated, in a way constrained by other energy balance terms. The results of energy balance modeling may be compared with ablation stake measurements to verify that the model produces a realistic melt rate.

… A host of other applications for the GC-Net data are forthcoming. Many of which I am interested in.

12 References

Abdalati, W. and K. Steffen, Passive microwave-derived snow melt regions of the Greenland ice sheet, *Geophysical Research Letters, 22*(7), 787-790, 1995.

Abdalati, W. and K. Steffen, Snow melt on the Greenland ice sheet as derived from passive microwave satellite data, *J. Climate, 10*(2), 165-175, 1997.

Abe-Ouchi, A., Blatter, H., and Ohmura, A., How Does the Greenland Ice Sheet Geometry Remember the Ice Age, *Global and Planetary Change, 9*(1/2), 133-142, 1994.

Albert, M. R., Properties and processes affecting sublimation rates in layered firn, In *Glaciers, ice sheets and volcanoes: a tribute to Mark F. Meier,* (Ed, Colbeck, S. C.) U.S. Department of the Army, Cold Regions Research and Engineering Laboratory, Hanover, NH, 1-4, 1996.

Ambach, W., Untersuchungen zum energieumsatz in der ablationszone des Grönlandischen inlandeises: nachtrag, In *Medd. Grönland*, Vol. 174, 311 pp., 1963.

Ambach, W., Climate Shift of the Equilibrium Line: Kuhn's Concept Applied to the Greenland Ice Cap, *Ann. Glaciol., 6*, 76-78, 1985.

Anderson, P. S., A method for rescaling humidity sensors at temperatures well below freezing, *J. Atmos. Oceanic Tech., 11*(11), 1388-1391, 1994.

Anderson, P. S., Reply to comments on: a method for rescaling humidity sensors at temperatures well below freezing, *J. Atmos. Oceanic Tech., 13*(4), 913-914, 1996.

Anklin, M., Bales, R. C., Mosley-Thompson, E. and Steffen, K., Annual accumulation at two sites in northwest Greenland during recent centuries, *J. of Geophys. Res., 103*(D22), 28775-22783, 1998.

Arya, S. P., Introduction to micrometeorology, Academic Press, 307 pp., 1988.

Bamber, J., Ekholm, S. and Krabill, W. B., A new, high-resolution digital elevation model of Greenland fully validated with airborne laser altimeter data, *J. Geophys. Res. Atmos.*, PARCA Issue), submitted.

Barlow, L. K., Rogers, J. C., Serreze, M. C. and Barry, R. G., Aspects of Climate Variability in the North Atlantic Sector: Discussion and Relation to the Greenland Ice Sheet Project 2 High-resolution Isotopic Signal, *J. Geophys. Res., 102*(C12), 26333-26344, 1997.

Barry, R. G. and Kiladis, G. N., Climatic characteristics of Greenland, In *Climatic and Physical Characteristics of the Greenland Ice Sheet,* (Ed, Radok, U.) CIRES, Boulder, CO, USA, 7-33, 1982.

Barry, R. G., Mountain Weather and Climate, 2nd Edition, Routledge, 402 pp., 1992.

Benson, C. S., Stratigraphic Studies in the Snow and Firn on the Greenland Ice Sheet, In *U.S. Army SIPRE Research Report*, Vol. 70 CRREL, pp. 93., 1962.

Bintanja, R., The contribution of snowdrift sublimation to the surface mass balance of Antarctica, *Ann. Glaciol., 27*, 251-259, 1998.

Bintanja, R., On the glaciological, meteorological, and climatological significance of Antarctic blue ice zones, *Rev. Geophys., 37*(3), 337-359, 1999.

Bintanja, R., Snowdrift suspension and atmospheric turbulence. Part I: Theoretical background and model description, *Boundary-Layer Meteorology, 95*(3), 343-368, 2000a.

Bintanja, R., Snowdrift suspension and atmospheric turbulence. Part II: Results of model simulations, *Boundary-Layer Meteorology, 95*(3), 369-395, 2000b.

Bøggild, C. E., Reeh, N. and Oertner, H., Modeling ablation and mass balance sensitivity to climate change of Storstrømmen, northeast Greenland, *Global and Planetary Change, 9*(1/2), 79-90, 1994.

Box, J. E. and Steffen, K., Sublimation estimates for the Greenland ice sheet using automated weather station observations, *J. Geophys. Res. Atmos.*, submitted.

Braithwaite, R. J. and Olesen, O. B., A simple energy balance model to calculate ice ablation at the margin of the Greenland ice sheet, *J. Glaciol., 36*, 222-228, 1990.

Bromwich, D. H., Chen, Q.-S., Bai, L.-S., Cassano, E. N. and Li, Y., Modeled precipitation variability over the Greenland ice sheet, *J. Geophys. Res. Atmos.*, PARCA Issue), submitted.

Bromwich, D. H., Du, Y. and Hines, K. M., Wintertime Surface Winds over the Greenland Ice Sheet, *Mon. Wea. Rev., 124*, 1941-1947, 1996.

Bromwich, D. H., Robasky, F. M., Keen, R. A. and Bolzan, J. F., Modeled variations in precipitation over the Greenland ice sheet, *J. Climate, 6*, 1253-1267, 1993.

Brutsaert, W., Evaporation into the atmosphere: theory, history, and applications,, Kluwer, 299 pp., 1982.

Budd, W. F., Dingle, W. R. J. and Radok, U., The Byrd Snow Drift Project: outline and basic results, In *Studies in Antarctic Meteorology*, Vol. 9 Antarctic Research Series AGU, 71-134, 1966.

Budyko, M. I., The effect of solar radiation variation on the climate of the Earth, *Tellus, 21*(5), 911-919, 1969.

Calanca, P., The Atmospheric Water Vapor Budget Over Greenland, In *Zürcher Geographische Schriften* ETH, Zürich, pp. 115 pp., 1994.

Cassano, J. J., Parish, T. R. and King, J., Evaluation of turbulent surface flux parameterizations for the stable boundary layer over Halley, Antarctica, *Mon. Wea. Rev., 129*, 26-46, 2001.

Cassano, J., Box, J. E., Bromwich, D., Li, L. and Steffen, K., Verification of polar MM5 simulations of Greenland's atmospheric circulation, J. Geophys. Res. Atmos., in press.

Chapman, S. F., Northern Lights: The Official Account of the British Arctic Air-Route Expedition, 1930-31, 263 pp., 1932.

Chen, Q.-S., Bromwich, D. H. and Bai, L., Precipitation over Greenland retrieved by a dynamic method and its relation to cyclonic activity, *J. Climate, 10*, 839-870, 1997.

Colbeck, S. C., Model of wind pumping for layered snow, *J. Glaciol., 43*(143), 60-65, 1997.

Crowley, T. J. and North, G. R., Paleoclimatology, Oxford University Press, 349 pp., 1991.

Cuffey, K. M. and Marshall, S. J., Substantial Contribution to sea-level rise during the last interglacial from the Greenland ice sheet, *Nature, 404*(4), 591-594, 2000.

Dahl-Jensen, D., Gundestrup, N., Keller, K., Johnsen, S., Gogineni, S.-P., Allen, C., Chuah, T., Miller, H., Kipfstuhl, S. and Waddington, E., A search in north Greenland for a new ice-core drill site, *J. Glaciol., 43*(144), 300-306, 1997.

Dalrymple, P. C., Lettau, H. H. and Wollaston, S. H., South Pole micrometeorological program: data analysis, In *Studies in Antarctic Meteorology*, Vol. 9 (Ed, Rubin, M. J.) AGU, Washington, D.C., 13-57, 1966.

Davis, C. H., Kluever, C. A., and Haines, B. J., Elevation change of the southern Greenland ice sheet, *Science, 279*, 2086-2088, 1998.

Dawson, A. G., Ice Age Earth: Late Quaternary Geology and Climate, Routledge, 293 pp., 1992.

Déry, S. J., Taylor, P. A. and Xiao, J., The thermodynamic effects of sublimating blowing snow in the atmospheric boundary layer, *B. Lay. Met.*, *89*, 251-283, 1998.

Dethloff, K., Rinke, A., Lehmann, R., Christensen, J., Botzet, M. and Machenhauser, B., Regional climate model of the Arctic atmosphere, *J. Geophys. Res.*, *101*(D18), 23401-23422, 1996.

Dudhia, J., A non-hydrostatic version of the Penn State - NCAR mesoscale model: validation tests and simulation of an Atlantic cyclone and cold front, *Mon. Wea. Rev.*, *121*, 1493-1513, 1993.

Dyer, A. J. and Hicks, B. B., Flux-gradient relationships in the constant flux layer, *Q. J. Roy. Met. Soc.*, *96*, 715-721, 1970.

Dyunin, A. K., Fundamentals of the theory of snow drifting, , Vol. Technical Translation 952 U.S.S.R. Izcest. Sibirsk, Otdel. Akad. Nauk./National Research Council, Ottawa, 1959.

Ekholm, S., A full coverage, high-resolution, topographic model of Greenland, computed from a variety of digital elevation data, *J. Geophys. Res.*, *B10*, 21961-21972, 1996.

Forrer, J. and Rotach, M. W., On the Turbulence Structure in the Stable Boundary Layer over the Greenland Ice Sheet, *B. Layer Met.*, *85*, 111-136, 1997.

Fujii, Y. and Kusunoki, K., The role of sublimation and condensation in the formation of the ice sheet surface at Mizuho Station, Antarctica, *J. Geophys Res.*, *98*, 4293-4300, 1982.

Garratt, J. R., The atmospheric boundary layer, Cambridge Univ. Press, 316 pp., 1992.

Gosink, J. P., The extension of a density current model of katabatic winds to include the effects of blowing snow and sublimation, *B. Lay. Met.*, *49*, 367-394, 1989.

Grell, G. A., Dudhia, J., and Stauffer, D. R., A description of the fifth-generation Penn State/NCAR mesoscale model (MM5), *NCAR Tech. Note,* NCAR/TN-398+STR, 1994.

Greuel, W., Numerical modeling of the energy balance and the englacial temperature at the ETH camp, Geogr. Inst. ETH, Zurich, 81 pp., 1992.

Hammer, C., Mayewski, P. A., Peel, D. Stuiver, M., Executive summary: GISP-2 and GRIP ice core results, *J. Geophys. Res., 102*(C12), 26315, 1997.

Henderson-Sellers, A., Contemporary Climatology, Wiley & Sons, pp., 1986.

Henneken, E. A. C., Bink, N. J., Vugts, H. F., Cannemeijer, F. and Meesters, A. G. C. A., A case study of the daily energy balance near the equilibrium line on the Greenland ice sheet, *Global and Planetary Change, 9*, 69-78, 1994.

Henneken, E. A. C., Meesters, A. G. C. A., Bink, N. J., Vugts, H. F. and Cannemeijer, F., Ablation near the equilibrium line on the Greenland ice sheet, southwest Greenland, July 1991, *Zeit. Gletsch. Glazialgeologie, 33*(2), 173-184, 1997.

Högström, U., Nondimensional wind and temperature profiles in the atmospheric surface layer: a re-evaluation, *B. Lay. Met, 42*(1/2), 55-78, 1988.

Huybrechts, P. H., The present evolution of the Greenland Ice Sheet: an assessment by modeling, *Global and Planetary Change, 9*(1/2), 39-45, 1994.

Inoue, J., Surface drag over the snow surface of the Antarctic plateau 1. factors controlling surface drag over the katabatic wind region, *J. Geophys. Res., 94*, 2207-2217, 1989.

Ishikawa, N., Owens, L. F. and Sturman, A. P., Heat balance characteristics during fine periods on the lower parts of the Franz Josef Glacier, south Westland, New Zealand, *Int. J. Clim., 12*, 397-410, 1992.

Jellinek, H. H. G., Compressive strength properties of snow, *U.S. Army Snow Ice and Permafrost Establishment (SIPRE)*, 16 pp., 1957.

Kameda, T., Azuma, N., Furukawa, T., Ageta, Y. and Takahashi, S., Surface mass balance, sublimation and snow temperatures at Dome Fuji Station, Antarctica, in 1995, In *Proceedings of the NIPR Symposium on Polar Meteorology and Glaciology*, Vol. 11 NIPR, Tokyo, Japan, 24-34, 1997.

Kaser, G., Measurement of evaporation from snow, *Archives for Meteorology, Geophysics, and Bio-climatology, 30*(4), 333-340, 1982.

Knight, C. A., Ice nucleation in the atmosphere, *Adv. Colloid. Interfac. Sci., 10*, 369-395, 1979.

Kobayashi, D., Studies of snow transport in low-level drifting snow, *Low Temperature Science Series, A*(24), 1-58, 1972.

Kojima, K., Evaporation rate of snow at the surface of a snow cover, observations in Sapporo and Moshiri, Hokkaido, *Low Temperature Science, 44*, 49-62, 1985.

Krabill, W., Abdalati, W., Frederick, E., Manizade, S., Martin, C., Sonntag, J., Swift, R., Thomas, R., Wright, W. and Yungel, J., Greenland Ice Sheet: high-elevation balance and peripheral thinning, Science, 289, 428-429, 2000.

Lee, L. W., Sublimation of snow in a turbulent atmosphere, U. of Wyoming, Laramie, WY, 162 pp., 1975.

Lettau, H., Wind and temperature profile prediction for diabatic surface layers including strong inversion cases, *B. Lay. Met., 17*, 443-464, 1979.

Li, L. and Pomeroy, J. W., Estimates of threshold wind speeds for snow transport using meteorological data, *J. Appl. Met., 36*(3), 205-21, 1997.

Lister, H. and Taylor, P. F., Heat balance and ablation on an Arctic glacier, *Meddr. Grönland, 158*(7), 1-54, 1961.

Loewe, F., Transport of snow on ice sheets by the wind, in studies on drifting snow, Melbourne University, Australia, 69 pp., 1970.

Long, D. G., and Drinkwater, M. R., Cryosphere Applications of NSCAT Data, *IEEE Trans. Geosci. and Remote Sens., in press*.

Makkonen, L., Comments on "a method for rescaling humidity sensors at temperatures well below freezing", *J. Atmos. Oceanic Tech., 13*(4), 911-912, 1996.

Mann, G. W., Surface heat and water vapor budgets over Antarctica, Environmental Centre, Leeds, UK, 279 pp., 1998.

Mann, G. W., Mobbs, S. D. and Anderson, P. S., Profile measurements of blowing snow at Halley, Antarctica, *J. Geophys. Res., 105*(D19), 24491-24508, 2000.

McKenna, N. and Nickling, W. G., Momentum Extraction with Saltation: Implications for Experimental Evaluation of Wind Profile Parameters, *B. Lay. Met., 68*, 35-50, 1994.

Mellor, M. and Radok, U., Some properties of blowing snow, In *Antarctic Meteorology*, Pergamon Press, 333-346, 1960.

Monteith, J. L. and Unsworth, M., Principles of environmental physics, Routledge, 291 pp., 1990.

Moseley-Thompson, E., McConnel, J., Bales, R., Li, Z., Steffen, K., Thompson, L. G., Edwards, R. and Bathke, D., Local to regional-scale variability of Greenland accumulation from PARCA cores, *J. Geophys. Res. Atmos.*, submitted.

Munn, R. E., Descriptive micrometeorology, Academic Press, 245 pp., 1966.

Nelson, J. A., A description of the fifth generation Penn State/NCAR mesoscale model (MM5), Western Region Technical Attachment, 1998.

Oerlemans, J., Possible changes in the mass balance of the Greenland and Antarctic ice sheets and their effects on sea level, in climate and sea level change, Cambridge University Press, 144-161, 1993.

Oerlemans, J., Bjornsson, H., Kuhn, M., Obleitner, F., Palsson, F., Smeets, C. J. P. P., Vugts, H. F. and de-Wolde, J., Glacio-meteorological studies on Vatnajokull, Iceland: an overview, *Boundary Layer Met., 92*(1), 3-26, 1999.

Oerlemans, J. and Vugts, H. F., A meteorological experiment in the melting zone of the Greenland ice sheet, *Bull. Amer. Met. Soc., 74*(3), 355-365, 1993.

Ohmura, A., New temperature distribution maps for Greenland, *Zeit. Gletsch. Glazialgeol., 23*(1), 1-45, 1987.

Ohmura, A., Calanca, P., Wild, M. and Anklin, M., Precipitation, accumulation, and mass balance of the Greenland ice sheet, *Zeit. Gletsch. Glazialgeol., 35*(1), 1-20, 1999.

Ohmura, A., Konzelmann, T., Rotach, M., Forrer, J., Wild, M., Abe-Ouchi, A. and Toritani, H., Energy balance for the Greenland ice sheet by observation and model computation, *In H. Jones, T. Davies, A. Ohmura, and E. Morris (eds.), Snow and ice covers: Interaction with the atmosphere and ecosystems, Number 223 in IAHS Publication,* 85-94, 1994.

Ohmura, A. and Reeh, N., New precipitation and accumulation maps for Greenland, *J. Glaciol., 37*(125), 140-148, 1991.

Ohmura, A., Wild, M. and Bengtsson, L., A possible change in mass balance of Greenland and Antarctica in the coming century, *J. Climate, 9*(9), 2124-2135, 1996.

Oke, T. R., Boundary layer climates, Methuen & Co., 435 pp., 1987.

Olesen, O. B. and Braithwaite, R. J., Field stations for glacier climate research, West Greenland, *In Oerlemans, J., (eds.), Glacier fluctuations and climate change. Dordrecht, Kluwer Academic Publishers,* 219-233, 1989.

Patterson, W. S. B., The physics of glaciers, Pergamon Press, 480 pp., 1994.

Piexoto, J. P. and Oort, A. H., Physics of climate, AIP, 520 pp., 1992.

Pomeroy, J. W., Wind transport of snow, In *Div. of Hydrology, U.* of Saskatchewan, Saskatoon, 226 pp., 1988.

Pomeroy, J. W. and Essery, R. L. H., Turbulent fluxes during blowing snow: field tests of model sublimation predictions, *Hydrol. Process., 13*, 2963-2975, 1999.

Pomeroy, J. W. and Gray, D. M., The Prairie Blowing Snow Model: characteristics, validation, operation, *J. Hydrology, 144*, 165-192, 1993.

Pomeroy, J. W. and Gray, D. M., Snowcover: accumulation, relocation and management, 144 pp., 1995.

Pomeroy, J. W. and Male, D. H., Optical properties of blowing snow, *J. Glaciol., 34*(116), 3-10, 1988.

Prandtl, L., Bericht ueber Untersuchungen zur ausgebileten turbulenz, *ZAMM, 3*, 136-139, 1925.

Reeh, N., Workshop on the calving rate of west Greenland glaciers in response to climate change, In Calving from Greenland glaciers, Danish polar Center, Copenhagen, DK, pp. 171 pp., 1994.

Reeh, N., Mass Balance of the Greenland Ice Sheet: Can Modern Observations Reduce the Uncertainty?, Geografiska Annaler, 81 A(4), 735-742, 1999.

Reynolds, O., On the extent and action of the heating surface of steam boilers, In *Proc. Manchester Lit Phil Soc*, 8, 1874.

Rinke, A., Dethloff, K., Spekat, A., Enke, W. and Hesselbjerg-Christensen, J., High resolution climate simulations over the Arctic, *Polar Research*, 18(2), 143-150, 1999.

Robasky, F. M. and Bromwich, D., Greenland Precipitation Estimates from the Atmospheric Moisture Budget, *Geophys. Res. Let., 21*(25), 2495-2498, 1994.

Schmidt, R. A. and Gluns, D. R., Sublimation of snow - The basics, In International Snow Science Workshop, October 4-8, Breckenridge, CO, USA., 1992.

Schmidt, R. A., Sublimation of Wind Transported Snow - A Model, USDA, Fort Collins, CO, pp. 24., 1972.

Schmidt, R. A., Properties of blowing snow, *Reviews of Geophysics and Space Physics, 20*(1), 39-44, 1982a.

Schmidt, R. A., Vertical profiles of wind speed, snow concentration, and humidity in blowing snow, *B. Layer Met., 23*, 223-246, 1982b.

Serreze, M. C., Rehder, M. C. and Barry, R. G., The distribution and transport of atmospheric water vapor over the arctic basin, *Int. J. Climatol*., 15, 709-727, 1995.

Serreze, M. C., Box, J. E., Barry, R. G. and Walsh, J. E., Characteristics of Arctic synoptic activity, 1952-1989, *J. Met. Atmos. Phys.*, 51(3-4), 147-164, 1993.

Shuman, C. A., Steffen, K., Box, J. E. and Stearns, C. R., A dozen years of temperature observations at the summit: central Greenland automatic weather stations 1987-1999, *J. Climate,* in press.

Simpson, C. J. W., North ice: the British North Greenland expedition, H & S, 384 pp., 1957.

Smeets, C. J. P. P., Duynkerke, P. G. and Vugts, H. F., Turbulence characteristics of the stable boundary layer over a mid-latitude glacier. Part I: A combination of katabatic and large-scale forcing, *B. Lay. Met., 87*(1), 117-145, 1998.

Souchez, R., The Buildup of the Ice Sheet in Central Greenland, *J. Geophys. Res., 102*(C12), 26317-26323, 1997.

Stearns, C. R. and Weidner, G. A., Sensible and Latent heat flux estimates in Antarctica, in Antarctic meteorology and climatology: studies based on automatic weather stations, *Antarctic Research Series, 61*, 109-138, 1993.

Steffen, K., Surface energy exchange at the equilibrium line on the Greenland ice sheet during onset of melt, *Ann. Glaciol., 21*, 13-18, 1995.

Steffen, K. and Box, J. E., Surface climatology of the Greenland ice sheet: Greenland Climate Network 1995-1999, *J. Geophys. Res. Atmos.,* in press.

Steffen, K., Box, J. E. and Abdalati, W., Greenland climate network: GC-Net, CRREL, 98-103 pp., 1996.

Steffen, K. and DeMaria, T., Surface energy fluxes of arctic winter sea ice in Barrow Strait, *J. Appl. Met., 35*(11), 2067-2079, 1996.

Stull, R. B., An introduction to boundary layer meteorology, Kluwer Publishers, 666 pp., 1988.

Tabler, R. D., New engineering criteria for snow fence systems, Nat Res. Council Trans. Res. Board, pp. 65-78., 1974.

Tabler, R. D., Estimating the transport and evaporation of blowing snow, In *Symp. Snow Mgmt. on the Great Plains*, Vol. 73 Great Plains Agricultural Council (GPAC), Bismark, ND, 85-104., 1975.

Tabler, R. D., Snow Transport as a Function of Wind Speed and Height, In *Cold Regions 6th Int. Specialty Conference, TCCP/ASCE*W. Lebanon, NH, 729-738., 1991.

Tabler, R. D., Design guidelines for the control of blowing and drifting snow, Strategic Highway Research Council, Washington, DC, 364 pp., 1994.

Tabler, R. D., Benson, C. S., Santana, B. W. and Ganguly, P., Estimating snow transport from wind speed records: Estimates versus measurements at Prudhoe Bay, Alaska, In *Western Snow Conference*, Sacramento, CA, 61-72., 1990a.

Tabler, R. D., Pomeroy, J. W. and Santana, B. W., Drifting snow, In *Cold Regions Hydrology and Hydraulics*, 95-145, 1990b.

Tabler, R. D. and Schmidt, R. A., Weather Conditions that Determine Snow Transport distances at a Site in Wyoming, In *Int. Symp. On the Role of Snow and Ice in Hydrology*, Vol. IAHS/UNESCO/WMO: Physics and Chemistry of Snowfall and Snow Distribution, Banff, Alberta, Canada, 118-127., 1972.

Thomas, R., Ice Sheets, Atlas of Satellite Observations Related to Global Change, Cambridge Univ. Press, 385-400, 1993.

Thomas, R., The Program for Arctic Regional Climate Assessment (PARCA): executive summary, *J. Geophys. Res.*, submitted.

Thomas, R., Akins, T., Csatho, B., Fahnestock, M., Gogineni, P., Kim, C. and Sonntag, J., Mass balance of the

Greenland ice sheet at high elevations, *Science, 289*, 426-427, 2000.

Thornthwaite, C. W. and Holzman, B., The Determination of evaporation from land and water surfaces, *Month. Wea. Rev., 67*, 4-11, 1939.

Thorpe, A. D. and Mason, B. J., The evaporation of ice spheres and ice crystals, *British J. Appl. Phys., 17*(4), 541-548, 1966.

Van-den-Broeke, M. R., Spatial and temporal variation of sublimation on Antarctica: Results of a high-resolution general circulation model, *J Geophys. Res., 102*(D25), 29765-29777, 1997.

Warrick, R. A., Provost, C. L., Meier, M. F., Oerlemans, J. and Woodworth, P. L., Changes in Sea Level, In *Climate Change 1995: The Science of Climate Change,* Cambridge Univ. Press, 358-405, 1996.

Webb, E. K., Profile relationships: the log-linear range, and extension to strong stability, *Q. J. Roy. Met. Soc., 96*, 67-90, 1970.

Wu, J., Evaporation due to spray, *J. Geophys. Res., 79*(27), 4107-4109, 1974.

Xiao, J., Bintanja, R., Déry, S. J., Mann, G. W. and Taylor, P. A., An intercomparison among four models of blowing snow, *Boundary Lay. Met., 97*(1), 109-135, 2000.

Zwally, H. J., Growth of Greenland Ice Sheet: Interpretation, *Science, 246*, 1589-1591, 1989.

Appendix

A. Monthly Latent Heat Fluxes based on a One-level Profile Method

Monthly latent heat fluxes based on the less reliable 'one-level' method are included here because there of interest for comparison with previous results from Antarctica and particularly because general atmospheric circulation models, such as those compared with GC-Net results in Chapter 7, employ similar assumptions of constant surface saturation and surface roughness.

The main distinction between the two level and one level method annual cycles is smaller one level method winter deposition. The relative peak in summer surface water vapor flux is often slightly larger for one level method results than two level method results. Interannual variability in the one level method results is not as great as for the two level methods, arising from the fact that the two level method is more sensitive to vertical specific humidity variations.

The results of the one level method are given for the same representative sites as above in the Appendix. The total surface water vapor flux from one level monthly means indicate greater surface water vapor fluxes at all sites (Table A.1) as compared to the two level results. The one level method monthly means are not greatly off those for many cases as compared to the 2LM monthly means covering the same time period. Wintertime 1LM results are very near zero. Surface water vapor fluxes increase as the latitude of the sites decreases resulting from increasingly longer and more intense ablation periods and implicating regional temperature variations. At the northern sites, latent heat fluxes are relatively small year round. The regional patterns of monthly and annual surface water vapor flux are best made in context of the sublimation maps produced from the results of either profile method-type in chapter 8. Furthermore, it is in this context that the major differences between the one level and two level methods are apparent.

Table A.1, Monthly Latent Heat Fluxes and the Corresponding Annual Sublimation Rate for Individual Years at GC-Net Sites based on the One Level Profile Method

Site	W m^{-2}	Jan.	Feb.	Mar	Apr	May	Jun	Jul	Aug	Sep	Oct	Nov	Dec	*Dm* [mm]	Year
Swiss Camp	mean	0.8	0.7	4.1	4.4	18.5	21.8	10.7	9.2	5.9	1.2	7.9	6.3	-91	1997
	1 σ	2.3	1.3	4.2	5.8	15.4	11.2	9.4	8.8	6.6	1.9	12.4	8.5		
CP1	mean	2.4	-0.2	0.1	3.7	6.1	7.5	5.3	4.2	0.3	-0.2	-0.4	-0.5	-27	1997.5 : 1998.4
	1 σ	5.2	0.2	0.9	3.9	5.8	5.3	5.0	4.7	1.5	0.6	0.8	0.7		
NASA-U	mean	0.3	-0.1	0.0	2.1	6.0	11.9	10.9	5.6	3.6	-0.0	-0.1	-0.3	-38	1998
	1 σ	1.2	0.2	0.4	3.0	6.4	8.7	7.2	5.2	4.8	0.3	0.7	0.3		
GITS	mean	0.3	-0.2	0.5	0.6	4.1	7.7	7.5	5.1	1.0	-0.0	0.0	-0.0	-25	1996
	1 σ	0.8	0.8	0.9	1.4	4.2	6.1	6.1	5.0	1.9	0.6	0.8	2.2		
Humboldt	mean	-0.3	-0.2	-0.0	0.6	2.7	7.4	9.0	3.3	1.7	-0.2	-0.2	-0.4	-22	1998
	1 σ	0.7	0.2	0.4	1.6	3.2	5.3	6.9	3.3	2.7	0.7	0.7	0.4		
Summit	mean	-0.2	-0.2	-0.1	0.1	2.0	4.9	4.0	2.0	0.5	-0.1	-0.1	-0.1	-10	1996.4 : 1999.5
	1 σ	0.2	0.2	0.2	0.7	3.1	5.8	4.5	3.1	1.3	0.2	0.2	0.2		
Tunu-N	mean	-0.5	-0.3	-0.3	0.3	2.3	5.6	6.6	3.2	1.1	2.0	1.3	-0.0	-20	1998
	1 σ	0.4	0.2	0.2	1.4	2.7	4.2	5.4	3.5	1.8	2.7	2.5	0.1		
DYE-2	mean	-0.5	-0.3	1.2	2.9	6.1	27.3	12.4	8.7	5.4	1.3	0.3	0.9	-67	1997
	1 σ	2.7	0.3	2.6	5.7	4.8	17.8	11.7	10.4	7.4	3.1	2.5	4.8		
JAR1	mean	11.3	4.8	9.5	6.6	20.0	30.1	12.9	12.4	13.7	5.6	14.6	14.8	-153	1997
	1 σ	20.7	7.2	11.7	9.1	16.3	21.7	15.1	13.8	15.9	7.6	19.2	19.7		
JAR1	mean	12.2	1.7	3.1	17.8	13.6	20.2	20.0	14.9	20.7	6.8	13.7	13.1	-154	1998
	1 σ	13.5	3.6	4.9	18.4	13.4	15.1	19.5	17.5	19.3	10.5	17.5	16.6		
Saddle	mean	-1.1	-0.5	-0.4	1.7	7.9	8.8	6.4	5.1	4.3	0.4	0.7	0.7	-34	1998
	1 σ	1.1	0.7	1.5	3.4	9.6	8.3	7.2	6.3	5.1	0.9	1.4	0.9		
Saddle	mean	0.1	0.3	0.9	2.4	4.8	6.3	9.4	5.9	2.3	0.3	0.0	-0.2	-31	1999
	1 σ	0.4	0.8	2.7	3.6	5.8	5.9	8.8	6.2	4.4	1.1	0.5	0.4		
South Dome	mean	*	*	0.1	5.2	6.8	6.4	9.7	5.6	2.2	1.8	0.1	-0.4	-35	1999
	1 σ			1.4	8.6	9.4	7.2	12.4	9.3	6.7	3.6	1.3	0.6		
NASA-E	mean	-0.3	-0.1	0.3	0.0	2.1	5.7	4.5	3.3	0.0	-0.2	-0.1	-0.4	-14	1997.4 : 1998.5
	1 σ	0.4	0.2	0.8	1.1	2.5	6.0	4.8	5.3	1.2	0.5	0.2	0.5		
CP2	mean	3.5	-0.0	0.5	5.2	9.3	19.6	9.4	7.9	4.5	0.8	1.6	0.9	-60	1997.4 : 1998.5
	1 σ	6.6	0.3	1.3	5.1	9.0	11.8	9.0	7.5	5.5	2.1	4.5	3.2		
NGRIP	mean	-0.4	-0.2	0.1	-0.3	0.7	4.3	2.9	1.6	0.0	-0.2	-0.2	-0.4	-7	1998
	1 σ	0.5	0.2	0.5	1.1	2.3	4.8	3.3	2.7	0.8	0.3	0.2	0.5		
NASA-SE	mean	-0.1	0.0	0.4	1.9	5.0	7.4	9.4	4.9	2.1	0.2	-0.2	-0.2	-29	1999
	1 σ	0.6	0.5	1.0	3.1	6.3	7.2	11.1	6.1	3.9	1.1	1.0	0.2		
JAR2	mean	5.8	8.1	6.6	21.9	13.9	41.4	22.2	16.9	20.1	13.4	7.6	8.2	-184	1999.8 : 2000.7
	1 σ	9.1	10.4	9.3	16.2	16.3	24.9	18.0	13.1	16.2	15.4	11.5	10.7		

* - insufficient data.

B. Eliminating the Effect of Compaction from Surface Height Records

At Summit, there is approximately 25 cm y^{-1} surface height reduction due to the compaction of the top 10 m of firn [*Gordon Hamilton*, personal communication]. The compaction between the surface and some depth *z* is modeled by integrating annual 1 cm incremental compaction values varying with depth according to an exponential curve fit to Hamilton's observation. The compaction rate at 10 m is set equal to 5% of the compaction rate from 1 cm to 2 cm from the surface.

$$C = 0.0312\int_1^z e^{-0.03}dz \qquad \text{Eq. A.1}$$

where *C* is the surface lowering (cm y^{-1}) from the surface to depth *z*. The depth of the GC-Net AWS masts varies from site to site depending on activation date and the accumulation rate. Using the average surface height increase given in *Steffen and Box,* [in press] and knowledge of the initial mast depth, annual mast depth values (Table B) are calculated and used with the compaction formulation to derive annual surface height reduction that would otherwise bias surface height measurements of accumulation or positive and negative surface height change components. Values of surface lowering with reference to the AWS mast-base are in the range of approximately 5 cm y^{-1} to 27 cm y^{-1}, respectively, while surface height increases due to accumulation range from 0.40 m at Tunu-N to 1.7 m at South Dome [*Steffen and Box,* in press].

Compaction should be a function of temperature, with larger firn deflation rates in summer when snow metamorphism peaks. However, given only one compaction estimate from Summit and that the compaction rate did not vary through the year, a temperature dependant compaction model is not developed.

Table A.2, End of Year Depth of GC-Net AWS Masts

Site	1995	1996	1997	1998	1999	2000
Swiss Camp	3.5	2.8	2.7	2.6	2.5	2.4
CP1	3.8	5.1	6.4	7.8	9.1	10.4
NASA-U	3.7	4.9	6.0	7.2	8.4	9.6
GITS	3.7	5.1	6.4	7.8	9.1	10.4
Humboldt Gl.	3.3	3.8	4.2	4.7	5.2	5.7
Summit	*	3.4	4.0	4.6	5.3	5.9
TUNU-N	*	2.7	3.1	3.5	3.9	4.3
DYE-2	*	3.5	4.5	5.4	6.3	7.2
JAR1	*	2.5	1.7	0.9	2.5	1.7
Saddle	*	*	3.8	5.0	6.3	7.6
South Dome	*	*	4.1	6.0	7.8	9.7
NASA-E	*	*	3.2	3.6	4.0	4.4
CP2	*	*	3.5	5.2	6.8	8.5
NGRIP	*	*	3.3	3.8	4.3	4.8
NASA-SE	*	*	*	3.2	5.2	7.2
KAR	*	*	*	*	2.9	4.9
JAR2	*	*	*	*	3.5	1.0

* - AWS not yet activated

C. Accumulation derived from Surface Height Measurements

Year-specific accumulation is derived using linear regression fits to daily surface height change measurements and assuming the depth density relationship derived in section 3.4. Swiss Camp and JAR1/JAR2 have non-linear surface height records that result in a zero or negative slope which makes it impossible to derive the accumulation rate using this method.

Table A.3, Accumulation [mm y^{-1}] Derived from Surface Height Measurements

Site	A 1995	A 1996	A 1997	A 1998	A 1999	A 2000	r^2 1995	r^2 1996	r^2 1997	r^2 1998	r^2 1999	r^2 2000	A**** (Ice Core)
Swiss Camp	**	**	**	**	**	**	*	0.11	0.22	0.17	0.3	0.32	500
CP1	409	519	444	232	*	411	0.76	0.93	0.88	0.85	0.61	0.92	480
NASA-U	326	400	512	243	470	186	0.82	0.88	0.90	0.94	0.97	0.76	330
GITS	531	406	*	*	232	260	0.96	0.90	*	*	0.87	0.79	350
Humboldt	97	218	191	203	174	269	0.52	0.90	0.93	0.9	0.96	0.87	140
Summit	***	274	216	186	271	126	*	0.84	0.97	0.97	0.86	0.66	200
Tunu-N	***	*	162	155	205	*	*	0.38	0.91	0.9	0.95	0.40	100
DYE-2	***	460	339	233	*	275	*	0.95	0.91	0.96	0.45	0.86	300
JAR1	***	**	**	**	**	**	***	0.34	0.43	0.57	0.31	0.38	550
Saddle	***	***	*	309	363	*	*	*	0.90	0.98	0.95	*	450
South Dome	***	***	*	517	456	*	*	*	0.85	0.97	0.9	*	670
NASA-E	***	***	*	204	271	*	*	*	0.87	0.94	0.96	*	150
CP2	***	***	*	322	*	*	*	*	0.89	0.86	0.38	*	670
NGRIP	***	***	*	188	103	190	*	*	*	0.96	0.88	0.91	170
NASA-SE	***	***	***	538	472	*	*	*	*	0.97	0.90	*	600
JAR2	***	***	***	***	*	*	*	*	*	*	0.68	0.62	550

* - insufficient data
** - linear fit does not represent accumulation due to non-linear surface height change.
*** - AWS not yet installed
**** - see section 3.4